Synthesis and Evaluation of GAT-1 Selective PET Probes

by

Alexandra Sowa

A dissertation submitted in partial fulfillment
of the requirements for the degree of
Doctor of Philosophy
(Medicinal Chemistry)
in the University of Michigan
2018

Doctoral Committee:

Professor Peter J.H. Scott, Chair
Professor Robert A. Koeppe
Research Professor Scott D. Larsen
Assistant Professor Anna Schwendeman

Alexandra R Sowa

sowa@umich.edu

ORCID iD: 0000-0003-3991-171X

Dedication

This dissertation is dedicated to my parents, John and Kathy Sowa, and to my fiancé Mitchell Dumond. Without their support, this wouldn't have been possible.

Acknowledgements

Less than 2% of Americans have earned a Ph. D., and few, if any, of those were earned alone. I have many people to thank for support, guidance, training, or just for making sure I was fed over the last 5 years.

Professor Peter J.H. Scott has made an excellent graduate mentor and PI. If I had joined another lab, I think I may have not made it through the whole program; his mentorship helped refocus me during many hurdles in the Ph.D. process. The radiochemistry group he leads, both clinical and research, is made up of many talented, and welcoming scientists. His dedication to this group helped shape my graduate experience. I would also like to express appreciation for my graduate committee, Scott Larsen, Robert Koeppe, and Anna Schwendeman. Thank you for agreeing to be part of my graduate career, and for the insight and advice you offered along the way.

In the Radiochemistry group at U of M, I would like to thank many people who positively impacted my graduate tenure, both professionally and socially. I had the distinct pleasure of working with Dr. Xia Shannon Shao, carbon-11 chemistry expert, as well as one of the kindest people you will meet. I am forever grateful for her time, patience and excellent teaching. I am also grateful for support from Missy Topper Rodnick for brief professional mentoring sessions, making herself available to train a graduate student, and, perhaps most importantly, for comic relief. I must also thank Timothy Desmond, FDG chemist, and biochemist extraordinaire, as well as Bradford Henderson, HPLC whisperer, and official signer of FDG batch records for their support both with aspects of my project

and for being great coworkers in clinical synthesis. Thanks must also be given to Brian Hockley, who guided my introduction to [^{18}F]-chemistry, offered career advice, and always encourages self-care and adventure, things that are typically under-used in most graduate careers.

Likewise, I would like to acknowledge both current and former members of the Scott Group: Stephen Thompson, Andy Mossine, So Jeong Lee, Stefan Verhoog, and Allen Brooks. These great scientists have offered the best support one could ask for in everything from synthesis troubleshooting to the best restaurant to go to. Thank you as well to my fellow graduate students. Thank you for sharing this experience with me. To Megan Stewart (KAW KAW!), thank you for sharing with me, both in the lab and outside of it. To Lindsey Drake, and Sean Tanzey, thank you for your input on drafts, presentations, outfit choices, and playlists.

A heartfelt thanks to my family and friends. From a young age, my parents, John and Kathy Sowa, impressed on me how important education is, although I'm not sure if they anticipated I would take it this far. They never questioned my decision to earn a doctorate, and that alone was support. I have been blessed with parents who don't ask why I want to do something, but instead ask how they can help me achieve my goals. Your support, through homecooked meals, brewery visits, or pep talks, was necessary for my success. I would also like to thank my best friends, Stevi Edmunds, and Haley Newton, for always being available either via phone or in person for pep talks, vent sessions, or ice cream. Lastly, I'm not sure how to thank Mitchell Dumond enough. I am eternally grateful for your endless support over the last five years. I love you.

Table of Contents

List of Tables

.

List of Figures

List of Schemes

List of Equations

Abstract

Positron emission tomography (PET) is a high resolution, non-invasive functional imaging technique used for observation of biochemical processes *in vivo.* This thesis describes work towards using this imaging modality to better understand the processes of the major inhibitory neurotransmitter gamma(γ)-amino butyric acid (GABA). The GABAergic system is understood to be involved in many neurological diseases and disorders including Alzheimer's disease, epilepsy, schizophrenia, autism and depression. In the GABAergic system, GABA receptors and transporters are targets for drug development as well as investigation as biomarkers. While imaging of the post-synaptic GABAergic receptor subtype $GABA_A$ is possible with the use of [^{11}C]flumazenil ([^{11}C]FMZ), there is no complimentary PET radiotracer enabling *in vivo* imaging of GABA in pre-synaptic neurons. Located pre-synaptically and in high abundance in areas such as the cortex and basal ganglia, GABA Transporter subtype 1 (GAT-1) presents as an interesting target for pre-synaptic GABA imaging. Studies have shown an increase in GAT-1 expression, especially in the cortex, in the schizophrenic brain. GAT-1 is responsible for removal of GABA from the synaptic cleft, thereby ending its action on post-synaptic GABA receptors. Tiagabine was approved by the FDA in 1997 and remains the only GAT-1 inhibitor available today. Many structure activity relationship (SAR) studies have sought to improve the selectivity and affinity of tiagabine for GAT-1. Some research has been successful in the radiolabeling of these compounds for imaging for preclinical evaluation, but as of yet, no radiotracer has proven successful or advanced to widespread

clinical use. To address this urgent need in functional neuroimaging, this work is focused upon developing a GAT-1 selective, blood-brain barrier (BBB) permeable radiotracer for use in PET imaging of the GABAergic system.

The synthesis and preliminary evaluation of a number of novel GAT-1 selective PET tracers is described herein. Scaffolds with high affinity and excellent selectivity for GAT-1 were used as leads for adaptation into new PET radiotracers. Successful [^{18}F]radiofluorination of one scaffold was promising, but subsequent *in vivo* evaluation indicated poor BBB permeability. Additional studies using carbon-11 to label additional small molecule GABA uptake inhibitors were undertaken to test our hypothesis that low brain uptake was due to the highly polar zwitterionic nipecotic acid moiety. As the acid group is necessary for high affinity binding to GAT-1, it cannot be simply removed or esterified. Therefore, future efforts in GAT-1 radiotracer design will need to investigate carboxylic acid bioisosteres in an attempt to improve brain uptake while maintaining affinity for GAT-1. Our preliminary efforts in this direction have focused upon a GAT-1 inhibitor bearing a thiazolyl bioisostere. Synthesis and preliminary evaluation of the new radiotracer are also described in this thesis, and the reasonable affinity for GAT-1 and excellent brain uptake show good promise for 2nd generation radiotracers going forward.

Chapter 1
Introduction

A. Positron Emission Tomography (PET) Imaging

Positron emission tomography (PET) is a non-invasive, high resolution, in vivo imaging modality that utilizes radiopharmaceuticals (PET tracers) to detect biological targets for the development of therapeutics, diagnosis of disease, and monitoring of treatments. The field of PET involves a bench to bedside path from the production of radionuclides, through radiochemistry, to administration and imaging of the radiopharmaceutical (Figure 1-1).[1]

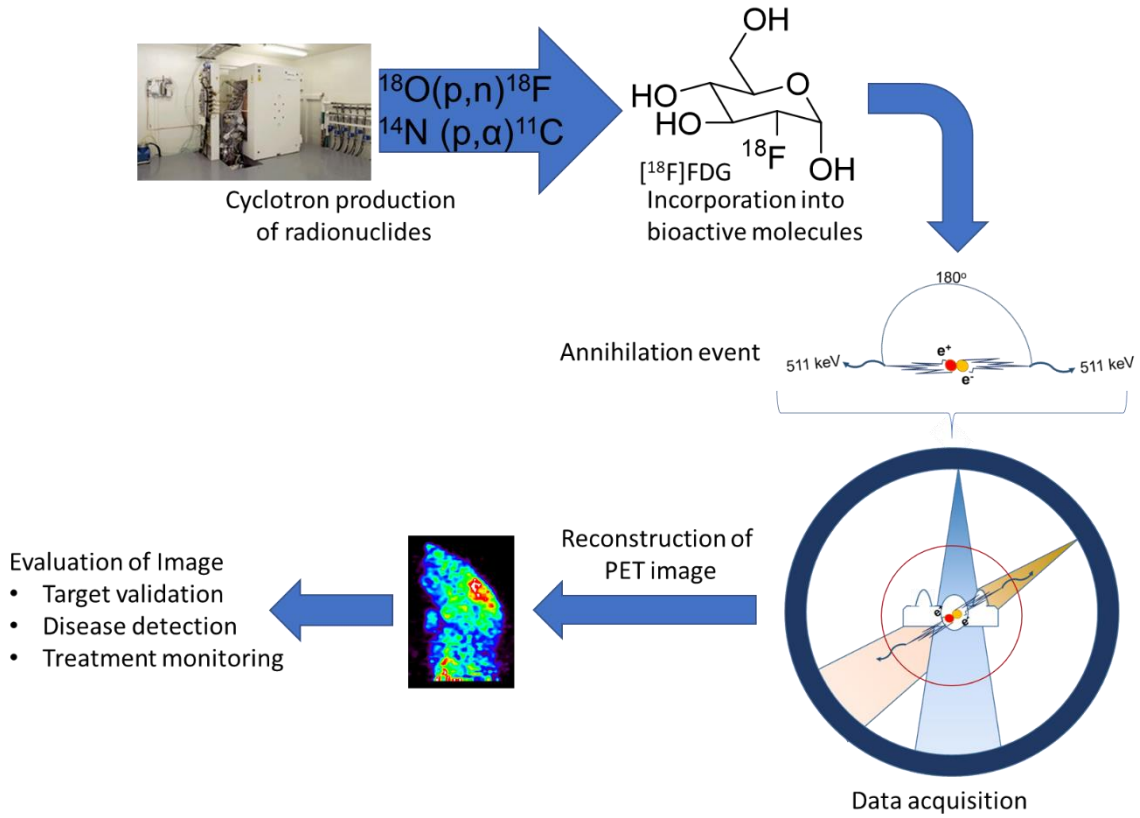

Figure 1-1: Bench to bedside path of a radiopharmaceutical.

Radionuclides can decay using one or more of six different paths depending on the energy and instability of the atoms. These methods of decay are described based on what particles are emitted or captured by the isotopes: spontaneous fission, isomeric transition, alpha (α) decay, beta (β^-) decay, positron (β^+) decay, or electron capture.[2] For PET imaging, atoms that reach stability via beta-plus (positron, β^+) emission are used to label bioactive molecules. These radiotracers are designed to be both selective and specific, with potent binding to their targets, while the radiochemistry is aimed at creating high-specific activity tracers. Specific activity refers to how much radioactivity there is per amount of molecular tracer (Ci/mmol). Both the potency and the specific activity allow PET imaging to be done with a microdose of the tracer (≤100 micrograms),[3] far below a pharmacological dose, attenuating the risk of toxicity or altering the natural state of the

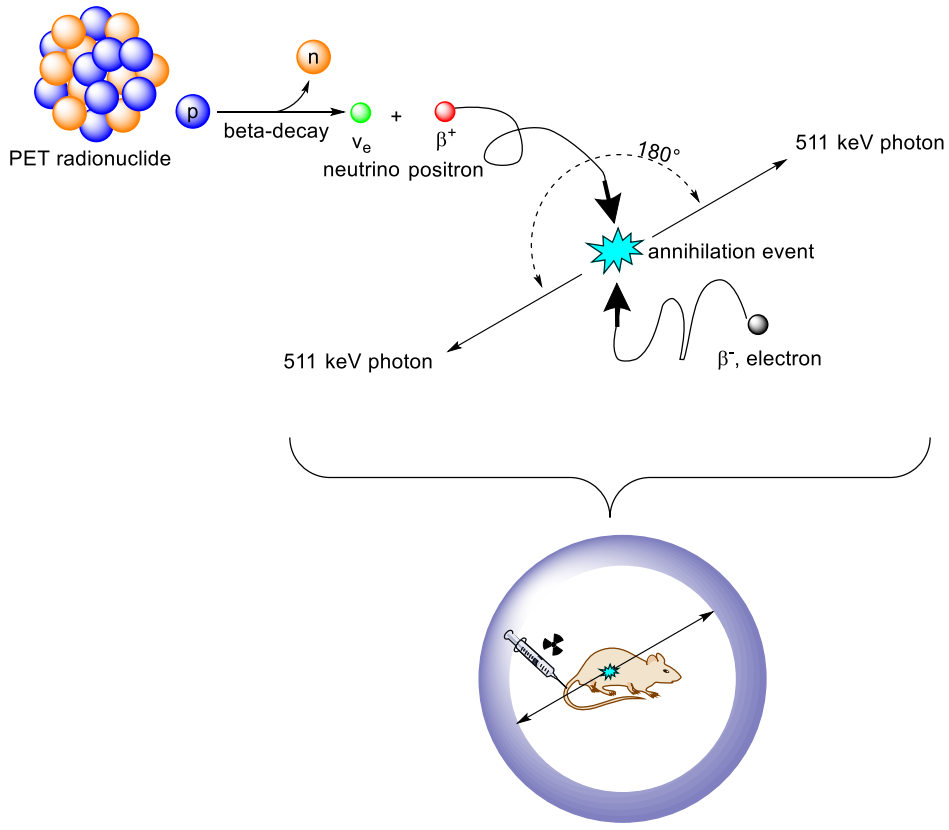

Figure 1-2: Beta decay of a positron emitting isotope.

subject. Production of these radiotracers take place in automated synthesis modules housed in lead lined boxes known as hot-cells.

i. Radionuclide Production

Radionuclides are atoms with excess nuclear energy, causing them to be unstable. Radionuclides can exist in nature, but the majority are produced with either a generator, nuclear reactor, or particle accelerator.[2] Generators contain a 'parent' radionuclide which decays producing the desired daughter nuclide. The daughter nuclide can then be

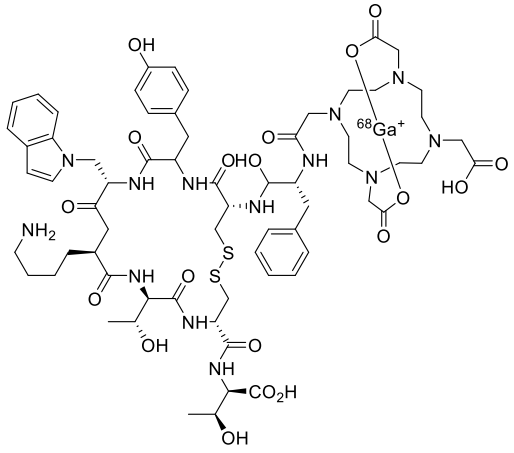

1.1, [^{68}Ga]DOTATATE

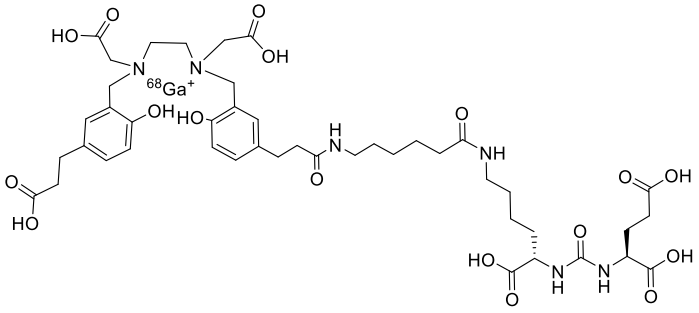

1.2, [^{68}Ga]PSMA-11

Figure 1-3: [^{68}Ga]-labeled PET tracers.

removed from the parent, via elution with saline or other methods, which then produces more of the desired radionuclide. For this reason, generators are sometimes referred to as 'cows' as they are 'milked' for the daughter nuclide. The parent nuclide could be the

product of uranium fission, a decay product from ^{233}U, or a product from a nuclear reactor or accelerator. The $^{99}Mo/^{99m}Tc$ generator is one of the most used in nuclear medicine,

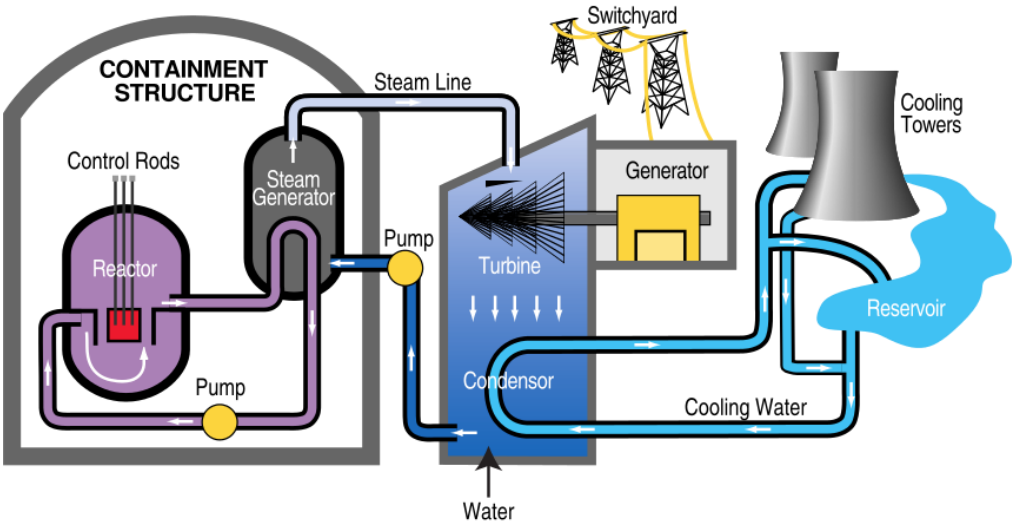

Figure 1-4: Schematic of a nuclear power reactor. Image from the public domain.

and the $^{68}Ge/^{68}Ga$ generator is becoming more widely used with the development and uptick in use of radiotracers such as ^{68}Ga-DOTATATE and ^{68}Ga-PSMA, Figure 1-3, for imaging of neuroendocrine tumors, and prostate cancer respectively.[4]

Nuclear reactors are devices that allow the initiation and containment of nuclear reactions involving neutrons, and are typically defined as either power or research reactors. Power reactors harness the thermal energy given off by fission reactions and convert it to electricity (Figure 1-4). Research reactors are of interest to produce radioisotopes for use in imaging and radio-therapies. Contrary to the energy producing power reactors, research reactors require the input of energy, and are solely used as to produce radionuclides.[5,6] Being able to control and accelerate neutrons is difficult due to their lack of charge, but the ability to control these reactions via a nuclear reactor enables access to many different interesting isotopes. The isotopes formed by nuclear reactors are the results of various nuclear reactions that take place when a neutron collides with an atom's nucleus. Radioisotopes are produced by bombarding a source (a specific

$$^{235}U \xrightarrow{\text{Fission}} {}^{99}Mo$$

$$^{98}Mo(p,g)^{99}Mo$$

Scheme 1-1: Production of ^{99}Mo by nuclear fission or proton bombardment.

element, or mixture of elements) with a neutron beam, initiating a nuclear reaction and resulting in a radionuclide. For example, technetium-99m (^{99m}Tc), the most widely used radioisotope in nuclear medicine, is produced from its parent molybdenum-99 (^{99}Mo). This parent isotope can be produced in a nuclear reactor via a variety of routes, depending on the parent nuclide, and the nuclear reaction that takes place. Two such routes, and the most common, are the fission of uranium-235 (^{235}U), and the bombardment of molybdenum-98 (^{98}Mo) with neutrons, followed by neutron capture.[7] This reactor-produced ^{99}Mo can then be used in a generator and ^{99m}Tc can be eluted as described above.

A third source for radionuclides, particle accelerators, are devices that use magnetic fields and high voltages to accelerate charged particles and concentrate them into a single ‘beam’. Accelerators can be large, such as the Large Hadron Collider (LHC) that is used primarily for experimental physics, or about the size of a washing machine,

Figure 1-5: Inside of a GE PETTrace cyclotron. Image courtesy of GE.

such as a medical radionuclide producing cyclotron (Figure 1-5). Cyclotron types are stratified by size, energy capability, or types of beams and radionuclides produced. In-house cyclotrons typically produce fluorine-18 and carbon-11 via proton irradiation of different targets.[8]

The production of ^{99}Mo via reactors was discussed above, but, because of the shortage of reactors capable of producing ^{99}Mo, including the shutdown of a main nuclear reactor in Australia,[9] other methods of producing the radionuclide have been investigated. This includes the proton irradiation of ^{100}Mo in a cyclotron to obtain ^{99m}Tc via the ^{100}Mo(p,2n)^{99m}Tc nuclear reaction.[7,10] Another example is the production of [^{18}F]fluoride, in which oxygen-18 enriched water is irradiated with a proton beam. The oxygen-18 then goes through the nuclear reaction ^{18}O(p,n)^{18}F. The [^{18}F]fluoride is obtained as a solution in the oxygen-18 enriched water; [^{18}F]fluoride can then be isolated via solid phase extraction or other methods, and then be used in radiofluorination reactions as discussed below.

Cyclotrons can also irradiate gaseous targets, such as in the production of carbon-11. The target is typically filled with ^{14}N-nitrogen enriched O_2 gas and irradiated with a proton beam. Carbon-11 is produced as [^{11}C]carbon dioxide ([^{11}C]CO_2), via the ^{14}N(p, α)^{11}C nuclear reaction. [^{11}C]CO_2 can then be used directly or undergo subsequent reactions to obtain other reagents (Scheme 1-9). Cyclotrons are also used to produce a multitude of other isotopes.[8] The examples given are some of the most common, especially when used for PET imaging, and both fluorine-18 and carbon-11 are utilized in this research.

Table 1-1: Commonly used radionuclides and important values. E_{max} is maximum energy of positron during decay. R_{max} is maximum range of positron in water. R_{mean} is mean range of positron in water.

Radionuclide	$t_{1/2}$ (min)	E_{max} (MeV)	R_{max} (mm)	R_{mean} (mm)
^{11}C	20.4	0.96	4.2	1.2
^{18}F	110	0.634	2.4	0.6
^{68}Ga	67.8	1.899	9.2	3.5

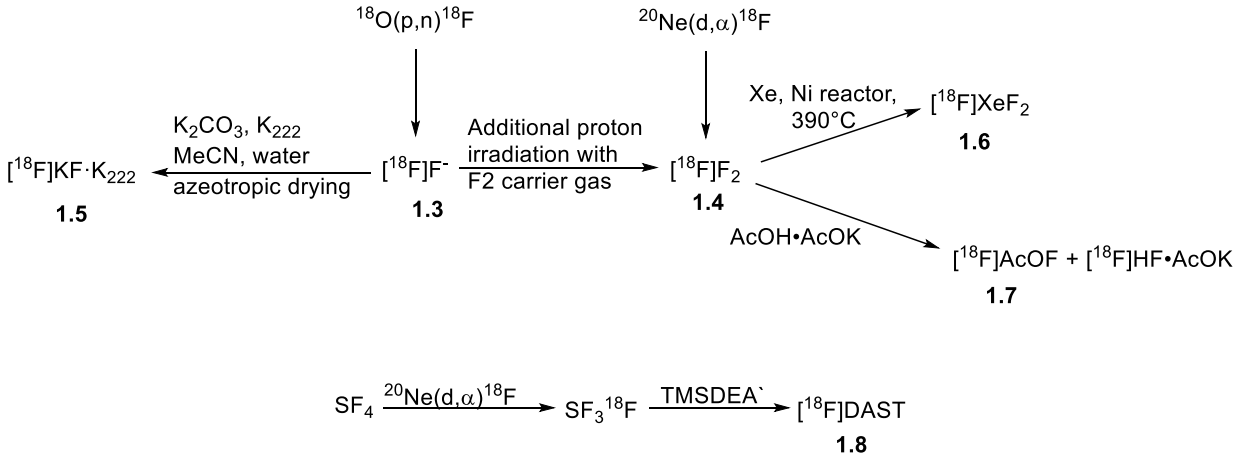

Scheme 1-2: Abbreviated summary of [^{18}F]Fluorine reagent preparation.

ii. [^{18}F]Fluorine labeling

Fluorine has long been incorporated into drug-like molecules by medicinal chemists to alter lipophilicity and protect metabolic soft spots.[11] As such, it has likewise been of interest to radiochemists who incorporate [^{18}F]fluorine into bioactive molecules, either as a bioisostere of a hydrogen atom or in place of a [^{19}F]fluorine or other halogen atom, to produce PET tracers. The existence of [^{18}F]fluorine was first reported in 1937 by AH Snell.[12] With a 109.7-minute half-life, low positron energy (E_{max}=0.65 MeV), and ready availability (from medical cyclotrons) in both nucleophilic and electrophilic forms, [^{18}F]fluorine has been widely used to prepare PET radiotracers since its discovery. The almost two-hour half-life of [^{18}F]fluorine is useful not only to radiochemists, as there is more time for syntheses, but also for clinical utility. Tracers incorporating [^{18}F]fluoride, as

well as [^{18}F]fluoride itself are regularly synthesized at cyclotron facilities and transported to surrounding PET centers that do not have a cyclotron on-site. Because of this, it is common that researchers translate [^{11}C]carbon radiotracers to [^{18}F]labeling, enabling more widespread use of these radioactive tools.[13,14] The low positron energy is key for the resolution of images produced with [^{18}F]fluorine labeled radiotracers; the lower the energy of the positron, the closer the annihilation event is to the location of the positron decay, increasing resolution. Reflecting these characteristics, many reactions have been developed for incorporating fluorine-18 into bioactive molecules, and developments have been discussed in a number of articles covering both the primary literature as well as patent applications.[1,4,11,15–27]

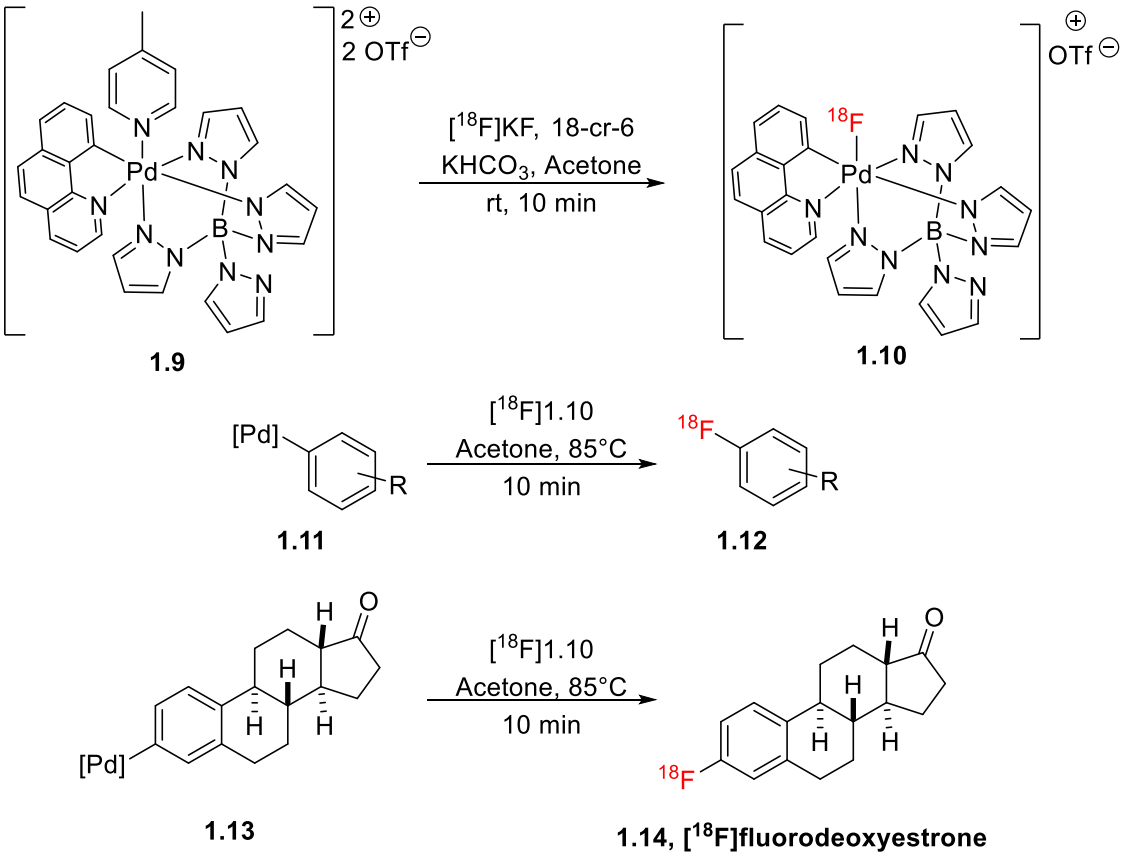

Scheme 1-3 Production of a palladium (IV) nucleophilic [^{18}F]fluoride source from electrophilic [^{18}F]F_2.

Electrophilic [^{18}F]fluorine can be produced by the ^{20}Ne(d,α)^{18}F reaction and is formed as [^{18}F]F_2 gas. For those working with a proton-only cyclotron, it is also possible to produce [^{18}F]F_2 gas via a two-step procedure. First a target containing [^{18}O]O_2 gas is bombarded with protons to produce [^{18}F]fluoride which adheres to the walls of the target. The rest of the [^{18}O]O_2 gas is collected and the target is filled with F_2 enriched gas and bombarded once again with protons to encourage isotopic exchange of ^{18}F for ^{19}F in the F_2 gas.[28] This [^{18}F]F_2 gas can be used as a fluorinating reagent itself or it can be used to

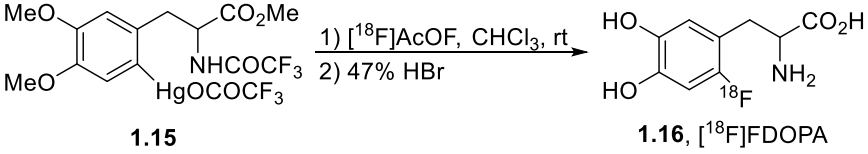

1.15 **1.16**, [^{18}F]FDOPA

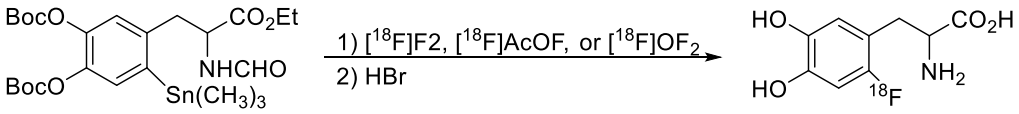

1.17 **1.16**, [^{18}F]FDOPA

Scheme 1-4:Nucleophilic demetallation production of [^{18}F] FDOPA.

produce other electrophilic fluorinating agents such as [^{18}F]XeF_2,[29] [^{18}F]AcOF,[30] or [^{18}F]DAST[31] (shown in Scheme 1-2). Syntheses with these reagents require complicated purification methods because of the ^{19}F present in the carrier gas, and so called a “carrier-added” reaction. This can lead to low specific activity and yields.[21,22] Specific activity (SA), measured in Ci/mg, or molar activity, measured in Ci/mmol, is the ratio of activity to the mass (or moles) of the tracer in the sample. Not every molecule in a radiotracer sample contains a radionuclide; if the SA is too low it would be necessary to inject too high of a mass of tracer to achieve an acceptable count/activity level.[32]

To combat the typically low specific activities resulting from electrophilic fluorinations, Hooker and Ritter worked to develop an electrophilic source of [^{18}F]fluorine in the form a palladium (IV) complex (shown in Scheme 1-3).[33] This high specific activity reagent, **1.10**, is synthesized from a nucleophilic [^{18}F]fluoride source, without the need for F_2 gas. This reagent is incredibly helpful for radiotracers inaccessible via nucleophilic fluorinations, but the disadvantages include the comparatively complicated palladium complex precursors, which also require additional quality control testing, and the need for a two-step procedure prior to radiolabeling of the precursor. Still, this palladium complex is encouraging in adapting traditional fluorination methods to radiochemistry.

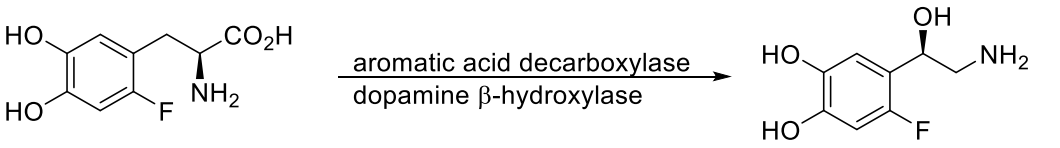

1.16, FDOPA

1.18, fluoro-norepiephrine

Scheme 1-5:Metabolism of [^{19}F]FDOPA to norepinephrine.

Electrophilic [^{18}F]fluorine has also been utilized in electrophilic aromatic substitution via demetallation of precursors such as those for production of L-3,4-dihydroxy-6-[^{18}F]fluorophenylalanine ([^{18}F]FDOPA), from **1.15**[34] and **1.17**[35](Figure 1-4). Although this method allowed the fluorination of electron-rich aryl molecules, the [^{18}F]FDOPA was produced in low specific activity due to these methods being carrier (F_2 gas) added. Efforts have been ongoing to find a high yielding, robust synthesis of [^{18}F]FDOPA, as it finds use in the imaging of neuropsychiatric disorders and diseases, and the detection of neuroendocrine tumors (NETs) and types of pancreatic cancer. This radiotracer began as an amino acid metabolism imaging agent where low specific activity production was acceptable, but as the use of [^{18}F]FDOPA expands to oncological

diagnosis, specific activity becomes more important. It was found that too low of specific activity in [^{18}F]FDOPA doses could cause pharmacological effects in patients with neuroendocrine tumors due to the [^{18}F]FDOPA being converted to noradrenaline in cancerous cells (Scheme 1-5).[36] In contrast to the electrophilic methods described above, aromatic substitution using nucleophilic [^{18}F]fluoride produces high specific activity tracers, although preparing fluorinated compounds from organometallic precursors is a recent development in which research is ongoing.[20–22] This chemistry is further below.

In the Scott Lab, a number of fluorine-18 chemistry methods are used on a regular basis, the majority of which involve the use of nucleophilic [^{18}F]fluoride. Nucleophilic [^{18}F]fluoride can be produced with a cyclotron via the ^{18}O(p,n)^{18}F nuclear reaction, as described above. Using this aqueous ion in reactions requires purifying it via solid phase extraction, typically by trapping the [^{18}F]fluoride on a quaternary methylammonium (QMA) cartridge and eluting the [^{18}F]fluoride with a phase transfer catalyst (PTC) and a basic counterion (usually K_2CO_3). This is followed azeotropic drying, relying on the PTC to solubilize the nuclide in a polar aprotic reaction solvent. In order for the [^{18}F]fluoride to be available for use in nucleophilic reactions, it is necessary to disrupt and discourage the strong hydrogen bonds it forms in water; this is where the PTC (e.g. cryptands such as Kryptofix$_{2,2,2}$) comes into play.[37] Although it has long been believed that the polar aprotic solvent is necessary for successful [^{18}F]fluorination, work done by Stewart and coworkers has suggested that an ethanol water mixture could provide both a “greener” and safer way of producing mass produced radiotracers such as [^{18}F]FDG.[38] Using the solvated [^{18}F]fluoride in nucleophilic aromatic and aliphatic substitution reactions is one of the most used and straightforward radiofluorination techniques, given that the desired precursor

can withstand the sometimes harsh reaction conditions. This method requires a precursor with an excellent leaving group such as a chlorine atom, nitro (NO_2^-) or trimethylamine

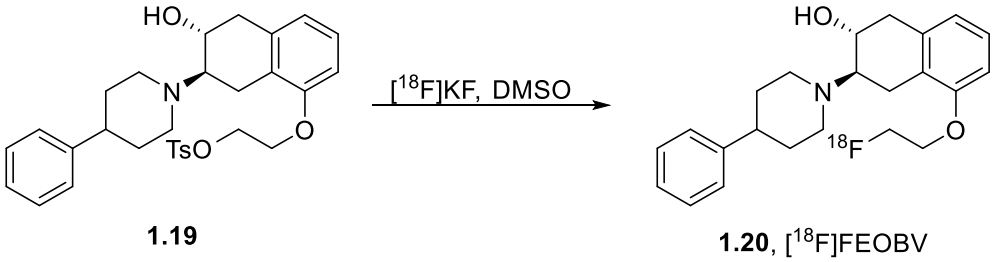

1.19 **1.20**, [^{18}F]FEOBV

Scheme 1-6: Radiofluorination to produce the VAChT PET tracer, [^{18}F]FEOBV.

(NMe_3^+), adjacent to an electron withdrawing group, as well as a high reaction temperature.[21] This will allow for a simple one-pot method resulting in high yields and specific activity. Of these nucleophilic substitutions, halogen exchange (halex) reactions, where [^{18}F]fluoride displaces a halogen such as chlorine, are highly attractive due to the stability of the precursors and the reliability of the reactions.

Use of nucleophilic [^{18}F]fluoride for radiofluorination of aliphatic groups is relatively straightforward and similar to the S_NAr reactions for aromatic fluorinations. A main difference here is there is no need for an activating group to be added to the precursor. However, it is still necessary to protect any areas that could be subject to attack by the nucleophilic [^{18}F]fluoride and have an excellent leaving group such as triflate or tosylate.[1] One such example of an aliphatic fluorination is the production of [^{18}F]fluoroethoxybenzovesamicol ([^{18}F]FEOBV), which is used for PET imaging of the vesicular acetylcholine transporter (VAChT).[39] In this reaction, shown in Scheme 1-6, a tosylate group (**1.19**) is replaced with nucleophilic fluoride (**1.20**).

When an electron rich aryl group requires radiolabeling, the chemistry has historically proven more complicated. A traditional S_NAr radiofluorination reaction depends on the electron poor (electrophilic) nature of the substrate so that the electron rich (nucleophilic) [^{18}F]fluoride can attack. Initially, it was possible to fluorinate on unactivated or electron rich aryl rings using nucleophilic [^{18}F]F_2, but, as discussed above, this results in low specific activity and therefore is not an attractive method for use in the clinic. To utilize high specific activity nucleophilic [^{18}F]fluoride, radiochemists depended on creative use of protecting groups to change the electronics of a precursor, or would radiolabel a precursor that could then undergo transformations such as oxidations to obtain the desired functional groups.[22]

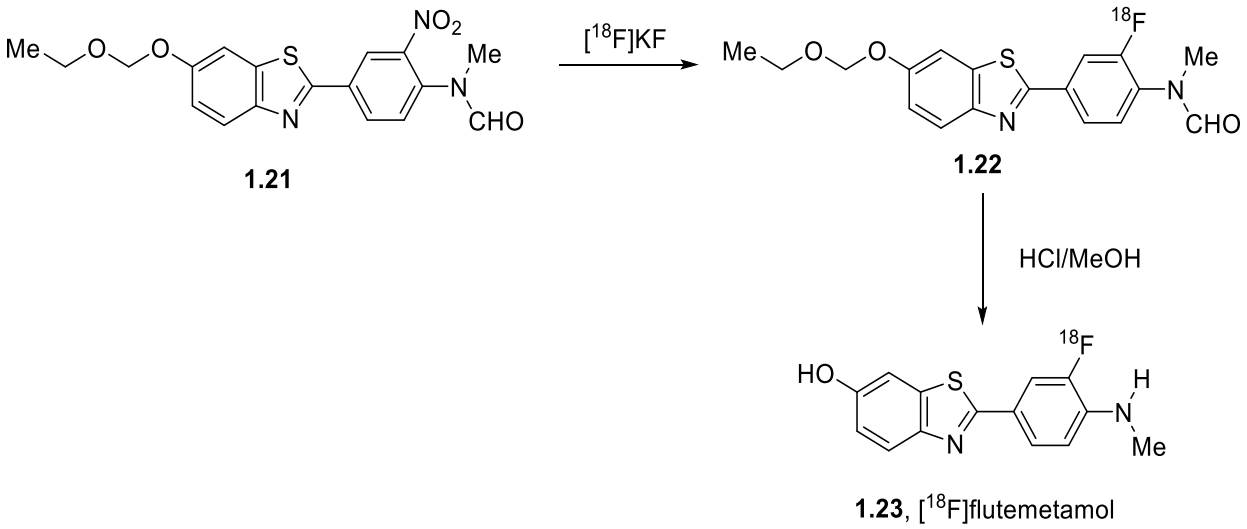

Scheme 1-7: Multi-step radiochemical synthesis of [^{18}F]Vizamyl

A simple example of this is the production of [^{18}F]flumetamol (**1.23**, trade name Vizamyl), for the imaging of amyloid burden (Scheme 1-7). In order to activate what is an electron withdrawing ring in the final product an aldehyde is used as a protecting group for the aniline. Radiofluorination provides the desired product, albeit after additional, and harsh, deprotection steps.[40] Although these methods were successful in producing the

desired products, clinical streamlined production with complicated chemistry is not sustainable. Daily production of radiotracers depends on quick (necessary due to the short half-life of the radionuclide) and straightforward syntheses with the fewest possible steps. Introduction of lengthy and complicated syntheses would increase the cost of radiopharmaceuticals (due to reagents, time, etc. needed for the syntheses), increase the failure rate of tracer production, and require more complicated training of each radiochemist (leading to another increase in cost). This has given rise to considerable research into development of facile methods for the direct radiofluorination of diverse aromatic and aliphatic substrates.

Following Hooker and Ritter's work with Pd(IV) described above (Scheme 1-3), Scott and Sanford introduced copper-catalyzed [^{18}F]fluorination reactions of aryl-iodonium salt precursors.[41] Progress to develop a mild, adaptable, repeatable and robust nucleophilic fluorination of electron rich aryl rings has been ongoing, and is now its own niche in the field of radiochemistry; the search is on for a shelf-stable precursor with a facile synthesis. These qualities will encourage the adaptation of the method by other labs and potentially clinical tracer production. Techniques from a variety of labs

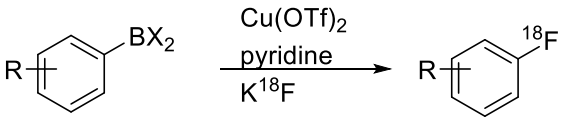

1.24 **1.25**

X = Boronic ester, BPin

Scheme 1-8: Radiofluorination of electron rich boronic acid or BPin precursors.

demonstrate the ability to use [^{18}F]KF·$K_{2,2,2}$ for the aryl fluorination of variously substituted aryl groups.[19,20,42] Examples of this can be seen in the adaptation of aryl fluorinations from the traditional organic chemistry lab to the radiochemistry lab, such as those resulting

from the collaboration of Melanie Sanford's and Peter Scott's groups.[16,17,26] Specifically, it was reported in 2015 that the copper-mediated nucleophilic fluorination of aryl borane species reported by the Sanford group is easily translated to radiochemistry, Scheme 1-8.[16,43] This is due to the high tolerance of various functional groups on the precursor, and also because of the use of KF, which, as discussed above, is a readily prepared and common radiofluorination reagent, in the [^{18}F]KF form. However similar these reactions may seem, optimization was required due to the differences in radiochemistry as compared to traditional organic chemistry, including the determination of the best eluent system for the production of [^{18}F]KF. In this specific example, it was found that a weakly basic mixture of K_2CO_3 and KOTf (1:73 ratio) increased the yield of the fluorination reaction by eluting 80% of the [^{18}F]fluoride off of the separation cartridge. The Scott group later reported successful resolution of two hurdles encountered when automating of this novel aryl fluoride synthesis: separation of a byproduct, as well as the order of addition of the reagents.[44] It is necessary to determine the specific order of reagent addition in automated radiochemical syntheses so that the synthesis module can be prepared accordingly as adjustments to the synthesis cannot be made after the activity has been delivered to the hot cell. Because of the breadth and sheer volume of the work done in this space many reviews have covered this subject.[1,20–23,45]

iii. Carbon-11 Labeling

Labeling bioactive molecules with [^{11}C]carbon is attractive as carbon atoms exist in all organic molecules and this radioactive nuclide can be incorporated into a multitude of scaffolds with no effect on the chemical composition or biological behavior of the molecule.[1,46,47] However, in order to incorporate this radionuclide into molecules, special attention must be given for two main reasons: (1) it has a very short half-life of 20 minutes requiring quick and reliable procedures, and (2) carbon-11 is produced from a cyclotron as $^{11}CO_2$ gas and so it is almost always necessary to perform multiple steps prior to labeling the precursor (Scheme 1-9). For this purpose, automated chemistry modules have been developed, such as the TracerLab $FX_{C\text{-}Pro}$ from GE, that contain appropriate equipment to transform the cyclotron produced carbon-11 reagent into other reagents.[48]

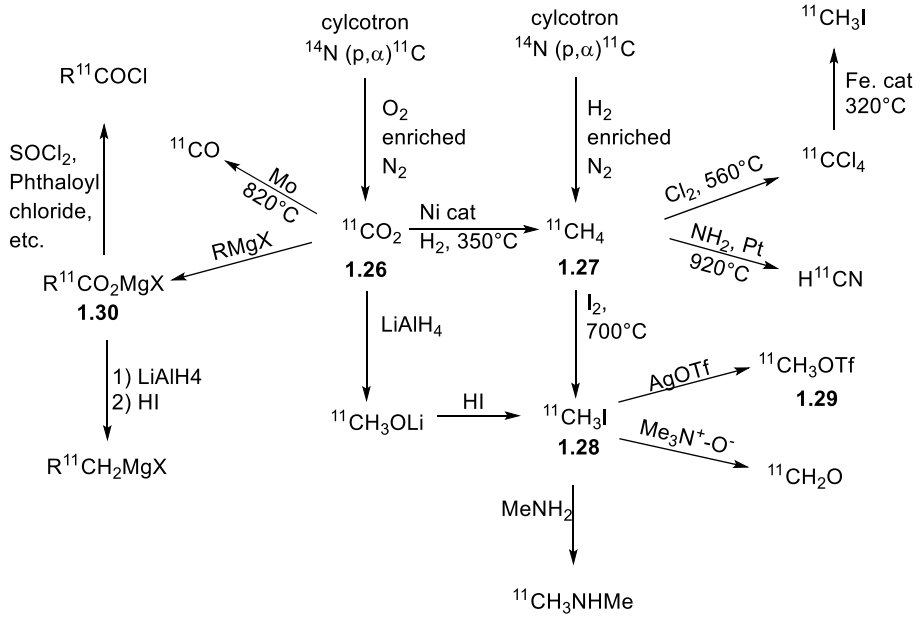

Scheme 1-9: A summary of [^{11}C]carbon chemistry methods.

For a standard methylation reaction, [^{11}C]CO_2 is reduced to [^{11}C]CH_4 using Ni and hydrogen. This [^{11}C]CH_4 is then pushed through a furnace containing I_2 at 750°C to produce [^{11}C]methyl iodide (**1.28**, [^{11}C]MeI). [^{11}C]MeI can be used for methylation or can

be transformed further by passing over a AgOTf column, resulting in the more reactive [^{11}C]methyl triflate (**1.29**, [^{11}C]MeOTf). These methylating reagents can then be used either in reactor (in solution) or 'loop' chemistry. The reactor is akin to organic chemistry in a round-bottomed flask, while loop chemistry is a radiochemistry variant of flow chemistry. In the former, the solvated precursor is added to the reactor as part of the

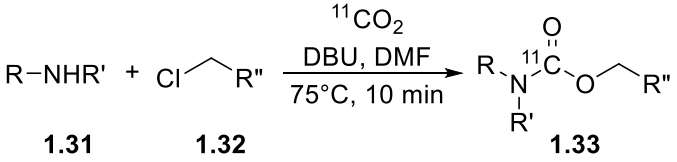

1.31 **1.32** **1.33**

Scheme 1-10: Production of [^{11}C]carbamates.

reaction set-up, and the methylating reagent ([^{11}C]MeI or [^{11}C]MeOTf) is bubbled through the solution. Any deprotections, or further chemistry is then completed in the reactor. For loop chemistry, the precursor is loaded into an HPLC injection loop and the solvent is dried/removed, leaving the precursor on the walls of the loop. The methylating reagent is then passed through the loop and reacts with the pre-loaded precursor. The product can then be directly injected into a semi-preparative HPLC system for purification. Although [^{11}C]methylation chemistry is the more common approach to synthesizing carbon-11 labeled radiotracers, it is also possible to use the [^{11}C]CO_2 directly from the cyclotron, in methods using CO_2 fixation chemistry.[47] This can be used to access a variety of chemical reagents and radiotracers possessing higher oxidation states without the need for additional reduction-oxidation chemistry steps in the hot-cell.[46,47] These methods can produce functional groups such as carbamates (**1.33**), amides, carboxylic acids, etc.

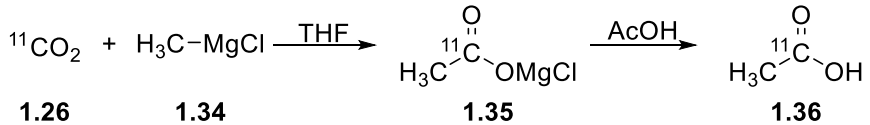

1.26 **1.34** **1.35** **1.36**

Scheme 1-11: Production of [^{11}C]acetate.

Access to carbamates via a one pot synthesis was reported by Hooker and coworkers,[49] which demonstrated a simple and efficient method for the direct incorporation of [^{11}C]CO_2 into radiopharmaceuticals; however, as carbamates are not an overly common functional group, one-pot methods with access to other functional groups are still desired (Scheme 1-10). For production of various other residues, it is first necessary to convert the [^{11}C]CO_2 to a more reactive species. As mentioned above, these conversions need to be high yielding and rapid. Grignard reagents are an attractive group of versatile reagents, and are used regularly in the production of [^{11}C]acetate (**1.36**) for myocardial imaging, Scheme 1-11.[50] These organometallic reagents are also used in the production of more complicated reagent/intermediates such as [^{11}C]carboxymagnesium halides (Scheme).[1,51] This requires use of fresh Grignard reagents, commercial or freshly synthesized, as atmospheric CO_2 can decrease specific activities and yields. A brief summary of [^{11}C] chemistry can be found in Scheme 1-9.

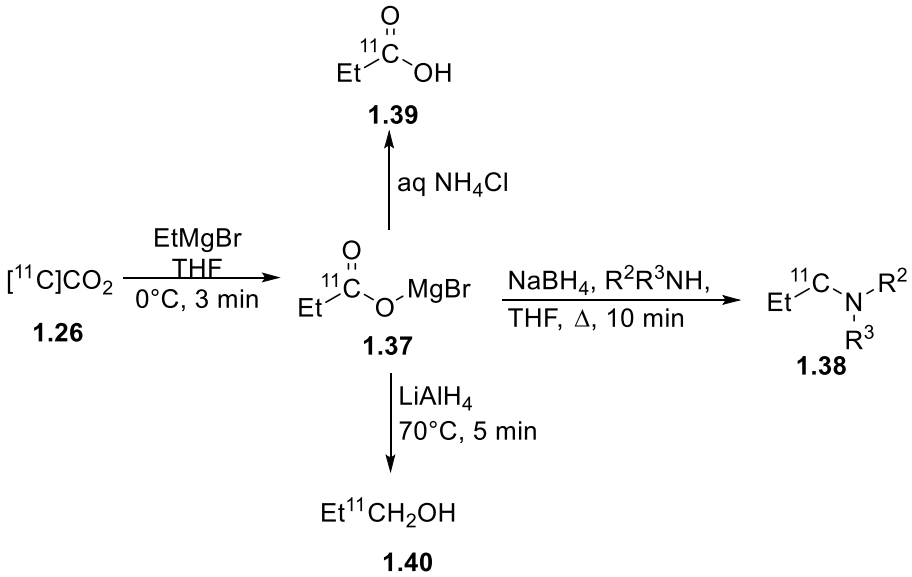

Scheme 1-12: Conversion of [^{11}C]CO_2 to carboxymagnesium halide and subsequent production of reagents.

iv. Common PET Tracers

PET imaging is a powerful tool used in a variety of fields including oncology,[52,53] cardiology,[54,55] and neurology.[56,57] As such, a multitude of tracers exist for use in each of these fields, and sometimes are used in multiple fields. The most common radionuclides used are ^{18}F-fluroine and ^{11}C-carbon, while use of ^{68}Ga-gallium is increasing in use as the technology and tracers become available. Each of the fields in which PET imaging is heavily used (oncology, neurology and cardiology), benefit from PET as the onset of symptoms, progress of disease and response to treatment vary so drastically between patients. Using specifically targeted radiotracers, doctors are able to both increase patient quality of life, as well as advance understanding of pathophysiology of a host of diseases.

Considered the powerhouse of PET imaging, [^{18}F]fludeoxyglucose ([^{18}F]FDG) is used in cardiac, neurological and oncological imaging. Uptake of the fluorinated sugar can highlight areas of increased metabolism, such as in tumors, or indicate loss of brain activity. First produced by the Brookhaven National Laboratory, [^{18}F]FDG is now produced at a multitude of centers worldwide and, of the 2 million PET scans conducted in the US each year, the vast majority are conducted with [^{18}F]FDG. [^{18}F]FDG, as a fluorinated glucose derivative, is taken up by cells the same as glucose would be via the glucose transporter (GLUTs), which leads to an increase in uptake in areas of increased metabolism such as tumors, and a decrease in uptake in areas of cell death, as in neurodegenerative diseases. It is a trapped metabolite trace, referring to how it is taken up by cells, but once phosphorylated by hexokinase (HK), the resultant [^{18}F]FDG-6-phosphate ([^{18}F]FDG6P) cannot enter the mitochondria (Figure 1-7). The radioactive

metabolite [^{18}F]FDG6P accumulates in the cells; in cancer cells, a downregulation of glucose-6-phosphatase (G6P) causes [^{18}F]FDG6P to accumulate at even higher levels.[58]

The long-time use, extensive characterization, FDA approval, ability for

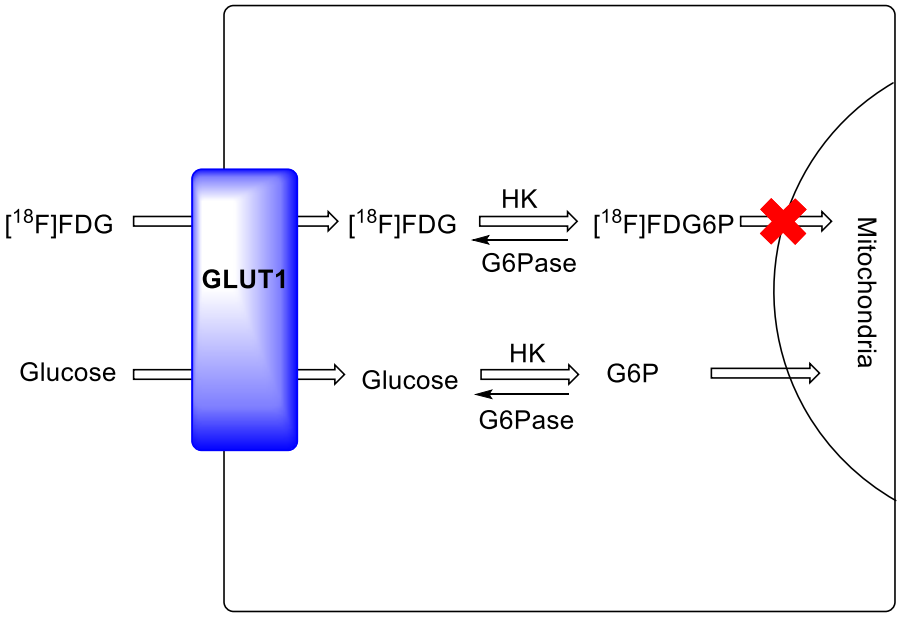

Figure 1-6: Uptake of glucose as compared to uptake of [^{18}F]FDG.

reimbursement, and widespread availability of the tracer itself allows [^{18}F]FDG to be used for a plethora of imaging applications. As more specific tracers are developed targeting biomarkers in individual diseases, [^{18}F]FDG remains to serve as the benchmark to which these novel tracers are compared. Its disadvantage lies in its unselective nature; FDG is a non-specific marker of glucose metabolism. Fortunately, there are a host of more selective radiotracers based on both endogenous substrates as well as carefully engineered molecular scaffolds.

Oncological imaging presents an interesting target as the image produced must differentiate between healthy tissue and the cancerous tumor. For this reason, often it is either the fuel (FDG or acetate) or building blocks (amino acids) that are used to image cancer cells. PET radiotracers used in oncological imaging, besides [^{18}F]FDG, include

[^{11}C]acetate (**1.36**), [^{11}C]methionine (**1.41**), [^{11}C]choline (**1.42**), [^{18}F]fluoromethylcholine (**1.43**), [^{18}F]fluroDOPA (**1.16**), [^{68}Ga]DOTATATE (**1.1**), and [^{68}Ga]PSMA (**1.2**).[52,59–61]

Acetate, as an endogenous substrate, has low toxicity risks and a straightforward

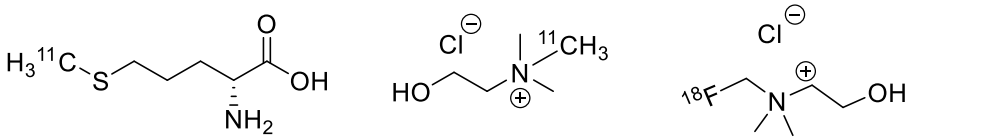

1.41, [^{11}C]methionine **1.42**, [^{11}C]choline **1.43**, [^{18}F]fluoromethylcholine

Figure 1-7: Commonly used PET Radiotracers.

synthesis. This radiotracer has applications in both cardiology and oncology, but its first application was in the study of myocardial oxygen utilization. This small molecule radiotracer finds utility in imaging prostrate and bladder cancer, as well as hepatocellular carcinoma (HCC) and renal cell carcinoma (RCC).[59] The wide utility and straightforward synthesis often make this tracer a common one in the toolboxes of PET centers. Prostate cancer is also imaged with choline, both in its [^{11}C] and [^{18}F] labeled forms. Both [^{11}C]choline and [^{18}F]fluoromethylcholine are also used in the imaging of gliomas.[60,62] [^{11}C]Methionine (**1.41**, [^{11}C]MET) finds use in the imaging of a broad range of cancers, including head and neck as well as lung and breast cancers. An *S*-[^{11}C]-methylated derivative of an endogenous amino acid [^{11}C]MET is incorporated into proteins, lipids, RNA and DNA, offering higher sensitivity than [^{18}F]FDG.[63]

PET tracers incorporating [^{68}Ga]gallium have become increasingly popular both because of the availability of [^{68}Ga]-generators and the development and evaluation of a series of prostate specific membrane antigen (PSMA) ligands, as well as DOTATATE which binds to the overexpressed somatostatin receptors in neuroendocrine tumors (NETs).[52,64,65] PSMA has been shown to be increased at levels up to 1000-fold in prostate cancer, offering an excellent target for imaging of this cancer.[52] [^{68}Ga]PSMA-11 (**1.2**) is a

common PSMA imaging agent, which accumulates even in small metastases. The ability to label PSMA ligands with different radionuclides enables the production of [^{177}Lu]PSMA, a partner radiotherapeutic to [^{68}Ga]PSMA-11, making PSMA-11 an excellent companion diagnostic agent.[52] [^{68}Ga]PSMA-11 has been shown to be a highly selective and useful agent in detection and staging in prostate cancer. A more recently developed [^{18}F]-labeled compound, fluciclovine (trade name Axumin) has also shown to be useful.[52] Comparisons of studies completed with [^{68}Ga]PSMA-11 or [^{18}F]axumin indicate that both of these tracers have utility in the detection and monitoring of prostate cancer and related metastases.[65,66] Another [^{68}Ga]-labeled PET imaging agent, [^{68}Ga]DOTATATE (**1.1**) is used in the detection of neuroendocrine tumors. The synthesis of this tracer involves the complexing of gallium-68 in the macrocyclic dodecanetetraacetic acid (DOTA), which is coupled with a somatostatin analogue tyrosine-3-octreotate (Tyr3-octreotate or TATE).[64] The DOTA chelating group can also be coupled with other somatostatin receptor targeted molecules, such as octreotide to form (DOTA-Phe-Tyr)octreotide (DOTATOC); however, DOTATATE has much higher affinity (10 fold, 0.2±0.04 nM vs. 2.5±0.5 nM) to somatostatin receptor subtype 2 (sst2), the subtype with upregulation in neuroendocrine tumors, *in vivo*.[67]

Neurological imaging is a multi-faceted, ever changing, and incredibly interesting field. Within neuroimaging, the heterogeneity of neurons and regions in the brain dictates the necessity for a broad range of tracers, much like the different types of cancers. [^{18}F]FDG is of course applied to neurological imaging, in that it can depict regions of the brain that have decreased glucose consumption, as in neurodegeneration as a result of dementia (Figure 1-8).

Although [^{18}F]FDG enables the imaging of glucose metabolism in the brain, the development of tracers selective for neurotransmitter systems, protein aggregates, enzymes or other more specific targets can offer more specific information. For example, dementia is a large area of study, and investigators are interested in understanding the pathology of the diseases like Alzheimer's disease (AD), Parkinson's disease (PD), or dementia with Lewy bodies (DLB), as well as attempting to detect the onset earlier and monitoring patient response to treatment. Following the theories resulting from biological work, PET seeks to offer *in vivo* evidence. An important goal of imaging in dementia is the differentiation between dementias such as Alzheimer's Disease (AD), Parkinson's Disease Dementia (PDD), Dementia with Lewy Bodies (DLB) or Frontotemporal Lobe Dementia (FTLD). Alzheimer's disease, currently understood as the most common type

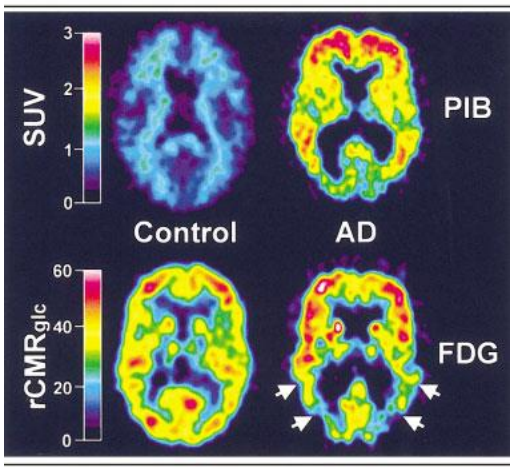

Figure 1-8: Comparison of FDG and PiB PET scans in AD vs healthy controls. FDG displayed as glucose metabolic rate ($rCMR_{glc}$). Reproduced with permission from Ref {Klunk 2004}

of dementia, is characterized by protein aggregates in the form of amyloid beta plaques (Aβ) and tau neurofibrillary tangles.[57] [^{11}C]Pittsburgh compound B (**1.45**, [^{11}C]PIB), the first radiotracer developed for the imaging of amyloid-beta plaque burden, is helpful in determining if a patient does indeed have amyloid burden, Figure 1-8.[68,69]

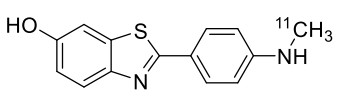

1.45, [^{11}C]PiB

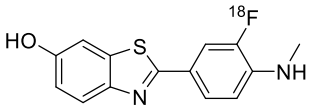

1.23, [^{18}F]Flutemetamol, Vizamyl

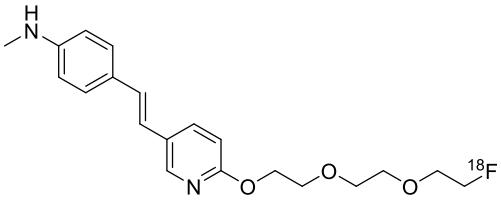

1.46, [^{18}F]Florbetapir, AMYViD

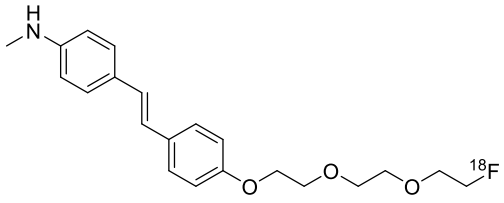

1.47, [^{18}F]Florbetaben, Neuraceq

Figure 1-9: FDA approved amyloid beta PET radiotracers.

Since the development of [^{11}C]PiB, three other amyloid targeting PET imaging agents have been approved by the FDA. [^{18}F]Florbetapir (**1.46**, AMYViD, [^{18}F]AV-45) was developed through work done by University of Pennsylvania researchers, and further investment by Avid Pharmaceuticals (which was later acquired by Eli Lilly).[70] AMYViD was approved by the FDA in 2012,[71] and is similar to [^{11}C]PiB as it also images amyloid burden, but the use of [^{18}F]fluorine, with a 109 minute half-life, allows more widespread use of the tracer. Two other compounds imaging amyloid burden and labeled with [^{18}F]fluoride include [^{18}F]flutemetamol (**1.23,** Vizamyl), and [^{18}F]florbetaben (**1.47,** NeuraCeq), approved by the FDA in 2013[72] and 2014[73] respectively. This information can then be used to populate clinical trials for anti-amyloid therapy, and patients can receive follow-up PET scans to confirm whether the therapy is indeed clearing plaques. Although it is agreed that imaging of amyloid burden could be instrumental in detection of early onset AD,[74] these [^{18}F]-labeled imaging agents need to be better characterized through further investigation.[75,76]

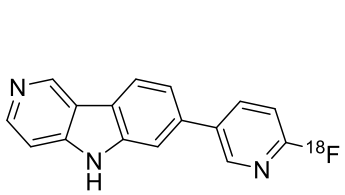

1.48, [^{18}F]AV-1451

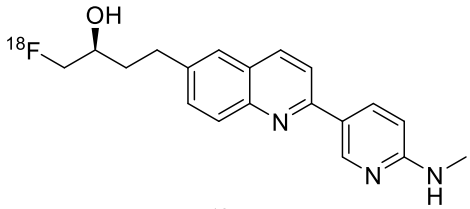

1.49, [^{18}F]THK-5351

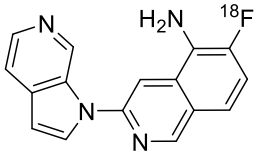

1.50, [^{18}F]MK-6240

Figure 1-10: PET radiotracers for the imaging of tau-protein burden.

A more recent development from Avid and Eli Lilly is the ^{18}F-labeled tau imaging agent [^{18}F]AV1451 (**1.48**, fluortaucapir, Figure 1-10), licensed from Siemens. When compared to another tau imaging agent [^{18}F]THK5351 (**1.49**) in AD or frontal temporal lobe dementia (FTLD) human tissues, [^{18}F]AV1451 was found to be better suited to imaging AD, while [^{18}F]THK5351 was more prominent in FTLD tissue.[77] Discovery and preliminary evaluation of another tau neurofibulary tangle (NFT) imaging agent, [^{18}F]-MK-6240 (**1.50**), was reported in 2016 by researchers from Merck.[78] These preliminary studies in non-human primates, as well as additional work in post-mortem human brain tissue, indicate that MK-6240 has excellent selectivity for NFT.[79] Despite the preliminary success with these Tau imaging agents, off target binding has been found and so work towards an optimal Tau tracer is ongoing.[79]

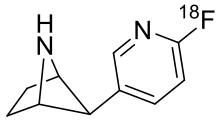

1.51, [^{18}F]Flubatine

Figure 1-11: Nicotinic AChR PET radiotracer
used in imaging of Parkson's patients.

Mild cognitive impairment and dementia can also be associated with Parkinson's Disease. Tracers targeting the dopaminergic and cholinergic system are often used to assist in treatment plan development. A clinical study done with [^{18}F]flubatine, **1.51**, Figure 1-11, a PET tracer targeting the nicotinic acetylcholine receptor, confirmed that some patients with PD could benefit from a therapeutic plan to restore acetylcholine production.[80]

Both PD and AD, along with other neurological disorders such as drug addiction and mood disorders, have roots in the serotonergic system. Serotonin and other small amino acids depend on the vesicular monoamine transporter 2 (VMAT2) for release into the synaptic cleft. Imaging of this transporter is possible through use of (+)-α-[^{11}C]dihydrotetrabenazine ([^{11}C]DTBZ (**1.52**), Figure 1.12).[81,82] Studies with [^{11}C]DTBZ and other tracers such as [^{11}C]carfentenil (**1.53**) (targeting the mu (μ)-opioid receptor), have helped to define addiction as a brain disease, advancing understanding of brain behavior and encouraging treatment development in this area.[83]

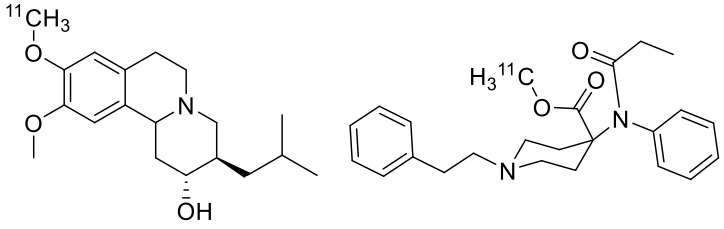

1.52, [^{11}C]DTBZ **1.53**, [^{11}C]CFN

Figure 1-12: PET tracers targeting the mu-opioid receptor.

Flumazenil (FMZ) is an antagonist of $GABA_A$ receptors that binds the benzodiazepine (BZD) binding site. First developed to counteract the effect of BZD overdoses, FMZ was translated to PET imaging as a [^{11}C]-labeled radiotracer (**[^{11}C]1.55**), and later was [^{18}F]-labeled (**[^{18}F]1.55**) (Figure 1-13).[13,84,85] [^{11}C]FMZ is used in imaging a

broad range of diseases including AD, Schizophrenia, epilepsy and drug addiction.[86] FMZ is discussed in more detail in Current GABA Imaging section.

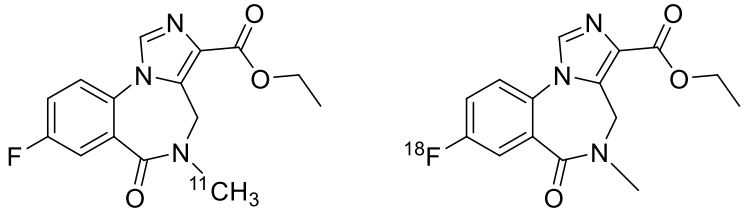

1.54, [^{11}C]FMZ **1.54**, [^{18}F]FMZ

Figure 1-13: Carbon-11 and fluorine-18 labeled flumazenil PET tracers.

v. General Production – Automated Synthesis

Automated synthesis of radiopharmaceuticals has become necessary for any tracers with hopes of being translated into clinical use. This was not always the case, and the amount of radiation that was handled in the recent past by radiochemists could come as a shock as compared to current standards. In the early days of radiochemistry, experiments were carried out much like traditional organic chemistry experiments, using vials, syringes and, sometimes, fume hoods. As the field is becoming more regulated, laboratories are moving to shielding hoods and workspaces with lead bricks. This is a technique still used today when radiochemists are using small amounts (a few milliCuries) of radioactivity for methodology, proof of concept, or preliminary studies. In a busy research lab, doing lead brick shielded manual chemistry is necessary, as time in the hot cells can be hard to schedule between pre-clinical animal studies, and clinical studies that need to be completed for the hospital.

Figure 1-14: An automated synthesis module for the preparation of radiotracers.

All the radiotracers produced in the U of M Cyclotron and Radiochemistry facility are synthesized using fully automated, computer-controlled synthesis modules (Figure 1-14) that are housed in lead-lined hot-cells. This ensures both the safety of the radiochemists as well as the safety of the patients as the radiotracers are synthesized according to cGMP. A typical production of a clinical dose begins with the cleaning of the hot-cell to remove residual reagents and solvents from previous production runs. After cleaning, the chemist will ensure the module is in the right configuration for the synthesis, double-checking lines, vials and valves are arranged correctly. For most clinical production runs, a cyclotron beam duration of 30 minutes is used, producing about 3 Ci [^{11}C]CO_2 or about 1.5 Ci of [^{18}F]fluoride. Before the beam is started and while the beam is running, the chemist (and second chemist) will prepare and insert the proper reagents, filters, vials, and cartridges before closing the hot cell. When the module has been prepared and the hot-cell has been closed, the chemist can then deliver the radioactivity to the cell. Each radiotracer has a specific program on the computer controlling the

module. The program includes a time list that issues commands to the module: how to modify the cyclotron produced radionuclide into a reagent, how long to stir the reaction and at what temperature, when to add the vials of other reagents, and when to inject onto the self-contained semi-preparative HPLC. Although, prior to injection on the HPLC, the synthesis is mostly automated, chemists watch the synthesis, noting detector values and flow rates to ensure the synthesis is going smoothly. They then watch the HPLC trace for the elution of the purified product peak, which they collect into a dilution flask within the hot cell. If reformulation from the HPLC solvent is necessary, the fraction containing pure product is diluted so that further purification over a C18 (or other purification) cartridge is possible. After the diluted product is trapped on the purification cartridge, it can then be eluted with ethanol and saline into the product vial, resulting in an isotonic injectable dose. This reformulation procedure if the HPLC solvent is injectable (≤10% EtOH, in a ≤20 mL dose).[87] This dose is then transferred to an aseptically assembled vial through a 0.22μm sterilizing filter before being removed from the hot-cell in a lead 'pig'. A small portion of the dose (~0.5 mL) is removed and submitted for quality control (QC) testing, where standards such as radiochemical purity, pH, identity, residual solvent levels and endotoxin levels can be tested. Because of the short half-lives of the radionuclides used (carbon-11, 20 minutes, fluorine-18, 110 minutes), every synthesis requires communication between the imaging suite and the radiochemistry facility to ensure proper delivery times.

vi. General Production – Quality Control

Each radiopharmaceutical is submitted to its own standard group of tests based on the IND, (A)NDA, or FDA approved syntheses. When the dose passes the necessary quality control (QC) checks, the dose can be sent to the hospital for patient scanning.

Radiopharmaceuticals produced using any amount of metals, for catalysis or present in the precursor, must undergo additional evaluation to confirm levels of the metal are below the threshold for an injectable compound. The thresholds acceptable for each of these tests is outlined by federal documents: United States Pharmacopeia (USP) 823, and title 21 of Code of Federal Regulations part 212 (21 CFR 212). USP 823 outlines specifications for compounding or combining multiple base ingredients; the production of [^{68}Ga]DOTATATE falls under this description as the [^{68}Ga]gallium produced by the generator is simply combined and complexed with a precursor resulting in a final injectable dose. Manufacturing of PET radiopharmaceuticals is outlined in 21CFR212; including production of [^{11}C]carbon and [^{18}F]fluorine labeled tracers.

Radiotracers produced in either method can be subjected to testing of pH, purity, identity of radionuclide via half-life measuring, residual solvents, residual metals and catalysts, as well as sterility and endotoxin tests. The pH of a dose is simply tested by placing a few drops on a pH test strip. Purity of a radiopharmaceutical can be measured by radioTLC (as in the case of [^{18}F]FDG) or radioHPLC with comparison against a non-radioactive reference standard. Half-life determination is necessary to ensure the correct radionuclide has been incorporated; this is done by measuring the radioactivity of a small sample of the dose at two separate times and calculating the half-life via Equation 1-1.

$$t_{1/2} = -\ln 2 \left(\frac{\text{time difference}}{\ln\left[\frac{\text{ending activity}}{\text{starting activity}}\right]} \right)$$

Equation 1-1: Calculation of half-life.

Residual solvent analysis is completed with gas chromatography (GC) analysis of a small sample as compared to a solvent standard. Residual catalysts and metals can be

tested for with a TLC plate with an appropriate stain for visualization. Endotoxin tests involve dispensing a diluted sample into a PTS cartridge in an endotoxin test machine. A more detailed discussion of how this pertains to production of [^{18}F]FDG is in Chapter 4 of this thesis.

Technology has steadily advanced in this field, including the automation and streamlining of quality control. Companies like LabLogic and Trace-Ability seek to make automated QC a mainstream technology in radiochemistry facilities. These instruments have the ability to test parameters such as pH, clarity, appearance, endotoxin, etc., and with a very small sample of the tracer itself.[88] Researchers also are interested in downsizing the production of radiopharmaceuticals with microfluidic technology. Archibald and coworkers at the University of Hull are hoping to also implement the use of a microfluidic chip for the QC testing of commonly used radiotracers such as FDG.[89] These technologies are still in the prototype and development phase, nevertheless it is an exciting time to watch new developments in the technology surrounding PET.

vii. Introduction to PET Scanners

Before a proper introduction to PET scanners can be described, it is necessary to understand how the recorded data originates. The radionuclide incorporated into a PET tracer is continually decaying from the moment the radionuclide is formed; the decay (transformation of a proton into a neutron in the radionuclide) releases a positron that collides with an adjacent electron in the tissue, in an event termed ‘annihilation’ (Figure 1-2). The annihilation causes two gamma (γ) rays (photons) to be released 180° opposite each other; these photons are said to be in coincidence with one another, referring to the fact that they originated at the same time from the annihilation event. The photons are

then detected by scintillation crystals in the PET scanner, which provides information about where the probe resides in the patient or animal being scanned.[1] Upon completion of the PET scan, a reconstructed image of the tissue or organ of interest is then produced by a computer that records each of these annihilation events, in a tomographic manner, collecting data on sections of the tissue.

The production of this image depends on the collection of data, correction of this data (detection of random (or false) coincident events, correction for photon attenuation and scatter in the body, and detector dead-time, etc.), and finally how the data is presented. PET imaging offers many advantages, but its main disadvantage lies in the technology used to collect the data and the algorithms and programs used to interpret it. The technology and algorithms have advanced impressively over the years, but it is still the human limit that is placed on this technology. As the technology has advanced over the past 50 years, resolution and sensitivity of PET images have increased. Originating with sodium iodide (NaI) crystals held by hand in the 1950s, today full ring PET scanners using bismuth germanate (BGO) or cerium-doped lutetium oxy-orthosilicate (LSO)

Figure 1-15: A GE Discovery MI PET Scanner. Image courtesy of GE.

crystals offer high resolution images and much higher sensitivity for detection of the coincidence photons, hence yield images of higher signal-to-noise.[90]

A PET scanner is comprised of multiple elements (Figure 1-15). There is the bed where the subject (human patient or animal) lies, and the array or gantry that contains scintillation crystals connected to photomultiplier tubes (PMTs) which serve as the detectors for data collection. The scintillation crystals are what detect the incident photons emitted from the radionuclide of the radiotracer, they absorb energy from the photons, raising electrons to an excited state, then re-emit this energy in the form of light. The chemical makeup of these scintillation crystals is important as the detectors must stand the test of time, be simple and (relatively) inexpensive to manufacture, and have chemical properties that make them attractive for PET detection. Common types of crystals include NaI, bismuth germinate (BGO), lutetium oxyorthosilicate doped with cerium (LSO), yttrium oxyorthosilicate doped with cerium (YSO), gadolinium oxyorthosilicate doped with cerium (GSO) depending on the level (price, age) of scanner, and the energy level of the radionuclides that will be used in the scanner the most.[39] The crystal choice is crucial in the determination of resolution and sensitivity. The size of the crystal is also important; too small of a crystal and the energy of the photon may not all be absorbed, too big of a crystal and spatial resolution is degraded.[91] The size and chemical makeup of the crystal can affect how it detects and absorbs the photons/energy resulting from the annihilation events.[42] The PMTs connected to these crystals generate an electrical signal in response to the light event (detection of the photon) in the scintillation crystal. This signal is recorded along with a time stamp and the height/level of the energy pulse. The energy of the pulses can be used to sort out pulses that are too low, resulting from Compton

scattering within the crystal, or too high, which could be the result of two or more photons detected by the crystal at the same time (this is one of the first steps where the data is 'cleaned up' and sorted for true coincident events). A very small amount of the annihilation events are actually detected by the PET scanner (1-10% depending on the scanner itself and the type of scan being done). Collimators or shields can be used around detectors to limit the absorbance of false coincident events to help de-convolute data. Detection of coincident photons is determined by both spatial and temporal factors. They must be detected within a very brief time window to be considered coincident events. The location of detection within the detector block is determined by data collected by the photo multiplier tubes (PMTs); from this data it is possible to calculate the center of the scintillation (where the photon's energy is dissipating from), and therefore the position of detection within the block.[93]

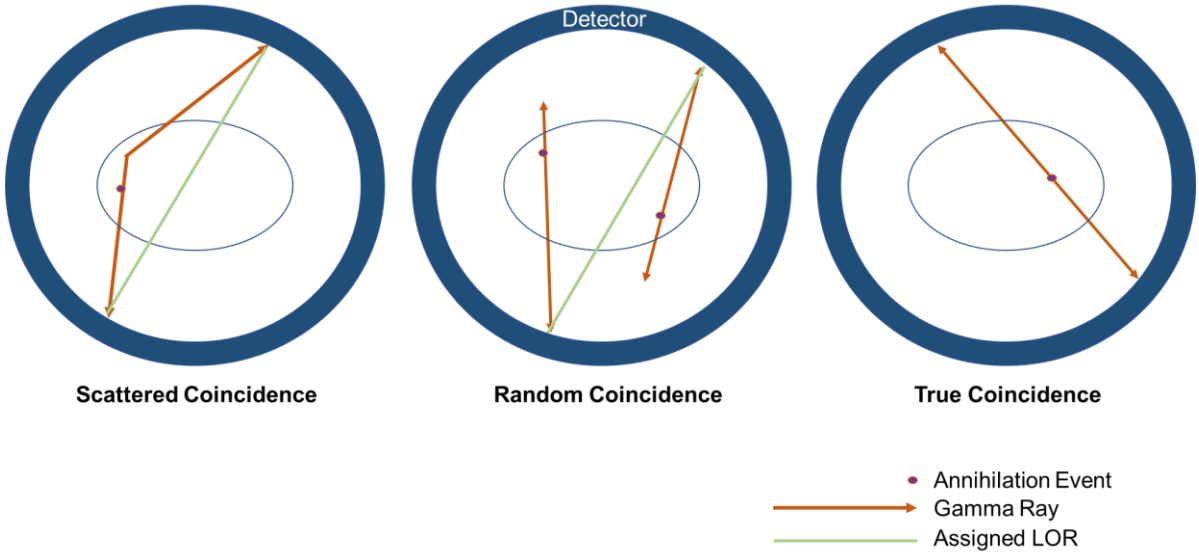

Figure 1-16: Examples of coincident events that occur during a PET scan. Image courtesy of Megan N. Stewart.

Raw data from a PET scan is acquired directly into what is known as a sinogram. This is done by recording the locations of the two detector crystals for each coincidence event, which then is recorded in a five-dimensional array of detected coincidences; four

spatial measures plus time. The four spatial measures include cylindrical coordinates in the x,y planes (r and θ), plus the location in the axial dimension (z), and finally the angle defined by the difference in the z-locations of the two detectors relative to the x-y plane (φ). The reason for the term sinogram is that if one looks at a plot of the r and θ sinogram values for given z and φ coordinates, each point of radioactivity will trace out a sinusoidal path within the plot.

A single point within the sinogram represents the number of coincidence events detected between any pair of detectors within the scanner. The line connecting these two detectors is called a line-of-response, or LoR. The complete sinogram for a scan is composed of the entire set of LORs within the scanner. The LoRs are also often called "projection rays" and the set of all LORs or rays at a given angular orientation are called a projection. Each LoR or projection ray is proportional (after corrections, see below) to the sum of radioactivity along that LoR.

The raw sinogram data is then converted into an estimate of the 3-dimensional (x,y,z) distribution of radioactivity within the scanner's field-of-view by the process called reconstruction from projections and yields the final images that are viewed and analyzed. The field of reconstruction from projections has a long history, as there have been many methods developed of the past 50 or more years, however, this is beyond the scope of this thesis

To better determine where along the LOR the annihilation event originated, time-of-flight (TOF) PET imaging can be used. This technique compares the times the photons were detected on either side of the LOR and calculates the approximate distance along the LOR. In the past, this was not traditionally used, as the detection needed for it to

provide sensitive and accurate images requires use of specific scintillation crystals. Today, TOF is getting closer to being adopted across PET imaging as the production of faster crystals and electronics of the detectors (better time sensitivity and faster processing) improves.[92]

Multiple factors can degrade the quality of the data acquired during a PET scan. Working our way from the beginning, the first factor that can negatively impact the PET scan is excess energy in the positron. The resolution of the image is inherently limited by the distance which the emitted positron travels before it participates in an annihilation event. This is typically around 1 mm for [^{18}F]fluorine .[94] Once the events have occurred and light is detected by the scintillation crystals, the events can be sorted into true, scattered, random or multiple coincidences. Scattered coincidences are when both photons from the same annihilation event are detected but one (or both) of the photons was scattered, or deflected, before it reached the detector(s) (Fig 1-16). The LOR between these detectors is then not a true representation of where the event occurred. Another type of mispositioned event, called a random coincidence, occurs when two photons are detected in the appropriate time window but originate from different annihilation events. The corresponding photons for these events may not have been detected.[92] Multiple coincidences occur when more than two photons are detected by the different detector crystals within the allotted time window; in this case it is impossible to determine which photon pair is the true coincidence, so the events are discarded.

A very important correction is to account for attenuation of photons within the body. Attenuation in PET imaging refers to photons that are scattered or absorbed in the subject, so they are not part of a true coincidence event. Attenuation typically occurs in

more dense tissue, making images reconstructed without corrections appear to have more tracer uptake in less dense areas (e.g. lungs, less dense, vs. the membrane between the lungs, denser) and in areas closer to the bodies surface. This demonstrates the necessity of corrected images, as they not only give a false reading visually, but when quantified with the drawing of ROIs can lead to incorrect determination of tracer uptake. For PET scanners without anatomical imaging modality (CT, MR), technicians must run a transmission scan. This involves the use of an external photon source that is rotated around the patient, between the patient and the detectors. The data from this scan is used to determine the amount of attenuation in the patient. Because patients vary, a transmission scan must be done before each patient scan. Transmission/background scans are also run with phantom subjects (a stationary source of radioactivity) to test the detectors and serve as a daily quality maintenance check. For PET/CT scanners, the CT scan is used for attenuation corrections.

Random coincidences can be corrected using either an equation which accounts for all events detected by detectors on either side of an LOR along with the allowed time window (what's the actual word for that?). Another method involved shifting the time window for one of the detectors but not the other. In this case there should be no true coincidences, and the number of false coincidences detected can be used as an estimate of the random coincidences that exist. This is sometimes translated into a sinogram for use in later processing.[91]

One problem in a ring type PET scanner is that the LORs can vary in length depending on which detectors are involved. If the LOR runs through the middle of the gantry the detectors on either side are the furthest apart as is possible for that scanner,

but an LOR that runs parallel to this in the periphery of the scanner will involve detectors that are closer together. The data acquisition will assume that all the LORs are the same length, and is corrected before image reconstruction with an 'arc correction.'[95] This correction becomes more important the smaller the diameter of the PET gantry (e.g. in small animal PET scanners, or dedicated brain scanners).

Different types of PET scanners can be separated first into their use: clinical human scans or pre-clinical animal studies (rodent, non-human primate, etc.). The best PET scanners are the full ring, but two- or three-plate as well as rotating partial rings are also available at a lower price and are used in smaller PET centers.

PET scanners are similar to instrumentation used for single photon imaging, although it is necessary to have detectors 180° apart from one another so that the incident photons can both be detected. The most obvious configuration to house the detectors is in a ring, although in early PET scanners the configuration consisted of two plates of detectors that were rotated around the subject. Having fewer detectors and needing to move them limits the events that can be detected and decreases the resolution of the images. One step towards increasing resolution was to add a third plate into the rotation. This presents another variability though as the three plates can be arranged differently: in a U-shape, spaced equally as a triangle, or varying throughout the scan. It has been found that the most desirable configuration for detectors in a PET scanner is a 'stack' of rings. This allows for a high detection of coincident photons and doesn't require moving parts during the scan.

The progression of PET scanner technology over the last 40 years in PET scanners can be seen in Figure The first image is from the PET III scanner developed at Washington State University by Ter-Pogossian and coworkers. Comparing the images on the left with the PET/CT images acquired years later underlines the impact that advancement of not only the instrumentation itself, but also the advancement of data processing has on the sensitivity and resolution of these images. The images on the right were acquired using Hoffman phantom, a model used for regular testing of the instruments.

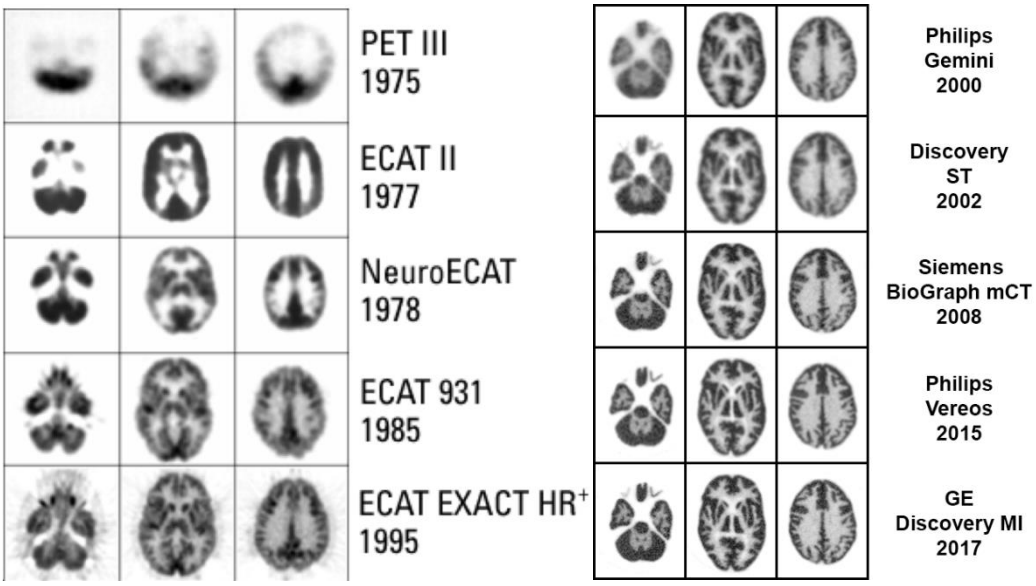

Figure 1-17: Brain images showing the gradual increase of sensitivity and resolution of PET scans. (Image courtesy of Dr. Michael Phelps, David Geffen, School of Medicine at UCLA, and Dr. Robert Koeppe, University of Michigan.)

Co-registering (overlapping and aligning) functional and anatomical imaging is a widely used technique to ensure proper assignment of structures in the body. Both preclinical and clinical PET scanners exist with CT or MRI capabilities. These machines enable the layering of both anatomical and biological images; this can create a more comprehensive image and enhances the interpretation of the data from the PET scan. The CT image can also be used for attenuation corrections, eliminating the need for a

transmission scan, therefore decreasing the time of the patient in the scanner and the dose they are exposed to. Preclinical imaging scanners used for the imaging of animals (rodents, non-human primates, etc.) are smaller than clinical human PET scanners. This offers better resolution as the detectors are closer together because the bore doesn't have to be as big. Preclinical scanners with an anatomical imaging modality (CT or MRI) are also available and allow for excellent evaluation of novel tracers.

An exciting, and very recent, development in PET scanners is a project based at University of California Davis called EXPLORER. Led by Simon Cherry, the goal of this multi-institution project is the development of a total-body PET scanner. This would enable the imaging of both brain and peripheral organs; this is both helpful for novel tracer evaluation, as well as staging and detection of cancer metastases. While it is currently possible to acquire a whole-body PET image, it requires multiple bed positions in the bore of the detector ring, and so data for each section of the body is acquired at a different time. The axial FOV of a traditional PET scanner is ~20 cm, meaning that 85-90% of the body is outside the FOV at any given point during a whole-body scan. A total-body PET scanner depends on a long axial FOV (~200 cm) so that the majority, if not all, of the body is inside the FOV for the entirety of the scan (Figure 1-18). This improves signal-to-noise ratios (SNR) greatly, increasing the effective sensitivity about 40 fold and enabling head to toe imaging.[96] It is suggested that this increase in sensitivity could allow for detection of smaller and low-contrast lesions and structures. If current sensitivity levels are acceptable for an image, the increase in sensitivity of total body PET allows for the decrease of time needed to scan or dose of injected radiotracer, an attractive option for pediatric patients.

A 40-fold increase in sensitivity also allows radiotracers to be followed twice as long as in traditional PET scanners (4-6 half-lives as compared to 3 half-lives on existing scanners). This is of use in the development of novel radiotracers, as the tracer can be observed at multiple time points, gaining more data about distribution, metabolism and excretion. In a clinical setting, this is incredibly useful, as it is suggested that [^{11}C]carbon tracers could be imaged for as long as 3 hours post injection, possibly simplifying the timing coordination between the production of radiotracers in the radiochemistry lab, and delivery to the PET imaging suite. The increase in sensitivity also increases the feasibility of multi-tracer studies, whereas the second tracer could be injected at a fraction of the typical activity level, decreasing interference with the first radiotracer. The increased sensitivity, combined with the entire body being inside the FOV for the length of the study allows for more complete kinetic analysis of tracers as well as total-body dynamic imaging. Kinetic analysis will also be assisted by all chambers of the heart, and major blood vessels being within the FOV for the entirety of the scan, enabling the use of image-derived input functions.

Initial reports and projections of this study state the need of the coupling of the total-body PET scanner with an anatomical imaging modality. MRI requires the movement of the bed from the MRI gantry and into the PET gantry, whereas CT and PET can be integrated into the same gantry. Due to the increased size of a total-body PET scanner it was decided that CT would be the most reasonable choice. After many years of planning, in mid-2017, the design of the first total-body PET/CT scanner was completed and parts were being manufactured.[96] Although the bulk of the challenges stemmed from economic and engineering hurdles, careful planning was required in order to optimize use of current

technology. For example, because of the increase of the FOV, coincidence electronics (instrumentation involved in detection and sorting of coincident events) will need to process a higher volume of events from an increased number of detectors. While true events are determined in real-time for traditional PET scans, it is more feasible for all events to be collected during a total-body PET scan, for later deconvolution. In this same vein, it was necessary to assemble an appropriate computational system to handle the large bulk of data produced by these scans; it is suggested that the number of events detected and recorded could exceed a hundred billion events, or >1 TB of data.[96]

Progress towards the development of a clinical total-body PET scanner include the mock-up of the gantry, bore and patient system. Researchers are using this mock-up to determine how a patient interacts with the scanner, in terms of both movement and correction of that movement, and any claustrophobic reactions. The mock-up is also being used to model personnel needs, and workflow changes.[96] Further development includes the design and building of a “mini EXPLORER” PET scanner, a long axial FOV PET scanner sized appropriately for total-body PET imaging of a mature Rhesus macaque monkey.[96,97] Initial studies found that this mini EXPLORER scanner was able to image all the major organs of the Rhesus monkey simultaneously with the use of [^{18}F]FDG. Included in this study was evaluation of the acceptance angle for the detectors. Acceptance angles are kept smaller (14° or 27°) in short axial FOV PET scanners to help correct for false or scattered events. In this evaluation of the mini EXPLORER, an acceptance angle of 46° was found to be well tolerated, trading higher sensitivity for a slight increase in scattered events.[97] These recently published reports are promising and

interesting and give excellent examples of what can yet be accomplished using PET imaging.

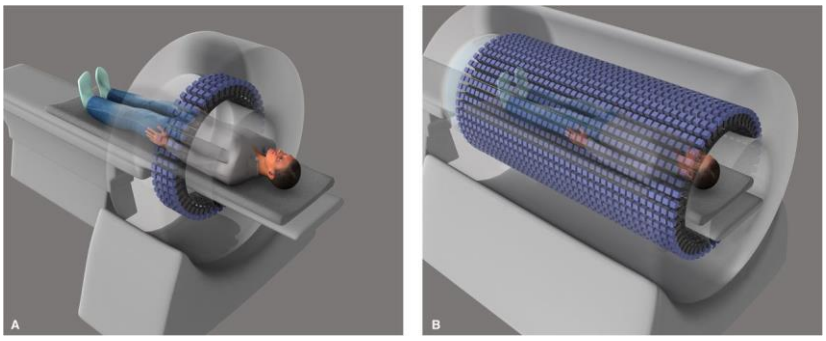

Figure 1-18: Comparison of traditional short axial FOV PET scanner (A), to a total-body long axial FOV PET scanner (B).Reprinted with permission from Elsevier Cherry, S. R.; Badawi, R. D.; Karp, J. S.; Moses, W. W.; Price, P.; Jones, T. Sci. Transl. Med. 2017, 9 (March 2017), 1–4.

B. The GABAergic System:

i. GABA and the CNS

The balance of excitatory and inhibitory neurotransmitters is what regulates all activities of the brain, including learning, sleeping, memory, and consciousness. When this balance is disrupted it leads to physiological and psychological disorders such as epilepsy, dementia, schizophrenia, and cognitive impairment.[98] Gamma(γ)-amino butyric acid (GABA, **1.55**) is the principal inhibitory neurotransmitter in the CNS, which is balanced by the excitatory neurotransmitter glutamate (**1.56**). As the major neurotransmitters in the brain, the GABA/glutamate system has been and continues to be studied extensively.

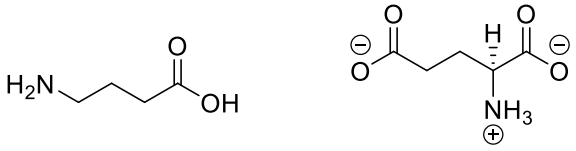

1.55, GABA, γ–amino butyric acid **1.56,** Glutamate

Figure 1-19: The neurotransmitters GABA and glutamate.

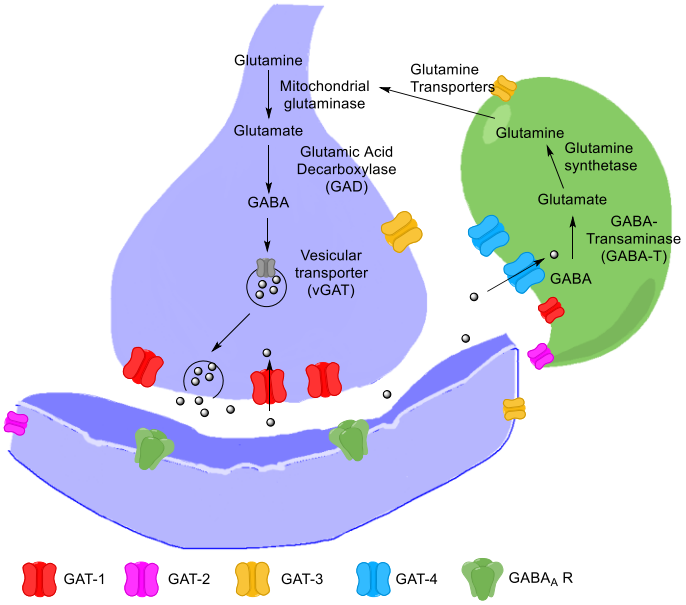

Figure 1-21: A representative GABA synapse with the GABA metabolic cycle.

First synthesized in 1883, GABA wasn't confirmed to be found in brain tissue until 1950, by three groups simultaneously.[99–101] It was later identified as a neurotransmitter in 1967 and 1968 by two groups of electrophysiologists.[102,103] Research has been ongoing to determine the importance of this neurotransmitter, expanding even faster after the discovery of the first benzodiazepine, chlordiazepoxide (**1.57,** trade name Librium), in 1957 by Sternbach and coworkers at Roche.[104,105] This serendipitous discovery is said to have originated from a lab cleaning that found a forgotten compound which was successful when tested.

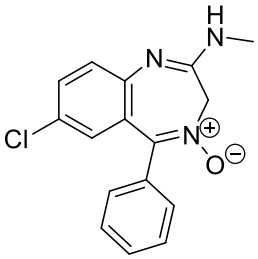

1.57, chlordiazepoxide

Figure 1-20: Chlordiazepoxide, the first benzodiazepine.

Benzodiazepines (BZ) are positive allosteric modulators of the $GABA_A$ receptor, an ionotropic ligand gated ion channel, and now represent a large and lucrative drug class. [106] Binding of BZs alone to a $GABA_A$ receptor will not elicit an effect; the binding of endogenous GABA is necessary for the receptor's ion channel to open.[107–109] The late

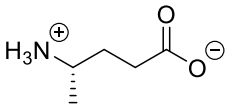

1.58, (*S*)-4-methyl GABA

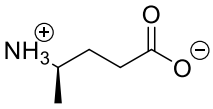

1.59, (*R*)-4-methyl GABA

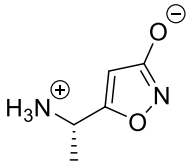

1.60, (*S*)-(-)-5-methylmuscimol

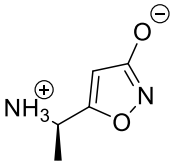

1.61, (*R*)-(-)-5-methylmuscimol

Figure 1-22: A sample of GABA analogs evaluated for determination of antagonists or agonists.

1970s and early 1980s found an increase in the development of GABAergic pharmaceutics, although the targets of these drugs may not have been immediately known. Towards this end, researchers used GABA as a lead and tested the effects of various GABA-related scaffolds, Figure 1-22.[110] These studies sought to differentiate these conformationally restricted cyclic amino-acid-type molecules as GABA antagonists, agonists, uptake inhibitors or others.[106] One such study evaluated methylated GABA analogs (**1.58**, **1.59**) as well as compounds based on muscimol (**1.60**,**1.61**) and found the methylated GABA analogs to be much better GABA uptake inhibitors.[110] It was known early on that GABA itself, as well as the more polar compounds being used in these studies, did not readily cross the blood brain barrier (BBB) when administered systemically. Effects of the drugs were observed when administered intracerebroventricularly.[111] Preliminary investigation of the use of pro-drugs of these compounds found increased brain penetration, but also limited desired anticonvulsant

activity and minor cholinergic toxicity.[111] These findings discouraged the use of nipecotic acid-like pro-drugs in the development of anticonvulsant therapeutics, and researchers instead turned to increasing the lipophilicity of the drugs in other ways. Avoiding the active carboxylic acid moiety of nipecotic acid, the obvious and attractive route was to introduce lipophilicity in the form of N-alkyl side chains.

Before the mechanism of actions of psychoactive drugs were understood, the clinical approach to treating neurological and psychological disorders was to prescribe drugs based on presenting symptoms and observe the effect they had to determine efficacy. Then with the development of knockdowns, animal models and tissue work, scientific studies could be done to determine if the GABAergic system was affected in different diseases.[104,106]

Today, there are over 50 benzodiazepines alone and even more drugs that target the GABAergic system to attenuate and treat symptoms of a variety of diseases and disorders, both neurological and systemic.[104] Inhibition of GABA uptake has been of interest in treating epilepsy for some time; research towards this end has also sought to differentiate between neuronal and glial uptake inhibition.[106,112,113] Neuronal uptake

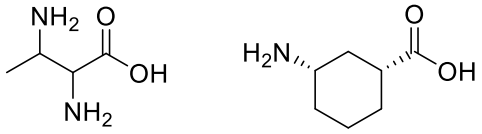

1.62, DABA **1.63**, ACHC

Figure 1-23: GABA uptake inhibitors found to be pro-convulsant.

inhibition initially was understood to increase the synaptic concentration of GABA, but it has also been found that neuronal GABA uptake inhibitors such as diaminobutyric acid (DABA, **1.62**) and *cis*-3-aminocyclohexane carboxylic acid (ACHC, **1.63**) are actually proconvulsant (causing seizures).[112,114] It is thought that the inhibition of neuronal GABA

uptake depletes the neuronal source of GABA, because the synaptic GABA is instead taken up by glial transporters, and once in the glial cells is catabolized and must be transported back to the neuron as glutamine and synthesized into GABA once again.[106]

Biologically, GABA is synthesized from its counterpart glutamate, via a decarboxylase, GAD. The biosynthesis of GABA takes place in a pre-synaptic neuron, after which it is packaged into a vesicular GABA transporter (vGAT) to be released into the synaptic cleft. When released into the synaptic cleft, GABA acts on any of the GABA receptors, and is then taken up by any of the GABA transporters (GAT-1, -2, -3, or -4). When GABA is taken up through the neuronal GAT-1 it is recycled back into vGAT for release into the synapse. Conversely, if GABA is taken up by GAT-3 on an astrocyte, it is catabolized into glutamate. Concurrently, alpha-ketoglutarate is converted into succinic semialdehyde, and can be used in the citric acid cycle as a source of energy.[115] The GABA shunt, the major metabolic pathway of GABA, is when the citric acid cycle is bypassed, and the α-ketoglutarate is converted to succinate via glutamate, GABA and succinic semi-aldehyde.[107,115]

Table 1-2: Correlation of aspects of the GABAergic system with neurological disorders.

Disease	Changes
Schizophrenia	↑ GAT-1 expression
Depression & Anxiety	↑ GABA plasma levels
Autism Spectrum Disorders	Mutation in GAT-1 gene (SLC6A1) and ↓ GAT-1 expression, mRNA (Fmr1 KO)
Parkinson's Disease	↓ GAT-1 activity
Epilepsy	GAT-1 inhibitor acts as anticonvulsant.
Alzheimer's Disease	↑ Astrocytic GABA

Disorders involving the GABAergic system are widespread; Alzheimer's Disease (AD), Parkinson's Disease (PD) and epilepsy combined affect nearly 10 million people in the US alone.[116,117] Dysfunction in the GABAergic system also affects the serotonergic and dopaminergic systems, and excess GABA was found to suppress the release of both dopamine and serotonin, leading to anxiety and depression related disorders.[108] As such, knowledge of the distribution of GABA receptors and transporters is necessary to better understand the physiology of the CNS and to develop more effective treatments and therapies for the diseases outlined in Table 1-2.[118–124]

ii. GABA Physiology

From the time that GABA was understood as a neurotransmitter in 1967,[102] there has been much interest in the pharmacology of the GABAergic system (see recent reviews).[104,106,125] These therapeutics target receptors, transporters and enzymes in the GABAergic system. For example, the target of the first class of GABAergic drugs, benzodiazepines, is a subtype of the GABA receptors, $GABA_A$.[104] Each $GABA_A$ receptor

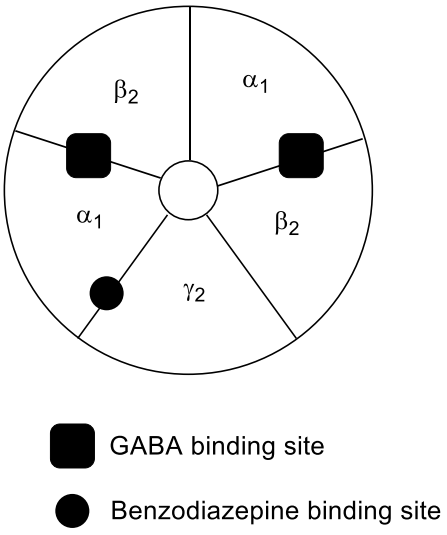

Figure 1-24: Top view of the pentamer of the most common isoform of $GABA_A$ receptors $2\alpha_1 2\beta_{2\gamma 2}$.

is comprised of five subunits which form heteroligomeric ligand gated ion channel. There are eight classes of these subunits, some with multiple variants (α_{1-6}, β_{1-3}, γ_{1-3}, δ, ε, π, θ, and ρ_{1-3});[126] the most common combination of these subtypes found in the mammalian brain is $2\alpha_1 2\beta_2\gamma_2$, Figure 1-24.[108] GABA acts allosterically on these receptors, binding to a specific GABA binding site, which activates the ion channel of the receptor. The ionotropic $GABA_A$ receptors are located post-synaptically in the GABAergic synapse and are responsible for the modulation of the membrane potential of the neuron is reside on, via the flow of chloride ions. As an inhibitory neurotransmitter, the binding of GABA to its receptors causes the hyperpolarization of the neuronal membrane, decreasing the excitability of the cell. Therapeutics targeting $GABA_A$ receptors either enhance (e.g. benzodiazepines, agonists) or decrease (e.g. flumazenil, an antagonist) the inhibitory action of the endogenous GABA.[104]

Sometimes referred to as $GABA_C$ receptor subtypes, $GABA_{A\text{-}rho}$ receptors are comprised of entirely rho (ρ) subunits and are expressed mainly in the mammalian retina.[127] It is still argued that these receptors are their own subtype as agonists and antagonists of both $GABA_A$ and $GABA_B$ receptors have no effect on the $GABA_{A\text{-}rho/C}$ receptors; however these receptors are also ionotropic, and mediate membrane potential through a chloride channel.[128]

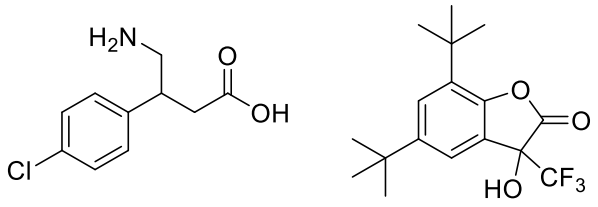

1.64, baclofen **1.65**, BHFF

Figure 1-25: Drugs that act on the $GABA_B$ receptor subtype.

$GABA_B$ receptors are metabotropic GPCRs located both pre- and post-synaptically, and also induce hyperpolarization of the membrane of their cells, albeit slower than their $GABA_A$ counterparts.[108] $GABA_B$ receptors are comprised of two subunits, $GABA_{B1}$ which contains the GABA binding site and $GABA_{B2}$ which is responsible for the binding of the G-coupled messenger proteins.[129] The activation of pre-synaptic $GABA_B$ receptors has the ability to regulate the release of neurotransmitters, like GABA and glutamate, serving as a feedback mechanism for the GABAergic system. This makes $GABA_B$ receptors an interesting therapeutic target; compounds targeting $GABA_B$ receptors include those for spasticity (baclofen, **1.64**), anxiety ((R,S)-5,7-di-tert-butyl-3-hydroxy-3-trifluoromethyl-3H-benzofuran-2-one, BHFF, **1.65**),[130] and autism.[131]

Enzymes necessary for the metabolism and catabolism of GABA include GABA transaminase (GABA-T, also known as GABA aminotransferase or GABA-AT) and glutamic acid decarboxylase (GAD). GABA-T, assisted by pyridoxal 5'-phosphate, is key in the degradation of GABA to succinic semialdehyde before its entrance into the citric acid cycle, and it is present in both glial and neuronal cells.[104,108,115] GABA-T is therapeutically targeted by drugs such as vigabatrin, which inhibit the breakdown of GABA for the treatment of epilepsy.[104] GAD exists in two isoforms, GAD_{65} and GAD_{67}, which both participate in the synthesis of GABA from glutamic acid, but in separate metabolic pathways.[132] These enzymes are expressed in all GABAergic neurons making these enzymes a therapeutic target for neurological diseases such as epilepsy. In Silverman and coworkers' search for a GABA-T inhibitor, pregabalin (Lyrica), was discovered.[133] Although the exact action of this drug is yet unknown, a dose dependent

increase in the activity of GAD can be observed, and it is regularly used in the treatment of disorders such as epilepsy and neuropathic pain.[134]

The action of GABA is mediated by its removal from the synapse by GABA transporters. There are four transmembrane transporter subtypes (GAT-1, -2, -3, and -4) which remove GABA from the synaptic cleft and one vesicular GABA transporter (VGAT) which is responsible for release of GABA into the synaptic cleft. All GABA transporters are members of the solute carrier 6 (SLC6) family.[135] GAT-4, also referred to as the betaine-GABA transporter 1 (BGT-1), is a peripheral GABA transporter that can also transport betaine and has been shown to be expressed mainly in the liver, with lower expression levels in other tissues such as hepatocytes and the leptomeninges.[136] GAT-2, like BGT-1, has found to be expressed in both the brain as well as peripheral tissues. In the brain, it has been found to be expressed in low levels in the meninges, and to a lesser extent on astrocytic cells.[112,135] GAT-3 is known to be located on glial cells and extrasynaptically, expressed at lower levels than GAT-1. GAT-2 and -3 are expressed at higher levels than GAT-1 systemically. In the CNS, GAT-3 is located mainly in the retina, olfactory bulb, and brainstem.[137] GAT-1, the most abundantly expressed GABA transporter, is located pre-synaptically and almost exclusively in the CNS. This transporter is discussed in more detail below.

Respective levels of the GABA transporter subtypes have been determined thus far using post-mortem tissue with fluorescent staining as well as observations of mRNA levels.[138,139] These methods are difficult to quantify reliably as staining can give inconsistent results, and mRNA levels are not always representative of expression of

protein in tissue.[140] This work seeks to offer a quantifiable, *in vivo* method for the observation of GAT-1 through the use of PET imaging.

iii. The importance of GAT-1

GABA transporter 1 (GAT-1) is one of four GABA transporters, GAT-1, GAT-2, GAT-3 and GAT-4/BGT-1. Of these four transporters, GAT-1, located on pre-synaptic GABA neurons, is the most abundant with levels higher in the cortex, and hippocampus (among other regions). In addition, it has been shown that the GABA receptor dysfunction is a result of the malfunction of GABA transporter 1 (GAT-1) in epileptic mice.[141] The binding capacity (B_{max}) of GAT-1 in control subjects has been determined *via* a brain homongenate assay method using [^{3}H]tiagabine giving a B_{max} in the frontal cortex of 3400 fmol/g protein.[142]

It was demonstrated that GABA could accumulate in incubated brain slices by Elliot and van Gelder in 1958[143] ten years before Iversen and Neal proved the existence of GABA uptake transporters in 1968.[144] First cloned and expressed in 1990 by Guastella and coworkers,[145] GAT-1 has been of interest as a pharmacological target for over 30 years. As Andersen and coworkers pointed out, inhibiting GABA uptake offers the potential for less side effects than a GABA agonist, as it is only enhancing the activity of endogenous GABA in synapses where it has been physiologically released.[146] The only

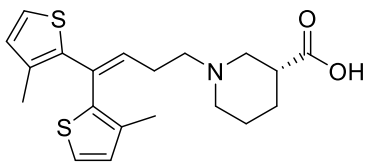

1.66, Tiagabine

Figure 1-26: The only FDA approved GAT-1 inhibitor, tiagabine (Gabitril).

FDA-approved GABA uptake inhibitor (GAT-1 selective) is the anti-convulsant tiagabine (Figure 1-26, **1.66**).[147]

Approved by the FDA in 1997, tiagabine is used as adjunctive therapy to attenuate epileptic seizures and has been the basis of many structure-activity relationship (SAR) and PET studies. To broaden the understanding and further the pharmacological relevance of GAT-1, many studies have been conducted to determine how GAT-1 is involved in the pathophysiology of different neurological diseases. For example, post-mortem studies on schizophrenic brains have shown an increase in [^{3}H]-tiagabine binding, indicating an increase in GAT-1 in these circumstances.[122] Additional work showed an inverse correlation between a [^{3}H]-tiagabine binding and the subject's age, demonstrating a decrease in GAT-1 expression in the aging brain.[123] Alzheimer's disease (AD) has a somewhat contradictory history with the GABAergic system. Some studies claim that GAT-1 levels are left unaffected by the disease,[121] while other reports argue that the GABAergic system is being glanced over in the efforts to understand the mechanisms underlying AD.[148] These studies, done either in post-mortem tissue or animal models, lack *in vivo* confirmation of their findings.

Previous studies have also sought to provide an initial map of distribution of the pre-synaptic GAT-1 via fluorescent labeling or observations of levels of GAT-1 mRNA; however, fluorescent staining can be inconsistent and levels of mRNA do not always directly represent levels of expressed protein.[140] In contrast to these *in vitro* and *ex vivo* techniques, PET imaging offers an advanced, non-invasive, *in vivo* technique that is used to determine the distribution and function of endogenous targets, particularly those that are over- or under-expressed in patients with a given disease when compared to healthy

subjects. This technique also acts as a companion diagnostic to help monitor patient response to therapy and stratify patients for a more personalized approach to medicine.[149–152]

iv. Current approaches for imaging of the GABAergic System

Currently multiple techniques for imaging of the GABAergic system exist. Magnetic resonance spectroscopy (MRS) has been used to determine concentration of GABA itself

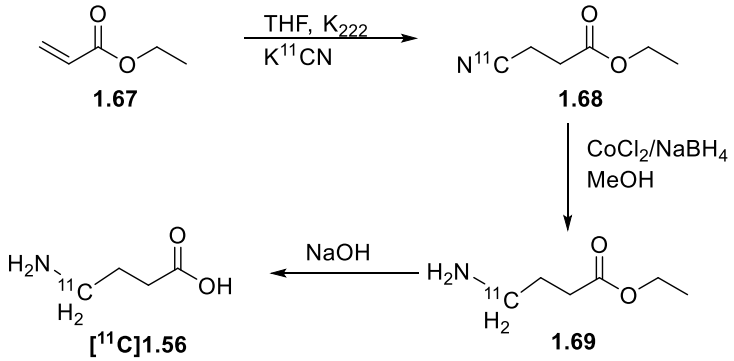

Figure 1-27: Synthesis of [^{11}C]GABA for use in PET imaging.

in vivo.[153] Although this method allows for the quantification of neurotransmitters *in vivo*, MRS is only capable of measuring total concentration in a limited region and is not able to distinguish between pools of neurotransmitters (e.g. is the neurotransmitter in a pre- or post- synaptic neuron, or in the synaptic cleft). Because of these limitations, more specific imaging modalities are necessary to draw relationships between neurotransmitter, receptor and transporter levels and various neurological disorders. PET imaging offers one such modality.

Initially, there were attempts to image the GABAergic system using simple ^{11}C-labeled GABA (**[^{11}C]1.56**) , but since GABA is not BBB permeable, this approach is not suitable for neuroimaging.[154] Currently in the clinic, studies with [^{11}C]flumazenil

([^{11}C]FMZ, **[^{11}C]1.55**, Figure 1-28) image the post-synaptic $GABA_A$ receptor. Researchers have sought to improve [^{11}C]FMZ, either by introducing a ^{18}F-label instead to lengthen

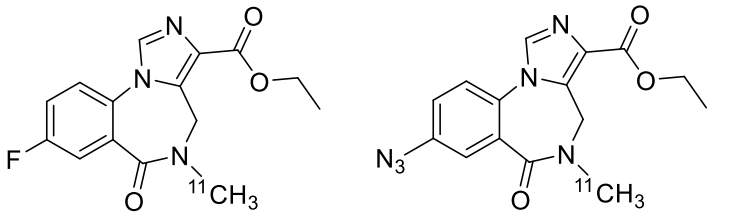

[^{11}C]1.55, [^{11}C]-FMZ **[^{11}C]1.70**, [^{11}C]Ro 15-4513

Figure 1-28: [^{11}C]FMZ and its azide analog [^{11}C]Ro 15-4513 for PET imaging of $GABA_A$ receptors.

scan time, and make the tracer available in areas without a cyclotron,[13,85] or by altering the molecule to enhance selectivity of the radiotracer for certain subtypes of the $GABA_A$ receptor.[13,155] Both [^{11}C]- and [^{18}F]- labeled FMZ have been used extensively in the exploration of the GABAergic system. A study using [^{11}C]FMZ disclosed that the administration of the GAT-1 inhibitor tiagabine (**1.66**) led to an increase in [^{11}C]FMZ binding, demonstrating how FMZ can be used to image changes in synaptic GABA concentration; this effect was later shown to be dose-dependent.[156,157] FMZ has also been found to have decreased binding in epileptic foci, assisting in pre-surgical preparations and evaluation of epileptic patients.[85,158] Yet another utility of FMZ is the stratification of stroke patients to better develop treatment for those with acute ischemic deficits as well as predict any subsequent stroke events.[159] Analysis of the studies above is possible due to FMZs excellent tracer properties: metabolites are non-BBB permeable, metabolism does not occur in the brain, it has low non-specific binding in the brain, and it has fast reversible kinetics.[160]

Many other studies have been done to image the GABAergic system, mainly targeting the $GABA_A$ receptor and its benzodiazepine binding complex.[161] A promising

tracer is [^{11}C]Ro 15-4513, an azide derivative of FMZ; preliminary studies of this [^{11}C]-labeled partial inverse agonist have indicated selectivity to the $GABA_A$ receptor α_5 subunit.[162] This same research group used [^{11}C]Ro 15-4513 to compare alcohol-dependent men with healthy controls and found decreased binding in the alcohol-dependent subjects, specifically in the nucleus accumbens and hippocampus. Previous studies of alcohol-dependent subjects with [^{11}C]FMZ have also found a decrease in binding, however in the frontal cortex, as [^{11}C]FMZ binds preferentially to the α_1 subtype GABA receptor found there.[163] A more recent study also found a decrease in [^{11}C]Ro 15-4513 in the nucleus accumbens in a group of opiate-dependent subjects, suggesting that the α_5 subunit has reduced levels in addiction in general.[162]

Currently, there are no specific radiotracers for pre-synaptic GAT-1 in clinical use. Development of a novel CNS tracer specific to GAT-1 will provide information on the concentration, location, and changes in GABAergic neurons that is currently impossible

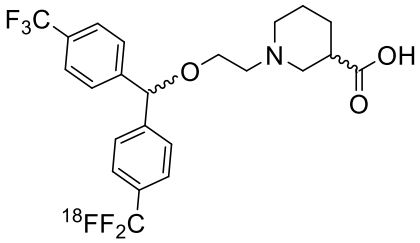

[^{18}F]1.71, [^{18}F]CI-966

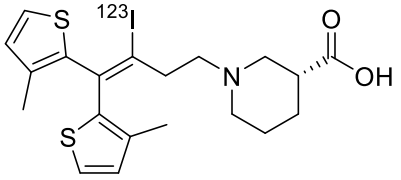

[^{123}I]1.72

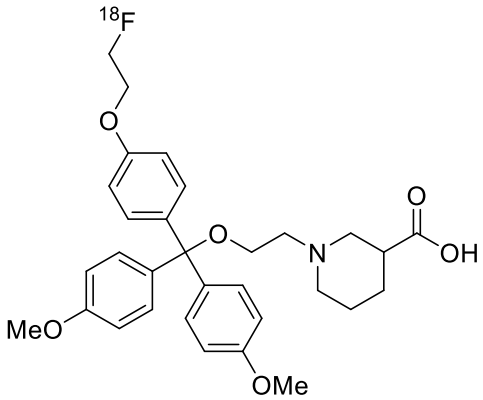

Figure 1-29: Previous efforts towards molecular imaging of GABA transporters.

to obtain due to lack of suitable *in vivo* imaging agent. Although work is being done to find an inhibitor of GAT-1 more potent than tiagabine, these studies are focused on developing a high-affinity, highly selective inhibitor for therapeutic use.[164,165] Previous work developing imaging agents targeting GABA transporters has involved radiolabeling of tiagabine (targeting GAT-1) or similar scaffolds selective for targeting other GABA transporters (GAT-2/3). For example, in 1990, Kilbourn and coworkers successfully radiolabeled an analogue of CI-966 (**1.71**), a compound developed by Parke-Davis;[166] this work was promising with *in vivo* evaluations indicating uptake of the radiotracer into the brain, albeit at fairly low levels.[167] More recent efforts include a study in which tiagabine was successfully labeled with iodine-123 for single photon emission computed tomography (SPECT) imaging, **[^{123}I]1.72**, Figure 1-29. However, *in vivo* testing showed that although the tracer passed through the BBB, it was quickly circulated and at 3 hours post injection was found in nasal mucosa and Hadrian glands and no longer in the brain (Figure 1-30).[168]

Schirrmacher *et al.* developed a PET ligand specific to GAT-3, (±)-(2-((4-([18F]fluoroethoxy)phenyl)bis(4-methoxyphenyl)methoxy)ethyl)piperidine-3-carboxylic

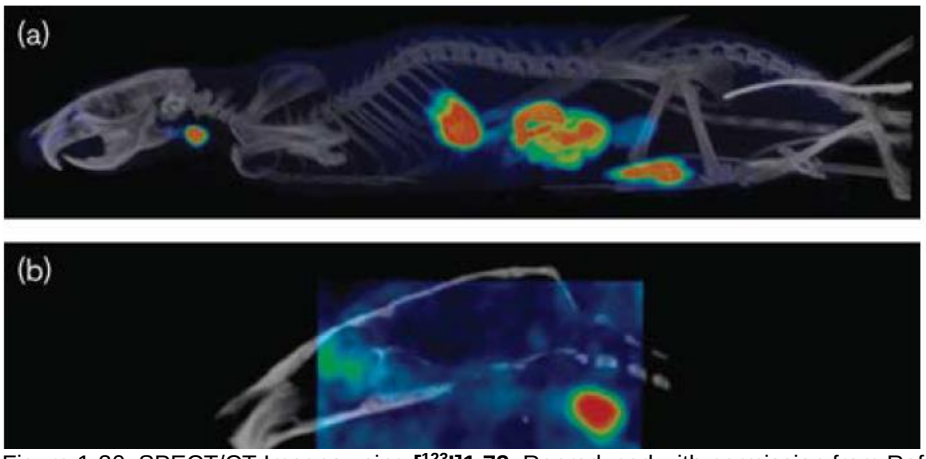

Figure 1-30: SPECT/CT Images using **[^{123}I]1.72**. Reproduced with permission from Ref {Schijns 2013}.

acid, **[^{18}F]1.73**. GAT-3 is largely expressed in glial cells, especially in the hypothalamus, and imaging of this transporter could offer an interesting and regionally specific perspective; however, targeting GAT-3 does not offer a complete comprehension of pre-synaptic irregularities throughout the brain.[169] These studies have been successful in radiolabeling but the novel radiopharmaceuticals are lacking in BBB permeability. Some cite the position of the radiolabel (e.g. ^{123}I on the olefin, Schijns 2013) for their lack of uptake,[168] while others targeted GABA transporters with low comparative expression in the brain (such as GAT-3) and demonstrated successful radiosynthesis with limited evaluation of the radioligand itself.[169]

A GAT-1 specific *in vivo* imaging agent has the potential to improve our understanding of the pathology of epilepsy, schizophrenia, and other diseases and, therefore, could positively impact the lives of numerous patients. The radiotracer(s) developed as a result of this research will provide new information about the role of GAT-1 in the pathophysiology of these disorders, which is currently limited to the data obtained mainly by pathologists during post-mortem studies. With *in vivo* imaging, more conclusive diagnostic techniques and more directed drug development is a real possibility that can lead to personalized treatment and better patient outcome.[150]

v. GABA Uptake Inhibitors

Even before the approval of tiagabine in 1997,[147] many studies had been conducted to develop molecules with potency and selectivity for GABA uptake inhibitors,[170,171] and efforts in this space continue today. The majority of these include a cyclic amino acid such as nipecotic acid (**1.74**) or guvacine (**1.75**), Figure 1-31; both of

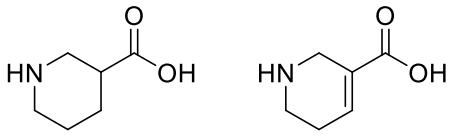

1.74, nipecotic acid **1.75**, guvacine

Figure 1-31: Cyclic amino acids used as GABA analogs.

which can be considered as conformationally restricted forms of GABA and thus essential for the activity of typical GABA uptake inhibitors. These amino acids are not BBB permeable themselves, and therefore they are typically connected to a diaryl moiety via an alkyl linker, Figure 1-32. The linker chain can be saturated or unsaturated, with or without heteroatoms such as O or N, and is 3-5 atoms long in most cases. The aryl residue the linker leads to could be two or three substituted phenyls, thiophenes, or a tricyclic group. Comparing these studies, it seems that selectivity between the GABA transporter subtypes (GAT-1 to -4) is achieved by altering these side chains and aryl groups.[146,170,171] For example, SNAP-5114 (**1.78**), with a triphenyl pendant shows

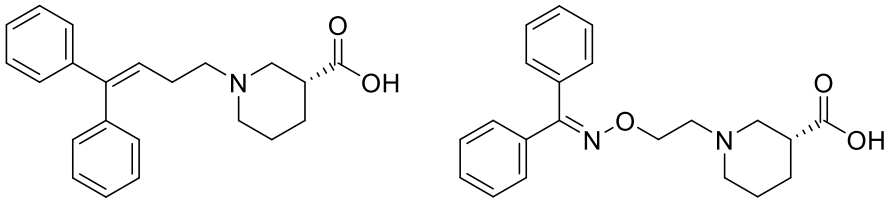

1.76, SK&F-89976-A **1.77**, NO-711

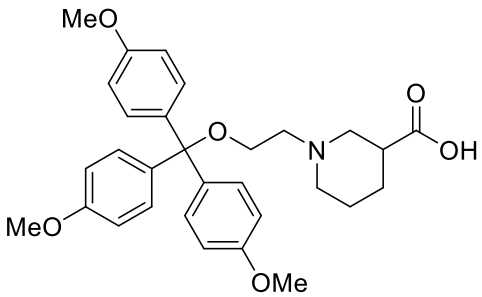

1.78, SNAP-5114

Figure 1-32: Examples of how differing aryl pendants can build selectivity between GAT subtypes.

selectivity for GAT-3, as opposed to NO-711 (**1.77**) or SK&F-89976-A (**1.76**) which show selectivity for GAT-1, Figure 1-32.

Some studies have also sought to determine the binding mode of these scaffolds by aligning GAT-1's gene sequence with the only transporter in the solute carrier family to be crystallized: a bacterial leucine transporter, LeuT.[172] These studies have mostly suggested that the carboxylic acid moiety on the nipecotic acid is necessary for inhibition of the transporter,[173,174] although one study suggested that it was in fact the piperidinyl amine that turns into the active site and participates in binding, at least for *N*-unsubstituted inhibitors.[175] Additionally, the aryl groups can participate in pi-pi stacking outside the binding pocket.[176]

Although most of the GABA uptake inhibition SAR studies have been focused on inhibition of neuronal GAT-1, a small number of studies have sought to inhibit the other subtypes of GABA transporters. A small library was synthesized targeting GATs 2 and 3. The researchers used amino-methyl tetrazoles as a bioisostere for the nipecotic acid moiety and experimented with size and composition of side chains to create selectivity for GAT subtypes.[177] This led to the development of inhibitors of GAT-2 (**1.79**) as well as GAT-4/BGT-1 (**1.80**, **1.81**) , Figure 1-33. GAT-3 has also been the subject of an inhibitor search,[178] although GAT-1 still attracts the most attention as the most promising of the

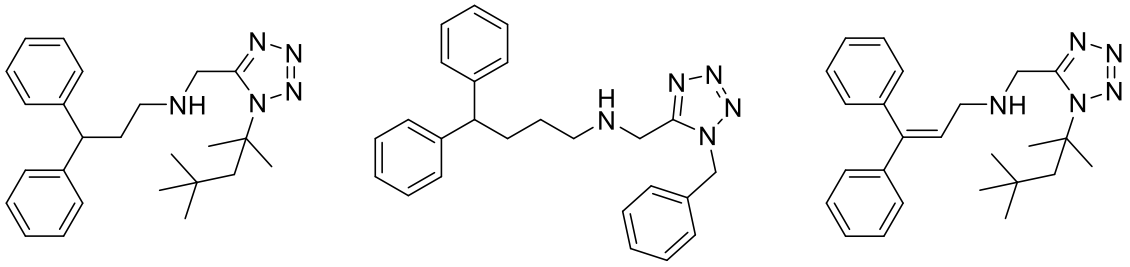

1.79, GAT-2 selelctive **1.80**, GAT-4 selective **1.81**, GAT-4 selective

Figure 1-33:Non-classical GABA uptake inhibitors with selectivity to GAT-2 and -4.

GABA transporters therapeutically and pharmacologically. By targeting this GABA transporter with PET imaging, we hope to learn more about the target engagement of the radiolabeled tracers, and about the distribution and activity of the transporter itself.

C. References

(1) Miller, P. W.; Long, N. J.; Vilar, R.; Gee, A. D. *Angew. Chemie - Int. Ed.* **2008**, *47* (47), 8998–9033.

(2) Saha, G. B. *Physics and Radiobiology of Nuclear Medicine*, 3rd ed.; Springer Science: New York, NY, 2006.

(3) *Biotechnology Law Report*. 2006, pp 167–174.

(4) Ross, T. L.; Wester, H. J. In *Handbook of Nuclear Chemistry*; Springer Science, 2011; pp 2021–2070.

(5) What Is A Nuclear Reactor? https://www.euronuclear.org/1-information/energy-uses.htm (accessed Jul 6, 2018).

(6) Non-Power Nuclear Applications: Research Reactors http://www.world-nuclear.org/information-library/non-power-nuclear-applications/radioisotopes-research/research-reactors.aspx (accessed Jul 6, 2018).

(7) Eisenhut, M.; Mier, W. In *Handbook of Nuclear Chemistry*; Springer Science, 2011; pp 2121–2142.

(8) Qaim, S. M. In *Handbook of Nuclear Chemistry*; Springer Science, 2011; pp 1903–1933.

(9) Corp, U. N. Australian Reactor Shutdown Highlights Vital Need for New Source of Medical Isotopes https://globenewswire.com/news-release/2018/07/16/1537584/0/en/Australian-Reactor-Shutdown-Highlights-Vital-

Need-for-New-Source-of-Medical-Isotopes.html (accessed Jul 22, 2018).

(10) Gumiela, M.; Dudek, J.; Bilewicz, A. *J. Radioanal. Nucl. Chem.* **2016**, *310* (3), 1061–1067.

(11) Gillis, E. P.; Eastman, K. J.; Hill, M. D.; Donnelly, D. J.; Meanwell, N. A. *J. Med. Chem.* **2015**, *58* (21), 8315–8359.

(12) Snell, A. H. In *Proceedings of the American Physical Society*; Pasadena, CA, 1937; pp 142–150.

(13) Rodnick, M. E.; Hockley, B. G.; Sherman, P.; Quesada, C.; Battle, M. R.; Jackson, A.; Linder, K. E.; Macholl, S.; Trigg, W. J.; Kilbourn, M. R.; Scott, P. J. *Nucl Med Biol* **2013**, *40* (7), 901–905.

(14) Brooks, A. F.; Rodnick, M. E.; Carpenter, G. M.; Scott, P. J. H. In *Radiochemical Syntheses: Further Radiopharmaceuticals For Positron Emission Tomography and New Strategies for Their Production*; 2015.

(15) Brust, P.; van den Hoff, J.; Steinbach, J. *Development of 18F-labeled radiotracers for neuroreceptor imaging with positron emission tomography*; 2014; Vol. 30.

(16) Mossine, A. V.; Brooks, A. F.; Makaravage, K. J.; Miller, J. M.; Ichiishi, N.; Sanford, M. S.; Scott, P. J. H. *Org. Lett.* **2015**, *17* (23), 5780–5783.

(17) Ichiishi, N.; Brooks, A. F.; Topczewski, J. J.; Rodnick, M. E.; Sanford, M. S.; Scott, P. J. H. *Org. Lett.* **2014**, *16* (12), 30–33.

(18) Vanderborn, D.; Sewing, C.; Herscheid, J. D. M.; Windhorst, A. D.; Orru, R. V. a; Vugts, D. J. *Angew. Chemie - Int. Ed.* **2014**, *53* (41), 11046–11050.

(19) Tredwell, M.; Preshlock, S. M.; Taylor, N. J.; Gruber, S.; Huiban, M.; Passchier, J.; Mercier, J.; Génicot, C.; Gouverneur, V. *Angew. Chemie - Int. Ed.* **2014**, *53*

(30), 7751–7755.

(20) Preshlock, S.; Tredwell, M.; Gouverneur, V. *Chem. Rev.* **2016**, *116* (2), 719–766.

(21) Brooks, A. F.; Topczewski, J. J.; Ichiishi, N.; Sanford, M. S.; Scott, P. J. H. *Chem. Sci.* **2014**, *5* (12), 4545–4553.

(22) Cole, E. L.; Stewart, M. N.; LIttich, R.; Hoareau, R.; Scott, P. J. H. *Curr. Top. Med. Chem.* **2014**, *14* (7), 875–900.

(23) Mossine, A. V; Thompson, S.; Brooks, A. F.; Sowa, A. R.; Miller, J. M.; Scott, P. J. *Pharm. Pat. Anal.* **2016**, *5* (5), 319–349.

(24) Brooks, A. F.; Drake, L. R.; Stewart, M. N.; Cary, B. P.; Jackson, I. M.; Mallette, D.; Mossine, A. V.; Scott, P. J. H. *Pharm. Pat. Anal.* **2016**, *5* (1), 17–47.

(25) van der Born, D.; Pees, A.; Poot, A. J.; Orru, R. V. A.; Windhorst, A. D.; Vugts, D. J. *Chem. Soc. Rev.* **2017**, *46* (15), 4709–4773.

(26) Makaravage, K. J.; Brooks, A. F.; Mossine, A. V.; Sanford, M. S.; Scott, P. J. H. *Org. Lett.* **2016**, *18* (20), 5440–5443.

(27) Bishop, A.; Satyamurthy, N.; Bida, G.; Barrio, J. R. *Nucl. Med. Biol.* **1996**, *23* (5), 559–565.

(28) Roberts, A. D.; Oakes, T. R.; Nickles, R. J. *Appl. Radiat. Isot.* **1995**, *46* (2), 87–91.

(29) Schrobilgen, G.; Firnau, G.; Chirakal, R.; Garnett, E. S. *JCS Chem Comm* **1981**, 198–199.

(30) Jewett, D. M.; Potocki, J. F.; Ehrenkaufer, R. E. *Synth. Commun.* **1984**, *14* (1), 45–51.

(31) Straatmannand, M.; Welch, M. *J. Nucl. Med.* **1977**, *18* (2), 151–158.

(32) Coenen, H. H.; Gee, A. D.; Adam, M.; Antoni, G.; Cutler, C. S.; Fujibayashi, Y.;

Jeong, J. M.; Mach, R. H.; Mindt, T. L.; Pike, V. W.; Windhorst, A. D. *Nucl. Med. Commun.* **2018**, *39* (3), 193–195.

(33) Lee, E.; Kamlet, A. S.; Powers, D. C.; Neumann, C. N.; Boursalian, G. B.; Furuya, T.; Choi, D. C.; Hooker, J. M.; Ritter, T. *Science.* **2011**, *334* (6056), 639–642.

(34) Luxen, A.; Barrio, J. R.; Bida, C. T.; Satyamurthy, N. In *Sixth International Symposium on Radiopharmaceutical Chemistry*; 1986; pp 1066–1067.

(35) Namavari, M.; Bishop, A.; Satyamurthy, N.; Bida, G.; Barrio, J. R. *Int. J. Radiat. Appl. Instrumentation. Part A* **1992**, *43* (8), 989–996.

(36) Koopmans, K.; Brouwers, A.; De Hooge, M.; Van der Horst-Schrivers, A.; Kema, I.; Wolffenbuttel, B.; De Vries, E.; Lager, P. *J. Nucl. Med.* **2005**, *46* (7), 1240–1243.

(37) Jacobson, O.; Kiesewetter, D. O.; Chen, X. *Bioconjug. Chem.* **2015**, *26* (1), 1–18.

(38) Stewart, M. N.; Hockley, B. G.; Scott, P. J. H. *Chem. Commun.* **2015**, *51* (79), 14805–14808.

(39) Kilbourn, M. R.; Hockley, B.; Lee, L.; Sherman, P.; Quesada, C.; Frey, K. A.; Koeppe, R. A. *Nucl. Med. Biol.* **2009**, *36* (5), 489–493.

(40) Jackson, A.; Smith, G.; Brown, S.; Morrison-Iveson, V.; Chau, W.; Durrant, C.; Wilson, I. *Eur J Nucl Med Mol Imaging* **2011**, *38 (Suppl)*, S231-232.

(41) Pike, V. W.; Aigbirhio, F. I. *J. Chem. Soc., Chem. Commun.* **1995**, No. 21, 2215–2216.

(42) Rühl, T.; Rafique, W.; Lien, V. T.; Riss, P. J. *Chem. Commun.* **2014**, *50* (45), 6056–6059.

(43) Ye, Y.; Schimler, S. D.; Hanley, P. S.; Sanford, M. S. *J. Am. Chem. Soc.* **2013**,

135 (44), 16292–16295.

(44) Mossine, A. V.; Brooks, A. F.; Bernard-Gauthier, V.; Bailey, J. J.; Ichiishi, N.; Schirrmacher, R.; Sanford, M. S.; Scott, P. J. H. *J. Label. Compd. Radiopharm.* **2018**, *61* (3), 228–236.

(45) Egerton, A.; Modinos, G.; Ferrera, D.; McGuire, P. *Neuroimaging studies of GABA in schizophrenia: A systematic review with meta-analysis*; Nature Publishing Group, 2017; Vol. 7.

(46) Scott, P. J. H. *Angew. Chemie - Int. Ed.* **2009**, *48* (33), 6001–6004.

(47) Rotstein, B. H.; Liang, S. H.; Holland, J. P.; Collier, T. L.; Hooker, J. M.; Wilson, A. A.; Vasdev, N. *Chem. Commun.* **2013**, *49* (50), 5621–5629.

(48) Shao, X.; Hoareau, R.; Runkle, A. C.; Tluczek, L. J. M.; Hockley, B. G.; Henderson, B. D.; Scott, P. J. H. *J. Label. Compd. Radiopharm.* **2011**, *54* (14), 819–838.

(49) Hooker, J. M.; Reibel, A. T.; Hill, S. M.; Schueller, M. J.; Fowler, J. S. *Angew. Chemie* **2009**, *121* (19), 3534–3537.

(50) Lodi, F.; Malizia, C.; Boschi, S. In *Radiochemical Syntheses: Radiopharmaceuticals for Positron Emission Tomography*; Scott, P. J., Hockley, B. G., Eds.; Wiley, 2012; pp 297–312.

(51) Perrio-Huard, C.; Aubert, C.; Lasne, M.-C. *J. Chem. Soc. Perkin Trans. 1* **2000**, *1* (3), 311–316.

(52) Evans, J. D.; Jethwa, K. R.; Ost, P.; Williams, S.; Kwon, E. D.; Lowe, V. J.; Davis, B. J. *Pract. Radiat. Oncol.* **2018**, *8* (1), 28–39.

(53) Delbeke, D. *J. Nucl. Med.* **1999**, *40* (4), 591–603.

(54) Manabe, O.; Ohira, H.; Yoshinaga, K.; Naya, M.; Oyama-Manabe, N.; Tamaki, N. *Ann. Nucl. Cardiol.* **2017**, *3* (1), 117–120.

(55) Zhuang, H.; Codreanu, I. *J. Biomed. Res.* **2015**, *29* (november 2014), 189–202.

(56) Tai, Y. F. *J. Neurol. Neurosurg. Psychiatry* **2004**, *75* (5), 669–676.

(57) Berti, V.; Pupi, A.; Mosconi, L. *Ann. N. Y. Acad. Sci.* **2011**, *1228* (1), 81–92.

(58) Basu, S.; Hess, S.; Nielsen Braad, P. E.; Olsen, B. B.; Inglev, S.; Høilund-Carlsen, P. F. *PET Clin.* **2014**, *9* (4), 355–370.

(59) Grassi, I.; Nanni, C.; Allegri, V.; Morigi, J. J.; Montini, G. C.; Castellucci, P.; Fanti, S. *Am. J. Nucl. Med. Mol. Imaging* **2012**, *2* (1), 33–47.

(60) DeGrado, T. R. *11C-Choline*; 2012.

(61) Pretze, M.; Wängler, C.; Wängler, B. *Biomed Res. Int.* **2014**, *2014*, 1–12.

(62) Leung, K. [18 F]Fluorocholine https://www.ncbi.nlm.nih.gov/books/NBK23563/ (accessed Jul 15, 2018).

(63) Leung, K. L-[Methyl-11C]Methionine https://www.ncbi.nlm.nih.gov/books/NBK23696/ (accessed Jul 15, 2018).

(64) Tran, K.; Khan, S.; Taghizadehasl, M.; Palazzo, F.; Frilling, A.; Todd, J. F.; AL-Nahhas, A. *Hell. J. Nucl. Med.* **2015**, *18* (1), 19–24.

(65) Calais, J.; Fendler, W. P.; Herrmann, K.; Eiber, M.; Ceci, F. *J Nuc Med* **2018**, *59* (5), 789–795.

(66) Bednarova, S.; Lindenberg, M. L.; Vinsensia, M.; Zuiani, C.; Choyke, P. L. *Transl. Androl. Urol.* **2017**, *6* (3), 413–423.

(67) Poeppel, T. D.; Binse, I.; Petersenn, S.; Lahner, H.; Schott, M.; Antoch, G.; Brandau, W.; Bockisch, A.; Boy, C. *J. Nucl. Med.* **2011**, *52* (12), 1864–1870.

(68) G. D. Rabinovici, A. J. Furst, J. P. O'Neil, C. A. Racine, E. C. Mormino, S. L. Baker, S. Chetty, P. Patel, T. A. Pagliaro, W. E. Klunk, C. A. Mathis, H. J. Rosen, B. L. Miller, W. J. J. *Neurology* **2007**, *68* (15), 1205–1212.

(69) Klunk, W. E.; Engler, H.; Nordberg, A.; Wang, Y.; Blomqvist, G.; Holt, D. P.; Bergström, M.; Savitcheva, I.; Huang, G. F.; Estrada, S.; Ausén, B.; Debnath, M. L.; Barletta, J.; Price, J. C.; Sandell, J.; Lopresti, B. J.; Wall, A.; Koivisto, P.; Antoni, G.; Mathis, C. A.; Långström, B. *Ann. Neurol.* **2004**, *55* (3), 306–319.

(70) Wong, D. F.; Rosenberg, P. B.; Zhou, Y.; Kumar, A.; Raymont, V.; Ravert, H. T.; Dannals, R. F.; Nandi, A.; Brasic, J. R.; Ye, W.; Hilton, J.; Lyketsos, C.; Kung, H. F.; Joshi, A. D.; Skovronsky, D. M.; Pontecorvo, M. J. *J. Nucl. Med.* **2010**, *51* (6), 913–920.

(71) Drug Approval Package: Amyvid (Florbetapir F18 Injection) https://www.accessdata.fda.gov/drugsatfda_docs/nda/2012/202008_Florbetapir_Orig1s000TOC.cfm.

(72) Drug Approval Package: Vizamyl (Flutemetamol F18) https://www.accessdata.fda.gov/drugsatfda_docs/nda/2013/203137_vizamyl_toc.cfm.

(73) Drug Approval Package: Neuraceq (Florbetaben F18) injection https://www.accessdata.fda.gov/drugsatfda_docs/nda/2014/204677orig1s000toc.cfm.

(74) Zwan, M. D.; Bouwman, F. H.; Konijnenberg, E.; Van Der Flier, W. M.; Lammertsma, A. A.; Verhey, F. R. J.; Aalten, P.; Van Berckel, B. N. M.; Scheltens, P. *Alzheimer's Res. Ther.* **2017**, *9* (1), 1–8.

(75) Yeo, J. M.; Waddell, B.; Khan, Z.; Pal, S. *Alzheimer's Dement. Diagnosis, Assess. Dis. Monit.* **2015**, *1* (1), 5–13.

(76) Morris, E.; Chalkidou, A.; Hammers, A.; Peacock, J.; Summers, J.; Keevil, S. *Eur. J. Nucl. Med. Mol. Imaging* **2016**, *43* (2), 374–385.

(77) Jang, Y. K.; Lyoo, C. H.; Park, S.; Oh, S. J.; Cho, H.; Oh, M.; Ryu, Y. H.; Choi, J. Y.; Rabinovici, G. D.; Kim, H. J.; Moon, S. H.; Jang, H.; Lee, J. S.; Jagust, W. J.; Na, D. L.; Kim, J. S.; Seo, S. W. *Eur. J. Nucl. Med. Mol. Imaging* **2017**, *45* (3), 432–442.

(78) Walji, A. M.; Hostetler, E. D.; Selnick, H.; Zeng, Z.; Miller, P.; Bennacef, I.; Salinas, C.; Connolly, B.; Gantert, L.; Holahan, M.; O'Malley, S.; Purcell, M.; Riffel, K.; Li, J.; Balsells, J.; Obrien, J. A.; Melquist, S.; Soriano, A.; Zhang, X.; Ogawa, A.; Xu, S.; Joshi, E.; Della Rocca, J.; Hess, F. J.; Schachter, J.; Hesk, D.; Schenk, D.; Struyk, A.; Babaoglu, K.; Lohith, T. G.; Wang, Y.; Yang, K.; Fu, J.; Evelhoch, J. L.; Coleman, P. J. *J. Med. Chem.* **2016**, *59* (10), 4778–4789.

(79) Hostetler, E. D.; Walji, A. M.; Zeng, Z.; Miller, P.; Bennacef, I.; Salinas, C.; Connolly, B.; Gantert, L.; Haley, H.; Holahan, M.; Purcell, M.; Riffel, K.; Lohith, T. G.; Coleman, P.; Soriano, A.; Ogawa, A.; Xu, S.; Zhang, X.; Joshi, E.; Della Rocca, J.; Hesk, D.; Schenk, D. J.; Evelhoch, J. L. *J. Nucl. Med.* **2016**, *57* (10), 1599–1606.

(80) Muller, M. L. [18F]flubatine: a novel biomarker of cognition in Parkinson's disease https://www.michaeljfox.org/foundation/grant-detail.php?grant_id=1264 (accessed Jul 16, 2018).

(81) Frey, K. A.; Wieland, D. M.; Kilbourn, M. R. *Adv. Pharmacol.* **1997**, *42* (C), 269–

272.

(82) Saulin, A.; Savli, M.; Lanzenberger, R. *Amino Acids* **2012**, *42* (6), 2039–2057.

(83) Wiers, C. E.; Cabrera, E.; Skarda, E.; Volkow, N. D.; Wang, G. J. *Prog Brain Res* **2016**, *224*, 175–201.

(84) Votey, S. R.; Bosse, G. M.; Bayer, M. J.; Hoffman, J. R. *Ann. Emerg. Med.* **1991**, *20*, 181–188.

(85) Vivash, L.; Gregoire, M.-C. C.; Lau, E. W.; Ware, R. E.; Binns, D.; Roselt, P.; Bouilleret, V.; Myers, D. E.; Cook, M. J.; Hicks, R. J.; O'Brien, T. J. *J Nucl Med* **2013**, *54* (8), 1270–1277.

(86) Moran, M. D.; Wilson, A. A.; Elmore, C. S.; Parkes, J.; Ng, A.; Sadovski, O.; Graff, A.; Daskalakis, Z. J.; Houle, S.; Chapdelaine, M. J.; Vasdev, N. *Bioorganic Med. Chem.* **2012**, *20* (14), 4482–4488.

(87) Serdons, K.; Verbruggen, A.; Bormans, G. *J. Nucl. Med.* **2008**, *49* (12), 2071.

(88) Ha, N. S.; Sadeghi, S.; van Dam, R. M. *Micromachines* **2017**, *8* (11), 3–7.

(89) Tarn, M. D.; Archibald, S. J.; Pamme, N. In *The 18th International Conference of Miniaturized Systems for Chemistry and Life Sciences (MicroTAS 2014), At San Antonio, Texas, USA*; 2014.

(90) Thompson, S.; Scott, P. J. H. In *Radiopharmaceutical Chemistry*; Lewis, J., Windhorst, A. D., Zeglis, B. M., Eds.; Springer, 2019.

(91) Badawi, R. Introduction to PET Physics https://depts.washington.edu/nucmed/IRL/pet_intro/toc.html (accessed Jul 18, 2018).

(92) Schmitz, R. E.; Alessio, A. M.; Kinahan, P. E. In *PET and PET/CT: A Clinical*

Guide; 2009; pp 1–14.

(93) D'Asseler, Y.; Vandenberghe, S.; Winter, F. D.; Walle, R. V; Koole, M.; Bouwens, L.; Lemahieu, I.; Dierckx, R. A. *Comput. Med. Imaging Graph.* **2001**, *25* (2), 87–96.

(94) Turkington, T. G. *J. Nucl. Med. Technol.* **2001**, *29* (1), 4–11.

(95) Fahey, F. H. *J Nucl Med Technol* **2002**, *30* (2), 39–49.

(96) Cherry, S. R.; Jones, T.; Karp, J. S.; Qi, J.; Moses, W. W.; Badawi, R. D. *J Nuc Med* **2018**, *59* (1), 3–12.

(97) Berg, E.; Zhang, X.; Bec, J.; Judenhofer, M. S.; Patel, B.; Peng, Q.; Kapusta, M.; Schmand, M.; Casey, M.; Tarantal, A. F.; Qi, J.; Badawi, R.; Cherry, S. R. *J. Nucl. Med.* **2018**, *59* (6), 993–999.

(98) Golan, D. E.; Armen H Tashjian, J.; Armstrong, E. J.; Armstrong, A. W. *Principles of Pharmacology: The Pathophysiologic Basis of Drug Therapy*, Second.; LIppincott Williams & Wilikins.

(99) Awapara, J.; Landua, A. J.; Fuerst, R.; Seale, B. *J. Biol. Chem.* **1950**, *187*, 35–39.

(100) Undenfriend, S. *J. Biol. Chem.* **1950**, *187*, 65–69.

(101) Roberts, E.; Frankel, S. *J. Biol. Chem.* **1950**, *187*, 55–63.

(102) Krnjević, K.; Schwartz, S. *Exp. brain Res.* **1967**, *3* (4), 320–336.

(103) Curtis, D. R.; Hösli, L.; Johnston, G. A. R.; Johnston, I. H. *Exp. Brain Res.* **1968**, *5* (3), 235–258.

(104) Froestl, W. *Future Med. Chem.* **2011**, *3* (2), 163–175.

(105) Sternbach, L. H. *J. Med. Chem.* **1979**, *22* (1), 1–7.

(106) Schousboe, A.; Madsen, K. K.; Barker-Haliski, M. L.; White, H. S. *Neurochem Res*

2014, *39* (10), 1980–1987.

(107) Watanabe, M.; Maemura, K.; Kanbara, K.; Tamayama, T.; Hayasaki, H. *Int. Rev. Cytol.* **2002**, *213*, 1–47.

(108) Brambilla, P.; Perez, J.; Barale, F.; Schettini, G.; Soares, J. C. *Mol. Psychiatry* **2003**, *8* (8), 715–715.

(109) Griffin, C. E.; Kaye, A. M.; Bueno, F. R.; Kaye, A. D. *Ochsner J.* **2013**, *13* (2), 214–223.

(110) Krogsgaard-Larsen, P. *J. Med. Chem.* **1981**, *24* (12), 1377–1383.

(111) Croucher, M. J.; Meldrum, B. S.; Krogsgaard-larsen, P. *Eur. J. Pharmacol.* **1983**, *89*, 217–228.

(112) Madsen, K. K.; White, H. S.; Schousboe, A. *Pharmacol. Ther.* **2010**, *125* (3), 394–401.

(113) Andersen, K. E.; Sorensen, J. L.; Lau, J.; Lundt, B. F.; Petersen, H.; Huusfeldt, P. O.; Suzdak, P. D.; Swedberg, M. D. B.; Sørensen, J. L. *J Med Chem* **2001**, *44* (13), 2152–2163.

(114) Høg, S.; Greenwood, J. R.; Madsen, K. B.; Larsson, O. M.; Frølund, B.; Schousboe, A.; Krogsgaard-Larsen, P.; Clausen, R. P. *Curr Top Med Chem* **2006**, *6* (17), 1861–1882.

(115) Bown, A. W.; Shelp, B. J. *Plant Physiol.* **1997**, *115* (1), 1–5.

(116) Cardarelli, W. J.; Smith, B. J. *Am. J. Manag. Care* **2010**, *16* (12 Suppl), S331–S336.

(117) Center for Disease Control and Prevention 2013.

(118) Borden, L. a.; Murali Dhar, T. G.; Smith, K. E.; Weinshank, R. L.; Branchek, T. a.;

Gluchowski, C. *Eur. J. Pharmacol. - Mol. Pharmacol. Sect.* **1994**, *269* (2), 219–224.

(119) Galvan, A.; Hu, X.; Smith, Y.; Wichmann, T. *Exp. Neurol.* **2010**, *223* (2), 505–515.

(120) Lu, Y.-R.; Fu, X.-Y.; Shi, L.-G.; Jiang, Y.; Wu, J.-L.; Weng, X.-J.; Wang, Z.-P.; Wu, X.-Y.; Lin, Z.; Liu, W.-B.; Li, H.-C.; Luo, J.-H.; Bao, A.-M. *BMC Psychiatry* **2014**, *14* (1), 123.

(121) Nägga, K.; Bogdanovic, N.; Marcusson, J. *J Neural Transm* **1999**, *106* (11–12), 1141–1149.

(122) Sundman-eriksson, I.; Blennow, K.; Davidsson, P.; Dandenell, A.-K.; Marcusson, J. *Neuropsychobiology* **2002**, *45* (3), 7–11.

(123) Sundman-Eriksson, I.; Allard, P. *Aging Clin Exp Res* **2006**, *18* (3), 257–260.

(124) Philippi, A.; Rousseau, F.; Roschmann, E. Human Autism Susceptibility Genes Encoding A Neurotransmitter Transporter and Uses Thereof. WO 2006/090288 A2, 2006.

(125) Lin, L.; Yee, S. W.; Kim, R. B.; Giacomini, K. M. *Nat. Rev. Drug Discov.* **2015**, *14* (8), 543–560.

(126) Sigel, E.; Steinmann, M. E. *J. Biol. Chem.* **2012**, *287* (48), 40224–40231.

(127) Zhang, D.; Pan, Z.-H.; Awobuluyi, M.; Lipton, S. A. *Trends Pharmacol. Sci.* **2001**, *22* (3), 121–132.

(128) Chebib, M.; Johnston, G. A. R. *J. Med. Chem.* **2000**, *43* (8), 1427–1447.

(129) Mott, D. In *Cellular and Molecular Neurophysiology*; Elsevier Ltd, 2015; pp 245–267.

(130) Froestl, W. *Adv. Pharmacol.* **2010**, *58* (C), 19–62.

(131) Cellot, G.; Cherubini, E. *Front. Pediatr.* **2014**, *2* (July), 1–11.

(132) Soghomonian, J. J.; Martin, D. L. *Trends Pharmacol. Sci.* **1998**, *19* (12), 500–505.

(133) Andruszkiewicz, R.; Silverman, R. B. *J. Biol. Chem.* **1990**, *265* (36), 22288–22291.

(134) Silverman, R. B. *Angew. Chemie - Int. Ed.* **2008**, *47* (19), 3500–3504.

(135) Scimemi, A. *Front. Cell. Neurosci.* **2014**, *8*, 1–14.

(136) Zhou, Y.; Holmseth, S.; Hua, R.; Lehre, a. C.; Olofsson, a. M.; Poblete-Naredo, I.; Kempson, S. a.; Danbolt, N. C. *AJP Ren. Physiol.* **2012**, *302* (3), F316–F328.

(137) Quandt, G.; Höfner, G.; Wanner, K. T. *Bioorganic Med. Chem.* **2013**, *21* (11), 3363–3378.

(138) Conti, F.; Minelli, A.; Melone, M. *Brain Res. Rev.* **2004**, *45* (3), 196–212.

(139) Minelli, a; Brecha, N. C.; Karschin, C.; DeBiasi, S.; Conti, F. *J. Neurosci.* **1995**, *15* (11), 7734–7746.

(140) Maier, T.; Güell, M.; Serrano, L. *FEBS Lett.* **2009**, *583* (24), 3966–3973.

(141) Crunelli, V.; Leresche, N.; Cope, D. W. *Jasper's Basic Mech. Epilepsies, 4th Ed. NCBI Bookshelf Online B. Version* **2012**, 1–17.

(142) Sundman Eriksson, I.; Allard, P.; Marcusson, J. *Brain Res.* **1999**, *851* (1–2), 183–188.

(143) Elliott, K. A. C.; van Gelder, N. M. *J. Neurochem.* **1958**, *3* (1), 28–40.

(144) Iversen, L. L.; Neal, M. J. *J. Neurochem.* **1968**, *15* (10), 1141–1149.

(145) Guastella, J.; Nelson, N.; Nelson, H.; Czyzyk, L.; Keynan, S.; Miedel, M. C.; Davidson, N.; Lester, H. A.; Kanner, B. I.; Guastella, J.; Nelson, N.; Nelson, H.; Czyzyk, L.; Keynan, S.; Miedel, M. A. Y. C. *Science (80-.).* **1990**, *249* (4974),

1303–1306.

(146) Andersen, K. E.; Lau, J.; Lundt, B. F.; Petersen, H.; Huusfeldt, P. O.; Suzdak, P. D.; Swedberg, M. D. B. *Bioorg. Med. Chem.* **2001**, *9*, 2773–2785.

(147) Drug Approval Package: Gabitril (Tiagabine) https://www.accessdata.fda.gov/drugsatfda_docs/nda/97/020646_gabitril_toc.cfm.

(148) Govindpani, K.; Guzmán, B. C. F.; Vinnakota, C.; Waldvogel, H. J.; Faull, R. L.; Kwakowsky, A. *Int. J. Mol. Sci.* **2017**, *18* (8), 1–41.

(149) Nguyen, N. C.; Yee, M. K.; Tuchayi, A. M.; Kirkwood, J. M.; Tawbi, H.; Mountz, J. M. *Front. Oncol.* **2018**, *8* (18), 1–9.

(150) S, S. *Curr. Drug Targets* **2016**, *17* (16), 1894–1907.

(151) Polyak, A.; Ross, T. L. *Curr. Med. Chem.* **2017**, 1–26.

(152) Barrington, S. F.; Johnson, P. W. M. *J. Nucl. Med.* **2017**, *58*, 1539–1544.

(153) Stagg, C. J.; Bachtiar, V.; Johansen-berg, H. *Commun Integr Biol* **2011**, *4* (October), 573–575.

(154) Antoni, G.; Langstrom, B. *J. Label. Compd. Radiopharm.* **1989**, *27* (5), 571–576.

(155) Lin, S.; Bois, F.; Holden, D.; Nabulsi, N.; Pracitto, R.; Gao, H.; Kapinos, M.; Teng, J.; Shirali, A.; Ropchan, J.; Carson, R. E.; Elmore, C. S.; Vasdev, N.; Huang, Y. *Mol. Imaging* **2017**, *16*, 1–10.

(156) Frankle, W. G.; Cho, R. Y.; Narendran, R.; Mason, N. S.; Vora, S.; Litschge, M.; Price, J. C.; Lewis, D. A.; Mathis, C. A. *Neuropsychopharmacology* **2009**, *34* (3), 624–633.

(157) Frankle, W. G.; Cho, R. Y.; Mason, N. S.; Chen, C. M.; Himes, M.; Walker, C.; Lewis, D. A.; Mathis, C. A.; Narendran, R. *PLoS One* **2012**, *7* (2), 1–9.

(158) Savic, I.; Roland, P.; Sedvall, G.; Persson, A.; Pauli, S.; Widen, L. *Lancet* **1988**, *332* (8616), 863–866.

(159) Heiss, W. D.; Sobesky, J.; Smekal, U. V.; Kracht, L. W.; Lehnhardt, F. G.; Thiel, A.; Jacobs, A. H.; Lackner, K. *Stroke* **2004**, *35* (8), 1892–1898.

(160) Oikonen, V. Analysis of [11C]flumazenil PET studies http://www.turkupetcentre.net/petanalysis/analysis_11c-flumazenil.html (accessed Aug 13, 2018).

(161) Andersson, J. D.; Halldin, C. *J Label. Comp Radiopharm* **2013**, *56* (3–4), 196–206.

(162) Lingford-Hughes, A.; Myers, J.; Watson, B.; Reid, A. G.; Kalk, N.; Feeney, A.; Hammers, A.; Ria??o-Barros, D. A.; McGinnity, C. J.; Taylor, L. G.; Rosso, L.; Brooks, D. J.; Turkheimer, F.; Nutt, D. J. *Neuroimage* **2016**, *132*, 1–7.

(163) Lingford-Hughes, A.; Reid, A. G.; Myers, J.; Feeney, A.; Hammers, A.; Taylor, L. G.; Rosso, L.; Turkheimer, F.; Brooks, D. J.; Grasby, P.; Nutt, D. J. *J. Psychopharmacol.* **2012**, *26* (2), 273–281.

(164) Knutsen, L. J. S.; Andersen, K. E.; Lau, J.; Lundt, B. F.; Henry, R. F.; Morton, H. E.; Nærum, L.; Petersen, H.; Stephensen, H.; Suzdak, P. D.; Swedberg, M. D. B.; Thomsen, C.; Sørensen, P. O. *J. Med. Chem.* **1999**, *42* (18), 3447–3462.

(165) Zhang, J. G.; Jiang, C. S.; Lin, G. Q.; Wen, R. *Chinese Chem. Lett.* **2005**, *16* (9), 1205–1208.

(166) Pavia, M. R. Various N-Substitued 3-Piperidine Carboxylic Acids or N-Substituted 3-Pyridinecarboxylic Acids and Derivatives Thereof. 4,772,615, 1988.

(167) Kilbourn, M. R.; Pavia, M. R.; Gregor, V. E. *Appl. Radiat. Isot.* **1990**, *41* (9), 823–

828.

(168) Schijns, O.; van Kroonenburgh, M.; Beekman, F.; Verbeek, J.; Herscheid, J.; Rijkers, K.; Visser-Vandewalle, V.; Hoogland, G. *Nucl. Med. Commun.* **2013**, *34* (2), 175–179.

(169) Schirrmacher, R.; Hamkens, W.; Piel, M.; Schmitt, U.; Lddens, H.; Hiemke, C.; Rsch, F. *J. Label. Compd. Radiopharm.* **2001**, *44* (9), 627–642.

(170) Braestrup, C.; Nielsen, E. B.; Sonnewald, U.; Knutsen, L. J. S.; Andersen, K. E.; Jansen, J. A.; Frederiksen, K.; Andersen, P. H.; Mortensen, A.; Suzdak, P. D. *J. Neurochem.* **1990**, *54* (2), 639–647.

(171) Andersen, K. E.; Braestrup, C.; Grønwald, F. C.; Jørgensen, A. S.; Nielsen, E. B.; Sonnewald, U.; Sørensen, P. O.; Suzdak, P. D.; Knutsen, L. J. S. *J. Med. Chem.* **1993**, *36* (12), 1716–1725.

(172) Yamashita, A.; Singh, S. K.; Kawate, T.; Jin, Y.; Gouaux, E. *Nature* **2005**, *437* (7056), 215–223.

(173) Skovstrup, S.; Taboureau, O.; Bräuner-Osborne, H.; Jørgensen, F. S. *ChemMedChem* **2010**, *5* (7), 986–1000.

(174) Petrera, M.; Wein, T.; Allmendinger, L.; Sindelar, M.; Pabel, J.; H??fner, G.; Wanner, K. T. *ChemMedChem* **2016**, *11* (5), 519–538.

(175) Wein, T.; Petrera, M.; Allmendinger, L.; H??fner, G.; Pabel, J.; Wanner, K. T. *ChemMedChem* **2016**, *11* (5), 509–518.

(176) Jørgensen, L.; Al-Khawaja, A.; Kickinger, S.; Vogensen, S. B.; Skovgaard-Petersen, J.; Rosenthal, E.; Borkar, N.; Löffler, R.; Madsen, K. K.; Bräuner-Osborne, H.; Schousboe, A.; Ecker, G. F.; Wellendorph, P.; Clausen, R. P. *J.*

Med. Chem. **2017**, *60* (21), 8834–8846.

(177) Schaffert, E. S.; Höfner, G.; Wanner, K. T. *Bioorg. Med. Chem.* **2011**, *19* (21), 6492–6504.

(178) Damgaard, M.; Al-Khawaja, A.; Vogensen, S. B.; Jurik, A.; Sijm, M.; Lie, M. E.; Baek, M. I.; Rosenthal, E.; Jensen, A. A.; Ecker, G. F.; Frolund, B.; Wellendorph, P.; Clausen, R. P. *ACS Chem Neurosci* **2015**, *6* (9), 1591–1599.

Chapter 2

GAT-1: Inhibitors and their adaptation into PET tracers

A. Introduction

i. Development of GAT-1 inhibitors

As discussed in Chapter 1, GAT-1 has been shown to be an interesting and promising target in the treatment of many neurological diseases and disorders, especially epilepsy. After the discovery and approval of the anticonvulsant tiagabine (Gabitril™, **2.1**),

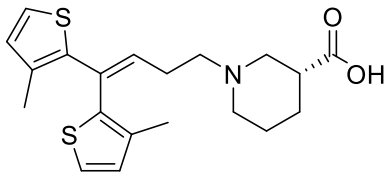

2.1

pIC_{50} = 6.88 (GAT-1)
K_i = 67 nM

Figure 2-1: Tiagabine, the only FDA approved GAT-1 inhibitor. K_i values as reported by Knutsen et al.

many structure-activity relationship studies for GAT-1 specific inhibitors have been published encouraging further exploration of this target. Improvements from earlier molecules, such as **2.2** and **2.3**, include lengthening the alkenyl chain, incorporating heteroatoms in the linker, use of both hetero- and carbonyl-aryl rings, and substitution at

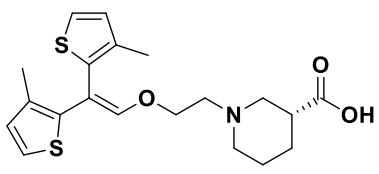

2.2, K_i=14±1 nM

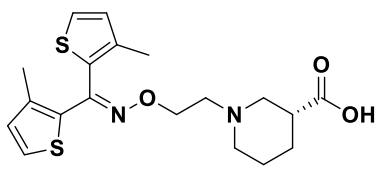

2.3, K_i=41±7 nM

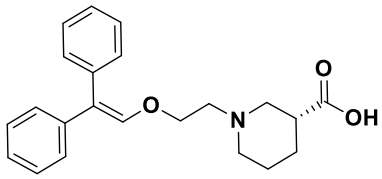

2.4, K_i = 86 nM

Figure 2-2: Comparison of GABA uptake inhibitors synthesized by Knutsen et al. (K_i values are as reported by Knutsen et al.)

the various positions on the aryl rings. The lengthening of the alkenyl chain shows enhanced binding, while substitution at the *ortho* position of the aryl rings is believed to be more tolerant of bulk,[1] leading to a wider range of possible substituents.

Andersen, Braestrup and coworkers have performed considerable work in this space, including the development of tiagabine as a GABA uptake inhibitor.[1–7] This work included the design of molecules that showed increased potency inhibiting GABA uptake compared to tiagabine (up to 50% increase in inhibition), which are of particular interest (Figure 2-2). This group also reported the superior inhibitory concentration of the vinyl ether (e.g. **2.2** and **2.4**) as opposed to other alkyl or hetero-atom containing linkers such as oximes (**2.3**).[1] Knutsen and coworkers suggest the increased electronegativity of the oxime containing molecules for their improved activity.[1] This series of papers (Synthesis of Novel GABA Uptake Inhibitiors, Parts 1-6[1–3,5–7]) has been instrumental in the further investigation of GABA uptake inhibition as a therapeutic strategy.

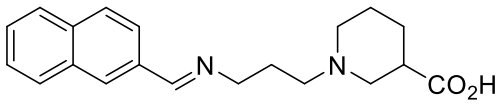

2.5

Figure 2-3: Schiff base derived GABA uptake inhibitor.

Even recent work concentrates on N-alkylated analogues of nipecotic acid. One example synthesized Schiff base analogs of nipecotic acid, and reported a molecule (**2.5**) with similar epilepsy prevention as tiagabine with slightly improved permeability as demonstrated by a PAMPA-BBB assay.[8] Unfortunately no cell based assays were reported with this molecule, making comparaison of **2.5** to the previosly mentioned compounds (**2.2**-**2.4**) difficult. Although these PAMPA assays give a very good estimate of permeability, it is no subtitution for an *in vivo* evaluation as can be done with PET.

ii. Unsymmetrical GAT-1 inhibitors

A study by Wanner and coworkers in 2013 demonstrated the successful use of an unsymmetrical lipophilic aryl moiety in the development of highly selective and potent GAT-1 inhibitors.[9] The library produced in the 2013 study expanded on work done by Andersen and coworkers[5] which had investigated the potency of an unsymmetrical lipophilic side chain, as opposed to the hitherto reported symmetrical GABA uptake inhibitors such as tiagabine. In previous studies by the same group,[1] they had discovered that unsymmetrically substituted aryl groups were well tolerated and were encouraged to synthesize and test a new series of unsymmetrical analogues. In Andersen's series, the

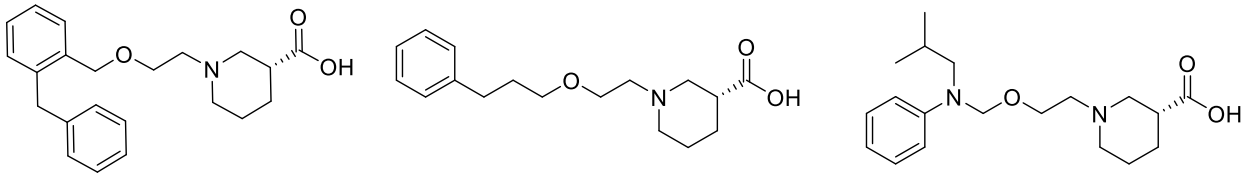

2.6, IC_{50} (nM) = 322 **2.7**, IC_{50} (nM) = 4500 **2.8**, IC_{50} (nM) = 282

Figure 2-4: Unsymmetrical, and singly substituted GABA uptake inhibitors synthesized by Knutsen, Andersen, and coworkers.

position of attachment to the ether linker was situated on one side of the pendant (**2.6**). In some cases, one of the aryl groups was omitted entirely (**2.7**), and while the activity was significantly decreased it could be rescued by replacing the aryl residue with some other bulky residue (**2.8**). Wanner and coworkers also hoped to improve on the selectivity and affinity of these series of molecules by combining the unsymmetrical bis-aromatic residue (as shown in **2.6**) with the ether or vinyl ether linker previously demonstrated by Andersen and coworkers to have enhanced GABA uptake inhibition properties (as shown in **2.2, 2.6**).[1] In order to fully evaluate this novel scaffold, the researchers also chose to variously substitute the aromatic residues with fluorine; as the most electronegative atom, it can both alter the electronics of the molecules for better protein-ligand interactions, and

is often employed to protect metabolically labile sites. Through the substitution with fluorine, they sought not only to improve the selectivity and affinity of these molecules but also further probe and understand the protein-ligand interaction of the GABA uptake inhibitors with the GABA transporters. This fluorine substitution also made for a decent selection of molecules that appeared amenable to radiolabeling, as the fluorine substituent could easily be replaced by a [^{18}F] substitution without altering the molecules properties. Three selected molecules from this library are shown in Figure 2-5. Comparing

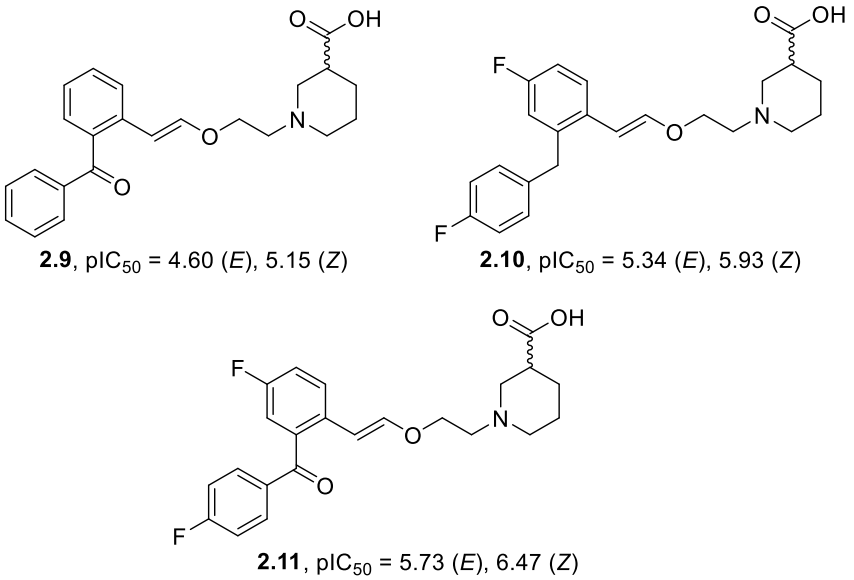

2.9, pIC_{50} = 4.60 (*E*), 5.15 (*Z*)

2.10, pIC_{50} = 5.34 (*E*), 5.93 (*Z*)

2.11, pIC_{50} = 5.73 (*E*), 6.47 (*Z*)

Figure 2-5: Lead compounds and pIC_{50} values as reported by Wanner and colleagues.

these molecules, it can be seen that the addition of aryl-fluorine substituents indeed does improve affinity of these molecules for GAT-1: **2.9** compared with **2.11**, pIC_{50} 4.60 and 5.73 respectively for the *E* isomers. Whereas, omission of the carbonyl in favor of a methylene linker in the diaryl moiety causes a decrease in affinity: **2.10** compared with **2.11**, pIC_{50} 5.34 and 5.73 respectively for the *E* isomers.

The lead compound produced by this study, **2.11**, has shown excellent potency for GAT-1 (1.86 µM and 339 nM for *E* and *Z* respectively, calculated from reported pIC_{50}

values) and 15 to 17 fold selectivity over the other GABA transporters (mGAT-2, -3, and -4).[9] Additionally, the c log P (calculated by ChemDraw) of the molecule is 1.9, an ideal number for CNS drugs. Encouraged by the success of this molecule *in vitro* it was chosen for adaptation into a GAT-1 selective PET radiotracer. This work commenced with efforts to label **2.11** with fluorine-18. It has been shown that *R*-nipecotic acid has better affinity than either *S*- or racemic nipecotic acid,[10] and so *R*-nipecotic acid was used for the synthesis of these molecules to boost affinity.

B. Results and Discussion

i. Synthesis of Reference Standards and Precursors

Development of a novel PET tracer requires the development of both a reference standard for quality control analysis, and a precursor molecule. This precursor molecule is the starting material that ideally requires a few simple steps, including radiolabeling, to produce the radiotracer. Precursor molecules should be able to be produced in large amounts, and be shelf stable, especially for translation to a clinically useful PET tracer.

Adaptation of these unsymmetrical, fluorinated GAT-1 inhibitors from potential therapeutic ligand to radiopharmaceutical was straightforward and successful.[11] The unsymmetrical diaryl ketone on compound **2.11** appeared attractive as a site where S_NAr radiofluorination could be employed to produce a radiotracer from a chlorinated (or nitro, or trimethylamino) precursor. The convergent synthesis of the molecules was designed by Wanner and coworkers via retrosynthetic analysis and involved alkylation of ethyl nipecotate **2.21** with the vinyl ether linker (**2.20**), in preparation for a Heck coupling with the aryl triflate bis-aromatic residue (**2.14a** or **b**).[9] Synthesis of the standard and precursor followed this published scheme, with minor additions, and resulted in good yield. This

synthesis (Scheme 2-1) began with the coupling of 4-fluorophenol **2.12** and either 4-fluoro or 4-chloro- benzoyl chloride (X = F, **2.13a**; X = Cl, **2.13b)** to form the esters **2.18a** and **2.18b**. Treating these intermediate esters with aluminum trichloride promoted a Fries rearrangement to give the *ortho*-acylated phenols **2.19a** and **2.19b**. The free alcohol was activated by conversion to the corresponding triflates **2.14a** and **2.14b** for use in a Heck coupling.

The nipecotate linker was formed by the tosylation of commercially available ethylene glycol vinyl ether **2.15** with tosyl chloride, and then alkylation of ethyl nipecotate ester **2.21** with this tosylated ether to give **2.16**. The Heck coupling of triflate, **2.14a** or **2.14b**, with the nipecotate linker **2.16** yielded (*R, E/Z*)-**2.17a** or (*R, E/Z*)-**2.17b** as a 72:28 mixture of *E* and *Z* isomers for both fluorinated and chlorinated molecules. While the reference paper reported successful separation of these isomers, this current work found that the separation was challenging, and was not optimized due to the negative preliminary *in vivo* evaluation of this compound.

Small changes made to the published route include the addition of triethylamine (TEA, Et_3N) to encourage the alkylation of the nipecotate ester, as well as the addition of triphenyl phosphine (PPh_3) as a ligand to assist in the Heck coupling to link the intermediates. Pre-stirring of the nipecotate ester (**2.21**) with TEA, before the addition of the tosylate (**2.20**), appears to assist in the deprotonation and therefore activation of the piperidinyl nitrogen as a stronger nucleophile to attack the electrophilic tosylate (**2.20**). The Heck coupling reaction was attempted ligand free, as reported in the reference literature,[9] but was unsuccessful. Addition of the triphenyl phosphine ligand resulted in successful Heck coupling to give (*R, E/Z*)-**2.17a** or (*R, E/Z*)-**2.17b** in yields of 20-48%.

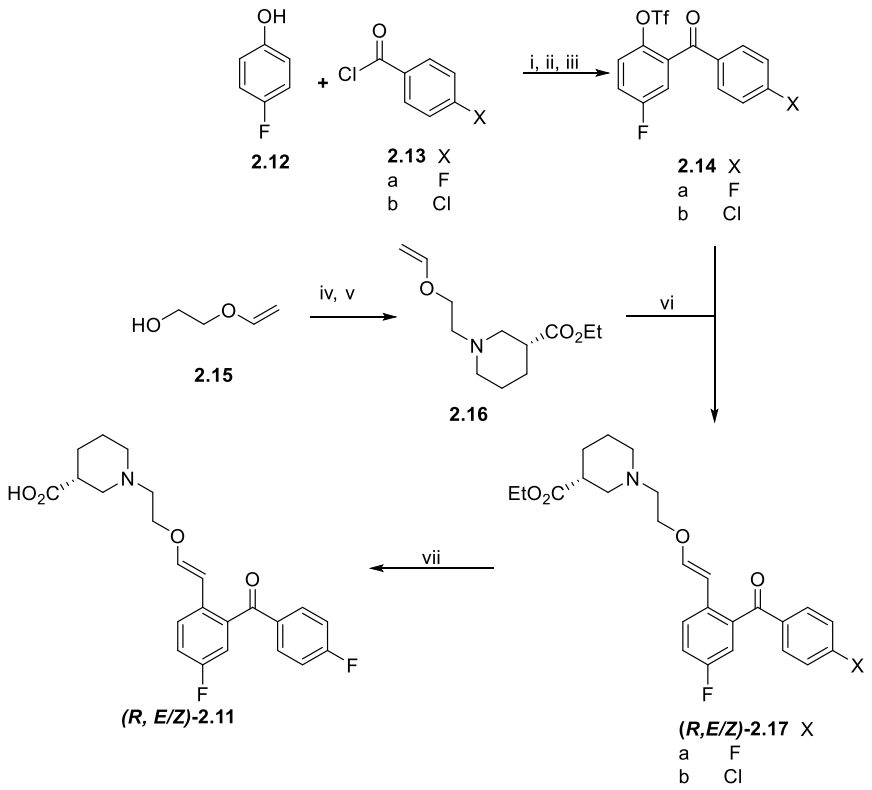

Scheme 2-1: Synthesis of precursor (*R,E/Z*)-**2.17b** and reference standard (*R,E/Z*)-**2.11**. Reagents and conditions: i) Et_3N, CH_2Cl_2, reflux, 1 h (X = F, 77% X=Cl, 83%); ii) $AlCl_3$, 200 °C, 30-40 min (X= F, 54%, X=Cl, 59%); iii) Tf_2O, 2,6-lutidine, CH_2Cl_2, 0 °C – rt, 36 h (X= F, 59% X=Cl, 61%); iv) TsCl, Et_3N, DMAP, CH_2Cl_2, 48 h (65%); v) Et_3N, (*R*)-**2.21**, rt, 16 h (50%); vi) $Pd(OAc)_2$, Et_3N, PPh_3, DMF, 80 °C, 48 h (X= F, 20%, X=Cl, 48%); vii) 2M LiOH, EtOH, 0 °C – rt, 0.5 h (X = F, 46%).

The chlorinated ester is the desired precursor for radiolabeling, (*R, E/Z*)-**2.17b**), while saponification of the fluorinated ester, (*R, E/Z*)-**2.17a** was necessary to generate unlabeled reference standard (*R, E/Z*)-**2.11**. The hydrolysis of the ester was first attempted with 12 M sodium hydroxide leading to incomplete conversion (<50% yield). Thus, the hydrolysis was then optimized with the use of 5M lithium hydroxide. Reaction times are also noted as what was found to be successful by the author and not necessarily what was reported by the literature. The substitution of **2.13b** for **2.13a** for production of the chlorinated precursor did not affect the yields of the reactions and in many cases the precursor intermediates were produced in better yields than the fluorinated standard. Both chloro-precursor, (*R, E/Z)*-**2.17a**, and fluoro-reference standard, (*R, E/Z*)-**2.11**, were characterized by NMR and mass spectrometry.

ii. [^{18}F]-Radiofluorination of Novel GAT-1 PET Tracers

Prior to the radiolabeling of precursors, reverse phase HPLC methods were developed for both semi-preparative purification and final product analysis that give elution of the standard at a reasonable retention time and separation from the precursor. The semi-preparative HPLC method is used in the hot cell for initial purification of the product from the reaction mixture. The analytical method served as the means for confirming the identity of the radiolabeled compound. Oftentimes, when chlorinated precursors are utilized for [^{18}F]fluorinations, there is difficulty achieving acceptable baseline separation between the precursor and the standard or final radiolabeled product. As (*R, E/Z)*-**2.11** and (*R, E/Z)*-**2.17b** are lipophilic molecules, Luna C18 columns were chosen for both purification and analysis. It is typical to use an HPLC solvent that is acetonitrile (MeCN) based, with a moderate concentration of ammonium acetate as buffer (NH_3OAc, 5-50 mM) with these columns. As the reference paper did not utilize HPLC purification of these compounds it was necessary to develop a new HPLC method for both semi-preparative purification as well as analytical evaluation. To first determine the

Table 2-1: HPLC conditions for **2.11** and **2.17a** radiochemistry with retention times.

	[^{18}F]-(*R*)-(*E/Z*)-*2.11*		[^{18}F]-(*R*)-(*E/Z*)-*2.17a*	
	QC	**Prep**	**QC**	**Prep**
Column	Luna C18 5µ 150 x 4.6 mm	Luna C18 10µ 250 x 10 mm	Luna C18 5µ 150 x 4.6 mm	Luna C18 10µ 250 x 10 mm
Buffer	35% MeCN 10mM NH_4OAc, pH 4.5	30% MeCN, 50 mM NH_4OAc, pH 6.0	70% MeCN, 10 mM NH_4OAc	70% MeCN, 10 mM NH_4OAc
Flow rate	2.0 mL/min	4.0 mL/min	1.5 mL/min	4.0 mL/min
Ret Time	3.8 min	18 - 19 min	4.9 min	14-15 min

appropriate concentration of MeCN in the HPLC solvent, a gradient method was run from 5 to 95% MeCN (Solvent B: water + 0.5% trifluoroacetic acid (TFA)). An overlay of the chromatogram with the gradient method gave an approximation of what concentration of MeCN will elute the compounds efficiently; for compound (*R,E/Z)*-**2.11** this gave an estimation of 50% MeCN, which was then adjusted to 35% after 50% gave elution of the standard with the solvent front. Slight acidification of the eluent ensured the protonation state of the carboxylic acid and gave a sharp peak (Figure 2-21). A quick but clean separation is necessary for the quality control of radioactive products, working within the constraints of a continually decaying product. Analytical HPLC methods for the ester, (*R,E/Z)*-**2.17a**, were developed in much the same way, without the need for additional acidification.

Semi-preparative HPLC conditions were first evaluated on HPLC instruments outside of the hot cell using reference standard and precursor to ensure efficient and clean separation. As any free [^{18}F]fluoride elutes within 5-6 minutes it is desired that the product elutes at 10-20 minutes with excellent separation from the precursor. For this purpose, oftentimes, longer (250 mm vs 150 mm) columns are used for semi-preparative HPLC, using the same type of column (e.g. C18) and solvent as the analytical method. A mixture of precursor and reference standard (coinjection) is injected on the HPLC system

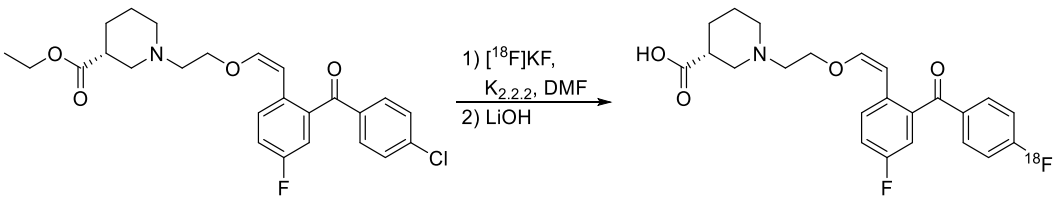

(*R,E/Z*)-**2.17b** (*R,E/Z*)-**[^{18}F]2.11**

Scheme 2-2: Optimized radiochemical synthesis of (*R,E/Z*)-**[^{18}F]2.11**.

to test its suitability. When an acceptable system is developed, it can then be moved to the hot-cell for a validation run before any *in vitro* or *in vivo* studies are scheduled.

Radiolabeling of chlorinated precursor (*R,E/Z)*-**2.17b** (Scheme 2-2) was performed using high-specific activity fluorine-18 prepared as [^{18}F]KF·$K_{2,2,2}$ for use in S_NAr radiofluorination of the chlorinated precursor. Initial radiolabeling of the unsymmetrical precursor (*R, E/Z)*-**2.17b** was tested via a small manual reaction (10 mCi of [^{18}F]fluoride) using standard S_NAr conditions ([^{18}F]KF and kryptofix-2.2.2 ($K_{2.2.2}$) in DMF, 130°C, 30 min), and successfully gave 13% radiochemical conversion (RCC) to (*R,E/Z*)-**[^{18}F]2.17a** (fluorinated ester) as determined by crude radio TLC (Figure 2-6, Scheme 2-3). Crude reaction mixture was spotted onto a silica TLC plate and ran in 20% EtOAc in hexanes TLC eluent.

We were confident in the radiolabeling of this precursor based upon this preliminary data, and next scaled up the radiolabeling for initial preclinical evaluation. Using higher amounts of ^{18}F (1.5 Ci) necessitated transferring the radiolabeling to a GE TRACERLab FX_{FN} automated synthesis module (Figure 2-7) in a lead-shielded hot-cell.

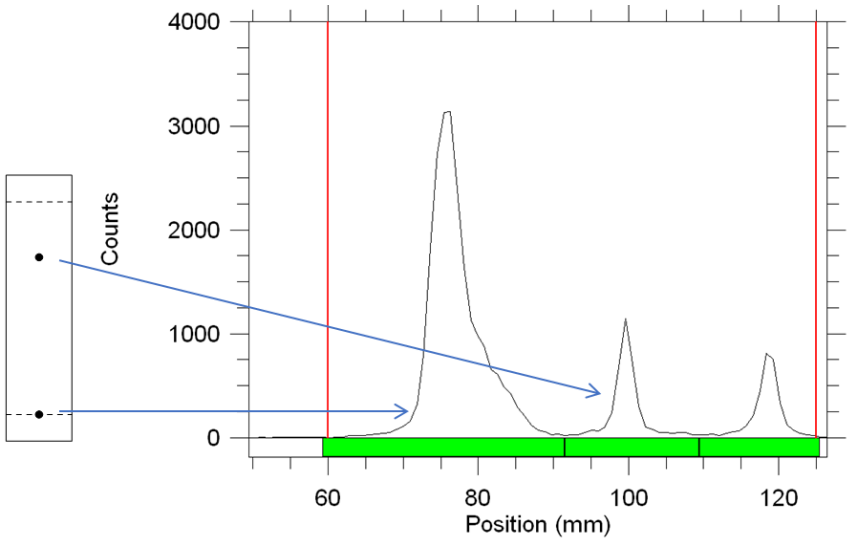

Figure 2-6: RadioTLC results of preliminary radiolabeling of [^{18}F]-(R, E/Z)-**2.17b**. Large peak near the baseline represents free [^{18}F]fluoride, and small peak at ~100mm represents product.

Figure 2-7: Picture of a TRACERLab$_{FX-N}$ installed in a lead lined hot-cell for [^{18}F]radiochemical syntheses.

Analysis of the crude reaction mixture confirmed formation of ester (*R,E/Z*)-**[^{18}F]2.17a** by comparing the radiochemical peak in HPLC with the UV peak of the unlabeled reference standard. Thus, we next moved forward to automating saponification of the ester with LiOH, and purification of the radiotracer using the synthesis module. The final step in developing a radiosynthesis procedure for a new PET tracer is to confirm that it can be reformulated into an injectable dose. This can either be accomplished by using an injectable mobile phase (usually ethanol / aqueous buffer), or by reformulating a non-injectable mobile phase. As stated above, the method developed for purifying (*R,E/Z*)-**[^{18}F]2.11** utilized 30% MeCN, and so the fraction collected from the semi-preparative HPLC (~2 min collection at 4 mL/min = 8 mL) contained 2.4 mL of MeCN. This fraction was diluted in ~50 mL of milliQ water so that the sample could be passed over a C18 cartridge and the organic molecule trapped on the cartridge. Once the molecule is trapped

on the cartridge, it is washed with sterile water to remove any residual MeCN and the product is then eluted with 0.5 mL ethanol and 4.5 mL 0.9% sterile saline into the product vial, resulting in an injectable dose formulated in 10% ethanol. This final dose is stirred for a short period of time before it is transferred into the final sterile dose vial. Sometimes this transfer happens through a 0.22 µm sterile filter if, for example, it will be employed in pre-clinical animal studies. Table 2-2 shows the reagents and materials used in the production of (*R,E/Z*)-**[^{18}F]2.11** and (*R,E/Z*)-**[^{18}F]2.17a**. In the final automated synthesis, the fluorine-18 labeled compound ((*R,E/Z*)-**[^{18}F]2.11**) was accomplished by subjecting chloro-precursor **2.17b** to standard S_NAr conditions ([^{18}F]KF and kryptofix-2.2.2 ($K_{2.2.2}$) in DMF, 130°C, 30 min) and saponification of the ester with LiOH (Scheme 2-2). Purification (semi-preparative HPLC, typical trace shown in Figure 2-8) and reformulation (C18 cartridge) provided 9.3±3.3 mCi of (*R,E/Z*)-**[^{18}F]2.11** (1% non-corrected RCY, 100% radiochemical purity and specific activity = 1702 Ci/mmol, n = 4). Synthesis of the ester radiotracer (*R,E/Z*)-**[^{18}F]2.17a**, followed the same procedure with the omittance of the final saponification step. The final automated procedure for synthesis of (*R,E/Z*)-**[^{18}F]2.11** and (*R,E/Z*)-**[^{18}F]2.17a** can be found in the experimental section of this chapter.

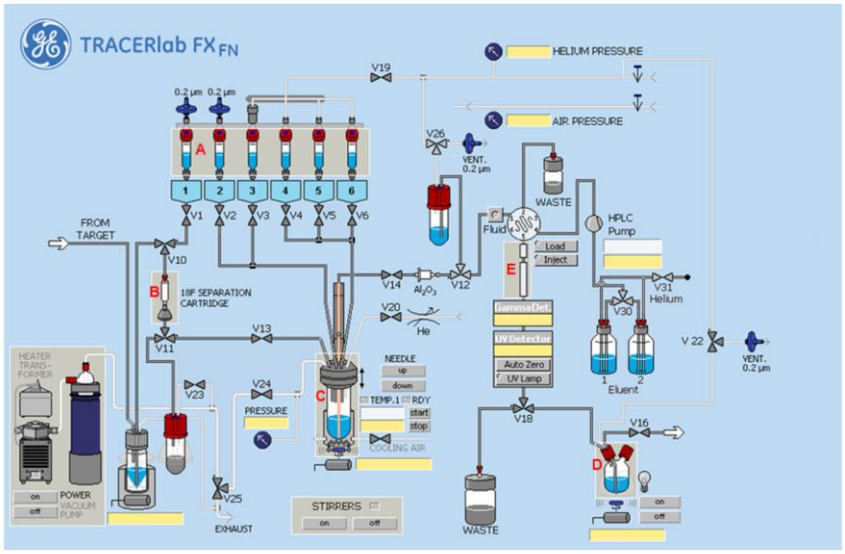

Figure 2-8: Computer controls for TRACERLab$_{FX-N}$ synthesis module. (A) Reagent vials. (B) QMA Sep-pak. (C) Reactor vial. (D) Product vial with final dose before sterile filtering. (E) Semi-preparative HPLC.

Table 2-2:Checklist for setup of radiochemical synthesis of [^{18}F]2.11 and [^{18}F]2.17a.

Part of synthesis module	Reagents, filter, or cartridge used
Vial 1	1.0 mg of precursor in 1.0 mL DMF
Vial 2	K_2CO_3 (3.5 mg in 0.5 mL H_2O)
Vial 3	Kryptofix (15 mg in 1.0 mL MeCN)
Vial 4	5 M LiOH (omitted when preparing ester)
Vial 5	0.17 mL glacial AcOH (omitted when preparing ester)
Vial 6	1.0 mL semi-prep HPLC buffer
Vial 7	4.5 mL 0.9% injectable saline buffer
Vial 8	0.5 mL dry injectable EtOH
Vial 9	6.0 mL MilliQ water
Dilution flask	50 mL water
Solid phase extraction cartridge	QMA Sep-pak Light
Purification cartridge	1cc Vac C18 cartridge
Dose vial	10 mL Sterile vial in nylon rabbit (prepared aseptically with sterile filter and [blue] filter for animal studies)

iii. *In vivo* Evaluation of Novel PET Tracers

Moving to *in vivo* evaluation at this point may seem a bit premature, however, because of how the radiotracer was designed (replacing a fluorine atom with a [^{18}F]fluorine atom), minimal chemical changes were made to the lead compound. The previously reported *in vitro* results of these molecules are encouraging in both the affinity and selectivity of this molecule for GAT-1 (5.73 pIC_{50} with no affinity for GAT-2, -3 or -4), and after successful radiolabeling and purification of the compound, *in vivo* evaluation is a logical step to development of a GAT-1 selective radiotracer. Brain uptake *in vivo* of these unsymmetrical radiotracers was first evaluated in Sprague-Dawley rats. Rats are typically used for the evaluation of novel imaging agents for the CNS as the brains are larger than mice and regions of interest can be adequately assigned and evaluated for distribution of the ligand. In initial evaluation of (*R,E/Z*)-**[^{18}F]2.11** in rat, a female Sprague-Dawley rat (289 g) was injected with (*R,E/Z*)-**[^{18}F]2.11** (0.479 mCi) i.v. via tail vein injection. The rat was scanned for 90 min post-injection of the radiotracer (see experimental section for

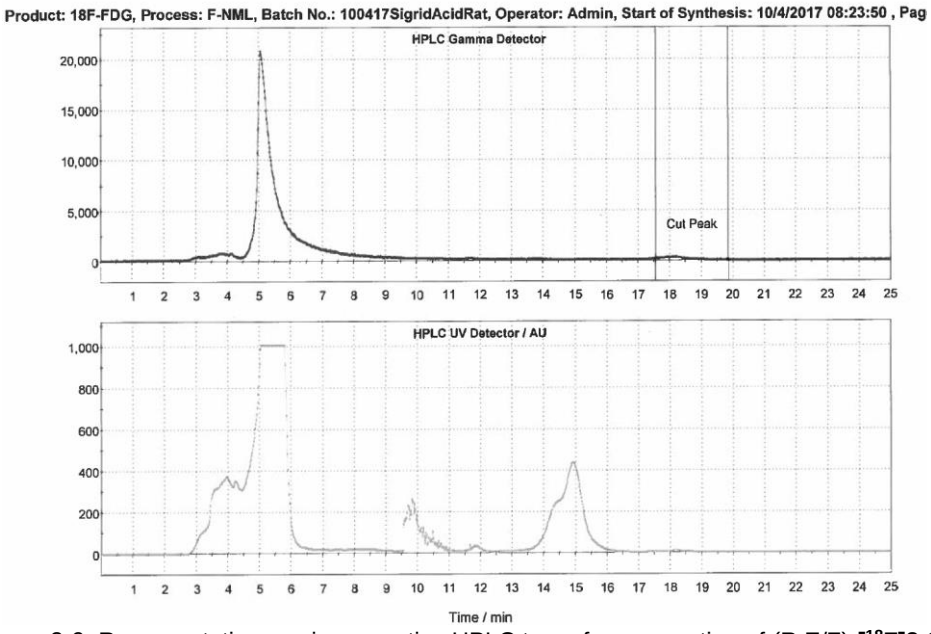

Figure 2-9: Representative semi-preparative HPLC trace for preparation of (R,E/Z)-**[^{18}F]2.11**

detailed scanning procedure) but unfortunately the PET scan revealed no brain uptake of the radiotracer (Figure **2-10).**

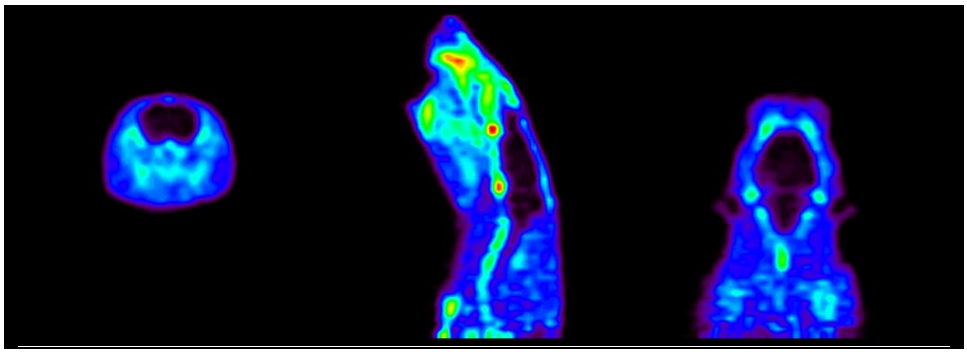

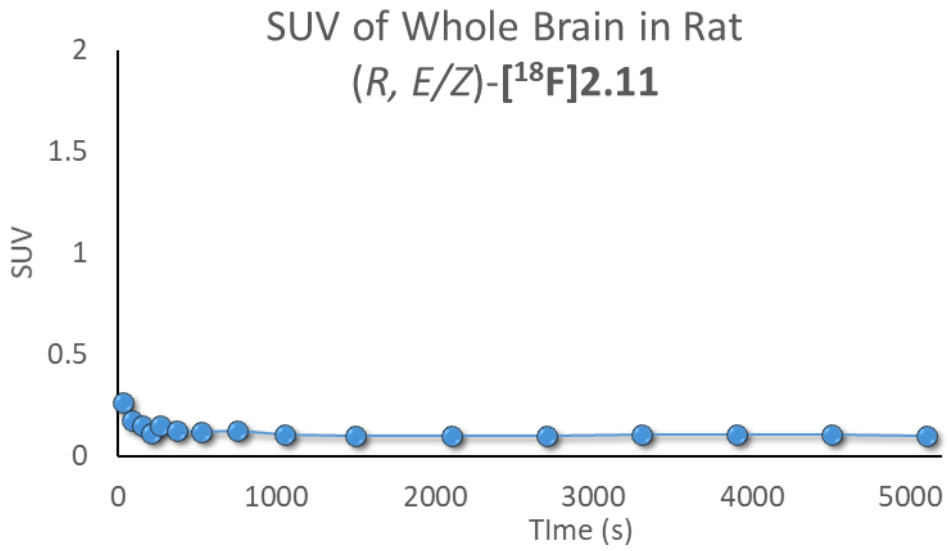

As rats have fast metabolism and much more active efflux transporters than non-human primates (NHP),[12] we were not discouraged by this initial result and tracer (*R,E/Z*)-**[^{18}F]2.11** was also evaluated in a mature female Rhesus Macaque monkey (n=2). Imaging studies were performed in a young, mature female rhesus monkey and radiotracer (*R,E/Z*)-**[^{18}F]2.11** (4.40 ± 0.20mCi) was injected i.v. via a venous catheter inserted into one hind limb of the monkey. The monkey was scanned for 90 min but these

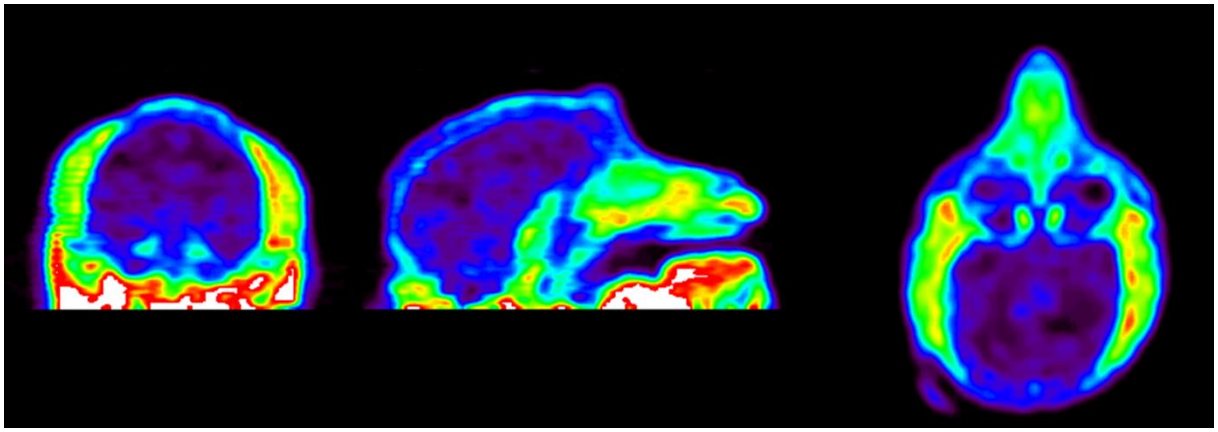

Figure 2-12: Results of *in vivo* evaluation of (*R,E/Z*)-**[^{18}F]2.11** in NHP.

studies also demonstrated no significant brain uptake of the tracer in the monkey brain (Figure 2-12).

To test if the lack of brain uptake was due to the actions of P-glycoprotein (P-gp), an efflux transporter at the blood-brain barrier, we repeated imaging of a rat with (*R,E/Z*)-**[^{18}F]2.11** (0.422 mCi) following pre-treatment with 50 mg/kg cyclosporine A, as we have done previously for other radiotracers.[13] Even with blocking the P-gp efflux transporter, BBB permeability of (*R,E/Z*)-**[^{18}F]2.11** was limited (Figure 2-14).

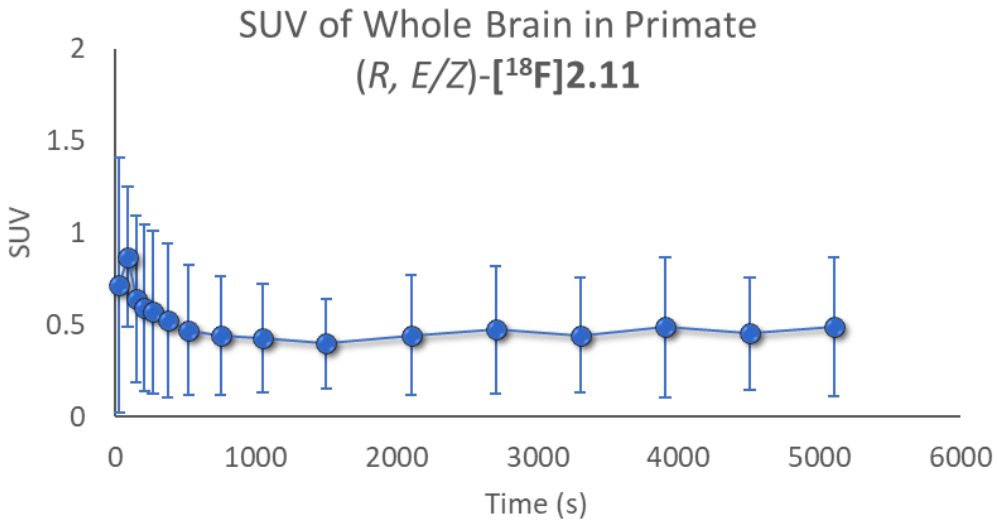

Figure 2-13: Time activity curve (TAC) of (*R,E/Z*)-**[^{18}F]2.11** in NHP.

With the hypothesis that **2.11** possesses properties consistent with BBB permeability (Table 2-3), the lack of brain uptake into the rat and monkey brain was unexpected. Curious if the carboxylic acid played a role in the BBB permeability of this

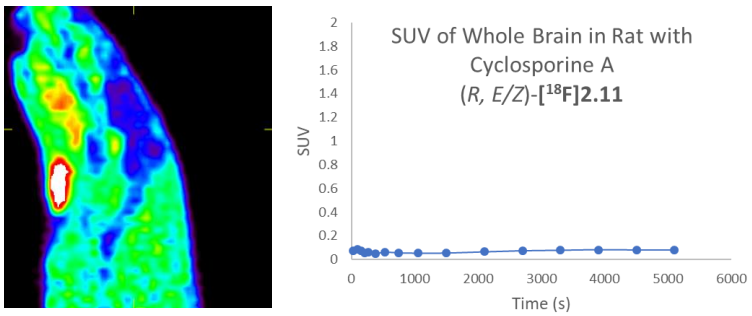

Figure 2-14: Image and SUV as a result of Pgp blocking of Cyclosporine A before administration of (*R*,*E*/*Z*)-**[^{18}F]2.11**.

Table 2-3: Comparison of lead compound **2.11** with typical values for successful radiotracers.

Property	Typical value for successful CNS drugs	Lead unsymmetrical compound (2.11)
clogp	1.5-2.7	1.81
clogD$_{7.4}$	0-3	2.56
tPSA	60-90	66.84 Å
molecular weight	≤400-600 g/mol	415 g/mol
heteroatoms (O+N)	≤5	5
Acidic pKa	>4	3.27
Basic pKa	<10	7.76

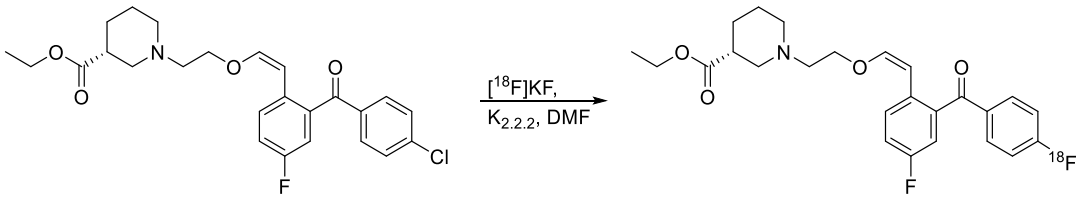

(*R*,*E*/*Z*)-**2.17b** (*R*,*E*/*Z*)-**[^{18}F]2.17a**

Scheme 2-3: Radiochemical synthesis of (*R*,*E*/*Z*)-**[^{18}F]2.17a**.

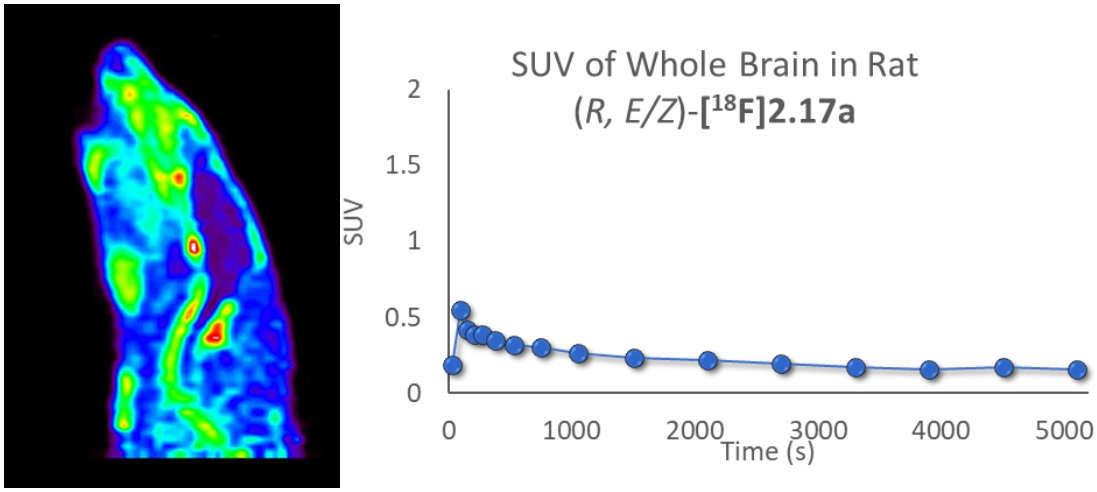

Figure 2-15: Image and SUV as a result of administration of (R,E/Z)-**[^{18}F]2.17a**.

molecule, the saponification of the ester was forgone to produce (*R,E/Z*)-**[^{18}F]2.17a** for additional *in vivo* evaluation (Scheme 2-3). This radiotracer was again initially evaluated in rat. A female Sprague-Dawley rat (289 g) was injected with (*R,E/Z*)-**[^{18}F]2.17a** (0.413 mCi) i.v. via tail vein injection and scanned for 90 min post-injection as before. However, PET studies again showed no brain uptake in rodent (Figure 2-15). In contrast to the result in rats, administration of the ester (*R,E/Z*)-**[^{18}F]2.17a** (3.20 ± 0.70 mCi, n = 2) gave significant brain uptake of radioactivity in cortex, thalamus, striatum and cerebellum (Figure 2-16, 2-17). The species differences between rodents and primates could be due to differences in esterase expression, as the hydrolysis of certain esters is known to be much faster in rat than monkey. This PET tracer may be behaving like a traditional pro-drug. This requires the ester to remain intact before crossing the BBB as the parent

molecule, and then be immediately cleaved to the acid form in order to bind to the GAT-1. Although prodrugs have been used previously in PET tracers,[14] in the case of (*R,E/Z*)-**[^{18}F]2.11**, while ester derivative (*R,E/Z*)-**[^{18}F]2.17a** crosses the BBB, a prodrug approach is not compatible with brain PET as it does not (easily) allow kinetic modelling of the imaging data (Figure 2-18). The levels of (*R,E/Z*)-**[^{18}F]2.17a** entering and leaving the brain will allow estimation of K_1 and k_2, but since (*R,E/Z*)-**[^{18}F]2.11** cannot cross the BBB (Figures 2-10 and 2-12 above), it will be trapped in the brain following any hydrolysis. As (*R,E/Z*)-**[^{18}F]2.11** cannot leave the brain, it will be extremely challenging (perhaps even impossible) to estimate separate values for rate of hydrolysis of (*R,E/Z*)-**[^{18}F]2.17a** into (*R,E/Z*)-**[^{18}F]2.11** (k_3), and the association of (*R,E/Z*)-**[^{18}F]2.11** to (k_4) or dissociation from

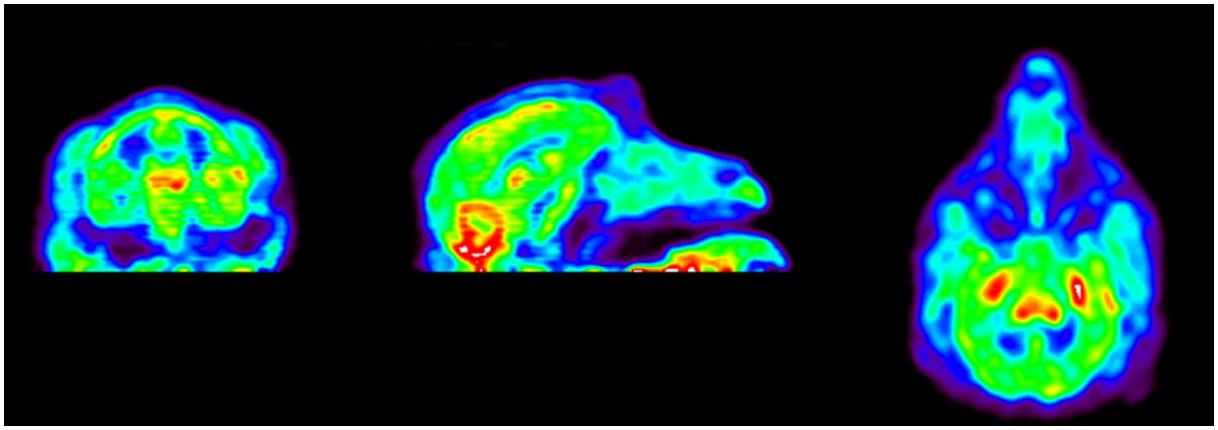

Figure 2-16: Results of *in vivo* evaluation of (*R,E/Z*)-**[^{18}F]2.17a**.

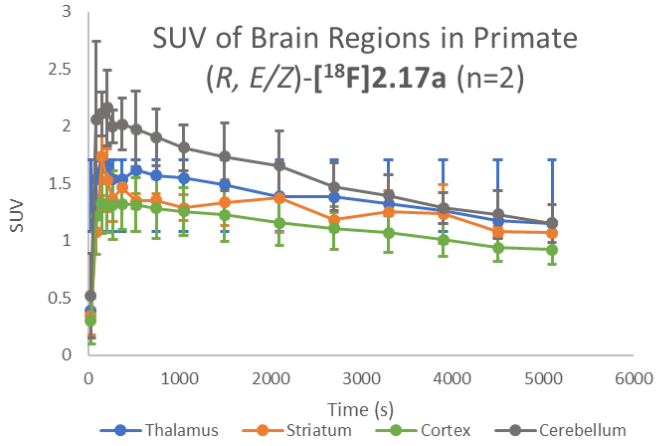

Figure 2-17: Regional time activity curves for (*R,E/Z*)-**[18F]2.17a** in NHP.

(k_5) the GAT-1 transporter. In an attempt to address this issue, the focus of this project was turned to analogs of nipecotic acid that contain a carboxylic acid bioisostere. Bioisosteres are alternative elements or functional groups that have similar size, volume, electronic and physicochemical properties to those they are intended to replace and which, when substituted into a drug molecule, generate a new derivative with similar biological properties to the original. Efforts to introduce a bioisostere to a GAT-1 tracer will be discussed in the next chapter.

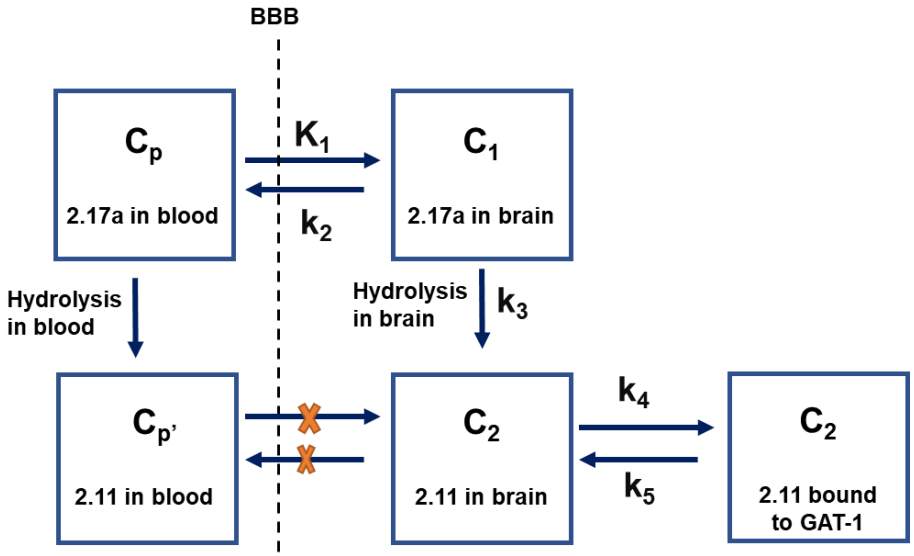

C. Experimental Methods

i. *Chemistry methods*

Reference standards *(R,E/Z)*-**2.11** and *(R,E/Z)*-**2.17a**, as well as precursor *(R,E/Z)*-**2.17b,** were synthesized through adaption of literature procedures.[9]

Compound 2.18

4-Fluorophenol (**2.12**, 141.5 mg, 1.26 mmol, 1.0 equiv.) was dissolved in CH_2Cl_2 (3.15 mL) in a flame dried flask, under argon. To this was added Et_3N (152.8 mg, 0.21 mL, 1.52 mmol, 1.2 equiv.), followed by dropwise addition of benzoyl chloride (**2.13**, 1.26 mmol,

1.0 equiv.). This mixture was then heated to reflux and stirred for 1 h. After this time, the reaction mixture was cooled, diluted with CH_2Cl_2, and washed with saturated $NaHCO_3$, water, and brine. The organic layer was dried (Na_2SO_4), concentrated and purified by flash chromatography (0-15% gradient of EtOAc in Hexanes) to give the title compounds.

4-Fluorophenyl 4-fluorobenzoate (2.18a)

Yield: 228.4 mg (77%) as a white solid.

^{1}H NMR (500 MHz, $CDCl_3$) δ 8.33 – 8.14 (m, 2H), 7.23 – 7.15 (m, 4H), 7.14 – 6.93 (m, 2H).

^{13}C NMR (126 MHz, $CDCl_3$) δ 198.94 (d, *J* = 2.5 Hz), 165.20 (d, *J* = 254.5 Hz), 159.27 (d, *J* = 1.6 Hz), 154.54 (d, *J* = 238.9 Hz), 133.48 (d, *J* = 3.3 Hz), 131.76 (d, *J* = 9.1 Hz, 2C), 123.93 (d, *J* = 23.5 Hz), 119.86 (d, *J* = 7.2 Hz), 118.53 (d, *J* = 6.3 Hz), 117.93 (d, *J* = 23.8 Hz), 115.81 (d, *J* = 22.2 Hz, 2C).

^{19}F NMR (470 MHz, $CDCl_3$) δ -108.89 (s), -120.50 (s).

HRMS: M^+ predicted m/z = 234.0492, actual m/z = 234.0500

4-Fluorophenyl 4-Chlorobenzoate (2.18b)

Yield: 207.8 mg (73 %) as a white solid.

^{1}H NMR (400 MHz, $CDCl_3$) δ 8.13 (d, *J* = 8.6 Hz, 2H), 7.49 (d, *J* = 8.5 Hz, 2H), 7.115-7.169 (m, 4H).

^{13}C NMR (126 MHz, $CDCl_3$) δ 164.33, 160.35 (d, J = 244.6 Hz), 146.55 (d, J = 2.9 Hz), 140.28, 131.52 , 128.99, 127.73, 123.01 (d, J = 8.6 Hz, 2C), 116.19 (d, J = 23.7 Hz, 4C).

^{19}F NMR (470 MHz, $CDCl_3$) δ -116.68.

HRMS: M^+ predicted m/z = 250.0197, actual m/z = 250.0190.

Compound 2.19

2.18 (2.13 mmol, 1.0 equiv.) was liquefied via heating and stirred in a 200°C sandbath. Aluminum trichloride (340.97 mg, 2.56 mmol, 1.2 equiv.) was added through the reflux condenser and the mixture was allowed to stir for 30-40 minutes. The reaction mixture was cooled to room temperature and the glass like product was crushed to a powder before being added to a mixture of ice water and 12 M HCl (20:1 H_2O:12 M HCl). This mixture was extracted several times with diethylether (Et_2O). The combined organic layers were then washed with water. The organic layer was dried (sodium sulfate), concentrated and purified via flash column chromatography (0- 15% gradient of EtOAc in Hexanes) to give the title compounds.

(5-Fluoro-2-hydroxyphenyl)(4-fluorophenyl)methanone (2.19a)

Yield: 370.2 mg (74%) as an off-white solid.

^{1}H NMR (400 MHz, $CDCl_3$) δ 11.59 (s, 1H), 8.21 (dd, *J* = 8.6, 5.4 Hz, 1H), 7.73 (dd, *J* = 8.6, 5.3 Hz, 1H), 7.25 – 6.99 (m, 5H).

^{13}C NMR (126 MHz, $CDCl_3$) δ 198.94 (d, *J* = 2.5 Hz), 165.20 (d, *J* = 254.5 Hz), 159.27 (d, *J* = 1.6 Hz), 154.54 (d, *J* = 238.9 Hz), 133.48 (d, *J* = 3.3 Hz), 131.76 (d, *J* = 9.1 Hz, 2C), 123.93 (d, *J* = 23.5 Hz), 119.86 (d, *J* = 7.2 Hz), 118.53 (d, *J* = 6.3 Hz), 117.93 (d, *J* = 23.8 Hz), 115.81 (d, *J* = 22.2 Hz, 2C).

^{19}F NMR (470 MHz, $CDCl_3$) δ -98.73 – -110.75 (m), -123.80 (td, *J* = 8.2, 4.2 Hz).

HRMS: Predicted $(M-H)^-$ = 233.042, actual = 233.0417.

(4-Chlorophenyl)(5-fluoro-2-hydroxyphenyl)methanone (2.19b)

Yield: 315.9 mg (63%) as an off-white solid.

^{1}H NMR (400 MHz, $CDCl_3$) δ 11.60 (s, 1H), 8.13 (d, J = 8.6 Hz, 1H), 7.65 (d, J = 8.5 Hz, 1H), 7.50 (dd, J = 9.2, 7.5 Hz, 2H), 7.20 – 7.02 (m, 3H).

^{13}C NMR (101 MHz, $CDCl_3$) δ 199.11 (d, J = 2.6 Hz), 162.90 (d, J = 277.0 Hz), 159.30 (d, J = 1.5 Hz), 154.50 (d, J = 238.9 Hz), 138.82, 135.50, 131.50 (d, J = 2.6 Hz), 130.56 (d, J = 21.2 Hz), 128.87 (d, J = 23.9 Hz), 124.21 (d, J = 24.1 Hz), 120.31 – 119.69 (m), 118.35 (d, J = 6.4 Hz), 117.86 (t, J = 23.2 Hz).

^{19}F NMR (470 MHz, $CDCl_3$) δ -122.60 – -124.08 (m).

HRMS: Predicted $(M-H)^-$ = 249.0124, actual = 249.0120.

4-Fluoro-2-(4-fluorobenzoyl)phenyl trifluoromethanesulfonate (2.14a)

2.19a (300 mg, 1.28 mmol, 1.0 eq) was dissolved in CH_2Cl_2 (3.2 mL). Collidine (631.35 mg, 0.69 mL, 5.21 mmol, 4.1 equiv) was added and the reaction mixture was stirred at 0°C for 15 min to equilibrate. Triflic anhydride (722.25 mg, 0.43 mL, 2.56 mmol, 2.0 equiv.) was added dropwise at 0°C and the reaction was warmed to rt and stirred for 48 hrs. After this time the reaction was diluted with ether and wash twice with water. The aqueous layer was extracted with further ether, and the organic layers were combined, washed with copper (II) sulfate solution, dried (MgSO4) and concentrated. The product was purified by flash column chromatography (0-10% gradient of EtOAc in Hexanes) to give triflate **2.14a.**

.

Yield: 357.2 mg (76 %) as a white solid.

^{1}H NMR (400 MHz, $CDCl_3$) δ 8.02 – 7.71 (m, 2H), 7.41 (dd, J = 9.1, 4.2 Hz, 1H), 7.32 (m, 1H), 7.30 – 7.21 (m, 1H), 7.24 – 7.12 (m, 2H).

^{13}C NMR (126 MHz, $CDCl_3$) δ 189.59, 166.36 (d, *J* = 257.5 Hz), 160.84 (d, *J* = 252.6 Hz), 142.20, 132.86 (d, *J* = 9.6 Hz, 2C), 132.22, 124.44 (d, *J* = 8.5 Hz), 119.45 (d, *J* = 23.9 Hz, 2C), 117.94, 117.74, 116.07 (d, *J* = 22.0 Hz, 2C).

^{19}F NMR (470 MHz, $CDCl_3$) δ -73.36, -100.33 – -105.21 (m), -110.69 (td, J = 7.5, 4.2 Hz).

HRMS: Predicted m/z $(M+Na)^+$ = 388.9877, actual = 388.9874.

2-(4-Chlorobenzoyl)-4-fluorophenyl trifluoromethanesulfonate (2.14b)

2.19b (546.5 mg, 2.18 mmol, 1.0 eq) was dissolved in CH_2Cl_2 (8.7 mL). Collidine (961.7 mg, 1.04 mL, 8.94 mmol, 4.1 equiv) was added and the reaction mixture was stirred at 0°C for 15 min to equilibrate. Triflic anhydride (1046.7 mg, 0.6 mL, 3.71 mmol, 1.7 equiv.) was added dropwise at 0°C and the reaction was warmed to rt and stirred for 48 hrs. After this time the reaction was diluted with ether and wash twice with water. The aqueous layer was extracted with further ether, and the organic layers were combined, washed with copper (II) sulfate solution, dried ($MgSO_4$) and concentrated. The product was purified by flash column chromatography (0-10% gradient of EtOAc in Hexanes) to give triflate **2.14b**.

Yield: 654.1mg (78%) as a white solid.

^{1}H NMR (500 MHz, $CDCl_3$) δ 7.80 – 7.71 (m, 2H), 7.50 – 7.45 (m, 2H), 7.42 (dd, J = 9.1, 4.2 Hz, 1H), 7.33 (ddd, J = 9.1, 7.2, 3.1 Hz, 1H), 7.26 (dd, J = 7.6, 3.1 Hz, 1H).

^{13}C NMR (126 MHz, $CDCl_3$) δ 189.95 (d, J = 1.6 Hz), 160.83 (d, J = 252.4 Hz), 142.27 (d, J = 3.3 Hz), 134.17, 133.84 (d, J = 6.9 Hz, 2C), 131.42, 129.10, 124.51 (d, J = 8.6 Hz), 119.61 (d, J = 23.9 Hz), 117.86 (d, J = 25.0 Hz, 2C), 117.10.

^{19}F NMR (470 MHz, $CDCl_3$) δ -73.36, -110.60 (td, J = 7.5, 4.2 Hz).

HRMS: Predicted m/z $(M+Na)^+$ = 404.9582, actual = 404.9579.

2-(Vinyloxy)ethyl 4-methylbenzenesulfonate (2.20)

Ether **2.15** (500 mg, 0.51 mL, 5.67 mmol, 1.0 eq) was dissolved in CH_2Cl_2 (5.5 mL). Et_3N (900.87 mg, 1.25 mL, 8.90 mmol, 1.57 equiv.) and DMAP (2.77 mg, 0.023 mmol, 0.004 equiv.) were added and the reaction mixture stirred at 0°C. A solution of TsCl (1297.2 mg, 6.80 mmol, 1.2 equiv.) in CH_2Cl_2 (9.0 mL) was added dropwise to the reaction mixture at 0°C. The reaction was allowed to warm to room temperature and stirred overnight. After this time the reaction mixture was diluted with CH_2Cl_2 and washed with water. The organic layer was dried (Na_2SO_4) and concentrated to give tosylate **2.20** which was used without further purification.

Yield: 1373.8 mg (quantitative) as a clear colorless oil.

^{1}H NMR (400 MHz, $CDCl_3$) δ 7.77 (m, 2H), 7.32 (m, 2H), 6.33 (dd, *J* = 14.3, 6.8 Hz, 1H), 4.24 – 4.18 (m, 2H), 4.10 (dd, *J* = 14.3, 2.4 Hz, 1H), 3.98 (m, 1H), 3.84 (dd, *J* = 5.4, 4.0 Hz, 2H), 2.42 (s, 3H).

^{13}C NMR (101 MHz, $CDCl_3$) δ 150.72, 145.05, 132.51, 130.44 – 128.19 (m, 2C), 126.84 (d J = 195.8zz, 2C), 88.49 – 86.59 (m), 68.27, 65.26, 21.52.

HRMS: Predicted m/z $(M+Na)^+$ = 265.0505, actual = 265.0509.

Ethyl (*R*)-1-(2-(vinyloxy)ethyl)piperidine-3-carboxylate ((*R*)-2.16)

Tosylate **2.20** (500 mg, 2.06 mmol, 1.0 eq) was weighed into flame dried flask and then purged with argon. (*R*)-Nipecotate, **2.21**, (647.7 mg, 0.64 mL, 4.12 mmol, 2.0 equiv.) was diluted in Et_3N (1042.36 mg, 1.45 mL, 10.3 mmol, 5.0 equiv.) and added dropwise to tosylate **2.20**. The reaction mixture was allowed to stir at room temperature for 7 hrs. After this time, the reaction was quenched with water and extracted with pentanes several times. The organic layers were combined, dried (K_2CO_3) and concentrated. The residue was purified by flash chromatography (Hexanes/EtOAc + 0.5% Et_3N) to yield (*R*)-**2.16**.

Yield: 326.5 mg (70%) as a yellow oil.

^{1}H NMR (500 MHz, $CDCl_3$) δ 6.48 (dd, *J* = 14.4, 6.8 Hz, 1H), 4.16 (dd, *J* = 14.4, 2.1 Hz, 1H), 4.11 (q, *J* = 7.1 Hz, 2H), 3.99 (dd, *J* = 6.8, 2.1 Hz, 1H), 3.79 (t, *J* = 5.8 Hz, 2H), 3.06

– 2.99 (m, 1H), 2.82 (d, *J* = 11.2 Hz, 1H), 2.68 (td, *J* = 5.7, 2.9 Hz, 2H), 2.62 – 2.53 (m, 1H), 2.21 (t, *J* = 10.8 Hz, 1H), 2.05 (td, *J* = 11.2, 2.9 Hz, 1H), 1.97 – 1.90 (m, 1H), 1.71 (m, 1H), 1.65 – 1.54 (m, 1H), 1.42 (qd, *J* = 11.7, 4.2 Hz, 1H), 1.24 (t, *J* = 7.1 Hz, 3H).

^{13}C NMR (101 MHz, $CDCl_3$) δ 173.96, 151.62, 86.26, 65.05, 60.18, 57.24, 55.67, 53.96, 41.67, 26.77, 24.44, 14.13.

HRMS: Predicted m/z (M+H)+ = 228.1594, actual = 228.1593.

(*R*,*E/Z*)-Ethyl-1-(2-((4-fluoro-2-(4-fluorobenzoyl)styryl)oxy)ethyl)piperidine-3-carboxylate, (*R,E/Z*)-2.17a

Palladium (II) acetate (21.8 mg, 0.10 mmol, 0.21 eq) and triphenyl phosphine (59.1 mg, 0.22 mmol, 0.49 eq) were dissolved in DMF (2.0 mL). A solution of **2.14a** (170.0 mg, 0.46 mmol, 1.0 eq) in DMF (0.5 mL) was added dropwise, followed by Et_3N (104.7 mg, 0.14 mL, 1.03 mmol, 2.25 eq). A solution of nipecotate linker (*R*)-**2.16** (185.8mg, 0.67 mmol, 1.54 eq) in DMF (0.5 mL) was then added and the reaction mixture which was stirred at 80°C for 48 h. After this time the reaction mixture was cooled, diluted with CH_2Cl_2 (7 mL), and washed with water (2x) and brine (2x). The organic fraction was dried (K_2CO_3) and concentrated. Purification by flash chromatography (Hex/EtOAc + 0.5% Et_3N) gave the title compound.

Yield: 78.2 mg (38 %) as a yellow oil.

^{1}H NMR (500 MHz, $CDCl_3$) δ 7.86 – 7.79 (m, 2H), 7.38 (dd, *J* = 8.7, 5.2 Hz, 1H), 7.16 – 7.12 (m, 2H), 7.11 (dd, *J* = 5.2, 3.3 Hz, 1H), 6.99 (ddd, *J* = 21.4, 8.6, 2.8 Hz, 1H), 6.83 (d, *J* = 12.9 Hz, 1H), 6.10 (d, *J* = 7.2 Hz, 1H), 5.77 (d, *J* = 12.9 Hz, 1H), 5.14 (d, *J* = 7.1 Hz, 1H), 4.12 (q, *J* = 7.1 Hz, 2H), 3.75 (t, *J* = 5.7 Hz, 2H), 2.99 – 2.94 (m, 1H), 2.74 (d, *J* = 11.2 Hz, 1H), 2.66 – 2.58 (m, 2H), 2.55 (m, 1H), 2.17 (m, 1H), 2.01 (td, *J* = 11.1, 3.0 Hz, 1H), 1.96 – 1.89 (m, 1H), 1.72 – 1.66 (m, 1H), 1.62 – 1.51 (m, 1H), 1.47 – 1.36 (m, 1H), 1.24 (m, 3H).

[Protons presenting at 5.14 and 6.10 ppm represent the *Z*-isomer, while protons at 5.77 and 6.83 ppm represent the *E*-isomer. The reaction yielded 32% of the *Z* isomer and 68% of the *E* isomer.]

^{13}C NMR (126 MHz, $CDCl_3$) δ 195.49, 174.02, 165.96 (d, J = 255.9 Hz), 160.38 (d, J = 247.3 Hz), 149.57, 147.41, 137.86 (d, J = 6.0 Hz), 133.44, 132.87 (d, J = 9.4 Hz, 2C), 131.42, 127.25, 117.34 (d, J = 21.1 Hz), 115.72 (d, J = 21.9 Hz, 2C), 114.95 (d, J = 23.0 Hz), 102.33, 101.29, 66.99, 60.31, 57.26, 55.71, 53.93, 41.74, 26.81, 24.49, 14.19.

[Carbons presenting at 101.29 and 147.41 pmm represent the *Z*-isomer, while carbons at 102.25 and 149.56 represent the *E*-isomer].

19F NMR (470 MHz, CDCl3) δ -104.12, -116.46 (d, J = 5.5 Hz).

HRMS: Predicted m/z (M+H)+ = 444.1981, actual = 444.1988.

(*R*,*E/Z*)- Ethyl-1-(2-((2-(4-chlorobenzoyl)-4-fluorostyryl)oxy)ethyl)piperidine-3-carboxylate (*R, E/Z*)-2.17b

Palladium (II) acetate (29.1 mg, 0.13 mmol, 0.21 eq) and triphenyl phosphine (78.7 mg, 0.30 mmol, 0.49 eq) were dissolved in DMF (1.6 mL). A solution of **2.14b** (233.4 mg, 0.61 mmol, 1.0 eq) in DMF (1.0 mL) was added dropwise, followed by Et_3N (135.6 mg, 0.19 mL, 1.34 mmol, 2.25 eq). A solution of nipecotate linker (*R*)-**2.16** (200.0 mg, 0.88 mmol, 1.54 eq) in DMF (1.0 mL) was then added and the reaction mixture which was stirred at 80°C for 48 h. After this time the reaction mixture was cooled, diluted with CH_2Cl_2 (7 mL), and washed with water (2x) and brine (2x). The organic fraction was dried (K_2CO_3) and concentrated. Purification by flash chromatography (Hex/EtOAc + 0.5% Et_3N) gave the title compound.

Yield: 159.1 mg (57 %) as a yellow oil.

^{1}H NMR (500 MHz, $CDCl_3$) δ 7.79 – 7.69 (m, 2H), 7.44 – 7.36 (m, 3H), 7.19 – 7.06 (m, 1H), 6.98 (ddd, J = 21.4, 8.6, 2.8 Hz, 1H), 6.82 (d, J = 12.9 Hz, 1H), 6.09 (d, J = 7.2 Hz, 1H), 5.77 (d, J = 12.9 Hz, 1H), 5.13 (d, J = 7.1 Hz, 1H), 4.12 (q, J = 7.1 Hz, 2H), 3.75 (t, J = 5.7 Hz, 2H), 2.96 (dd, J = 10.7, 3.9 Hz, 1H), 2.74 (d, J = 11.3 Hz, 1H), 2.64 – 2.57 (m, 2H), 2.57 – 2.49 (m, 1H), 2.18 (t, J = 10.7 Hz, 1H), 2.01 (td, J = 11.1, 3.0 Hz, 1H), 1.96 – 1.91 (m, 1H), 1.74 – 1.66 (m, 1H), 1.62 – 1.51 (m, 1H), 1.46 – 1.37 (m, 1H), 1.24 (t, J = 7.1 Hz, 3H).

[Protons presenting at 5.13 and 6.09 ppm represent the *Z*-isomer, while protons at 5.77 and 6.82 ppm represent the *E*-isomer. The reaction ratio was 72:28, E:Z.]

^{13}C NMR (126 MHz, $CDCl_3$) δ 195.81, 173.99, 160.38 (d, *J* = 247.4 Hz), 149.65, 147.43, 139.99 (d, *J* = 7.5 Hz), 137.59 (d, *J* = 6.2 Hz), 135.06 (d, *J* = 88.8 Hz), 131.75 – 131.11 (m, 2C), 128.87 (d, *J* = 12.0 Hz), 127.89, 127.33 (d, *J* = 7.5 Hz), 117.49 (dd, *J* = 85.7, 21.2 Hz), 115.41 (d, 2 C, *J* = 22.9 Hz), 114.71 (d, *J* = 22.9 Hz), 102.33, 101.34, 71.37, 60.32, 57.26, 55.72, 53.92, 41.74, 26.81, 24.49, 14.20.

[Carbons presenting at 101.34 and 147.43 pmm represent the *Z*-isomer, while carbons at 102.33 and 149.65 represent the *E*-isomer].

^{19}F NMR (376 MHz, $CDCl_3$) δ -116.37.

HRMS: Predicted m/z $(M+H)^+$ = 460.1685, actual 460.1685.

(*R*,*E*)-1-(2-((4-Fluoro-2-(4-fluorobenzoyl)styryl)oxy)ethyl)piperidine-3-carboxylic Acid (Reference Standard (*R,E/Z*)-2.11)

Ester (*R,E/Z*)-**2.17a**(50.0mg, 0.1 mmol, 1.0 eq) was dissolved in ethanol (1.0 mL). Aq. LiOH (10M, 0.3 mL) was added dropwise and the reaction was stirred at room temperature for 3 h. Upon completion, the reaction was concentrated, and the resulting residue was dissolved in water and cooled to 0°C. The pH was adjusted to 2 with 1N HCl while keeping the temperature below 5°C, and the product was extracted from the aq. layer with CH_2Cl_2 (2 x 25 mL). The organic fraction was dried ($MgSO_4$), concentrated and purified by flash chromatography (Hex:EtOAC + 0.05% Et_3N) to give reference standard (*R,E/Z*)-**2.11**.

Yield: 21.4 mg (46%) as a yellow oil.

^{1}H NMR (500 MHz, $CDCl_3$) δ 7.78 (dt, J = 8.8, 4.7 Hz, 2H), 7.42 (dd, J = 8.7, 5.2 Hz, 1H), 7.16 – 7.09 (m, 3H), 6.97 (dd, J = 8.4, 2.7 Hz, 1H), 6.79 (d, J = 12.7 Hz, 1H), 6.06 (d, J = 7.2 Hz, 1H), 5.87 (d, J = 12.8 Hz, 1H), 5.22 (d, J = 7.1 Hz, 1H), 4.18 (dd, J = 30.3, 7.6 Hz, 2H), 3.05 (m, 4H), 2.20 – 1.98 (m, 3H), 1.88 (s, 2H), 1.74 – 1.34 (m, 2H).
[Protons presenting at 5.22 and 6.06 ppm represent the *Z*-isomer, while protons at 5.87 and 6.79 ppm represent the *E*-isomer. This standard contained both isomers, 28% *Z* and 72% *E*].

^{13}C NMR (126 MHz, $CDCl_3$) δ 195.36, 174.37, 166.02 (d, *J* = 256.2 Hz), 160.50 (d, *J* = 48.6 Hz), 148.01, 145.87, 137.81 (d, *J* = 5.9 Hz), 133.25, 132.97 (d, *J* = 9.2 Hz, 2C), 130.45 (d, *J* = 3.5 Hz), 129.30, 118.18 – 117.20 (m), 115.90 (d, *J* = 21.9 Hz, 2C), 115.53 (d, *J* = 22.7 Hz), 104.44, 103.31, 64.32, 56.15, 54.20, 53.22, 39.05, 24.91, 21.92.
[Carbons presenting at 103.31 and 145.87 ppm represent the *Z*-isomer, while carbons at 104.44 and 148.01 represent the *E*-isomer.]

^{19}F NMR (376 MHz, $CDCl_3$) δ -103.77, -115.64.

HRMS: Predicted m/z $(M+H)^+$ = 416.1668, actual 416.1668.

ii. *Radiochemistry methods*

General Considerations.

Unless otherwise stated, reagents and solvents were commercially available and used without further purification: sodium chloride, 0.9% USP, and sterile water for injection, USP, were purchased from Hospira; ethanol was purchased from American Regent; HPLC grade acetonitrile was purchased from Fisher Scientific. Other synthesis components were obtained as follows: sterile filters were obtained from Millipore; sterile product vials were purchased from Hollister-Stier; QMA-light and C18-light Sep-Paks were purchased from Waters Corporation. QMA-light Sep-Paks were flushed with 10 mL each, ethanol, water, 0.5 M $NaHCO_3$, and further water prior to use. C18 Sep-Paks were flushed with 10 mL of ethanol followed by 10 mL of sterile water prior to use. Analytical HPLC was performed using a Shimadzu LC-2010A HT system equipped with a Bioscan B-FC-1000 radiation detector and a UV detector.

Radiosynthesis of (*R,E/Z*)-[^{18}F]2.11

[^{18}F]Fluoride was produced via the $^{18}O(p,n)^{18}F$ nuclear reaction using a GE PETTrace cyclotron (40 μA beam for 30 min generated ~1500 mCi of [^{18}F]fluoride). The [^{18}F]fluoride was delivered to a GE TRACERLab FXFN synthesis module (in a 1.5 mL bolus of [^{18}O]water) and trapped on a QMA-light Sep-Pak to remove [^{18}O]water. [^{18}F]Fluoride was eluted into the reaction vessel using K_2CO_3 (3.5 mg in 0.5 mL of water). A solution of $K_{2.2.2}$ (15 mg in 1 mL of acetonitrile) was added to the reaction vessel, and the resulting solution was azeotropically dried by heating the reaction vessel to 100 °C

and drawing vacuum for 4 min. After this time, the reaction vessel was subjected to an argon stream and simultaneous vacuum draw for an additional 4 min.

Chlorinated precursor ((*R,E/Z*)-**2.17b**) (2.5 mg dissolved in 1.0 mL of DMF) was delivered to the reaction vessel, and the reaction was stirred for 30 min at 130°C to give (*R,E/Z*)-**[^{18}F]2.17a**. After this time the reactor was cooled to 100°C, 5 M LiOH (1 mL) was added, and the hydrolysis reaction was stirred for 15 min. After this time the reactor was cooled to 50°C and neutralized by addition of glacial AcOH (0.3 mL). The mixture was stirred for 1-2 minutes and then diluted with semi-preparative HPLC solvent (2 mL). The reaction mixture was purified by semipreparative HPLC (column: Phenomenex Luna C18, 250 mm x 10 mm; mobile phase: 50 mM NH_4OAc in 30% MeCN, pH 6.0 adjusted with AcOH, flow rate = 4.0 mL/min). The product peak (retention time ~18-19, Figure 2-19) was collected and diluted into a round bottom flask containing milliQ water (50 mL). The resulting solution was passed through a 1 cc vac C18 Sep-Pak to remove organic solvent while trapping (*R,E/Z*)-**[^{18}F]2.11**. The Sep-Pak was washed with sterile water (6 mL), and (*R,E/Z*)-**[^{18}F]2.11** was eluted with 0.5 mL EtOH, followed by 4.5 mL saline. The final formulated dose was passed through a 0.22 μm sterile filter into a sterile dose vial to give 9.3 ± 3.3 mCi (344.1 ± 122.1 MBq) of (*R,E/Z*)-**[^{18}F]2.11** (1.0% non-corrected RCY, 100% RCP (column: Phenomenex Luna C18 5μ150 x 4.6 mm; mobile phase: 35% MeCN 10mM, NH_4OAc, pH 4.5, flow rate = 2.0 mL/min, UV: 254 nm; Figure 2-21), high specific activity (1702 Ci/mmol) and pH = 5.5, n = 4).

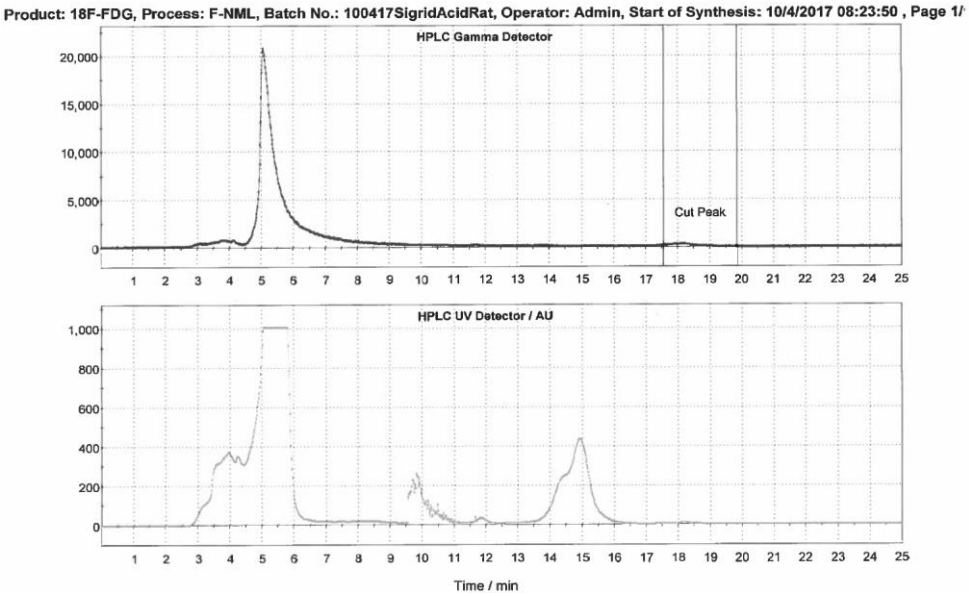

Figure 2-19: Representative semi-preparative HPLC trace from preparation of (*R,E/Z*)-**[^{18}F]2.11**. "Cut peak" depicts volume collected for dose.

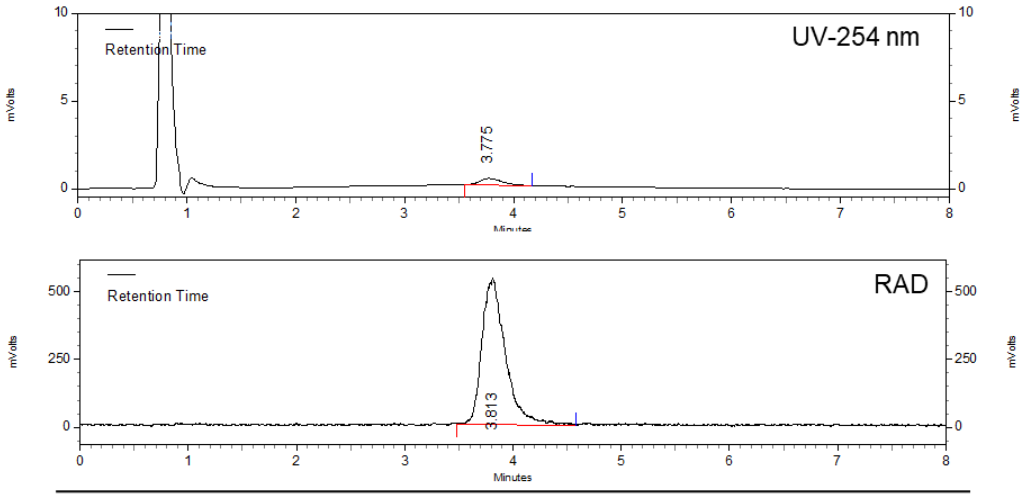

UV Detector Ch1-254nm Results

Retention Time	Area	Area %	Height	Width	S/N (ASTM)
3.775	5474	100	382	0.625	0.07

RAD Results

Retention Time	Area	Area %	Width
3.813	8130607	100	1.10

Figure 2-20: Representative quality control HPLC trace of prepared dose (*R,E/Z*)-**[^{18}F]2.11.**

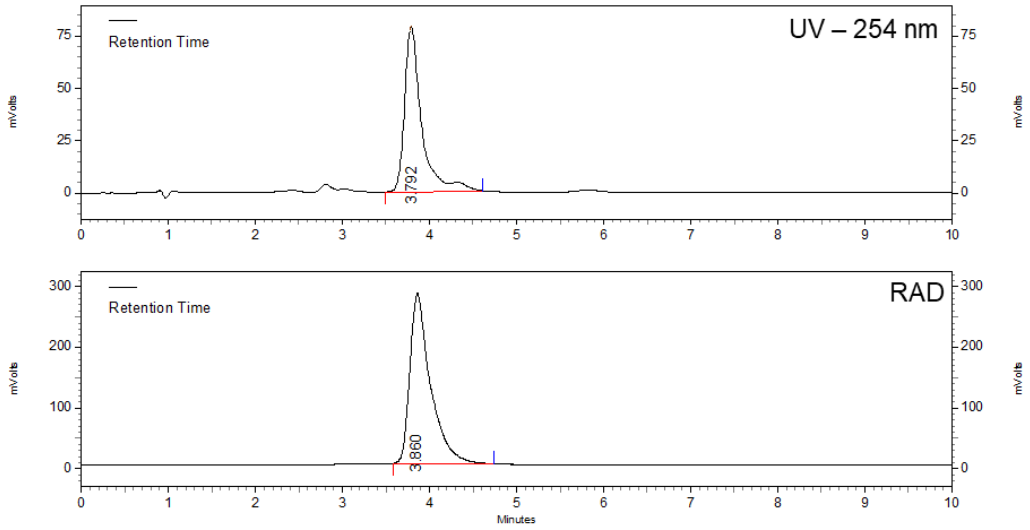

UV Detector Ch1-254nm Results

Retention Time	Area	Area %	Height	Width	S/N (ASTM)
3.792	1073902	100	78962	1.125	44.15

Gamma Results

Retention Time	Area	Area %	Width
3.860	4604652	100	1.16

Figure 2-21: Representative coinjection HPLC trace of prepared dose of (*R,E/Z*)-**[^{18}F]2.11** with standard (*R,E/Z*)-**2.11**

Radiosynthesis of (*R,E/Z*)-[^{18}F]2.17a

(*R,E/Z*)-**[^{18}F]2.17a** was produced as described for (*R,E/Z*)-**[^{18}F]2.11.** After radiofluorination, the reaction vessel was cooled to 50°C and semi-preparative HPLC mobile phase was added (2 mL). The reaction mixture was then purified by semi-preparative HPLC (column: Phenomenex Luna C18, 250 mm x 10 mm; mobile phase: 10 mM NH_4OAc in 70% MeCN, flow rate = 4.0 mL/min). The product peak (retention time ~14-15 minutes, Figure 2-22) was collected and reformulated in the same way as (*R,E/Z*)-**[^{18}F]2.11**. The final formulated dose was passed through a 0.22 µm sterile filter into a

sterile dose vial to give 7.7 ± 3.5 mCi (284.9 ± 129.5 MBq) of (*R,E/Z*)-**[^{18}F]2.17a** (1.3% non-corrected RCY, 100% RCP (column: Phenomenex Luna C18 5µ150 x 4.6 mm; mobile phase: 70% MeCN 10mM NH_4OAc, flow rate = 1.5 mL/min, UV: 254 nm; Figure 2.23), moderate effective specific activity (250 Ci/mmol), and pH = 5.5, *n* = 4).

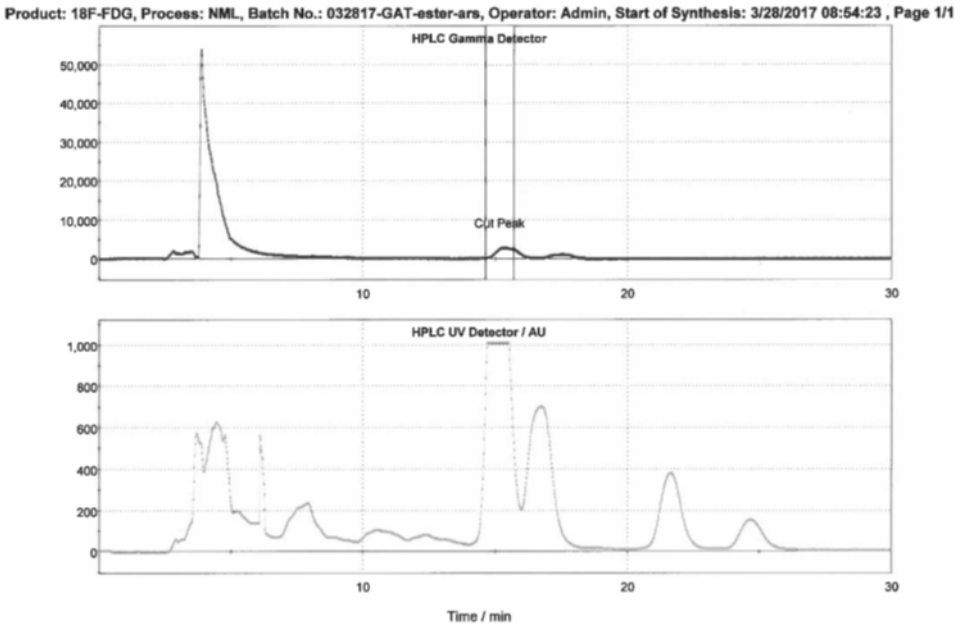

Figure 2-22: Representative semi-preparative HPLC trace from preparation of (*R,E/Z*)-**[^{18}F]2.17a**. "Cut peak" depicts volume collected for dose.

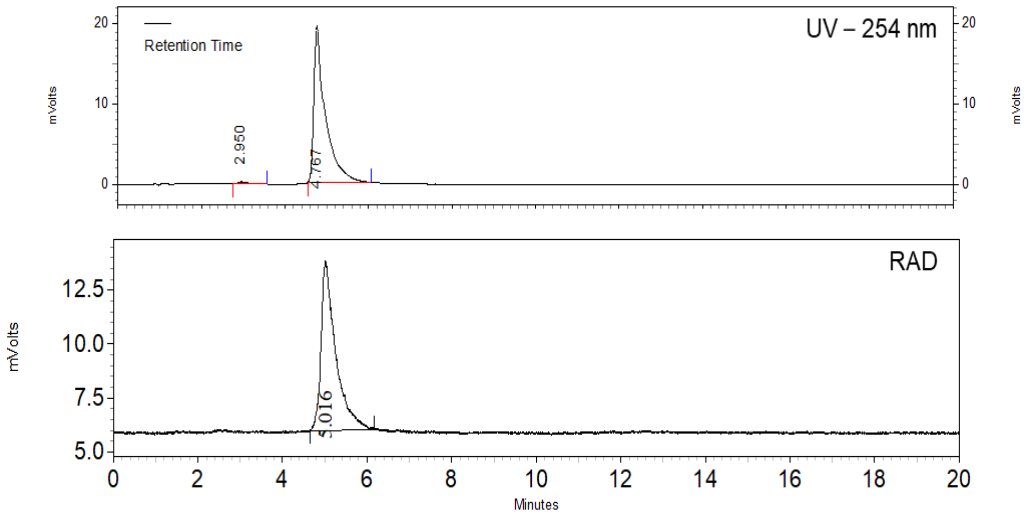

UV Detector Ch1-254nm Results					
Retention Time	Area	Area %	Height	Width	S/N (ASTM)
2.950	4004	1	269	0.808	3.14
4.767	370751	99	19480	1.533	139.87

Gamma Results			
Retention Time	Area	Area %	Width
5.016	188293	100	1.50

Figure 2-23: Representative quality control HPLC trace of prepared dose (*R,E/Z*)-**[^{18}F]2.17a**.

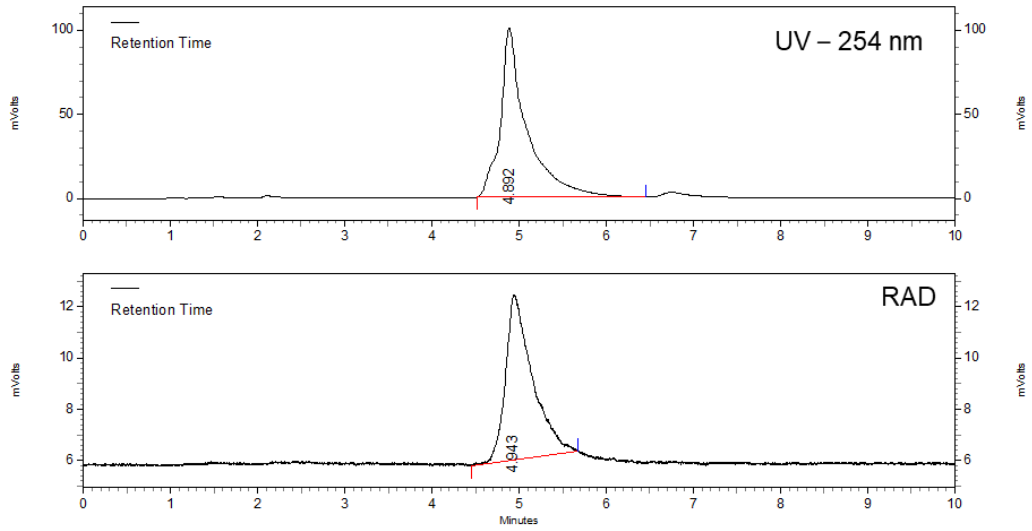

UV Detector Ch1-254nm Results					
Retention Time	Area	Area %	Height	Width	S/N (ASTM)
4.892	2116280	100	100408	1.942	236.21

Gamma Results			
Retention Time	Area	Area %	Width
4.943	138050	100	1.22

Figure 2-24: Representative coinjection HPLC trace of prepared dose of (*R,E/Z*)-**[^{18}F]2.17a** with standard (*R,E/Z*)-**2.17a**.

iii. ***In vivo methods***

MicroPET imaging was done in a microPET R4 or microPET P4 for 60-90 minutes following injection of each radiotracer. Images were reconstructed using 3D maximum a *priori* (3D MAP) program.

General considerations

All animal PET imaging experiments were conducted under the supervision of the University of Michigan and its Institutional Animal Care and Use Committee (IACUC) according to approved protocols and all applicable federal, state, local and institutional laws or guidelines governing animal research. Imaging studies were conducted using a Concorde Microsystems P4 PET scanner as described below.

Rodents

Anesthesia was induced in healthy, female Sprague-Dawley rats (279-369 g) using isoflurane/O_2, and anesthesia was maintained with 2-4% isoflurane/O_2 throughout the imaging studies. Body temperature was maintained by a heating pad. Following a transmission scan for attenuation correction, the animals were injected (*i.v.* via intravenous tail vein) with the radiotracer as a bolus over 1 min (Table 2-4), and the brain imaged for 90 minutes.

Primate Imaging

Imaging studies were performed in a young, mature female rhesus monkey. The animal was anesthetized in the home cage with ketamine and transported to the PET imaging

suite. The monkey was intubated for mechanical ventilation, and anesthesia was continued with isoflurane. Anesthesia was maintained throughout the duration of the PET scan. A venous catheter was inserted into one hind limb and the monkey was placed on the PET gantry with its head secured to prevent motion artifacts. Following a transmission scan, radiotracers were administered in a bolus dose over 1 minute (Table 2-4). Emission data were collected beginning with the injection and continued for 90 minutes.

Table 2-4:Collected data for all in vivo studies completed with(R,E/Z)-**[^{18}F]2.11** and (R,E/Z)-**[^{18}F]2.17a**.

Summary of Animal studies of (*R,E/Z*)-[^{18}F]2.11 and (*R,E/Z*)-[^{18}F]2.17a							
	Rat 1048	Rat 1050	Mnky 315	Mnky 331	Mnky 313	Mnky 333	Rat 1104
Form	**(*R,E/Z*)-[^{18}F]2.11**	**(*R,E/Z*)-[^{18}F]2.17a**	**(*R,E/Z*)-[^{18}F]2.11**	**(*R,E/Z*)-[^{18}F]2.11**	**(*R,E/Z*)-[^{18}F]2.17a**	**(*R,E/Z*)-[^{18}F]2.17a**	**(*R,E/Z*)-[^{18}F]2.11** (w/Pgp block)
Weight (g)	289	279	7929	8680	7935	8620	359
Amount Injected	0.479	0.413	4.197	4.6	3.904	2.5	0.422
Volume (mL)	0.3	0.28	4.2	2.4	2.5	4.4	0.5
Time @ EOS	9:50	10:00	10:04	10:15	10:21	10:25	10:22
Time @injection	10:52	10:43	10:24	10:21	11:15	10:32	10:38
Time difference (min)	62	43	20	6	54	7	16
Decay corrected dose injected (mCi)	0.71	0.54	4.76	4.78	5.49	2.61	0.47
Specific Activity (Ci/mmol)	1700	30	1700	1700	30	30	1700
MW (g/mol)	415.16	443.5	415.16	415.16	443.5	443.5	415.16
Injected Mass (ug)	0.17	8.01	1.16	1.17	81.11	38.63	0.11

Image Analysis

Upon completion of the PET scans, emission data were corrected for decay, dead time and random coincidences before reconstruction using an iterative ordered subset expectation maximization–maximum a posteriori (MAP) method to generate

reconstructed images. Frames were summed, smoothed, and regions-of-interest (ROIs) were defined manually for the whole brain over multiple adjacent frames in the sagittal projection. The volumetric ROIs were then applied to the full dynamic data sets to obtain regional tissue time-radioactivity data. Standardized uptake values (SUVs) were calculated for each region of interest.

D. References

(1) Knutsen, L. J. S.; Andersen, K. E.; Lau, J.; Lundt, B. F.; Henry, R. F.; Morton, H. E.; Nærum, L.; Petersen, H.; Stephensen, H.; Suzdak, P. D.; Swedberg, M. D. B.; Thomsen, C.; Sørensen, P. O. *J. Med. Chem.* **1999**, *42* (18), 3447–3462.

(2) Andersen, K. E.; Braestrup, C.; Grønwald, F. C.; Jørgensen, A. S.; Nielsen, E. B.; Sonnewald, U.; Sørensen, P. O.; Suzdak, P. D.; Knutsen, L. J. S. *J. Med. Chem.* **1993**, *36* (12), 1716–1725.

(3) Andersen, K. E.; Sørensen, J. L.; Huusfeldt, P. O.; Knutsen, L. J. S.; Lau, J.; Lundt, B. F.; Petersen, H.; Suzdak, P. D.; Swedberg, M. D. B. *J. Med. Chem.* **1999**, *42* (21), 4281–4291.

(4) Jorgensen, A. S.; Andersen, K. E.; Sonnewald, U. Novel N-substituted azaheterocyclic carboxylic acids. EP 0 374 801 A2, 1989.

(5) Andersen, K. E.; Lau, J.; Lundt, B. F.; Petersen, H.; Huusfeldt, P. O.; Suzdak, P. D.; Swedberg, M. D. B. *Bioorg. Med. Chem.* **2001**, *9*, 2773–2785.

(6) Andersen, K. E.; Begtrup, M.; Chorghade, M. S.; Lee, E. C.; Lau, J.; Lundt, B. F.; Petersen, H.; Sorensen, P. O.; Thogersen, H. *Tetrahedron* **1994**, *50* (29), 8699–8710.

(7) Andersen, K. E.; Sorensen, J. L.; Lau, J.; Lundt, B. F.; Petersen, H.; Huusfeldt, P. O.; Suzdak, P. D.; Swedberg, M. D. B.; Sørensen, J. L. *J Med Chem* **2001**, *44* (13), 2152–2163.

(8) Seth, A.; Sharma, P. A.; Tripathi, A.; Choubey, P. K.; Srivastava, P.; Tripathi, P. N.; Shrivastava, S. K. *Med. Chem. Res.* **2018**, *27* (4), 1206–1225.

(9) Quandt, G.; Höfner, G.; Wanner, K. T. *Bioorganic Med. Chem.* **2013**, *21* (11), 3363–3378.

(10) Høg, S.; Greenwood, J. R.; Madsen, K. B.; Larsson, O. M.; Frølund, B.; Schousboe, A.; Krogsgaard-Larsen, P.; Clausen, R. P. *Curr Top Med Chem* **2006**, *6* (17), 1861–1882.

(11) Sowa, A. R.; Brooks, A. F.; Shao, X.; Henderson, B. D.; Sherman, P. S.; Arteaga, J.; Stauff, J.; Lee, A. C.; Koeppe, R. A.; Scott, P. J. H.; Kilbourn, M. R. *ACS Chem. Neurosci.* **2018**. DOI: 10.1021/acschemneuro.8b00183.

(12) Palner, M.; Kornum, B. R.; Rahman, O.; Knudsen, G. M.; Hammarlund-udenaes, M.; Applied, U.; Systems, G. P. E. T.; Healthcare, G. E. **2009**, *37* (3), 635–643.

(13) Shao, X.; Carpenter, G. M.; Desmond, T. J.; Sherman, P.; Quesada, C. A.; Fawaz, M.; Brooks, A. F.; Kilbourn, M. R.; Albin, R. L.; Frey, K. A.; Scott, P. J. H. *ACS Med. Chem. Lett.* **2012**, *3* (11), 936–941.

(14) Wang, J. Q.; Zhang, Z.; Kuruppu, D.; Brownell, A. L. *Bioorganic Med. Chem. Lett.* **2012**, *22* (5), 1958–1962.

Chapter 3

Investigation of Bioisosteres for Improved BBB Permeability

A. Introduction

i. Use of Bioisosteres in Medicinal Chemistry

Bioisosteres have long been a strategy in the enhancement or diminution of different characteristics of a drug candidate when developing new therapeutics. First described as 'isosteres' by Langmuir in 1919, the word was used to describe categories of different functional groups, atoms and molecules sorted according to their physicochemical properties.[1] Six years after the publication of Langmuir's paper, Grimm's Hydride Displacement Law was presented (Table 3-1). This law stated that any atom up to four places to the right of a noble gas on the periodic table could bond one to four hydrogen atoms to form an isostere of the atom that many places to the left or right of

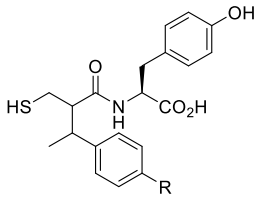

3.1, R = OH
3.2, R = F

R	ACE IC_{50} nM	NEP IC_{50} nM
OH	7.9	9.0
F	6.9	5.9

Figure 3-1: A fluorine (**3.2**) for hydroxy (**3.1**) replacement in the development of dual ACE & NEP inhibitors.

itself.[2] An example of this still used today is the bioisterism of an -OH group for a fluorine atom, as can be seen in the development of dual inhibitors of epithelial neutral endopeptidase (NEP) and endothelial angiotensin-converting enzyme (ACE) for the treatment of hypertension (Figure 3-1).[2,3] Replacing the hydroxyl group on **3.1**, with a

Table 3-1: Each column depicts a family of isosteres according to Grimm's Hydride Displacement Law.

C	N	O	F	Ne	Na
	CH	NH	OH	FH	-
		CH_2	NH_2	OH_2	FH_2^+
			CH_3	NH_3	OH_3^+
				CH_4	NH_4^+

fluorine atom (**3.2**), slightly improves the potency of this molecule (Figure 3-1). Oxygen is one place to the left of fluorine, a noble gas; oxygen bonded to one hydrogen can then serve as an isostere to fluorine. Erlenmyer aimed to expand Grimm's and Langmuir's definition of 'isostere' in 1932, when he proposed that the term be applied to elements, ions or molecules which have the same valence electrons.[4] This led to elements within the same columns of the periodic table being grouped as isosteres among themselves, as well as the grouping of electronically similar rings as ring isosteres. When these properties began to be used to modify and enhance molecules with biological activity the term 'bioisostere' was used; the term being coined in the early 1950s by Friedman[5] and later reevaluated by Thornber.[6] As with most terms in the scientific community, definitions of bioisostere can vary slightly depending on who is defining it, and Thornber argues that the term 'isostere' has become loosely defined, even as soon as 1979.[6] Friedman's original definition of 'bioisostere' was any "compounds [that]…fit the broadest definition for isosteres and have the same type of biological activity"[5]. In medicinal chemistry, it is generally understood that bioisosteres are a group of atoms or functional groups that have similar properties and when employed in a scaffold elicit a similar effect on the same biological target. These isosteres or bioisosteres can be sorted into classical and non-classical families.[2,6] Isosteres considered to be classical adhere to the original description

Table 3-2: Classical bioisosteric replacements.

Classical bioisosteres					
Monovalent	-F -H	$-NH_2$ -OH	-SH -OH	-F -Me -OH $-NH_2$	-Cl -Br -SH -OH
Divalent	-C=C- -C=O -C=N- -C=S	-C-C-C- -C-O-C- -C-NH-C- -C-S-C-			
Trivalent	-C-C=C- -C-N=C-				
Tetra substituted	$-C-NMe_3^+$ $-C-CMe_3$				
Ring Equivalents	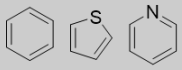				

of isosteres and are similar both electronically and sterically (Table 3-2). When isosteres/bioisosteres stray from this definition, it is considered non-classical bioisosterism. Bioisosteres in a non-classical family could differ in electronic behavior, shape, size, or even number of atoms. When bioisosteres are used for drug development it seems as though they are mostly non-classical, as some property of the molecule needs adjusting (e.g. lipophilicity, pKa, size, etc.) and therefore some property of the isosteric replacement must change as well. This is demonstrated in Figure 3-2. In the search for a more potent and less toxic muscarinic antagonist, researchers explored non-classical bioisosterism in using cyclic moieties in replacement of a non-cyclic moiety (the methyl ester on arecoline, **3.3**). Both the fused ring systems (**3.4**, **3.5**) and replacement of the ester with a heterocycle (**3.6-3.9**) resulted in compounds with affinity for muscarinic receptors (although the R values affected this in some cases).[2,7] Thornber also outlines that it is important to consider the roles which parts of molecules may have (structural, receptor interactions, pharmacokinetics, or metabolism); he points out that usually the role that a certain part of a molecule plays in its activity is unknown. Today, 40 years later, it is possible, through molecular modeling or evaluation of crystal structures, to determine

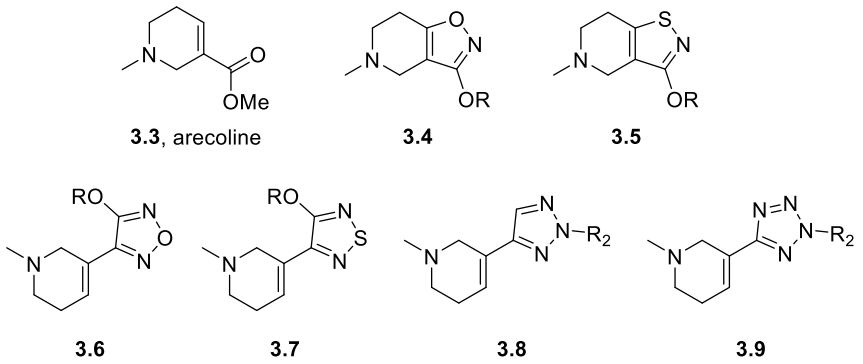

Figure 3-2: Non-classic bioisosteres in the development of a more potent muscarinic agent.

not only the role a certain part of a molecule plays in its biological activity, but also how much that certain moiety can change before interactions and therefore activity is lost. Whereas Langmuir was concerned with finding isosteres that behaved more or less the same, the best bioisosteres are those that remain *almost* the same, fine tuning specific characteristics for a pharmacological need.[1,6] The use of bioisosteres is common in the development of novel drugs and in improving existing drugs. They can be used to block metabolically labile sites, encourage solubility, or limit toxicity.

As would be expected, the most commonly used bioisosteres correspond to functional groups that are found often in biologically relevant molecules. These include carboxylic acids, alcohols, aryl and hetero rings, carbonyls, and even hydrogen itself. As a functional group present in a plethora of endogenous and exogenous substrates, carboxylic acid is of particular interest in drug design and therefore bioisosteric replacement. Many studies and reviews have been completed to better understand what affects bioisosteres have the molecules compared with a carboxylic acid. One such study sought to provide a more comprehensive data set for carboxylic acid bioisosteres.[8] In this research, Ballatore and coworkers chose a simple molecule, phenylpropionic acid, and exchanged the carboxylic acid for various bioisosteres, recording chemical characteristics

of each one, either calculated or experimental, enabling the reader to make informed decisions on which bioisostere fits their need. The comparison of over 30 bioisosteres on a single scaffold is incredibly helpful to evaluate the specific effect each of these bioisosteres has on the molecule as a whole. Another of the same group's papers is more traditional in its review and includes specific examples of where bioisosterism was employed successfully.[9] Of note are the angiotensin II type 1 (AT1) receptor antagonists, the development of which used bioisosterism to both increase potency, but also to increase oral bioavailability, as seen in Figure 3-3. Replacement of the carboxylic acid moiety on **3.10**, with a tetrazole group (**3.11**) shows a 10-fold increase in potency (0.23 μM to 0.019 μM) and a drastic improvement of oral bioavailability (dosing decreased from 11 mg/kg to 0.59 mg/kg).

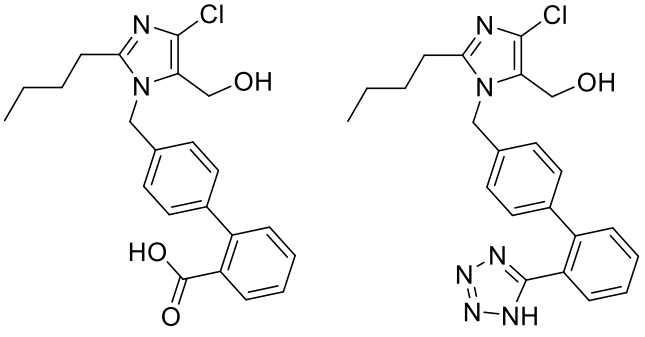

	3.10	**3.11**
IC_{50}	0.23 uM	0.019 uM
Oral dose	11 mg/kg	0.59 mg/kg

Figure 3-3: AT1 receptor antagonists and their respective inhibition and dosing.

ii. Use of Bioisosteres in PET

Bioisosteres are also highly important in the development of PET radiotracers as the design of radiotracers, although very similar to the design of therapeutics, necessitates very specific parameters. Firstly, it is important that the biological half-life of

the bioactive molecule matches with the half-life of the radionuclide on the radiotracer. Secondly, it is best for both physician and patient if the molecule reaches its target in a short amount of time, is biologically available at a microdose, and it is necessary that the tracer can achieve these goals without the need for titration of doses. Regulations require small amounts of radiotracer be used for PET imaging, so it is very important that the drug is highly specific and selective for its target. It is also necessary to be able to radiolabel the molecule without altering its biological properties; this is where bioisosteric replacement is used the most.

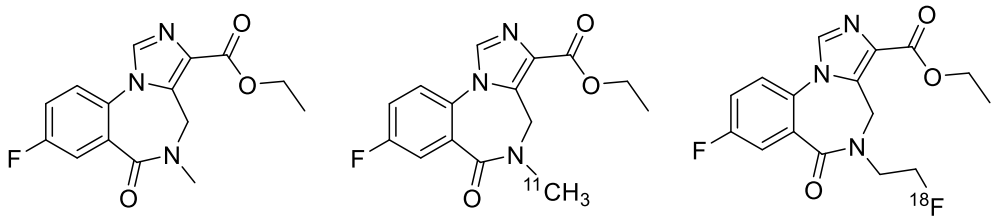

3.12, Flumazenil (FMZ)

[^{11}C]3.12, [^{11}C]FMZ

[^{18}F]3.13, [^{18}F]FEFMZ

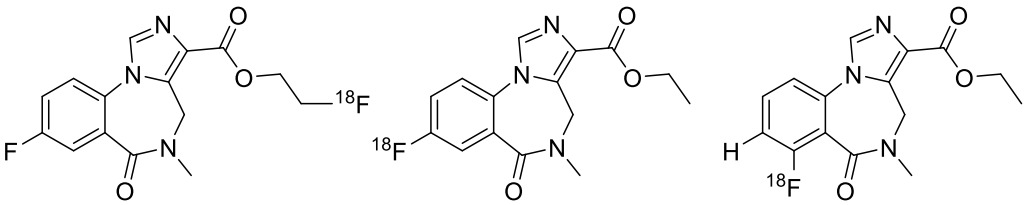

[^{18}F]3.14, [^{18}F]FFMZ

[^{18}F]3.12, [^{18}F]FMZ

[^{18}F]3.15, [^{18}F]AH114726

Figure 3-4: FMZ and related radiotracers.

One of the most common bioisosteric replacements in PET is to substitute a group (or atom) for a fluorine, specifically [^{18}F]fluorine; this is due to the ideal half-life (110 minutes) and availability of [^{18}F]fluorine (can be produced on site, or delivered to radiochemistry facilities) as previously described.[10] Fluorine can be used to replace another halogen, such as chlorine, or hydrogen or hydroxyl groups. Notably however, it is important to evaluate the biological activity of the radiolabeled molecule, as the fluorine may alter it. In some cases, bioisosterism can make the radiochemical synthesis of a

radiotracer more straight forward, as well as improve the properties of the radiotracer. Consider the flumazenil (**3.12**) derivatives shown in figure 3-4. The fluorinated derivative, [^{18}F]FFMZ (**[^{18}F]3.14**) was developed with the belief that the fluorine could be placed on the ester as a bioisostere. Unfortunately, both [^{18}F]FFMZ and [^{18}F]FEFMZ (**[^{18}F]3.13**) did not display satisfactory characteristics *in vivo* when compared to [^{11}C]FMZ.[11,12] At this point [^{18}F]FMZ (**[^{18}F]3.12**), an isotopolog of FMZ had been developed, but reported syntheses gave yields below 10%.[13] With the desire for another [^{18}F]fluorine labeled benzodiazepine related PET tracer, AH114726 was adapted for radiolabeling by Rodnick and coworkers.[12] It can be said that the relocation of the aryl fluorine substituent to the *ortho* position relative to the carbonyl gives a bioisosteric structural isomer. This allows a simplified S_NAr [^{18}F]fluorination of a precursor, increases the yield up to 24%, and the radiotracer exhibits similar activity to [^{11}C]FMZ.[12] In this case, a bioisostere in the right location on the molecule helped to preserve characteristics of the parent molecule as well as allow for translation of the scaffold into PET imaging. This speaks both to the necessity of re-evaluation of a tracer after bioisosterism, as well as suggests that protons on an aromatic ring are tolerant of substitution with fluorine.

B. Evaluation of [^{11}C]-labeled GABA Analogs

i. Radiochemical Syntheses of [^{11}C]-Nipecotic Acid and Ester

In the development of a GAT-1 selective radioligand, thus far, the candidates have not been found to be BBB permeable. It is known that the lipophilic side chain of tiagabine

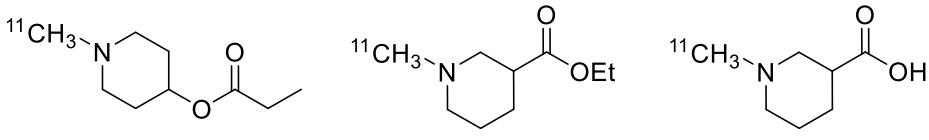

3.16, [^{11}C]PMP **[^{11}C]3.17** **[^{11}C]3.18**

Figure 3-5: Small molecule [^{11}C]-labeled radiotracers, [^{11}C]PMP, **[^{11}C]3.17**, and **[^{11}C]3.18**.

and related molecules assists in brain penetration at high doses titrated over weeks,[14] however, as found in Chapter 2, these molecules lack the brain penetration to be successful CNS PET tracers. To test our hypothesis that the carboxylic acid moiety is inhibiting the BBB penetration, both nipecotic acid (**3.20**) and ethyl nipecotate ester (**3.19)**

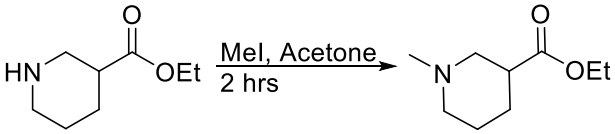

3.19 **3.17**

Scheme 3-1: Synthesis of the reference standard **3.17**.

were *N*-methyl-[^{11}C]-methylated (Scheme 3-1) to generate **[^{11}C]3.18** and **[^{11}C]3.17**, respectively, for evaluation *in vivo*. The simple molecule nipecotic acid was chosen to be evaluated as it is both the active moiety of the GAT-1 inhibitors, but also contains the potentially problematic carboxylic acid functional group. It was expected that *N*-methyl nipecotic acid should not cross the BBB while the *N*-methyl ethyl nipecotate ester should be BBB permeable due to increased lipophilicity. Previous work done in this area includes the *N*-[^{11}C]-methylation of nipecotic acid in the search for an appropriate radiotracer for acetylcholinesterase (AChE);[15,16] this work ultimately led to the selection of 1-[^{11}C]methylpiperidin-4-yl propionate ([^{11}C]PMP, **[^{11}C]3.16**) for the imaging of AChE.

The precursor for both the acid and ester radiotracers **[^{11}C]3.17** and **[^{11}C]3.18** was the commercially available ethyl ester nipecotate, **3.19**. Reference standard N-methyl nipecotic acid (**3.18**) was also purchased, and the N-methyl ether ester nipecotate (**3.17**) was prepared in 20% yield by simple N-methylation with methyl iodide (Scheme 3-1). The

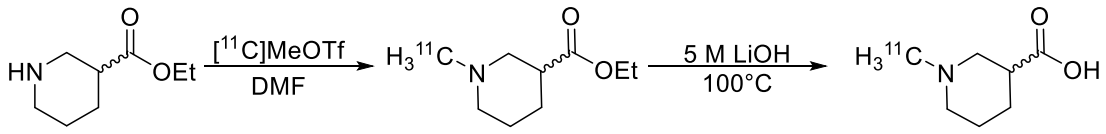

3.19 **[^{11}C]3.17** **[^{11}C]3.18**

Scheme 3-2: Radiochemistry for the preparation of **[^{11}C]3.17** and **[^{11}C]3.18**.

poor UV absorbance of these molecules (at typical HPLC wavelengths, 220, 254, 280 nm) required additional development of HPLC methods and the use of an ion chromatography system equipped with an electrochemical detector for analysis. The ester precursor and standard were visible at 220 nm (Figure 3-16), and an HPLC equipped with an ion-detector was used for the analysis of the N-methyl nipecotic acid as it was not visible by the HPLC UV lamp (Figure 3-19). Both molecules (ester, **[^{11}C]3.17** and acid, **[^{11}C]3.18**) were produced successfully using [^{11}C]MeOTf prepared in a TracerLab $FX_{C\text{-}Pro}$ synthesis module (Scheme 3-2). In the production of **[^{11}C]3.18**, hydrolysis took place immediately after methylation with 5M LiOH at 100°C. Purification on a semi-preparative HPLC in ethanolic buffer gave an injectable dose.

ii. *In vivo* evaluation of [^{11}C]-N-Methyl Nipecotic Acid and Ethyl Ester

These radiotracers were evaluated in Sprague-Dawley rats (n=2 for each molecule) to observe the effects *in vivo*. In initial evaluation of (*R/S)*-**[^{11}C]3.18** in rat, a female Sprague-Dawley rat (369 g) was injected with (*R/S*)-**[^{11}C]3.18** (0.489 mCi) i.v. via tail vein injection. After the rat was scanned for 60 min post-injection of the radiotracer (see experimental section for detailed scanning procedure) [^{11}C]N-methyl nipecotic acid (**[^{11}C]3.18**), which has been studied previously,[16] demonstrated no brain uptake as expected (Figure 3-6). Following our hypothesis that the carboxylic acid was inhibiting

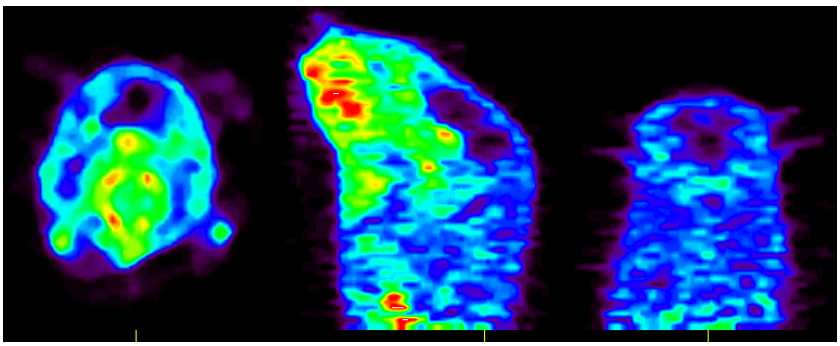

Figure 3-6: Results from in vivo evaluation of (R/S)-**[^{11}C]3.18** in rodent.

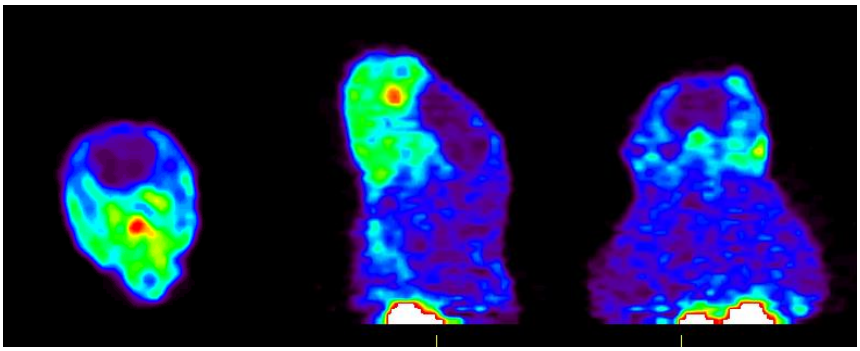

Figure 3-7: Results from in vivo evaluation of (R/S)-**[^{11}C]3.17** in rodent.

brain uptake of (*R/S*)-**[^{11}C]3.18**, the ester form, (*R/S*)-**[^{11}C]3.17** was then isolated and evaluated in rodent (287 g, 0.505 mCi dose i.v. via tail vein injection). We were surprised to also observe lack of brain uptake for ester (*R/S*)-**[^{11}C]3.17** (Figure 3-6). This was surprising not just because of the increased lipophilicity but also because of the fact that it is identical in molecular weight and has a similar structure to [^{11}C]PMP (**3.16**), which is brain penetrant. These results along with the comparison of the N-methyl nipecotic acid to the normally accepted parameters for a successful CNS drug candidate (Table 3-3) led us to investigate whether the use of a carboxylic bioisostere may increase BBB permeability of these GAT-1 inhibitors.

Table 3-3: Comparison of properties of N-methyl nipecotic acid and nipecotate ester.

Property	Typical value for successful CNS drugs	N-methyl nipecotic acid, 3.18	N-methyl nipecotate ester, 3.17
clogp	1.5-2.7	-1.65	0.88
clogD$_{7.4}$	0-3	-1.62	-.27
tPSA	60-90	40.54 Å	29.54
Molecular Weight	≤400-600 g/mol	143 g/mol	171 g/mol
heteroatoms (O+N)	≤5	3	3
Acidic pKa	>4	3.22	N/A
Basic pKa	<10	9.60	8.65

C. BIOISOSTERISM OF NIPECOTIC ACID

As a large neuronal network with a wide range of therapeutic possibilities, it is unsurprising that the GABAergic system has been the subject of a number of bioisosterism studies.[17–22] Some of these molecules incorporate bicyclic systems based on natural products such as muscimol.[23] Others remain closer to more classical bioisosteres, mainly for a carboxylic acid, such as sulfonamides and hydroxamic acids.[9,19] To move forward with the development of a brain-permeable GAT-1 radiotracer, a number of carboxylic acid bioisosteres were considered. A common bioisostere for carboxylic acids, hydroxamic acid was briefly considered, but the acidity and susceptibility of the moiety to be charged at physiological pH made its qualities too alike to a carboxylic acid and we reasoned hydroxamic derivatives could have difficulties crossing the BBB. Sulfonamides offer another option for the replacement of a carboxylic acid (Table 3-4, entry 4, **3.22**). They were one of the first employed in the improvement in drug design as demonstrated by their use in a class of antibacterial agents.[9] The isomeric ß-alanine

Table 3-4: Select bioisosteres of nipecotic acid.

	Entry	Molecule	Name	ClogP	Included in assay?
3.20	1	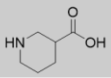	Nipecotic acid	-2.20	Y
3.19	2	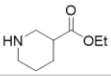	Ethyl nipecotate ester	1.06	Y
3.21	3	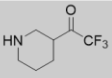	Trifluoromethyl ketone	0.79	N
3.22	4	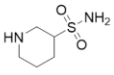	Sulfonamide	-0.93	Y
3.23	5	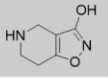	THPO	-0.39	Y
3.24	6	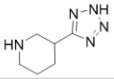	Tetrazole	-0.33	Y
3.25	7	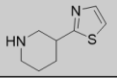	Thiazole	0.837	N

analogue 4,5,6,7-tetrahydroisoxazolo[4,5-c]pyridin-3-ol (THPO, Table 3-4, entry 5, **3.23**), one of the bicyclic systems based on the natural product muscimol, was also a viable

Table 3-5: Results from [^{3}H]GABA uptake inhibition assay using rat brain homogenate.

	Name	% inhibition	normalized to tiagabine
3.22	Sulfonamide	4	14.29
3.23	THPO	-6	-21.43
3.24	Tetrazole	9	32.14
3.19	Nipecotate Ester	-4	-14.29
3.18	N-methyl Nipecotic acid	-3	-10.71
	Tiagabine	28	100.00
	Unsymmetrical ester	8	28.57
	Unsymmetrical Acid	2	7.14

option displaying both the planar shape of a carboxylic acid and containing the necessary hydrogen bond donor in the hydroxy group.[19,24,25] Tetrazoles, such as **3.24**, entry 6 in Table 3-4, are one of the most commonly used bioisosteres for carboxylic acid, given the acidic proton and planar shape of the moiety. They are slightly larger than the carboxylic acid group, but also have an increased lipophilicity desirable for BBB penetration.[9] Another bioisostere, not commercially available, but which has been claimed to be made in a patent,[26] is the trifluromethyl ketone of nipecotic acid (Table 3-4, entry 3, **3.21**). The trifluoromethyl ketone offers higher lipophilicity with weak acidic character that could helpful in the development of a BBB permeable molecule. A variety of routes were attempted to obtain this bioisostere, but unfortunately these were unsuccessful.[27–29]

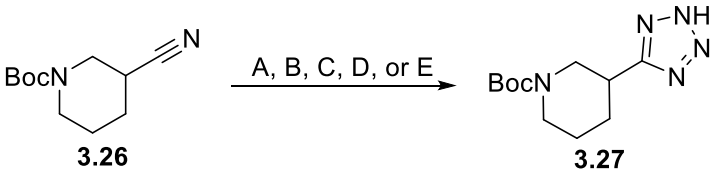

3.26 3.27

A. NaN_3, I_2, DMF, 120°C
B. NaN_3, $ZnCl_2$, THF, 70°C
C. NaN_3, $ZnCl_2$, IPA:H_2O, 80°C
D. NaN_3, TEA·HCl, NMP, 140°C
E. NaN_3, DMF, 100°C, 48 h

Scheme 3-3:Multiple methods for production of tetrazoles from a cyano starting material.

Three commercially available bioisosteres (sulfonamide, THPO, and tetrazole, entries 4, 5 and 6 in Table 3-4) were chosen for evaluation in an assay run by Cerep PanLabs. In this uptake inhibition assay the compounds were tested for their ability to inhibit uptake of [^{3}H]GABA in rat brain homogenate. The three bioisosteres were submitted alongside tiagabine, the unsymmetrical molecules discussed in Chapter 2 as well as ethyl nipecotate ester. For preliminary data, only one concentration of each sample was run in duplicate. This assay returned interesting results (Table 3-5). Normalizing the inhibition concentrations to the value reported to tiagabine (the internal positive standard), it is found that the tetrazole gives the best inhibition in this assay encouraging further investigation of this bioisostere. Moving forward, various routes were attempted for the synthesis of a precursor and standard of the tetrazole containing molecule. While commercially available, development of a radiochemical synthesis, including *in vitro* validation required a larger amount of material, and, assuming it is synthetically accessible via an in-house synthesis, this would be the more economical route. While ^{13}C-carbon NMR did confirm the production of the tetrazole (Scheme 3-3, Figure 3-8), the separation of the tetrazole from the cyano-piperidine proved difficult due to the delicate balance of pK_as of the tetrazole (~5.0) and piperidine (~9.0). Purification

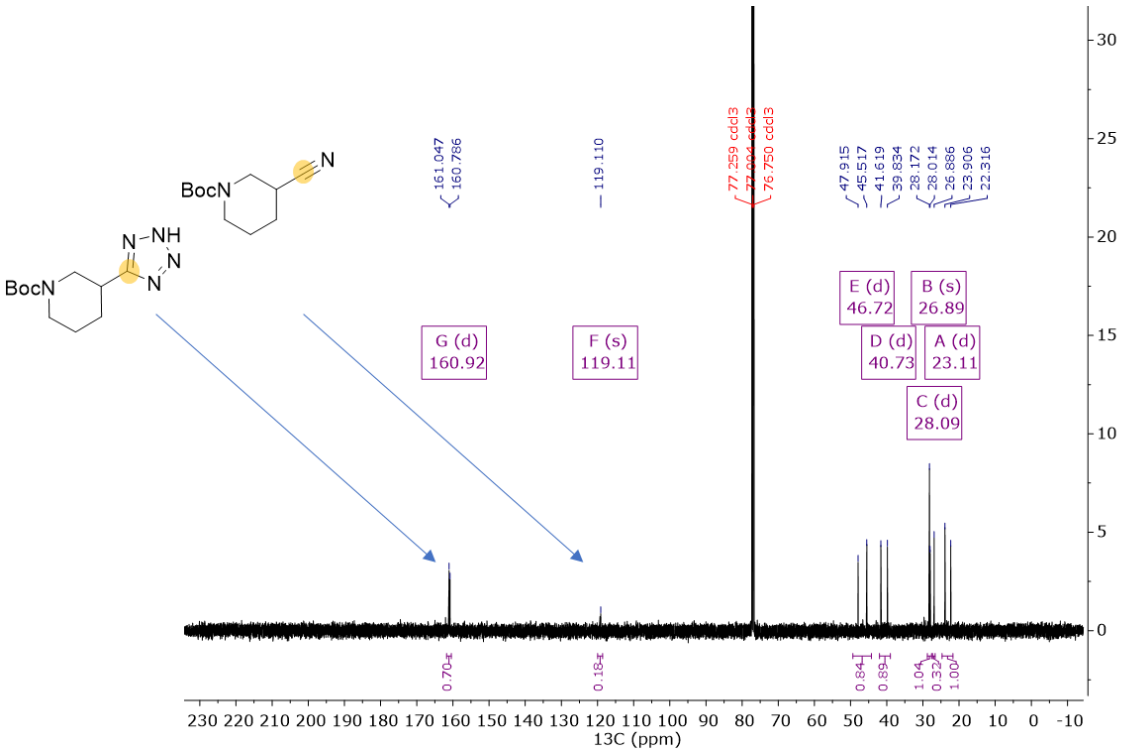

Figure 3-8: ^{13}C-NMR spectra of a inseparable mixture of cyano (120 ppm) and tetrazole (160 ppm).

efforts ranges from attempted flash column chromatography with varied solvent systems (Hex:EtOAc, Hex:EtOAc+ 0.5% TEA, DCM:MeOH, EtOAc:MeOH), as well as pH manipulation during work up of the reaction. Both acidification and basification of the aqueous layer of the reaction resulted in the extraction of a mixture of starting material and product in the organic layer, as evident by crud TLC as well as ^{13}C-NMR (Figure 3-8). Synthesis attempts of this and other bioisosteres can be found in the experimental section of this chapter.

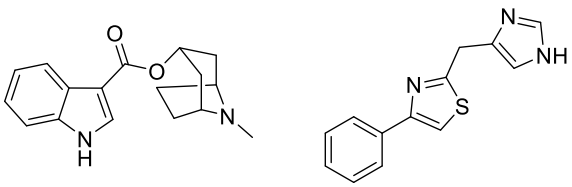

3.28, K_i = 2.7 nM

3.29, K_i = 1.0 nM

Figure 3-9: Example of thiazolyl bioisosterism in the development of 5-HT$_3$ receptor antagonists.

Stemming from the assay success (and elusive promise) of the tetrazole, another heterocycle, thiazole, was investigated. Thiazolyls have been successfully incorporated into CNS agents, including those targeting dopamine receptors.[30] They have also been used as bioisostere for a carbonyl group in serotonin receptor subtype 3 (5-HT_3) antagonists.[31] Rosen and colleagues were able to replace a carbonyl moiety, which participates in binding to 5-HT_3 receptors, with a thiazolyl linker, and maintained activity and selectivity over other serotonin receptors, as well as other receptors and binding sites in the brain (Figure 3-9). These reported results led to the investigation of a thiazolyl piperidine as a possible bioisostere for the acid functionality of nipecotic acid in the development of a GAT-1 selective radiotracer.

D. Thiazole For Use as a Bioisostere of Nipecotic Acid

i. Radiochemical Synthesis

The precursor 3-(1,3-thiazol-2-yl)piperidine (**3.30**) is commercially available and was purchased from Enamine. This bioisostere was then evaluated *in vivo* similar to the evaluation of N-methyl nipecotic acid and ester described earlier. To do this, the reference standard was synthesized via a simple N-methylation (Scheme 3-4). An HPLC method was developed for the semi-preparative purification of the product, and then the analysis of the identity of that product in the final dose form. Initially, an ethanolic buffer system was used for both semi-preparative and analytical HPLC. Although successful in

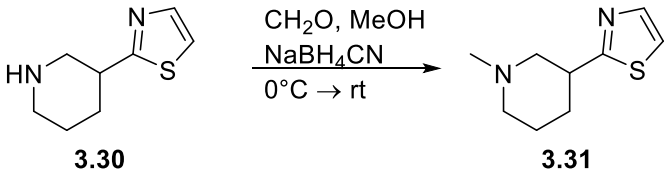

3.30 **3.31**

Scheme 3-4: Methylation for formation of thiazolyl reference standard.

separating the product, the peaks were broad, and the radiochemical yields were low using this system. Switching to an acetonitrile eluent, buffered with ammonia, the peaks were much sharper (Figure 3-21) and yields >100 mCi in the final, injectable dose were obtained (HPLC parameters can be found in the experimental section of this chapter).

The piperidinyl thiazole precursor was labeled with [^{11}C]MeOTf prepared in a TracerLab FX$_{C\text{-}Pro}$ as described previously. After methylation the reaction mixture was diluted with semi-preparative HPLC buffer and injected onto a semi-preparative Gemini NX C18 250 x 10 mm HPLC column. The product peak was collected and diluted in 50 mL milliQ water. The product was then trapped on a 1cc Vac C18 cartridge; the cartridge was rinsed with further milliQ water, and the product eluted with ethanol followed by saline. This purified and reformulated dose was then transferred to a sterile 10 mL vial (assembled aseptically, and with a sterile filter for NHP studies). RCYs of [^{11}C]**3.31** were 131 ± 62 mCi at EOS, corresponding to 15% non-corrected radiochemical yield (n = 6). Radiochemical purity was >99%, produced in high specific activity (>2500 Ci/μmol).

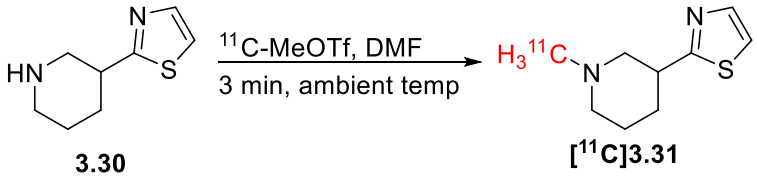

3.30 **[^{11}C]3.31**

Scheme 3-5: [^{11}C]Methylation of the commercially available thiazole to produce [^{11}C]N-methyl piperidinyl thiazole.

ii. *In Vivo* Evaluation of [^{11}C]-N-methyl Thiazolyl Piperidine

This novel radiotracer (**[^{11}C]3.31**) was first evaluated *in vivo* to determine whether the substitution of the carboxylic acid with a thiazole resulted in a BBB permeable molecule. As with the other radiotracers discussed within, the tracer was first evaluated in Sprague-Dawley rats. A female Sprague-Dawley rat (425 g) was injected with **[^{11}C]3.31** (0.50 ± 0.04 mCi) i.v. via tail vein injection. The rat was scanned for 60 min post-injection of the radiotracer (see experimental section for detailed scanning procedure). Compared to the rat images produced with [^{11}C]-N-methyl nipecotic acid **3.18** and ester **3.17**, the thiazole displayed excellent brain uptake (Figure 3-10). Whole brain time-radioactivity curves (Figure 3-11) revealed a peak standardized uptake value (SUV) of 4. Encouraged

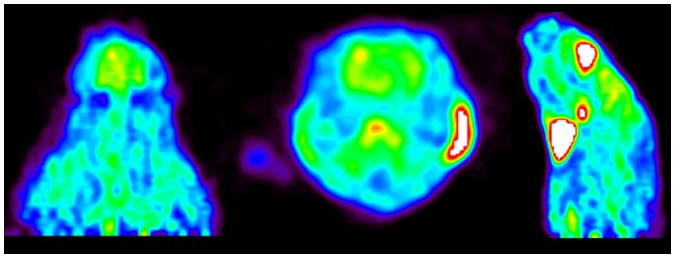

Figure 3-10: Results of in vivo evaluation of **[^{11}C]3.31** in rodent.

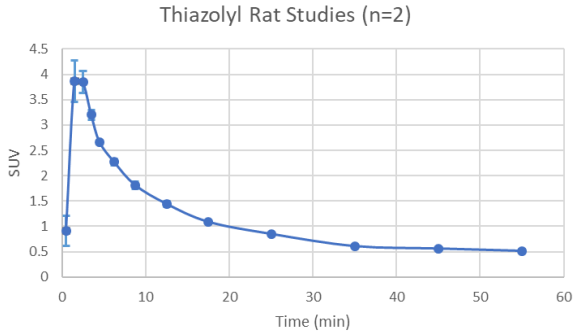

Figure 3-11: Average time activity curve for 2 rodent studies with standard deviation bars.

by this success the radiotracer was also evaluated in non-human primates. Imaging studies were performed in a young, mature female rhesus monkey and radiotracer

[^{11}C]3.31 (4.56 ± 0.44 mCi) was injected i.v. via a venous catheter inserted into one hind limb of the monkey. The monkey was scanned for 60 min and the images also revealed high brain uptake of the radiotracer (Figure 3-12). Time-radioactivity curves (Figure 3-13) revealed a whole brain SUV of 4, and the patterns displayed in the brain suggest uptake of the tracer in the cortex and striatum, where GABA neurons are known to be highly expressed.[32]

iii. *In vitro* Evaluation of [^{11}C]-N-methyl Thiazolyl Piperidine

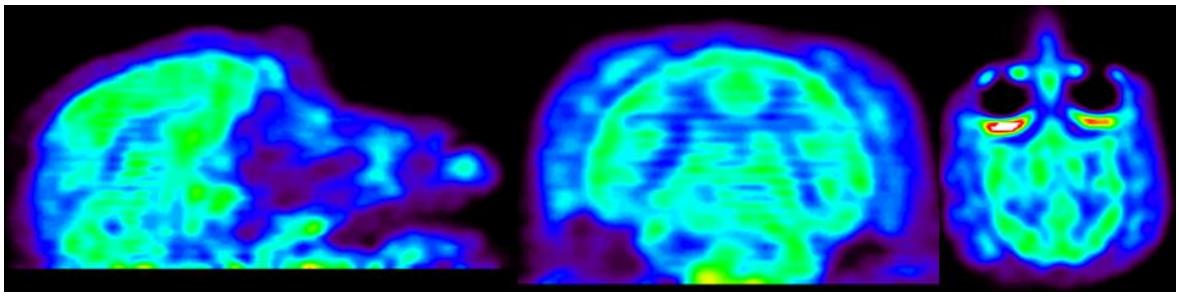

Figure 3-12: Results of in vivo evaluation of **[^{11}C]3.31** in NHP.

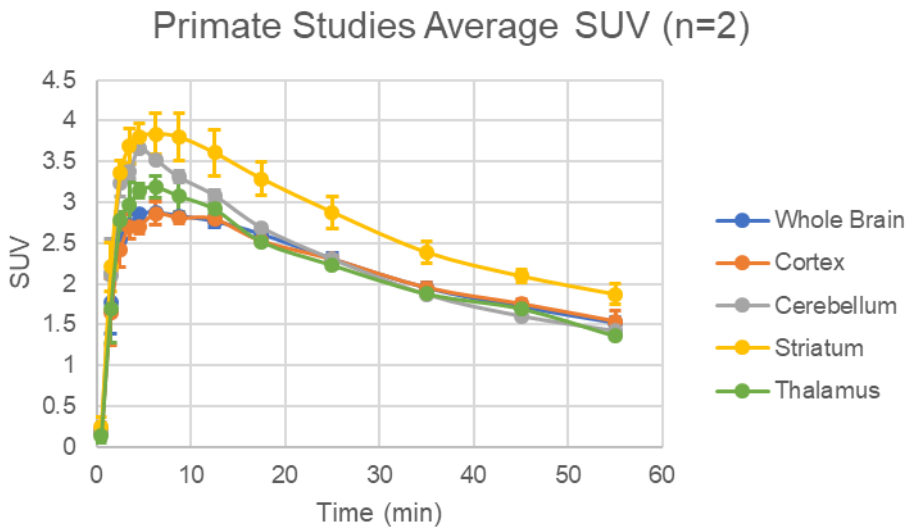

Figure 3-13: Regional and whole brain TACs showing enhanced uptake in the striatum of **[^{11}C]3.31**.

Radiotracer **^{11}C]3.31** displayed excellent brain uptake and appeared to be localizing to areas of higher GAT-1 expression. Thus, we undertook in vitro studies to

confirm affinity of **3.31** for the GAT-1 target. This was investigated through a series of *in vitro* experiments: immunohistochemistry (IHC) with GAT-1 specific antibodies to confirm presence of the target in the tissue samples, and autoradiography with **[^{11}C]3.31** to confirm colocalization of radiotracer binding with IHC. Frozen rat brain was sliced into 20 µm slices on a microtome and mounted onto slides and placed into a -80°C freezer until the time of the assay. Radiotracer **[^{11}C]3.31** was prepared as described above and diluted to proper concentration, 25 nM, for the assay at hand.

These studies commenced with staining brain slices (human and rat) with anti-GAT-1 antibodies to confirm the presence of GAT-1 in the tissue type (rat vs human) and area of brain being used. Once the target (GAT-1 in this case) was confirmed in the tissue, adjacent slices of tissue were employed for autoradiography studies using both the labeled radiotracer and the cold reference standard. The first study was to determine the time needed to get saturation of the tissue/target with the radiotracer. Tissue slices (on slides, but not fixed) were incubated in a solution containing 25 nM concentration of the of the tracer along with a smaller dilution (10 µM) of cold standard, and a separate set of slides are incubated in a solution with radiotracer and a 1000x fold (10 mM) reference standard. The tissues incubated for different amounts of time (2, 5, 10, 15, and 30 minutes) before the slide is rinsed/washed, and the tissue is wiped off the slide and placed into a vial for measurement with a scintillation/gamma counter. The cold reference standard is included in this study to determine (roughly) any amount of non-specific binding. This will give the equilibration/saturation time of the tissue with the radiotracer so that subsequent studies can be timed accordingly.

This study is then repeated again for determination of K_D and B_{max}, only this time, slides were incubated for 15 minutes in an increasing concentration of cold reference standard with 25 nM tracer. The slides were then removed from solution, rinsed with additional PBS, and dried on a hot plate at for 5 minutes. The slides were then placed in an autoradiograph developing cassette for 5 minutes, before imaging with a Fujifilm BAS-1800 Bioimaging Analyzer System. Scatchard analysis of the resulting data allows for the calculation of dissociation constant (K_D) and binding potential (B_{max}) (Figure 3-14, inset). This initial study gives a K_D of 2.26±0.46 nM and a B_{max} of 0.34± 0.03 fmol/µg protein.

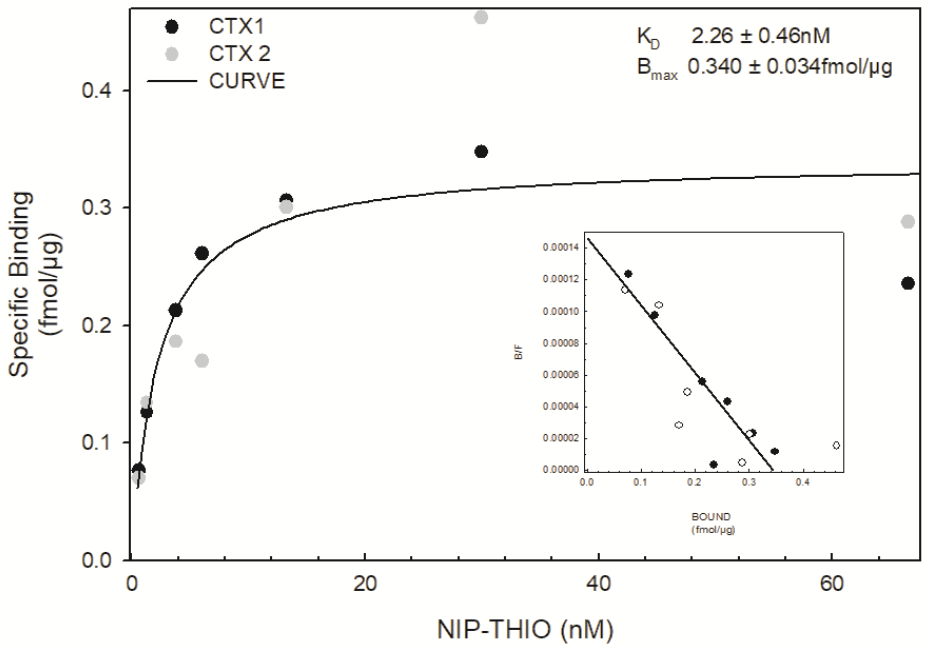

Figure 3-14: Saturation binding curve resulting from preliminary in vitro studies, and Scatchard analysis (inset) to determine K_D and B_{max} of **[^{11}C]3.31**.

E. Experimental Methods

i. Chemistry Methods

Ethyl 1-methylpiperidine-3-carboxylate (**3.17**, reference standard, Scheme 3-1)

A 1.0 M solution of nipecotate (*R,S*)-**3.21** (500.0 mg, 3.18 mmol, 1.0 equiv.) in THF (0.7 mL) was prepared in a flame-dried flask. Iodomethane (541.6 mg, 0.24 mL, 3.81 mmol, 1.2 equiv) was added dropwise and the reaction was allowed to stir for 3-4 hours at room temperature. Upon completion, the reaction was quenched with aq. $NaHCO_3$, and extracted with diethyl ether. The organic layer was dried ($MgSO_4$), filtered and concentrated to give the title compound.

Yield: 98.5 mg (18 %) as a clear oil.

^1H NMR (400 MHz, $CDCl_3$) δ 4.06 (q, J = 7.1 Hz, 2H), 2.93 – 2.80 (m, 1H), 2.65 (m, 1H), 2.52 (ddt, J = 11.1, 10.3, 3.9 Hz, 1H), 2.22 (s, 3H), 2.05 (t, J = 10.8 Hz, 1H), 1.89 (m, 2H), 1.71 – 1.62 (m, 1H), 1.62 – 1.46 (m, 1H), 1.35 (m, 1H), 1.18 (t, J = 7.2 Hz, 3H).

^{13}C NMR (101 MHz, $CDCl_3$) δ 174.08, 60.33, 57.37, 55.62, 46.54, 41.88, 26.37, 24.63, 14.18.

HRMS: M^+ predicted m/z = 171.1259, actual m/z = 171.1332.

Thiazole chemistry:

Cold reference standard (**3.31**) was synthesized by N-methylation of commercially available 3-(1,3-Thiazol-2-yl)piperidine (**3.30**).

2-(1-methylpiperidin-3-yl)thiazole (3.31, Scheme 3-4)

Method A: 3-(1,3-Thiazol-2-yl)piperidine (**3.30**, 163.5 mg, 0.97 mmol, 1.0 equiv) was dissolved in THF (1.35 mL). To it, methyl iodide (0.07 mL, 165.5 mg, 1.16 mmol, 1.2 equiv) was added dropwise. The reaction was stirred at room temperature until starting material was consumed. Upon completion, the reaction was quenched with aq. $NaHCO_3$, and extracted with diethyl ether. The organic layer was dried ($MgSO_4$), filtered and concentrated. Crude product contained side products and starting material. Purification attempts via flash column chromatography were not successful.

Method B: 3-(1,3-Thiazol-2-yl)piperidine (**3.30**, 100.0 mg, 0.59 mmol, 1.0 equiv) was dissolved in MeOH (0.6 mL) and cooled to 0°C. To it was added formaldehyde (0.22 mL of 30% aqueous solution, 1.78 mmol, 3.0 equiv). Keeping the reaction at 0°C, $NaBH_4CN$ (73.7 mg, 1.17 mmol, 2.0 equiv) was added portion wise. The reaction was allowed to come to room temperature and stir overnight. Upon consumption of starting material, the reaction was rotovapped to dryness, and the residue dissolved in an ethyl acetate: water mixture (1:1). The aqueous layer was extracted with ethyl acetate, and the combined organic layers were washed with water and brine. The organic layer was dried over Na_2SO_4, filtered and rotovapped giving the title compound.

Yield: 97.2 mg, 90% as yellow oil.

^{1}H NMR (400 MHz, $CDCl_3$) δ 7.65 (d, J = 3.4 Hz, 1H), 7.17 (d, J = 3.2 Hz, 1H), 3.28 (tt, J = 10.7, 3.9 Hz, 1H), 3.13 (d, J = 11.6 Hz, 1H), 2.79 (dd, J = 11.9, 5.1 Hz, 2H), 2.29 (s, 3H), 2.17 (t, J = 10.8 Hz, 1H), 2.10 (m, 2H), 2.01 (td, J = 11.4, 3.3 Hz, 1H), 1.82 – 1.63 (m, 2H), 1.52 (qd, J = 11.8, 4.4 Hz, 1H).

^{13}C NMR (101 MHz, $CDCl_3$) δ 173.35, 141.98 (d, J = 30.0 Hz), 117.87 (d, J = 35.8 Hz), 61.14, 55.55 (d, J = 27.5 Hz), 46.36 (d, J = 19.8 Hz), 40.76, 30.70, 24.88.

HRMS: M^+ predicted m/z = 183.0950, actual m/z = 183.0950.

Other Investigated Bioisosteres

The following are experimental data for both attempted and successful chemical syntheses done towards the development of a bioisosteric replacement for nipecotic acid.

1-benzylpiperidine-3-carboxylic acid, 3.32

Method A: Nipecotic acid (500 mg, 3.87 mmol, 1.5 equiv) and benzaldehyde (0.27 mL, 273.8 mg, 2.58 mmol, 1.0 equiv) were added to a flame dried flask and diluted in MeOH (12 mL). To the flask was added $NaBH_3CN$ (2431.9 mg, 38.7 mmol, 15.0 equiv) portionwise, and acetic acid (0.3 mL). The reaction was stirred for 2 hours at room temperature before being neutralized to pH 7 with saturated aqueous $NaHCO_3$. The reaction was diluted in ethyl acetate, and the layers separated. The organic layer was

washed with brine before being dried over Na_2SO_4 and concentrated via rotovap. No product was formed.

Method B: In a flame dried flask, nipecotic acid (250.0 mg, 1.94 mmol, 1.0 equiv), K_2CO_3 (1340.6 mg, 9.70 mmol, 5.0 equiv), benzyl bromide (0.69 mL, 995.5 mg, 5.82 mmol, 3.0 equiv), and DMF (2.52 mL) were combined. The reaction was heated at 70°C for 22 hours. TLC of the reaction showed remaining starting material; additional K_2CO_3 (300 mg) was added and the reaction was stirred an additional 4 hours. The reaction was cooled to room temperature and diluted in ethyl acetate and water. The layers were separated, and the organic layer washed with 1.0 M HCl, water and brine. The organic layer was then dried over Na_2SO_4, filtered and rotovapped. Product could not be confirmed, and so the second step of the reaction (deprotection of the carboxylic acid) was forgone.

Ethyl 1-benzylpiperidine-3-carboxylate, 3.33

Ethyl nipecotate ester (0.30 mL, 300.0 mg, 1.91 mmol, 1.5 equiv) and benzaldehyde (0.13 mL, 134.7 mg, 1.27 mmol, 1.0 equiv) were added to a flame dried flask in THF (9.0 mL). To the flask was added $NaBH(OAc)_3$ (3.36 mL, 403.78 mg, 19.05 mmol, 15.0 equiv) portionwise, followed by Na_2SO_4 (100 mg, 0.7 mmol, 0.55 equiv). Glacial acetic acid (17M, 0.15 mL, 2.54 mmol, 2.0 equiv) was added dropwise. The reaction was stirred at room temperature for 2 hours before progress was checked by TLC. Additional THF (1.0 mL), and Na_2SO_4 (50 mg) were added after 2 hours and the reaction was allowed to stir for 2 days. The reaction was then diluted in water, neutralized to pH 7 with saturate

aqueous $NaHCO_3$, and extracted 2x with ethyl acetate. The organic layer was separated, washed with brine, dried over Na_2SO_4 and then rotovapped to give product.

Yield: 295.5 mg, 94% as an oil.

^1H NMR (400 MHz, $CDCl_3$) δ 7.38 – 7.16 (m, 5H), 4.09 (qd, J = 7.1, 0.8 Hz, 2H), 3.51 (q, J = 13.2 Hz, 2H), 2.99 – 2.89 (m, 1H), 2.72 (d, J = 11.4 Hz, 1H), 2.58 (tt, J = 10.3, 3.8 Hz, 1H), 2.21 (t, J = 10.6 Hz, 1H), 2.12 – 1.98 (m, 1H), 1.94 – 1.85 (m, 1H), 1.74 – 1.65 (m, 1H), 1.63 – 1.51 (m, 1H), 1.42 (s, 1H), 1.21 (t, J = 7.1 Hz, 3H).

Ethyl 1-tritylpiperidine-3-carboxylate, 3.34

Triphenylmethyl chloride (Ph_3CCl, 389.5 mg, 1.4 mmol, 1.1 equiv), and ethyl nipecotate ester (0.2 mL, 200.0 mg, 1.27 mmol, 1.0 equiv) were dissolved in DCM (0.53 mL) in a flame dried flask and stirred for 5 minutes. To this mixture, Et_3N (0.62 mL, 450.3 mg, 4.45 mmol, 3.5 equiv) was added dropwise, and the reaction stirred for 1 hour at room temperature. The reaction was then diluted in ethyl acetate, and the layers separated. The organic layer was washed 5x with water, before the organic layer was concentrated via rotovap. Flash column chromatography (gradient, Hexanes: Ethyl Acetate) gave the title compound.

Yield: 147.8 mg, 29% as white solid.

^{1}H NMR (400 MHz, $CDCl_3$) δ 7.64 – 7.43 (m, 6H), 7.30 (ddd, J = 15.3, 8.3, 6.5 Hz, 8H), 7.20 (d, J = 7.4 Hz, 1H), 4.18 – 3.95 (m, 2H), 3.42 (s, 1H), 3.16 (q, J = 7.0 Hz, 1H), 2.87 (s, 1H), 2.08 (s, 1H), 1.79 (d, J = 37.8 Hz, 1H), 1.52 (d, J = 24.3 Hz, 1H), 1.28 (m, 5H).

1-(tert-butoxycarbonyl)piperidine-3-carboxylic acid, 3.35

Method A: Nipecotic acid (250.0 mg, 1.94 mmol, 1.0 equiv) was dissolved in DCM (~1.425 mL) in a flame dried flask. To it was added Et_3N (0.7 mL, 510.4 mg, 5.04 mmol, 2.6 equiv). In another flask or vial, Boc_2O (464.9 mg, 2.13 mmol, 1.1 equiv) was dissolved in DCM (~1.0 mL) and added portion wise to nipecotic acid. The reaction was stirred at room temperature for 12 hours. The reaction was diluted in DCM and washed with water. The organic layer was dried over Na_2SO_4, filtered and concentrated via rotovap. Product was not confirmed by NMR.

Method B: Nipecotic acid (600 mg, 4.65 mmol, 1.0 equiv) and MeOH (23.25 mL) were combined in a flame dried flask under argon. To the reaction, Et_3N (18.5 mL, 25.482 g, 251.8 mmol, 54.1 equiv) was added in two parts, 5 minutes apart. The reaction was then cooled to 0°C before the addition of Boc_2O (1217.9 mg, 5.58 mmol, 1.2 equiv). The reaction is allowed to come to room temperature while it stirs for 48 hours. Confirming consumption of starting material by TLC, the reaction is diluted in a mixture of DCM:water (50 mL:10 mL). This mixture is cooled to 0°C and the pH adjusted to 3.5 (done carefully, adding acid (HCl) dropwise). The organic layer was then separated, and the aqueous layer was extracted with DCM. The combined organic layers were dried over $MgSO_4$,

filtered and concentrated via rotovap. Purification by flash column chromatography gave the title compound.

Yield: 727.7 mg, 68% as white solid.

^{1}H NMR (400 MHz, $CDCl_3$) δ 11.65 (s, 1H), 4.01 (s, 1H), 3.82 (d, J = 13.4 Hz, 1H), 2.99 (s, 1H), 2.78 (t, J = 11.6 Hz, 1H), 2.40 (ddd, J = 10.3, 6.3, 3.9 Hz, 1H), 2.00 (dd, J = 13.0, 4.6 Hz, 1H), 1.72 – 1.49 (m, 2H), 1.38 (s, 9H).

N-hydroxypiperidine-3-carboxamide, 3.36

Method A:[33] Ethyl nipecotate ester (0.25 mL, 250.0 mg, 1.59 mmol, 1.0 equiv) was dissolved in methanol (2.0 mL) in a flame dried flask. In a separate flask, a slurry was made from KOH (711.2 mg, 9.54 mmol, 6.0 equiv), $HONH_2{\cdot}HCl$ (331.5 mg, 4.77 mmol, 3.0 equiv), and methanol (2.0 mL). This slurry was added portionwise to the ester mixture, and the reaction was stirred at room temperature, monitoring by TLC. After 18h a small product spot emerged, and the reaction was heated at 50°C for an additional 2 hours. The reaction was then acidified to pH 4 with 3 M HCl before removing organic solvent via rotovap. The residue was diluted in water, and this mixture was extracted with ethyl acetate until TLC confirmed no product was left in the aqueous layer. The organic layer was dried over Na_2SO_4, filtered and rotovapped. Product formation could not be confirmed by NMR.

Method B:[33] Ethyl nipecotate ester (0.03 mL, 31.4 mg, 0.2 mmol, 1.0 equiv), $HONH_2 \cdot HCl$ (41.7 mg, 0.6 mmol, 3.0 equiv), KOH (89.46 mg, 1.2 mmol, 6.0 equiv), and methanol (1.0 mL) were all added to a 10 mL microwave reaction tube. The reaction was irradiated in a microwave at 150 W, 80°C for 6 minutes. After the microwaving, the reaction was acidified to pH 4 with 3 M HCl and concentrated via rotovap. The residue was diluted in water and extracted with ethyl acetate. The organic layer was concentrated via rotovap. Product formation not confirmed by NMR.

Tert-butyl 3-((diethoxymethyl)(ethoxy)phosphoryl)-3-hydroxypiperidine-1-carboxylate[17], 3.37

N-boc piperidone (200.0 mg, 1.01 mmol, 1.0 equiv), ethyl (2,2-diethoxyethyl)phosphinate (198.1 mg, 1.01 mmol, 1.0 equiv), and Et_3N (0.14 mL, 102.2 mg, 1.01 mmol, 1.0 equiv) were combined in a flame dried flask under argon. The reaction was heated at 100°C for 3 hours before being cooled to room temperature. The reaction was diluted in 100 mL DCM, and this organic mixture was washed with each ice cold 4M HCl, saturated $NaHCO_3$ and brine. The organic layer was then dried over Na_2SO_4, filtered, and rotovapped. TLC showed conversion, but NMR could not confirm product formation.

tert-butyl 3-(2,2,2-trifluoroacetyl)piperidine-1-carboxylate, 3.38

Method A:[27] N-Boc Nipecotic acid (300 mg, 1.31 mmol, 1.0 equiv) was suspended in toluene (3.3 mL) in a flame dried flask under argon. Trifluoroacetic acid was added at room temperature, and then the reaction was cooled to 0°C. Pyridine (0.63 mL, 621.7 mg, 7.86 mmol, 6.0 equiv) was added dropwise. The reaction was then heated to 60°C and

stirred overnight. The reaction was checked by TLC, and when starting material was consumed, the reaction was cooled to 0°C. Water (2.62 mL) was added slowly to the reaction, before heating to 45°C for 2 hours. The reaction was then cooled to room temperature and the layers separated. The aqueous layer was extracted with MTBE which was combined with the organic layer. This organic layer was washed with 1 N NaOH before drying over $MgSO_4$, filtering and rotovapping. No product was recovered.

2,2,2-trifluoro-1-(piperidin-3-yl)ethan-1-one, 3.21

Method A:[27] Nipecotic acid (500 mg, 3.87 mmol, 1.0 equiv) was suspended in toluene (1.5 mL) in a flame dried flask under argon. Trifluoroacetic acid (1.29 mL, 1951.2 mg, 9.29 mmol, 2.4 equiv) was added to the flask dropwise at room temperature. The reaction was then cooled to 0°C in an ice water bath. Pyridine (2.59 mL, 2540.7 mg, 32.12 mmol, 8.3 equiv) was then added slowly to the reaction at 0°C. The reaction was then heated to 50°C and stirred for 24 hours. After this time, the reaction was again cooled to 0°C, and water (~500 mL) was added slowly to quench the reaction. The aqueous reaction mixture was then heated to 45°C and stirred for 2 hours, after which the reaction was diluted with ethyl acetate. The layers were separated, and the organic washed with water followed by saturate aqueous $NaHCO_3$. The organic layer was then dried over Na_2SO_4, filtered and concentrated via rotovap. No product was recovered.

Method B:[27] Nipecotic acid (500 mg, 3.87 mmol, 1.0 equiv) was suspended in toluene (9.67 mL) in a flame dried flask under argon. Trifluoroacetic acid (2.42 mL, 3658.7 mg, 17.42 mmol, 4.5 equiv) was added to the flask dropwise at 0°C in an ice water bath.

Pyridine (1.87 mL, 1836.7 mg, 23.22 mmol, 6.0 equiv) was then added slowly to the reaction at 0°C. The reaction was then heated to 60°C and stirred for 4 hours before checking by TLC. After starting material was consumed, the reaction was cooled to room temperature, and water (7.74 mL) was added slowly over 5 minutes, keeping the reaction temperature below 40°C. The aqueous reaction mixture was then heated to 60°C and stirred for 1 hour and then cooled to room temperature. The reaction was diluted with hexanes and water. The layers were separated, and the aqueous extracted with hexanes. The combined organic layers were then washed with water, and then dried over Na_2SO_4, filtered and concentrated via rotovap. No product was recovered.

Method C:[27] Nipecotic acid (300 mg, 2.32 mmol, 1.0 equiv) was suspended in toluene (5.8 mL) at room temperature. Trifluoroacetic acid (TFAA, 1.45 mL, 2192.7 mg, 10.44 mmol, 4.5 equiv) was then added to the reaction before cooling to 0°C. Pyridine (1.12 mL, 1101.1 mg, 13.92 mmol, 6.0 equiv) was then added dropwise. The reaction was stirred overnight, allowing it to come to room temperature. The reaction was then cooled to 0°C once again before adding 5.0 mL water. The reaction was then stirred for 24 hours. There was no formation of product.

Method D:[27] Nipecotic acid (300 mg, 2.32 mmol, 1.0 equiv) was dissolved in DCM (4.54 mL) at room temperature in a flame dried flask. Trifluoroacetic acid (1.45 mL, 2192.7 mg, 10.44 mmol, 4.5 equiv) was added before cooling the reaction to 0°C. Pyridine (1.12 mL, 1101.1 mg, 13.92 mmol, 6.0 equiv) was then added dropwise in two parts. The reaction was stirred, allowing to come to room temperature while being monitored by TLC. Upon

consumption of starting material, the reaction was cooled to 0°C, and 5.0 mL of water was added slowly. The reaction was again allowed to come to room temperature while stirring, and the progress monitored by TLC. The crude reaction mixture did not show product. The crude reaction was then diluted in hexanes and water. The aqueous layer was extracted with hexanes; the combined organic layers were dried over Na_2SO_4 and rotovapped (Sample A). The aqueous layer was neutralized with NaOH, and again extracted with hexanes; this organic layer was kept separate (sample B). The aqueous layer was then made basic with NaOH and extracted with ethyl acetate (Sample C). Samples A and C had promising NMR spectra (^1H and ^{19}F), and nominal mass spectroscopy showed product in sample C. However, attempting purification of sample C resulted in loss of product.

1-(1-benzylpiperidin-3-yl)-2,2,2-trifluoroethan-1-one, 3.39

Ethyl 1-benzylpiperidine-3-carboxylate (295.5 mg, 1.19 mmol, 1.0 equiv) and $TMS{\cdot}CF_3$ (0.19 mL, 186.28 mg, 1.31 mmol, 1.1 equiv) were added to a flame dried flask in DME (0.32 mL). To the flask was added cesium fluoride (CsF, 3.6 mg, 0.02 mmol, 0.02 equiv). The reaction was stirred at room temperature for 2 hours, monitoring by TLC. Starting material consumption was slow, and so the reaction was allowed to stir for 4 days. Upon starting material consumption, HCl (2mL, 4 M) was added to the reaction and it was allowed to stir at least 2 hours. The reaction was then extracted with diethyl ether. The organic layers were combined, dried over Na_2SO_4, filtered, and rotovapped. Formation of product could not be confirmed by NMR.

2,2,2-trifluoro-1-(1-tritylpiperidin-3-yl)ethan-1-one, 3.40

Method A:[28,29] Ethyl 1-tritylpiperidine-3-carboxylate (3.36, 148.0 mg, 0.37 mmol, 1.0 equiv.) was added to a flame dried flask under argon with TMS·CF_3 (0.06 mL, 58.3 mg, 0.41 mmol, 1.1 equiv) and DME (0.10 mL). To it was added CsF (1.1 mg, 0.007 mmol, 0.02 equiv), and the reaction was allowed to stir at room temperature for 2 hours. Checking by TLC showed no product forming, and so the reaction was heated at 35°C overnight. The reaction was acidified with 4 N HCl (1 mL) and stirred for 2 additional hours. TLC showed emergence of new spot. The reaction was extracted with diethyl ether (Et_2O), dried over Na_2SO_4, and rotovapped. NMR could not confirm product and showed remaining starting material.

2,2,2-trifluoro-1-(1-methylpiperidin-3-yl)ethan-1-one, 3.41

Method A: N-methyl nipecotic acid (143.2 mg, 1.0 mmol, 1.0 equiv) and TMS·CF_3 (0.16 mL, 156.42 mg, 1.1 mmol, 1.1 equiv) were added in DME (0.3 mL) to a flame dried flask. To the flask was added CsF (31.04 mg, 0.02 mmol, 0.02 equiv) and the reaction was allowed to stir until consumption of starting material as monitored by TLC (about 45 hours). The reaction was acidified with 4 N HCl (1 mL) and stirred for 1 hour. The reaction was rotovapped to dryness, and no product was recovered as observed by TLC and NMR.
Method B: N-methyl nipecotic acid (143.2 mg, 1.0 mmol, 1.0 equiv) and TMS·CF_3 (0.18 mL, 177.75 mg, 1.25 mmol, 1.25 equiv) were added in DME (0.3 mL) to a flame dried flask cooled to -78°C. To the flask was added TBAF (0.03 mL of a 1 M solution, 0.025 mmol, 2.5 mol %), and the reaction was allowed to come to room temperature, stirring until consumption of starting material as monitored by TLC (about 45 hours). The reaction

was acidified with 4 N HCl (1 mL) and stirred for 1 hour. The reaction was rotovapped to dryness, and no product was recovered as observed by TLC and NMR.

Tetrazole Chemistry:

For the synthesis of both compound **3.24** (intended precursor) and **3.44** (reference standard) multiple reagents were investigated for the formation of a tetrazole from a cyanopiperidine. While under some conditions, formation of the tetrazole was observed via ^{13}C-NMR, it was not possible to separate the product from the cyano-starting material.

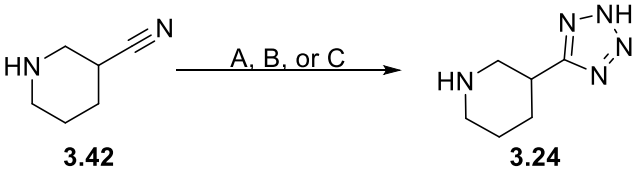

3.42 **3.24**

A: NaN_3, TEA-HCl, DMF, 100°C
B: NaN_3, TEA-HCl, DMF, MW, 130°C
C: NaN_3, I_2, DMF, 120°C

Scheme 3-6: Attempted syntheses of intended tetrazole precursor from piperidine-3-carbonitrile.

1-methylpiperidine-3-carbonitrile, 3.43

Piperdine-3-carbonitrile, **3.44**, (0.13 mL, 124.18 mg, 1 mmol, 1.0 equiv) was added to a flame dried flask with THF (1.4 mL) under argon. Methyl iodide (0.15mL, 340.66 mg, 2.4 mmol, 2.4 equiv) was added dropwise at room temperature. The reaction was stirred at room temperature for 3 hours. When a precipitate formed, 5% NaOH (1.5 mL) was added to re-dissolve it. The reaction was extracted with ethyl acetate, and the organic layer dried over $MgSO_4$, filtered and concentrated. TLC showed complete consumption of starting material. Product was used without further purification.

Yield: 89.4 mg, 72% as oil.

^{1}H NMR (400 MHz, $CDCl_3$) δ 2.99 (dd, J = 8.3, 4.2 Hz, 1H), 2.76 (td, J = 8.3, 3.9 Hz, 2H), 2.54 – 2.35 (m, 2H), 2.26 (s, 3H), 1.94 – 1.70 (m, 2H), 1.68 – 1.40 (m, 2H).

^{13}C NMR (101 MHz, $CDCl_3$) δ 121.13, 57.08, 55.09, 46.21, 27.38 (d, J = 69.1 Hz, 2C), 23.56.

HRMS: M^+ predicted m/z = 124.1000, actual m/z = 124.0997.

1-methyl-3-(2H-tetrazol-5-yl)piperidine, 3.44

Method A: 3-(2H-tetrazol-5-yl)piperidine hydrochloride (50 mg, 0.326 mmol, 1.0 equiv) was diluted in THF (0.5 mL) in a flame dried flask. To the flask was added Et_3N (0.1 mL, 65.97 mg, 0.652 mmol, 2.0 equiv), and the mixture was allowed to stir ~5 minutes. Methyl iodide (0.024 mL, 55.6 mg, 0.392 mmol, 1.2 equiv) was added dropwise, and the reaction was stirred at room temperature, monitoring by TLC. When starting material appeared consumed, the reaction was quenched with excess saturated aqueous $NaHCO_3$. The aqueous reaction mixture was then extracted with diethyl ether. The organic layers were combined, dried over $MgSO_4$, filtered and concentrated. Product formation could not be confirmed by NMR.

Method B: 1-methylpiperidine-3-carbonitrile (**3.43**, 89.4 mg, 0.72 mmol, 1.0 equiv), NaN_3 (70.2 mg, 1.08 mmol, 1.5 equiv), and DMF (1.8 mL) were added to a flame dried flask

under argon. To the flask was added I_2 (42.02 mg, 0.166 mmol, 0.23 equiv), and the reaction was heated to 120°C and stirred overnight. TLC showed conversion of starting material, and so the reaction was cooled to room temperature and diluted in water. The pH was adjusted to 4 with 1 M HCl. The reaction was extracted with ethyl acetate, and the combined organic layers washed with brine. The organic layers were dried over $MgSO_4$, filtered and concentrated. Analysis with ^{13}C-NMR shows conversion to the desired product, with remaining starting material.

3-(2H-tetrazol-5-yl)piperidine, 3.24

Method A:[34] Piperidine-3-carbonitrile, **3.42**, (0.21 mL, 200 mg, 1.61 mmol, 1.0 equiv) was diluted in DMF (3.2 mL) in a flame dried flask under argon. To the flask was added NaN_3 (314.0 mg, 4.83 mmol, 3.0 equiv), and TEA·HCl (664.85 mg, 4.83 mmol, 3.0 equiv). The flask was heated to 100°C overnight. TLC showed consumption of starting material. The reaction was cooled to 0°C, and EtOAc:4 M HCl (10 mL: 2 mL) was added to the flask. This was allowed to stir ~15 minutes. The layers were then separated, and the organic layer washed with 2 N HCl 5x. The organic layer was dried over Na_2SO_4, filtered and rotovapped. No product was formed according to NMR.

Method B:[34] Piperidine-3-carbonitrile, **3.42**, (0.1 mL, 100.0 mg, 0.81 mmol, 1.0 equiv), NaN_3 (157.97 mg, 2.43 mmol, 3.0 equiv), TEA·HCl (334. 5 mg, 2.43 mmol, 3.0 equiv), and DMF (1.6 mL) were all combined in a 10 mL microwave reaction tube. The reaction was run in a microwave at 130°C, 150 W, 250 psi for 2 hours. The reaction was cooled and a mixture of EtOAc:4 N HCl (20 mL: 5 mL) was added to the reaction at 0°C. This

was allowed to stir ~5 minutes. The layers were then separated, and the organic layer washed with 1 N HCl x 5 times. The organic layer was dried over Na_2SO_4, filtered and concentrated. This product, when placed under house vacuum, decomposed. No product was recovered.

Method C:[35] Piperidine-3-carbonitrile, **3.42**, (0.05 mL, 50 mg, 0.4 mmol. 1.0 equiv), NaN_3 (39.01 mg, 0.6 mmol, 1.5 equiv), and DMF (1.0 mL) were added to a flame dried flask under argon. To the flask was added iodide (I_2, 18.0 mg, 0.071 mmol, 0.18 equiv). The reaction was heated to 120°C and stirred overnight. Upon consumption of starting material, the reaction was diluted in ethyl acetate and 4 M HCl. The aqueous layer was separated and extracted twice with ethyl acetate. The combined organic layers were washed twice with each saturated aqueous $Na_2S_2O_3$ and water. NMR of the crude reaction mixture showed formation of product with remaining starting material. Purification of product was attempting using flash column chromatography (silica, hexanes:ethyl acetate gradient), but no separation was achieved.

Tert-butyl 3-(2H-tetrazol-5-yl)piperidine-1-carboxylate, 3.27

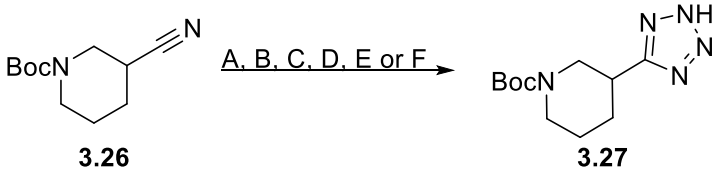

3.26 **3.27**

A. NaN_3, I_2, DMF, 120°C
B. NaN_3, $ZnCl_2$, THF, 70°C
C. NaN_3, $ZnCl_2$, IPA:H_2O, 80°C
D. NaN_3, TEA·HCl, NMP, 140°C
E. NaN_3, DMF, 100°C, 48 h
F. TMS·N_3, Bu_2SnO, Toluene, 95°C

Scheme 3-7: Attempted methods for the production of a tetrazolyl piperidine.

Method A:[35] Tert-butyl 3-cyanopiperidine-1-carboxylate, **3.26**, (135 mg, 0.64 mmol. 1.0 equiv), NaN_3 (62.6 mg, 0.96 mmol, 1.5 equiv), and DMF (1.0 mL) were added to a flame dried flask under argon. To the flask was added iodide (I_2, 29.0 mg, 0.115 mmol, 0.18 equiv). The reaction was heated to 120°C and stirred overnight. Upon consumption of starting material, the reaction was diluted in ethyl acetate and 4 M HCl. The aqueous layer was separated and extracted twice with ethyl acetate. The combined organic layers were washed twice with each saturated aqueous $Na_2S_2O_3$ and water. NMR of the crude reaction mixture showed formation of product with remaining starting material. Purification of product was attempting using flash column chromatography (silica, hexanes:ethyl acetate gradient), but no separation was achieved.

Method B:[36] Tert-butyl 3-cyanopiperidine-1-carboxylate, **3.26**, (100.0 mg, 0.47 mmol, 1.0 equiv), and NaN_3 (30.0 mg, 0.47 mmol, 1.0 equiv) were added to a flame dried flask with DMF (1.0 mL). This flask was purged with argon and allowed to stir at room temperature for 10 minutes. To the flask was added $ZnCl_2$ (0.67 mL of 0.7M solution in THF, 0.47 mmol, 1.0 equiv), and this was allowed to stir an additional 5 minutes at room temperature. The reaction was then equipped with a reflux condenser and heated to 70°C. The reaction was allowed to reflux at 70°C for 4 hours, and the reaction cooled to room temperature. The reaction was concentrated, and the crude residue analyzed by NMR, which did not show formation of product.

Method C:[37] Tert-butyl 3-cyanopiperidine-1-carboxylate, **3.26**, (200.0 mg, 0.95 mmol, 1.0 equiv) and NaN_3 (123.57 mg, 1.9 mmol, 2.0 equiv) were added to a flask with a 1:2 mixture

IPA:H_2O (1.5 mL: 3.0 mL). To the flask was added $ZnCl_2$ (0.67 mL 0.7M Solution in THF, 0.47 mmol, 0.5 equiv). The reaction was heated to reflux (80°C), and stirred for 16 hours, after which it was cooled to room temperature. To the reaction was added 4 N HCl (0.5 mL) and ethyl acetate (3 mL), and the reaction was stirred until all the solids were dissolved, adding more ethyl acetate if necessary. The layers were separated, and the aqueous layer was extracted twice with ethyl acetate. The combined organic layers were dried over Na_2SO_4, filtered and rotovapped. NMR did not confirm formation of product.

Method D:[38] Tert-butyl 3-cyanopiperidine-1-carboxylate, 3.28, (200.0 mg, 0.95 mmol, 1.0 equiv), NaN_3 (185.3 mg, 2.85 mmol, 3.0 equiv), and TEA·HCl (196.15 mg, 1.425 mmol, 1.5 equiv) were all combined with NMP (7.6 mL) and stirred for 2 minutes at room temperature. The flask was equipped with a reflux condenser, heated to 140°C, and refluxed for 6 hours. The reaction was monitored by TLC, and when reaction slowed or stopped it was cooled to room temperature. The reaction was diluted with water before adjusting the pH to 4 with 1 N HCl. The aqueous mixture was extracted three times with ethyl acetate. The combined organic layers were washed with NH_4Cl and brine, dried over $MgSO_4$, filtered and rotovapped. NMR showed a mixture of product and starting material, but purification via flash column chromatography was not successful.

Method E:[39] Tert-butyl 3-cyanopiperidine-1-carboxylate, **3.26**, (105.14 mg, 0.5 mmol, 1.0 equiv) and DMF (2.5 mL) were added to a flame dried flask under argon. To the flask was added NaN_3 (97.515 mg, 1.5 mmol, 3.0 equiv); this was allowed to stir for 2 minutes. The reaction was then heated to 100°C and allowed to stir for 48 hours, checking reaction progression by TLC. The reaction was then cooled to room temperature, diluted with 50

mL ethyl acetate, and washed with brine three times. The combined organic layers were dried over Na_2SO_4, filtered, and rotovapped. Crude NMR showed formation of product. Purification via flash column chromatography (DCM:MeOH gradient on silica) was not able to separate the starting material from the product.

Method F:[7] Tert-butyl 3-cyanopiperidine-1-carboxylate, **3.26**, (200.0 mg, 0.95 mmol, 1.0 equiv), and Bu_2SnO (34.9 mg, 0.14 mmol, 0.15 equiv) were added to a flame dried flask under argon. To these reagents was added toluene (1.9 mL), and $TMS{\cdot}N_3$ (0.25 mL, 218.9 mg, 1.9 mmol, 2.0 equiv) at room temperature. The reaction was then heated to 95°C overnight (15 hours). Up to 4 more equivalents of $TMS{\cdot}N_3$ was added, and the reaction was stirred for another 6 hours at 95°C. When starting material was consumed, the reaction was allowed to cool to room temperature before being rotovapped to dryness. The product should precipitate when the residue is triturated with cold hexanes. NMR analysis of the resulting precipitate did not confirm product formation.

i. Radiochemistry methods

Unless otherwise stated, reagents and solvents were commercially available and used without further purification: sodium chloride, 0.9% USP, and sterile water for injection, USP, were purchased from Hospira; ethanol was purchased from American Regent; HPLC grade acetonitrile was purchased from Fisher Scientific. Other synthesis components were obtained as follows: sterile filters were obtained from Millipore; sterile product vials were purchased from Hollister-Stier; C18-light Sep-Paks were purchased from Waters Corporation. C18 Sep-Paks were flushed with 10 mL of ethanol followed by

10 mL of sterile water prior to use. Analytical HPLC was performed using a Shimadzu LC-2010A HT system equipped with a Bioscan B-FC-1000 radiation detector and either a UV detector (**[^{11}C]3.17** and **[^{11}C]3.31**) or CDD-10Avp conductivity detector with temperature-controlled cell (**[^{11}C]3.18**).

Radiosynthesis of [^{11}C]3.17

Carbon-11 was produced via the $^{14}N(p,\alpha)^{11}C$ nuclear reaction using a GE PETTrace cyclotron (40 μA, 30 min beam provided ~3 Ci of carbon-11 as [^{11}C]CO_2). [^{11}C]CO_2 was transferred to a TracerLab $FX_{C\text{-}Pro}$ automated radiochemistry synthesis module and converted to [^{11}C]CH_3OTf *via* [^{11}C]CH_3I (~400 or 850 mCi, based on a 15 or 30 minute beam time) as previously described.[40] [^{11}C]CH_3OTf was bubbled through the reaction charged with a solution of nipecotate precursor **3.19**(1 mg in 0.1 mL DMF) for 3 min at room temperature. The reaction mixture diluted with semi-preparative HPLC solvent (0.5 mL) and purified by semi-preparative HPLC (column: Phenomenex Luna C18 (2), 250 mm x 10 mm; mobile phase: 20 mM NH_4OAc in 10% EtOH, flow rate: 4 mL/min, UV: 220 nm). The product was collected (retention time ~18-19 min, Figure 3-15) and, given the injectable mobile phase, the dose was passed directly through a 0.22 μm sterile filter into a sterile dose vial to give 52 ± 12 mCi (1924 ± 444 MBq) of **[^{11}C]3.17**, 2% non-corrected RCY based upon [^{11}C]CO_2, 100% radiochemical purity (RCP) (column: Phenomenex Omega Polar RP; mobile phase: Gradient (0-50%) MeCN in water + 0.5% TFA, flow rate = 1.5 mL/min, UV: 220 nm; figure 3-16), high specific activity (>2500 Ci/mmol), and pH = 5.5, n = 2.

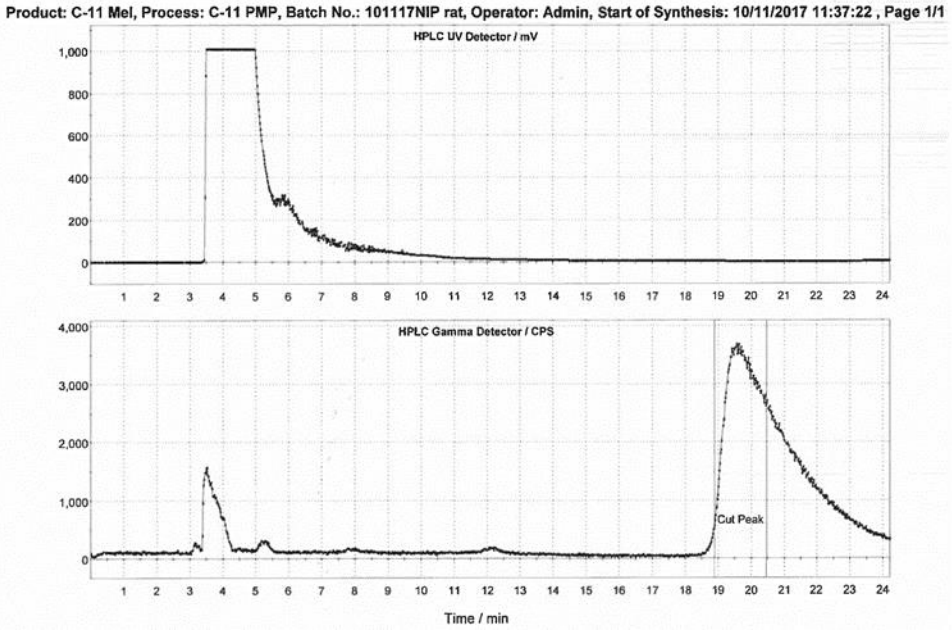

Figure 3-15 : Representative semi-preparative HPLC trace from preparation of **[^{11}C]3.17**. "Cut peak" depicts volume collected for dose.

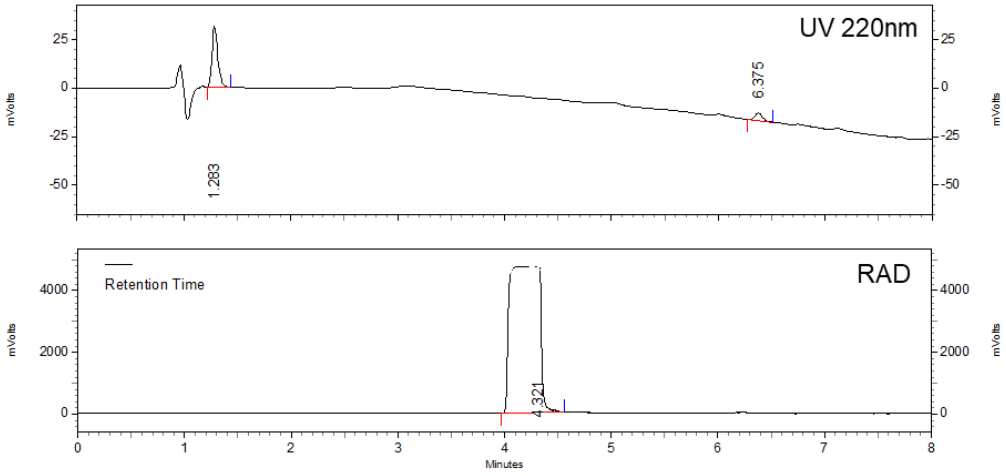

UV Detector Ch2-220nm Results

Retention Time	Area	Area %	Height	Width	S/N (ASTM)
1.283	119572	17	31421	0.225	2.29
6.375	18450	3	3922	0.242	6.23

RAD Results

Retention Time	Area	Area %	Width
4.321	91252905	100	0.59

Figure 3-16: Representative Quality Control HPLC trace of prepared dose of **[^{11}C]3.17**.

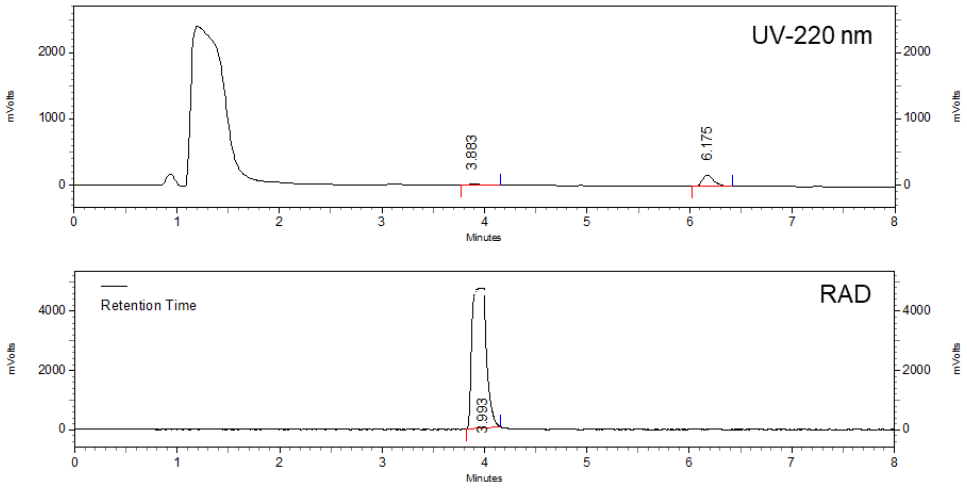

UV Detector Ch2-220nm Results

Retention Time	Area	Area %	Height	Width	S/N (ASTM)
3.883	155095	11	18134	0.383	0.05
6.175	1237309	89	166633	0.392	34.01

RAD Results

Retention Time	Area	Area %	Width
3.993	45921892	100	0.33

Figure 3-17: Representative coinjection HPLC trace of prepared dose of **[^{11}C]3.17** with standard ester.

Radiosynthesis of [^{11}C]3.18

Ester **[^{11}C]3.17** was prepared as described above. After the methylation, the reaction vessel was heated to 100°C and 5 M LiOH (0.5 mL) was added. The reaction was stirred for 5 min to generate **[^{11}C]3.18**, cooled to 40°C and diluted with semi-preparative HPLC solvent (0.5 mL). The reaction mixture was purified by semi-preparative HPLC (column: Gemini-NX C18, 250 mm x 10 mm; mobile phase 20 mM NH_4OAc in 5% EtOH, flow rate = 2 mL/min for 5 min and then then 1 mL/min, UV: 220 nm). The product was collected (retention time ~7-8 min, Figure 3-18) and, given the injectable mobile phase, the dose was passed directly through a 0.22 µm sterile filter into a sterile dose vial to give 113± 17 mCi (4181± 629 MBq) of **[^{11}C]3.18**, 4% non-corrected RCY based upon [11C]CO_2, >98% RCP (column: Phenomenex IP-Pak Cation M/D 150 x 3.9 mm; mobile phase: 5 mM HCl, flow rate = 2.0 mL/min, UV: 220 nm + CDD electrochemical detector; Figure 3-19), high specific activity (>2500 Ci/mmol), pH = 5.5, n = 2.

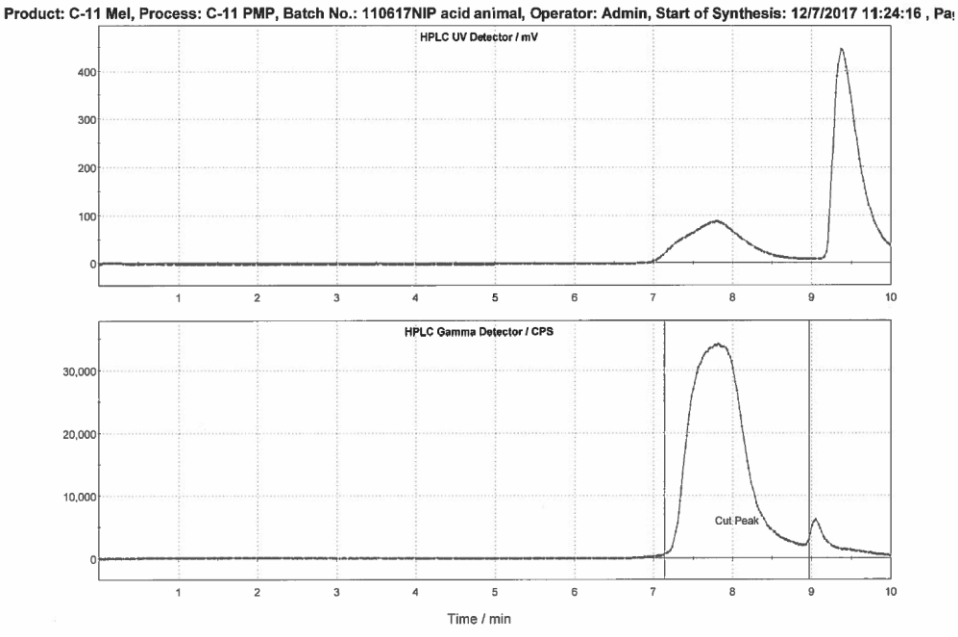

Figure 3-18: Representative semi-preparative HPLC trace from preparation of **[^{11}C]3.18**. "Cut peak" depicts volume collected for dose.

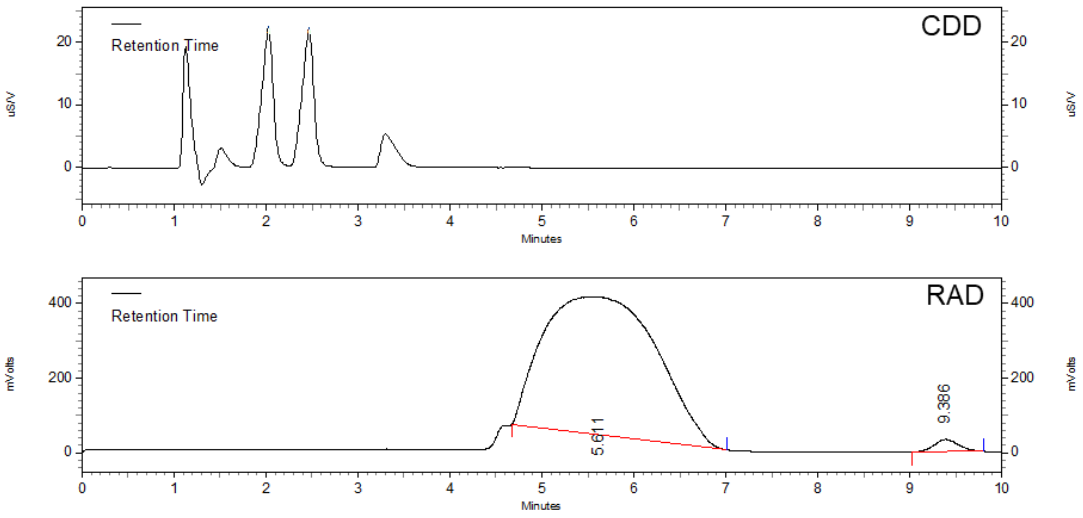

Bioscan RAD Results

Retention Time	Area	Area %	Height	Width	S/N (ASTM)
5.611	31759489	98	369573	2.337	71.01
9.386	607065	2	32871	0.772	41.50

Figure 3-19: Representative quality control HPLC trace of prepared dose **[^{11}C]3.18** This molecule, lacking appreciable UV detection, was monitored by a Shimadzu CDD-10Avp.

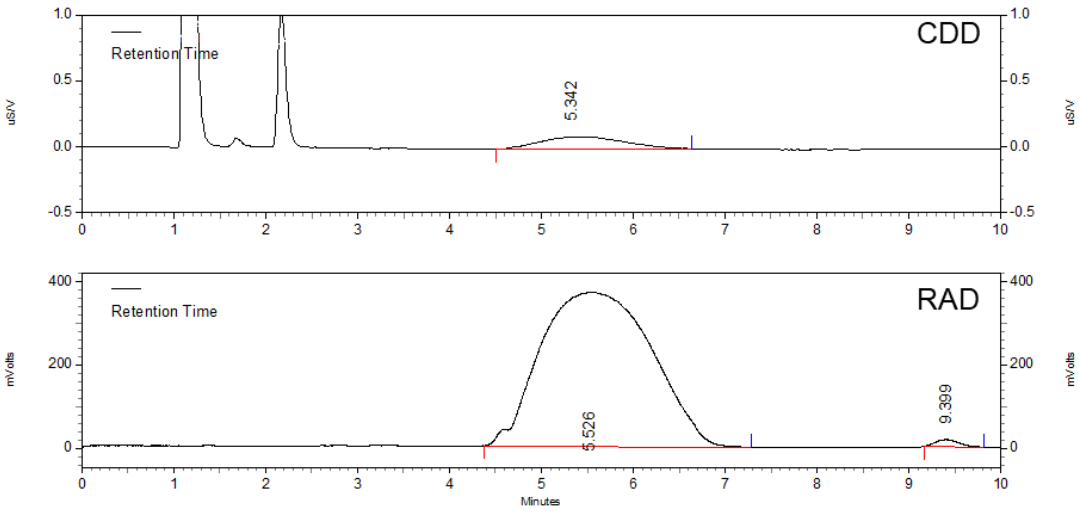

CDD-10Avp Results

Retention Time	Area	Area %	Height	Width	S/N (ASTM)
5.342	6052	100	95	2.125	0.03

Bioscan RAD Results

Retention Time	Area	Area %	Height	Width	S/N (ASTM)
5.526	31196607	99	370967	2.905	424.09
9.399	291937	1	17115	0.642	16.73

Figure 3-20: Representative coinjection HPLC trace of prepared dose of **[^{11}C]3.18** with reference standard acid. This molecule, lacking appreciable UV detection, was monitored by a Shimadzu CDD-10Avp.

Radiosynthesis of [^{11}C]3.31

Carbon-11 was produced via the ^{14}N(p,α)^{11}C nuclear reaction using a GE PETTrace cyclotron (40 μA, 30 min beam provided ~3 Ci of carbon-11 as [^{11}C]CO_2). [^{11}C]CO_2 was transferred to a TracerLab $FX_{C\text{-}Pro}$ automated radiochemistry synthesis module and converted to [^{11}C]CH_3OTf *via* [^{11}C]CH_3I (~400 or 850 mCi, based on a 15 or 30 minute beam time) as previously described.[40] [^{11}C]CH_3OTf was bubbled through the reaction charged with a solution of 3-(1,3-Thiazol-2-yl)piperidine precursor **3.30** (0.8 mg in 0.2 mL

DMF) for 3 min at room temperature. The reaction mixture diluted with semi-preparative HPLC solvent (0.5 mL) and purified by semi-preparative HPLC (column: Gemini NX, 250 mm x 10 mm; mobile phase: 30% MeCN, 50mM NH_4OAc, pH 10 (adjusted with NH_4OH), flow rate: 4 mL/min, UV: 220 nm). The product was collected (retention time ~8-9 min, Figure 3-21) and diluted in 50 mL milliQ water. The diluted product was then trapped on a 1cc Vac C18 cartridge. The cartridge was rinsed with an additional 6 mL of MilliQ water before the product was eluted with 0.5 mL ethanol and 4.5 mL saline solution. The dose was then passed through a 0.22 µm sterile filter into a sterile dose vial to give131±62 mCi (4900±2300 MBq) of **[^{11}C]3.31**, 15% non-corrected RCY based upon [^{11}C]CO_2, 100% radiochemical purity (RCP) (column: Kinetix Evo 250 x 4.6 mm; mobile phase: 20% MeCN, 50 mM NH_4HCO_3, pH 10 (adjusted with NH_4OH), flow rate = 2.0 mL/min, UV: 254 nm; figure 3-22), high specific activity (>2500 Ci/mmol), and pH = 6.0, n = 6.

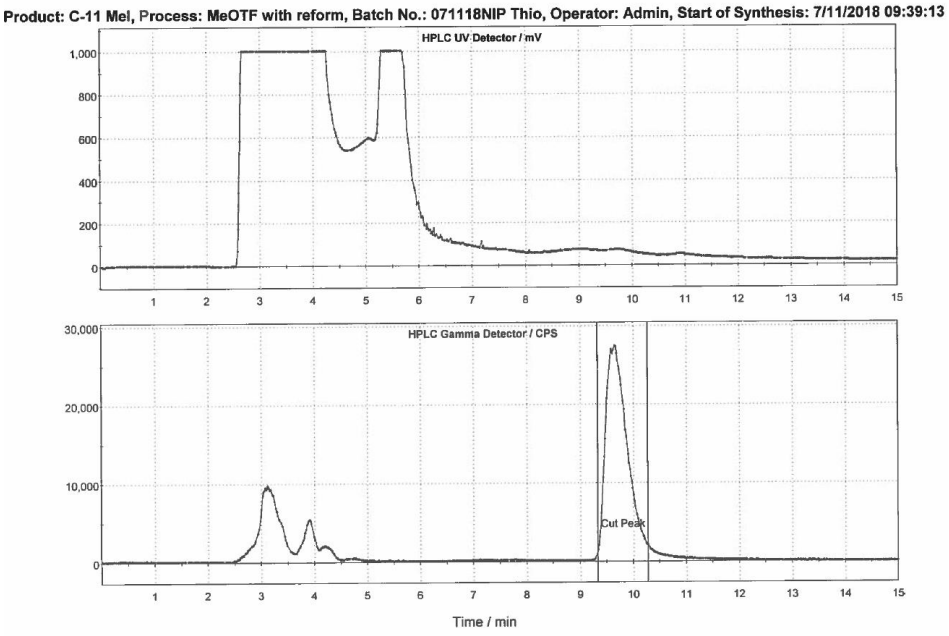

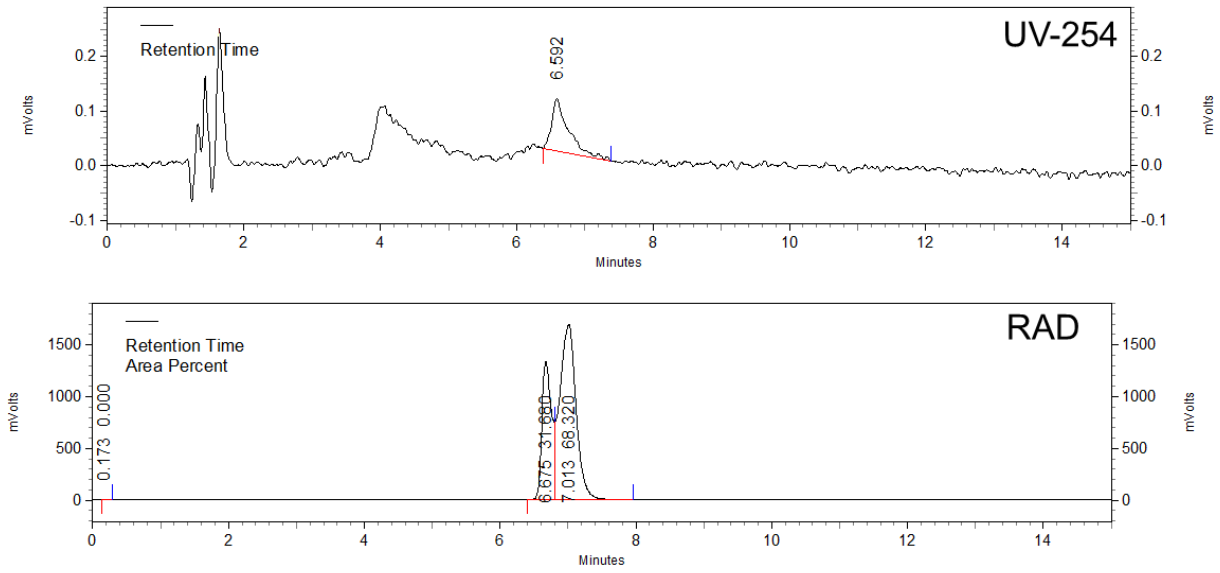

Figure 3-22: Representative Quality Control HPLC trace of prepared dose of **[^{11}C]3.31**.

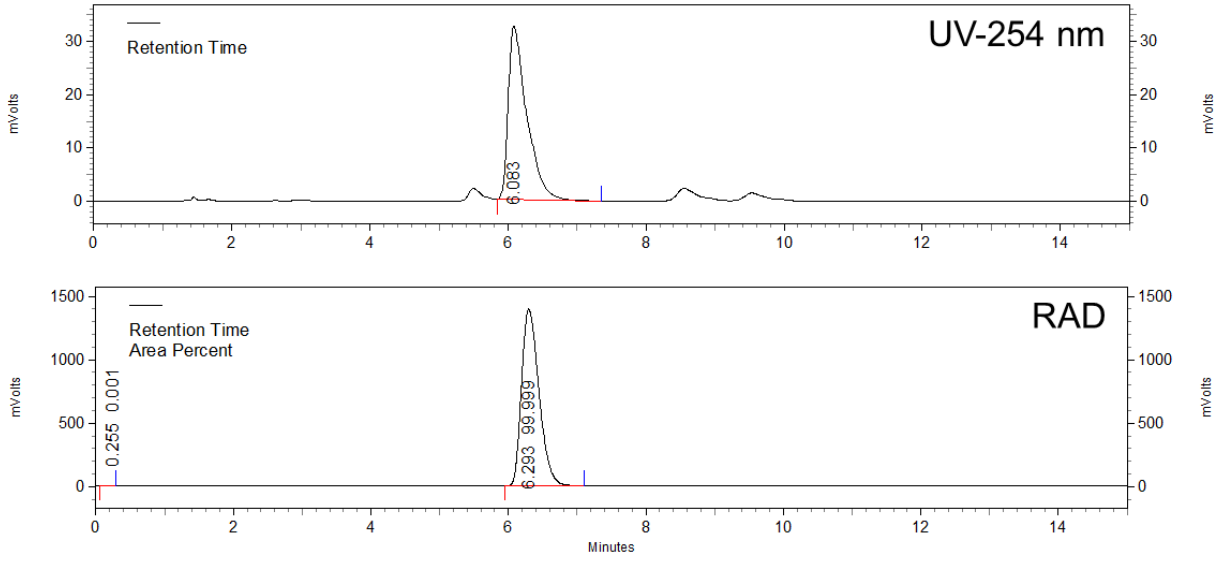

Figure 3-23: Representative coinjection HPLC trace of prepared dose of **[^{11}C]3.31** with **3.31** reference standard.

ii. *In vivo* Methods

General Considerations

Images were reconstructed using 3D maximum a priori (3D MAP) program. All animal PET imaging experiments were conducted under the supervision of the University of Michigan and its Institutional Animal Care and Use Committee (IACUC) according to approved protocols and all applicable federal, state, local and institutional laws or guidelines governing animal research. Imaging studies were conducted using a Concorde Microsystems P4 PET scanner as described below.

Rodents

Anesthesia was induced in healthy, female Sprague-Dawley rats (279-369 g) using isoflurane/O_2, and anesthesia was maintained with 2-4% isoflurane/O_2 throughout the imaging studies. Body temperature was maintained by a heating pad. Following a transmission scan for attenuation correction, the animals were injected (i.v. via intravenous tail vein) with the radiotracer as a bolus over 1 min (Table 3-6), and the brain imaged for 90 minutes.

Primates (NHP)

Imaging studies were performed in a young, mature female rhesus monkey. The animal was anesthetized in the home cage with ketamine (acid and ester compounds) or telazol (thiazole compound) and transported to the PET imaging suite. The monkey was intubated for mechanical ventilation, and anesthesia was continued with isoflurane. Anesthesia was maintained throughout the duration of the PET scan. A venous catheter

was inserted into one hind limb and the monkey was placed on the PET gantry with its head secured to prevent motion artifacts. Following a transmission scan, radiotracers were administered in a bolus dose over 1 minute (Table 3-6). Emission data were collected beginning with the injection and continued for 90 minutes.

Table 3-6: Compiled in vivo evaluation data.

Parameter	Rat				Primate	
Form	NIP Ester	NIP Acid	NIP-Thio	NIP-Thio	NIP-Thio	NIP-Thio
Weight (g)	287	369	427	424	8341	8720
Amount Injected (mCi)	0.505	0.489	0.542	0.46	4.13	5.0
Volume (mL)	0.75	0.2	1.0	0.5	4.4	2.0
Specific Activity (Ci/mmol)	2500	2500	2500	2500	2500	4541

Image Analysis

Upon completion of the PET scans, emission data were corrected for decay, dead time and random coincidences before reconstruction using an iterative ordered subset expectation maximization–maximum a posteriori (MAP) method to generate reconstructed images. Frames were summed, smoothed, and regions-of-interest (ROIs) were defined manually for the whole brain over multiple adjacent frames in the sagittal projection. The volumetric ROIs were then applied to the full dynamic data sets to obtain regional tissue time-radioactivity data. Standardized uptake values (SUVs) were calculated for each region of interest.

F. REFERENCES

(1) Langmuir, I. *J. Am. Chem. Soc.* **1919**, *41* (10), 1543–1559.

(2) Patani, G. a; LaVoie, E. J. *Chem. Rev.* **1996**, *96* (8), 3147–3176.

(3) Fournié-Zaluski, M.; Gonzalez, W.; Turcaud, S.; Pham, I.; Roques, B. P.; Michel, J. B. *Proc. Natl. Acad. Sci. U. S. A.* **1994**, *91* (9), 4072–4076.

(4) Lima, L.; Barreiro, E. *Curr. Med. Chem.* **2005**, *12* (1), 23–49.

(5) Friedman, H. L. In *First Symposium on Chemical-Biological Correlation*; Washington, DC, 1951.

(6) Thornber, C. W. *Chem. Soc. Rev.* **1979**, *8* (4), 563.

(7) Moltzen, E. K.; Pedersen, H.; Bøgesø, K. P.; Meier, E.; Frederiksen, K.; Sánchez, C.; Lembøl, H. L. *J. Med. Chem.* **1994**, *37* (24), 4085–4099.

(8) Lassalas, P.; Gay, B.; Lasfargeas, C.; James, M. J.; Tran, V.; Vijayendran, K. G.; Brunden, K. R.; Kozlowski, M. C.; Thomas, C. J.; Smith, A. B.; Huryn, D. M.; Ballatore, C. *J. Med. Chem.* **2016**, *59* (7), 3183–3203.

(9) Ballatore, C.; Huryn, D. M.; Smith, A. B. *ChemMedChem* **2013**, *8* (3), 385–395.

(10) Gillis, E. P.; Eastman, K. J.; Hill, M. D.; Donnelly, D. J.; Meanwell, N. A. *J. Med. Chem.* **2015**, *58* (21), 8315–8359.

(11) Odano, I.; Halldin, C.; Karlsson, P.; Varrone, A.; Airaksinen, A. J.; Krasikova, R. N.; Farde, L. *Neuroimage* **2009**, *45* (3), 891–902.

(12) Rodnick, M. E.; Hockley, B. G.; Sherman, P.; Quesada, C.; Battle, M. R.; Jackson, A.; Linder, K. E.; Macholl, S.; Trigg, W. J.; Kilbourn, M. R.; Scott, P. J. *Nucl Med Biol* **2013**, *40* (7), 901–905.

(13) Schirrmacher, R.; Kostikov, A.; Massaweh, G.; Kovacevic, M.; Wangler, C.; Theil,

A. In *Radiochemical Syntheses: Radiopharmaceuticals for Positron Emission Tomography*; Scott, P. J., Hockley, B. G., Eds.; Wiley, 2012; pp 111–123.

(14) Cleton, A.; Altorf, B. A.; Voskuyl, R. A.; Danhof, M. *Eur. J. Pharm. Sci.* **2000**, *12* (2), 141–150.

(15) Nguyen, T. B.; Snyder, S. E.; Kilbourn, M. R. *Nucl. Med. Biol.* **1998**, *25* (8), 761–768.

(16) Kilbourn, M. R.; Nguyen, T. B.; Snyder, S. E.; Sherman, P. *Nucl. Med. Biol.* **1998**, *25* (8), 755–760.

(17) Kehler, J.; Stensbol, T. B.; Krogsgaard-Larsen, P. *Bioorg Med Chem Lett* **1999**, *9* (6), 811–814.

(18) Andersen, K. E.; Sørensen, J. L.; Huusfeldt, P. O.; Knutsen, L. J. S.; Lau, J.; Lundt, B. F.; Petersen, H.; Suzdak, P. D.; Swedberg, M. D. B. *J. Med. Chem.* **1999**, *42* (21), 4281–4291.

(19) Høg, S.; Greenwood, J. R.; Madsen, K. B.; Larsson, O. M.; Frølund, B.; Schousboe, A.; Krogsgaard-Larsen, P.; Clausen, R. P. *Curr Top Med Chem* **2006**, *6* (17), 1861–1882.

(20) Vogensen, S. B.; Jorgensen, L.; Madsen, K. K.; Jurik, A.; Borkar, N.; Rosatelli, E.; Nielsen, B.; Ecker, G. F.; Schousboe, A.; Clausen, R. P. *Bioorg Med Chem* **2015**, *23* (10), 2480–2488.

(21) Borisova, T.; Pozdnyakova, N.; Shaitanova, E.; Gerus, I.; Dudarenko, M.; Haufe, G.; Kukhar, V. *Bioorganic Med. Chem.* **2017**, *25* (2), 759–764.

(22) Borisova, T.; Pozdnyakova, N.; Shaitanova, E.; Gerus, I.; Dudarenko, M.; Mironets, R.; Haufe, G.; Kukhar, V. *Bioorg Med Chem* **2015**, *23* (15), 4316–4323.

(23) Bolvig, T.; Larsson, O. M.; Pickering, D. S.; Nelson, N.; Falch, E.; Krogsgaard-Larsen, P.; Schousboe, A. *Eur. J. Pharmacol.* **1999**, *375* (1–3), 367–374.

(24) Falch, E.; Perregaard, J.; Frølund, B.; Søkilde, B.; Buur, A.; Hansen, L. M.; Frydenvang, K.; Brehm, L.; Bolvig, T.; Larsson, O. M.; Sanchez, C.; White, H. S.; Schousboe, A.; Krogsgaard-Larsen, P. *J. Med. Chem.* **1999**, *42* (26), 5402–5414.

(25) Clausen, R. P.; Frølund, B.; Larsson, O. M.; Schousboe, A.; Krogsgaard-Larsen, P.; White, H. S. *Neurochem. Int.* **2006**, *48* (6–7), 637–642.

(26) Edmonson, S. D.; Chang, L.; Kar, N. F.; Morriello, G. J.; Moyes, C. R.; Shen, D.-M.; Zhu, C.; Anthony, N. J.; Jones, P.; Smith, G. F.; Scott, M. E.; Thompson, C. F.; Jung, J.; Cammarano, C.; Hoffman, D. M. Novel Pyrrolidine Derived Beta 3 Adrenergic Receptor Agonists. US 2012/0225886 A1, 2012.

(27) Reeves, J. T.; Gallou, F.; Song, J. J.; Tan, Z.; Lee, H.; Yee, N. K.; Senanayake, C. H. *Tetrahedron Lett.* **2007**, *48* (2), 189–192.

(28) Singh, R. P.; Shreeve, J. M. *J Org Chem* **2000**, *65* (18), 3241–3243.

(29) Singh, R. P.; Cao, G.; Kirchmeier, R. L.; Shreeve, J. M. *J. Org. Chem.* **1999**, *64* (8), 2873–2876.

(30) Wang, X.; Bhatia, P. A.; Daanen, J. F.; Latsaw, S. P.; Rohde, J.; Kolasa, T.; Hakeem, A. A.; Matulenko, M. A.; Nakane, M.; Uchic, M. E.; Miller, L. N.; Chang, R.; Moreland, R. B.; Brioni, J. D.; Stewart, A. O. *Bioorganic Med. Chem.* **2005**, *13* (15), 4667–4678.

(31) Rosen, T.; Nagel, A. A.; Rizzi, J. P.; Ives, J. L.; Daffeh, J. B.; Ganong, A. H.; Guarino, K.; Heym, J.; McLean, S.; Nowakowski, J. T. *J.Med.Chem.* **1990**, *33* (10), 2715–2720.

(32) Sundman-Eriksson, I.; Allard, P. *J. Affect. Disord.* **2002**, *71* (1–3), 29–33.

(33) Massaro, A.; Mordini, A.; Reginato, G.; Russo, F.; Taddei, M. *Synthesis (Stuttg).* **2007**, No. 20, 3201–3204.

(34) Yoneyama, H.; Usami, Y.; Komeda, S.; Harusawa, S. *Synth.* **2013**, *45* (8), 1051–1059.

(35) Das, B.; Reddy, C. R.; Kumar, D. N.; Krishnaiah, M.; Narender, R. *Synlett* **2010**, No. 3, 391–394.

(36) Vorona, S.; Artamonova, T.; Zevatskii, Y.; Myznikov, L. *Synth.* **2014**, *46* (6), 781–786.

(37) Demko, Z. P.; Sharpless, K. B. *Org. Lett.* **2002**, *4* (15), 2525–2527.

(38) Lemieux, R. M.; Barbosa, A. J. del M.; Bentzien, J. M.; Brunette, S. R.; Chen, Z.; Cogan, D.; Gao, D. A.; Heim-Riether, A.; Horan, J. C.; Kowalski, J. A.; Lawlor, M. D.; Liu, W.; McKibben, B.; Miller, C. A.; Moss, N.; Tschantz, M. A. X. Z.; Yu, H.; Yu, Y. Derivatives of [6,7-dihydro-5H-imidazo[1,2-A]imidazole-3-carboxylic acid amides. WO 2009/070485 A8, 2009.

(39) Morriello, G. J.; Chang, L.; Edmondson, S. D. Novel pyrrolidine derived beta 3 adrenergic receptor agonists. WO 2012058130, 2012.

(40) Shao, X.; Hoareau, R.; Runkle, A. C.; Tluczek, L. J. M.; Hockley, B. G.; Henderson, B. D.; Scott, P. J. H. *J. Label. Compd. Radiopharm.* **2011**, *54* (14), 819–838.

Chapter 4

[^{18}F]Fludeoxyglucose (FDG): Use and Production

A. Introduction

PET radiochemistry exists at the intersection between organic chemistry and nuclear medicine. The short-lived radionuclides used make the synthesis of PET radiopharmaceuticals for clinical care quite unique. They are made on demand, and frequently used within minutes to a few hours after end-of-synthesis. Since PET radiopharmaceuticals are used in clinical care, they need to be manufactured according to current Good Manufacturing Practice (cGMP), and there are strict quality control testing requirements before a dose can be released to the clinic. In addition to understanding the synthesis and pre-clinical evaluation of new PET radiopharmaceuticals as outlined in the earlier Chapters of this thesis, appreciation of how PET radiopharmaceuticals are synthesized for clinical use has also been an essential part of my graduate student training. Thus, during my tenure as a graduate student, I was trained in the production of [^{18}F]FDG for clinical use at the University of Michigan hospital. As FDG is an important PET tracer for molecular imaging, this chapter describes the history of FDG, updates to the production of FDG that I was involved in and uses of the radiotracer.

[^{18}F]FDG is by far the most produced and used radiotracer. This fluorinated glucose derivative is a non-specific trapped metabolite that images increase (or decrease) of metabolic activity. First evaluated in humans at Brookhaven National Laboratory in

1976,[1,2] FDG was the first commonly used PET radiopharmaceutical, and it is still widely used to this day.

i. Development and use of [^{18}F]FDG as a radiotracer

The development of [^{18}F]FDG began in 1969 with the synthesis of the non-radioactive isotopolog 2-deoxy-2-fluoro-D-glucose by Pacák and coworkers.[3] Almost 10 years later, a collaboration between researchers at Brookhaven National Laboratory (BNL) and the University of Pennsylvania culminated in the first reported synthesis of [^{18}F]fludeoxyglucose, known today as [^{18}F]FDG.[1] Using nucleophilic [^{18}F]F_2 gas (produced by the ^{20}Ne(d,α)^{18}F nuclear reaction), researchers were able to fluorinate 3,4,6-tri-O-acetyl-D-glucal (Scheme 4-1). Interestingly, Ido and coworkers reported a dual radiofluorination across the double bond in the glucal precursor. It could be argued today that the intermediates formed were only radiofluorinated at one position due to our knowledge that [^{18}F]F_2 gas is a low specific activity [^{18}F]fluorine source comprising of ^{18}F-

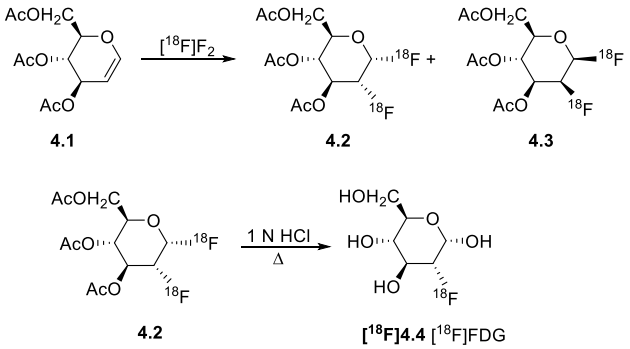

Scheme 4-1: First synthesis of [^{18}F]FDG using [^{18}F]F_2 gas.

^{19}F, Figure 4-1. This produced a mixture of two isomers **4.2** and **4.3**, which were separated by gas-liquid partition chromatography (GLPC); hydrolysis with HCl, followed by three column purifications (ion retardation for neutralization, alumina column for excess fluoride removal, and another ion retardation column), gave [^{18}F]FDG, **[^{18}F]4.4**, in 8%

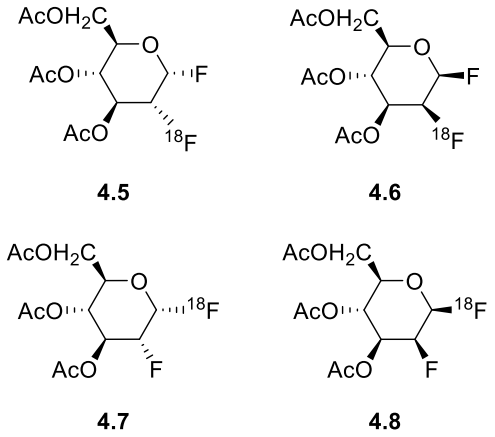

Figure 4-1: Alternative by-products that may have been formed in Scheme 4-1.

radiochemical yield. While this yield can be seen as impressive for a novel radiotracer (some novel tracers are produced in 1-3% radiochemical yields), today [^{18}F]FDG is regularly produced in yields in excess of 70% using nucleophilic [^{18}F]fluoride in automated synthesis modules. The nucleophilic fluorination reaction (Scheme 4-2) uses mannose triflate precursor **4.9**, which is radiofluorinated in a nucleophilic substitution reaction with [^{18}F]KF prepared by azeotropic drying of cyclotron produced [^{18}F]fluoride in the presence of the crown ether Kryptofix-2.2.2 ($K_{2.2.2}$), potassium carbonate (K_2CO_3), water and acetonitrile. The resultant 2-[^{18}F]-fluo-1,3,4,6-tetra-O-acetyl D-glucose ([^{18}F]FTAG, **4.10**) is then trapped on a tC_{18} cartridge and converted to [^{18}F]FDG through the alkaline hydrolysis of the acetyl protecting groups with 2 N NaOH. It is neutralized with a citrate

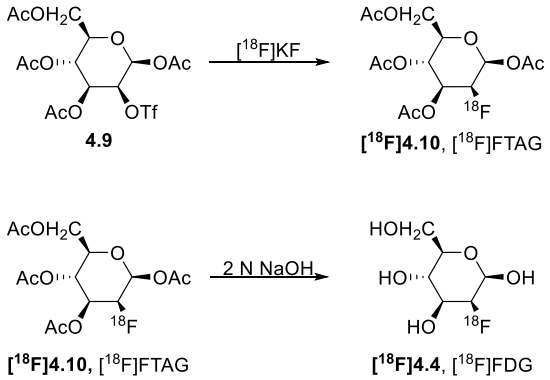

Scheme 4-2: Synthesis of [^{18}F]FDG as it takes place in the GE FASTLab DUO Citrate cassette.

buffer before [^{18}F]FDG is eluted off the tC$_{18}$ cartridge using water. For further purification the neutralized [^{18}F]FDG solution is passed through a tC$_{18}$ plus cartridge for the removal

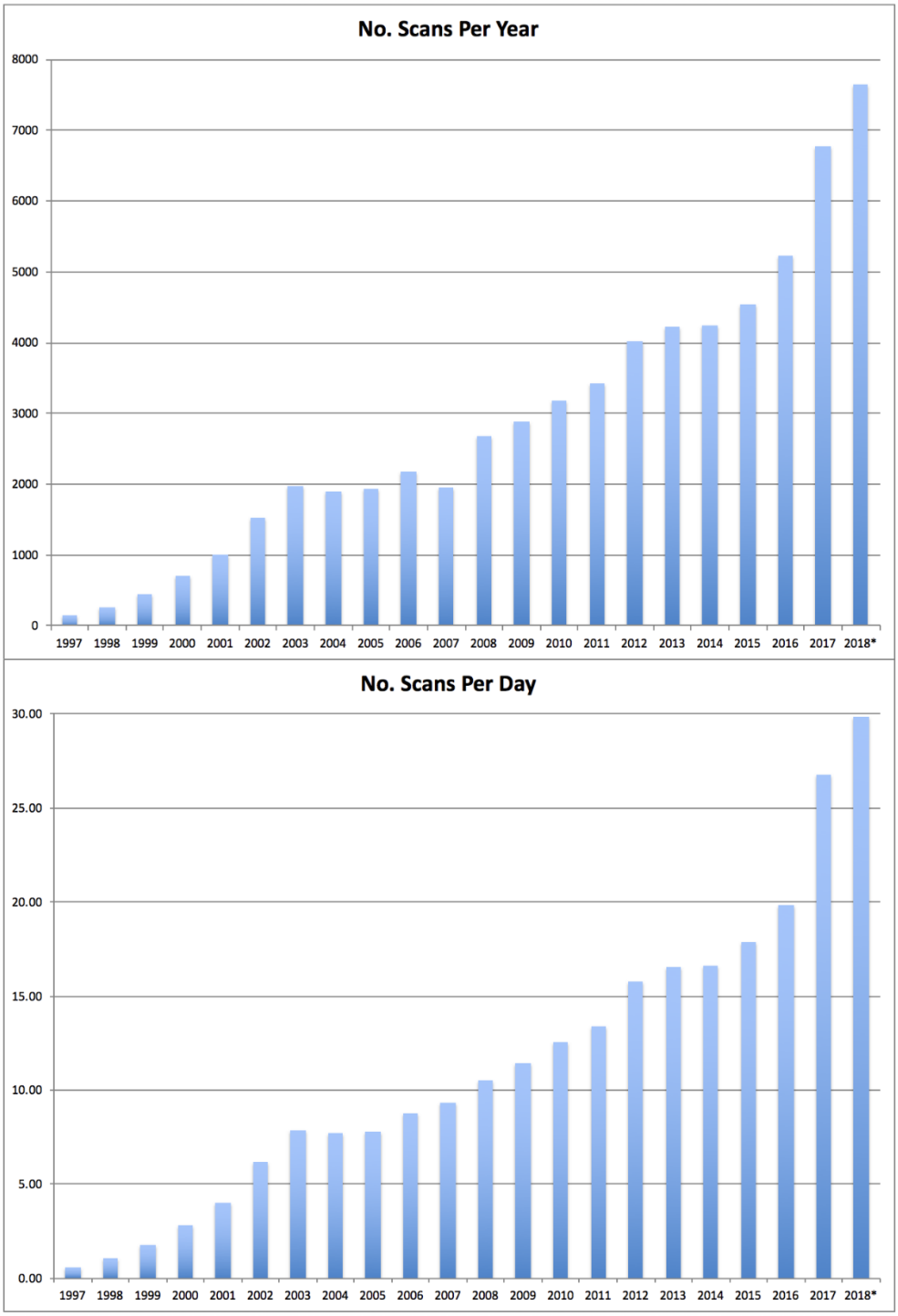

Figure 4-2: Clinical-PET utilization at the University of Michigan PET Center (*estimated).

of non-polar by-products as well was partially hydrolyzed intermediates. Final purification is through an alumina cartridge to remove any residual unreacted [^{18}F]fluoride ions.

The first in human scan of [^{18}F]FDG took place in August of 1976 at the Hospital of the University of Pennsylvania in collaborating with scientists at BNL,[4] and its use increased with the advancement of the technology of cyclotrons for production of radionuclides, as well as the development of more sophisticated PET imaging scanners (see Chapter 1). 1994 saw approval of FDG by the US FDA,[5] and the radiotracer was indicated for use in oncology,[6–8] neurology,[9,10] and cardiology.[11–13] Following approval, reimbursement by the Centers for Medicare and Medicaid has led to steady growth in FDG PET, and the tracer continues to be used almost 25 years later. Reflecting this, an estimated 1.945 million FDG PET (and PET/CT) studies occurred in the United States in 2017, an increase of 15% from 2015, and makes FDG PET a multimillion dollar market in its own right.[14] The last 20 years have shown a steady increase in demand for clinical PET scans within Michigan Medicine (Figure 4-2). In 1997, three years after FDA approval of FDG, 151 patients received clinical PET scans (0.6 per day over 250 scanning days), compared to 6,777 in 2017 (26.79 per day over 253 scanning days), a 45-fold increase in scans each year over 20 years. In addition, Michigan Medicine has received a number of inquiries about the possibility of our center supplying FDG to various outside entities.

ii. Clinical Utility and Importance of [^{18}F]FDG

As a fluorinated glucose analog, [^{18}F]FDG is able to take advantage of the increased glucose uptake of tumors. Similar to glucose, [^{18}F]FDG is taken up by cells through the cell membrane assisted by glucose transporter 1 (GLUT1), and then is

phosphorylated by hexokinase yielding FDG-6-phosphate (FDG-6-P). At this point, the FDG-6-phosphate is now trapped inside the cell: once phosphorylated it cannot leave the cell, and it cannot be further metabolized as the 2'-hydroxyl group of glucose has been replaced with [^{18}F]fluorine and prevents FDG from entering the glycolysis pathway (Figure 4-3). In healthy cells, FDG-6-P can be dephosphorylated by the enzyme glucose-6-phosphatase to regenerate FDG. Levels of glucose-6-phosphatase are reduced in cancer cells resulting in preferential accumulation of [^{18}F]FDG-6-phosphate in tumors.[15] Notably,

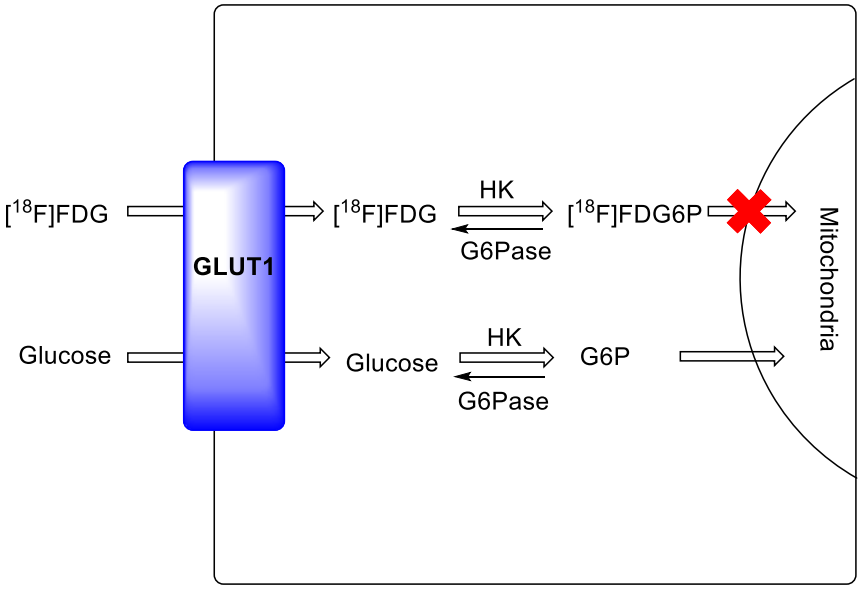

Figure 4-3: Biology of FDG and glucose uptake into cells.

accumulation of [^{18}F]FDG does not happen in tumors alone, and can also be found in sites of inflammation or infection.[16]

Not long after [^{18}F]FDG was approved by the FDA in 1994, it found utility in the imaging of multiple cancer types; it is instrumental in the differentiation between benign and malignant lesions, determining the stage of malignant lesions, as well as detecting any recurrence and monitoring treatment progression.[8] A comprehensive discussion of the use of FDG in tumor imaging is beyond the scope of this thesis, but its use can be

highlighted through several representative examples. In 2016, Avril and colleagues discussed the usefulness of [^{18}F]FDG in monitoring treatment response of breast cancer in a review covering multiple clinical studies.[6] Two notable studies evaluated the usefulness in HER2 positive breast cancer as well as triple negative breast cancer (TNBC), the two most aggressive subtypes. Groheux and coworkers demonstrated that in HER2 positive breast cancer patients, [^{18}F]FDG imaging was a good early indicator of whether the patients would respond positively to neoadjuvant therapy or if they were at high risk for residual tumors.[17] This can be seen in comparing Figure 4-4 to Figure 4-5; figure 4-4 shows a patient who responded well to two cycles of therapy (SUV A and B, 16.1, compared with SUV C and D, 1.6), while figure 4-5 shows a patient with a small increase in SUV (SUV A and B, 11.1, compared with SUV C and D, 12.7). After this treatment monitoring scan, a new therapy was initiated for the patient in figure 4-5. Although cancer-specific PET agents are continually being developed and moved to the clinic (for example [^{68}Ga]PSMA and [^{11}C]choline for the imaging of prostate cancer[18]), [^{18}F]FDG continues to be the most employed radiotracer for oncology PET imaging to date.

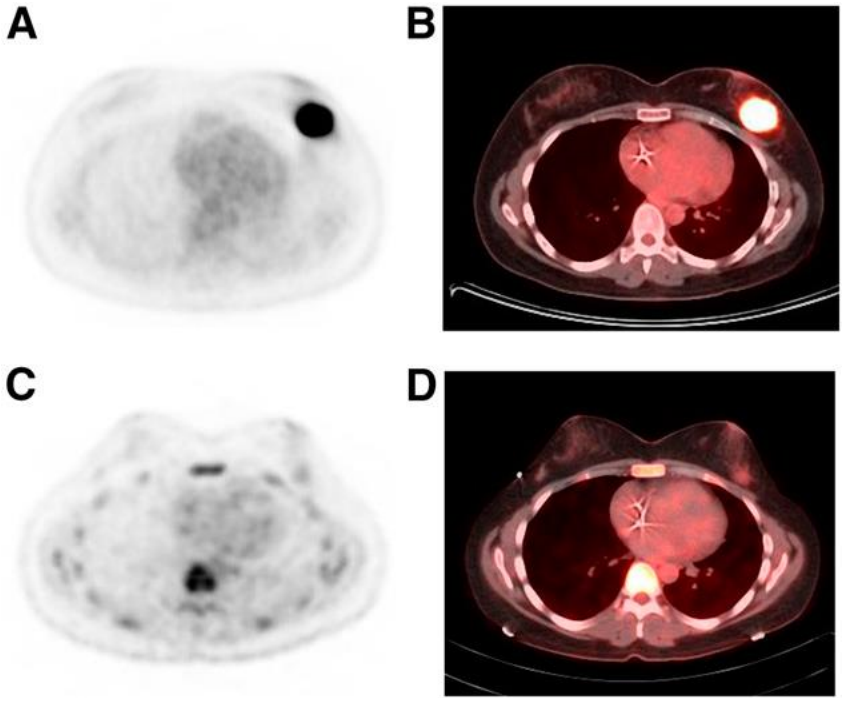

Figure 4-4: :(A and B) Baseline [^{18}F]FDG PET (A) and fused [^{18}F]FDG PET/CT (B). (C and D) After 2 cycles of neoadjuvant therapy, significant reduction in tumor [^{18}F]FDG uptake, 10-fold decrease in SUV was seen in [^{18}F]FDG PET (C) and fused [^{18}F]FDG PET/CT (D). This research was originally published in JNM. Avril, S. et al. [^{18}F]FDG PET/CT for Monitoring of Treatment Response in Breast Cancer. J Nucl Med. 2016;57:34S-39S. © SNMMI.

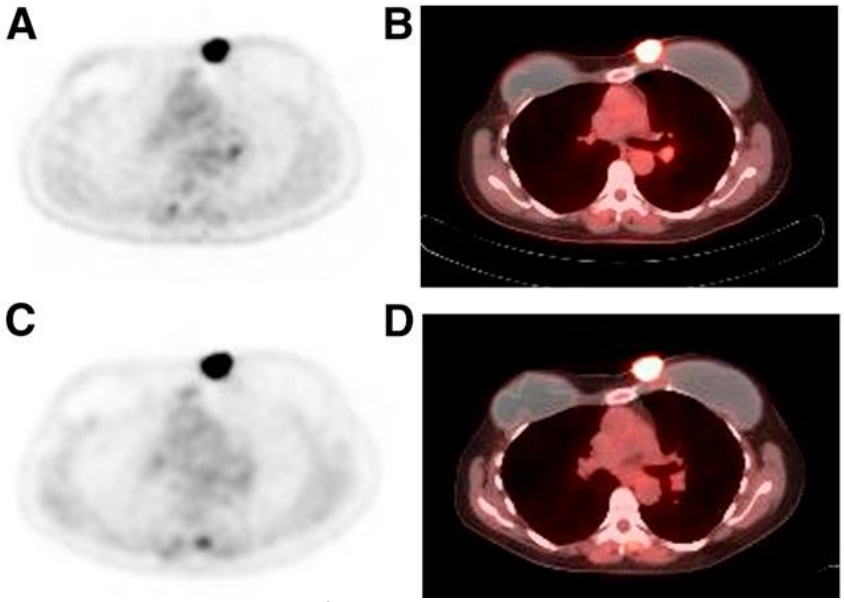

Figure 4-5:(A and B) Baseline [^{18}F]FDG PET (A) and fused [18F]FDG PET/CT (B). (C and D) After 2 cycles of neoadjuvant therapy, with little change in SUV, was seen on [^{18}F]FDG PET (C) and fused [^{18}F]FDG PET/CT (D). This research was originally published in JNM. Avril, S. et al. [^{18}F]FDG PET/CT for Monitoring of Treatment Response in Breast Cancer. J Nucl Med. 2016;57:34S-39S. © SNMMI

Use of [^{18}F]FDG for the imaging of cardiac sarcoidosis takes advantage of the tendency for the tracer to accumulate in inflammatory tissue. Cardiac sarcoidosis is the accumulation of inflammatory cells into non-caseating granulomas on the heart.[12] Currently immunosuppressants are used for the treatment of cardiac sarcoidosis, although data to support this is limited. Ahmadian and coworkers sought to evaluate the effectiveness of this treatment via [^{18}F]FDG PET imaging of patients prior to and after immunosuppressant therapy.[11] Although a decrease in [^{18}F]FDG uptake was observed visually in patients post-therapy, more studies are necessary to develop a quantitative method for interpretation of these types of scans.

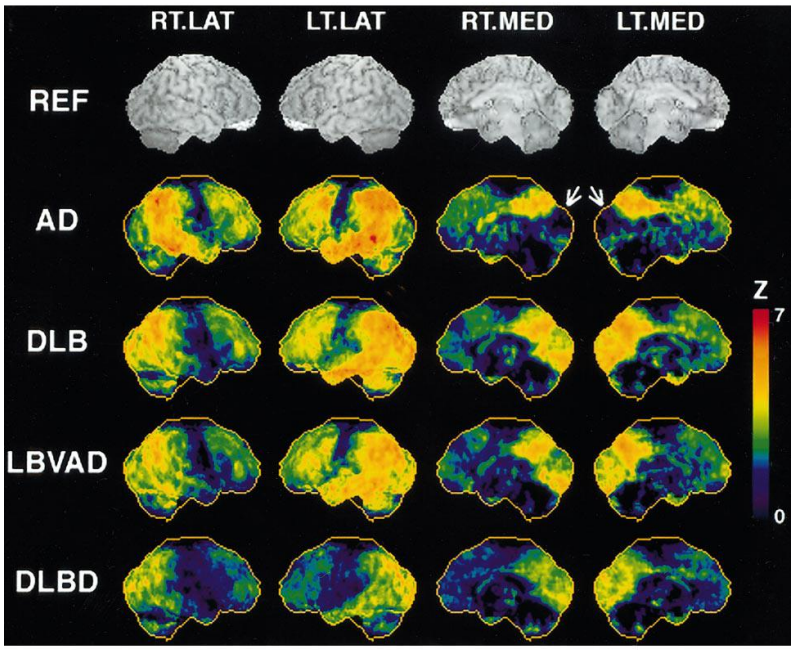

Figure 4-6: Example images of how FDG can be used to stratify different types of dementia. Uptake between Alzheimer's disease (AD) and Dementia with Lewy Bodies (DLB) differs especially in the lateral cortices (arrows). Other dementia types represented are Lewy body variant of Alzheimer's disease (LBVAD), and pure diffuse Lewy body disease (DLBD) This research first published in Minoshima, S.; Foster, N. L.; Sima, A. A. F.; Frey, K. A.; Albin, R. L.; Kuhl, D. E. Ann. Neurol. **2001**, 50 (3), 358–365.

While [^{18}F]FDG works as a positive indicator for cancer, in neurodegeneration a decrease in [^{18}F]FDG accumulation indicates an area of lower brain activity. Alzheimer's disease (AD), accounts for 50-60% of all dementia cases, and is the fourth leading cause

of death in individuals over 65 years.[19] Minoshima and coworkers found in 2001, that it is possible to differentiate between AD and Dementia with Lewy Bodies (DLB) using FDG; an important characterization, as the dementias are caused by different protein aggregates, and therefore require different treatment, Figure 4-6.[20]

Outside of dementia, [^{18}F]FDG is also used for imaging of patients with partial epilepsy.[21] Temporal lobe epilepsy (TLE) is the most common of the types of partial epilepsy in adults; it is often medically intractable, leaving the patients with only the option of brain surgery. [^{18}F]FDG PET imaging has assisted in pre-operative evaluations where magnetic resonance (MR) is not successful in identifying the epileptic focus.[22]

iii. cGMP methods & Regulation of FDG and other PET drugs

[^{18}F]FDG was developed in an academic setting as a research tool. As it transitioned into clinical use, it was manufactured according to the US Pharmacopeia and regulated by State Boards of Pharmacy but was outside the jurisdiction of the FDA. When [^{18}F]FDG was found to have widespread clinical utility, and the use of the radiotracer in a clinical setting increased drastically, the FDA determined that it was necessary to regulate the manufacturing of [^{18}F]FDG, as well as other radiopharmaceuticals, in a way similar to traditional drug manufacturing. In 1995, the first rule for current Good Manufacturing Practices (cGMP) in PET drugs was proposed.[23] As stated earlier, radiopharmaceuticals are unique among pharmaceuticals in that they contain short-lived radioisotopes, making the manufacturing, and regulation of them drastically different in some respects to traditional therapeutic pharmaceuticals. These short-lived radioisotopes necessitate the daily synthesis of the tracers, while limiting the shelf life or time window that they can be used. These obvious differences made it incredibly difficult for PET centers to adhere to

the same regulations in place at traditional pharmaceutical manufacturers, such as pre-release sterility testing.[24] The FDA regulation of PET drugs was in limbo until 1997, when a Congress initiated bill, the Food and Drug Modernization Act (FDAMA), included a provision directing the FDA to create a new pathway for the approval of PET drugs as well as cGMP for the production thereof "[in] order to take account of the special characteristics of compounded positron emission tomography drugs and the special techniques and processes required to produce these drugs."[25] Three years after this bill was signed into law by President Bill Clinton, the FDA published its own review of the PET literature in the Federal Register.[26] This document allowed PET drug manufacturers to apply for an ANDA by referencing the Federal Register notice for safety and effectiveness of the produced drugs, instead of applying for a New Drug Application (NDA), which is lengthier, requires extensive clinical trial data and is subject to high filing fees.[27] This is especially of interest in academic hospital settings, such as at the University of Michigan. Early site-specific NDA approvals served as a precedent for other sites of PET drug manufacturing; by 2011, not just [^{18}F]FDG, but the use of [^{18}F]NaF (used for bone scans), and [^{13}N]ammonia (used in cardiac imaging) were approved.

Current good manufacturing practice guidelines are useful for the production of radiopharmaceuticals for standard of care, ensuring safety through the testing of each human dose for purity, strength, identity, and quality. cGMP guidelines (coupled with NDAs or ANDAs) are heavily responsible for the safety and regulation of PET drug manufacturing in the United States today. These are culminated in title 21 of the *Code of Federal Regulations* part 212 (21 CFR 212).[27] For PET drugs that are used for clinical research purposes (i.e. they are not used for standard of care and insurance companies

are not charged), manufacturers are required to have FDA approval through an investigational new drug (IND) application, or have local Radioactive Drug Research Committee Approval if the studies are for basic science purposes.

In the United States, Federal agencies besides the FDA involved in regulating PET drugs include the Nuclear Regulatory Commission (NRC), while local regulatory bodies such as Radiation Safety Devices (RSS) and Occupational Safety and Environmental Health (OSEH) provide regulatory oversight at the University of Michigan.

B. Results and Conclusions

i. Current Methods for FDG production

Due to the widespread use and need for production of [^{18}F]FDG, multiple companies offer synthesis modules and reagent kits or cassettes so that FDG manufacturers and researchers across the globe are able to produce [^{18}F]FDG according to cGMP, as well as other pertinent regulatory guidelines. Recently there has been an update in the technology for the production of [^{18}F]FDG, with the introduction of the General Electric (GE) FASTLab 2, Figure 4-7. This new technology enables PET manufacturing sites to purchase assorted cassettes to produce different radiotracers, including FDG. Specifically, the [^{18}F]FDG Duo Citrate cartridges, Figure 4-8, allow for the synthesis of two doses per cassette, using only one synthesis modules and therefore one hot-cell (lead-lined box where automated synthesis modules are housed). Where before labs like the facility at U of M would use two hot-cells and two synthesis modules each day, only one is now necessary.

Figure 4-7: FASTLab 2 synthesis module. Image courtesy of GE.

Before the implementation of the FASTLab modules, each of two mini-cells (lead lined cells, smaller than the other “hot-cells”) housed a TracerLab MX-FDG synthesis module. Reagent kits were purchased from either ABX or Rotem companies that were compatible with these synthesis modules. Each day, both modules would be used, one for the morning dose, and one for the afternoon dose; this in turn irradiated both of these mini-cells. Now, with the implementation of the FASTLab 2 synthesis module using the FDG Duo Citrate cassette, it is possible to produce both the morning and the afternoon doses from a single module and mini-cell. The introduction of the FASTLab 2 synthesis modules has simplified the daily routine of [^{18}F]FDG production chemists and increased the yields produced, allowing the Michigan Medicine Radiology department to complete more scans and extend their scanning hours, better serving patient need.

ii. Production of [18F]FDG using the FASTLab 2 Synthesis Module

The [^{18}F]FDG synthesis begins with the cleaning of the mini-cell. This includes removal of the previously used cassette and disposal of it in an appropriate radioactive waste container, as well as emptying of the main waste container and removal of old [^{18}O]-water from the cyclotron target. When the cassette and waste has been removed, the inside of the mini-cell is cleaned with non-shedding wipes and sterile, 70% isopropyl alcohol (IPA); this is done once per day, before the first synthesis in a given mini-cell. For each synthesis of [^{18}F]FDG there is a production chemist, and a quality control (QC) chemist. The production chemist begins by starting the FASTLab automated synthesis program and assembling a new cassette in a Class 5 laminar flow hood which has also

Figure 4-8 FASTLab Duo Citrate cassette for [^{18}F]FDG synthesis. Image courtesy of GE.

been cleaned with sterile 70% IPA. Assembly of the FASTLab cassettes is simple and straightforward; it requires the attachment of a sterile filter to the air inlet and visual inspection of each of the pre-assembled reagent vials, cartridges and syringes. The cassette can then be installed on the FASTLab module, two product transfer lines are attached to the cassette and fed through to the product collection area, and the program

can be directed to initiate tests on the cassette. These tests are to ensure proper activation of syringes, and integrity of the cassette.

While the tests are running, the production chemist again cleans the laminar flow hood with sterile 70% IPA and assembles the intermediate dose vial. This assembly includes a 30 mL sterile vial connected to a 10 mL sterile vent vial and a 4-way stopcock. To the 30 mL vial is added sterile water and sodium phosphate buffer. These are to ensure that each dose has the appropriate osmolality (270-330 mOsmol/kg, as indicated by the ANDA). The 10 mL sterile vent vial is a vial connected to an extension line fitted with a 0.20 µm filter to ensure that the intermediate vial can vent without chance of overspill of radioactive product. The 4-way stopcock is how the whole intermediate/vent assembly is attached to the cassette via a 21" product transfer line and to the dispensing cassette used for final purification and dose separation. The 30 mL vial is placed into a lead "pig" with the extension lines and vent vial on the outside; the stopcock is connected to the appropriate product transfer line (depending on first or second synthesis). (A lead "pig" is a lead vial holder which is used for shielding radioactive samples when they must be transported).

During this time the QC chemist initiates irradiation of the cyclotron target for production of [^{18}F]fluoride (starting the beam). The time and current of this beam varies based on factors including how much activity the cyclotron has been producing, or how much activity the PET imaging suite has indicated they need. The beam current is typically between 40-50 µA, and the beam is typically 20-30 minutes long. While the beam is running, and the production chemist is preparing the synthesis module, the QC chemist will start the gas chromatography so that reference standards for system suitability can

be run prior to the dose sample. They will also set up the rest of the necessary QC tests. It is also necessary to strip the Manuela (a dispensing hot-cell which houses the drug dispensing module) and clean it with sterile 70% IPA. The production chemist will, for the third and final time, clean the laminar flow hood with sterile 70% IPA, and assemble the dispensing cassette. Assembly of the dispensing cassette includes ensuring all connections on the pre-assembled cassette are tight and inserting vent needles into each of four vials before attaching them to the cassette using the included needles. These vials,

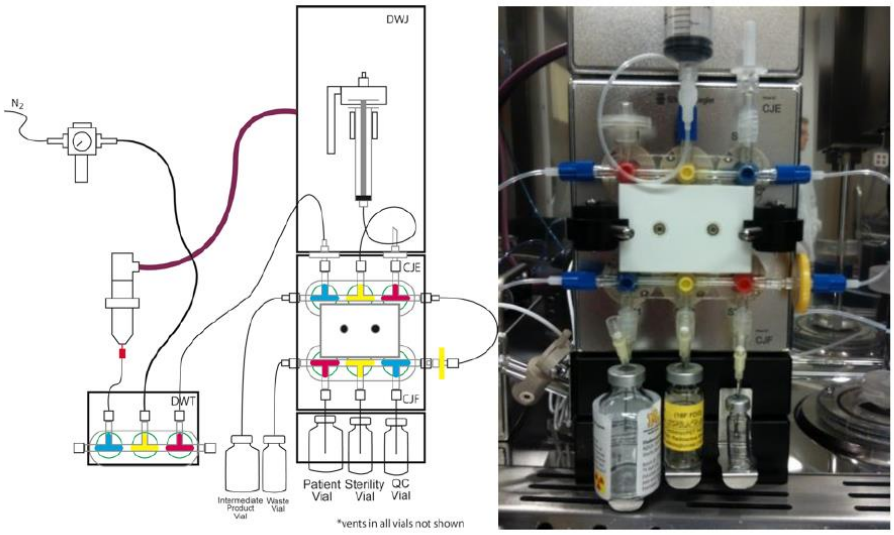

from left to right, are the waste vial, dose vial (30 mL), sterility test vial (10 mL) and the QC vial (2 mL). This assembly must be aseptic and sterile; to monitor this two agar touch plates are placed in the hood and the chemist will place each finger on the left and right touch plates. Monitoring the left and right hand separately can assist in troubleshooting a method if there is consistent contamination on only a single hand. The assembled dispensing cassette can then be mounted onto the dispensing module (Figure 4-9) in the clean Manuela following the prompts on the dispensing program.

The sterile dispensing cassette aliquots a small volume (~0.5 mL) for immediate QC testing and 2.5 mL for sterility testing to be completed later. Lastly, the remaining volume that is the patient dose (24-26.0 mL) is dispensed into a sterile dose vial. The sterile filter on the dispensing cassette is the first QC test; ensuring that the filter is intact is of the utmost importance in producing a safe and sterile dose. When dispensing is finished, the QC vial is given to the QC chemist so that they may begin testing. The sterility vial is placed in a lead pig so that sterility can be completed when the dose has been allowed to decay. The dose vial is weighed inside the Manuela using a simple balance, and the dose activity measurement is taken in the dose calibrator in the hot cell. The sterile filter that the dose was dispensed through is tested by a bubble point test. This requires the filter to be connected to a gas line, then to a needle, and the needle placed in water. Nitrogen is then pushed over the filter until a steady stream of bubbles appears. For the filter to pass, it is necessary to hold to a pressure above 30 psi.

iii. Quality Control of [^{18}F]FDG

QC testing takes about 30 minutes. Prior to the synthesis of FDG, when the cyclotron beam is running, the QC chemist assembles the tests they will need in a lead shielded work area as described above. This includes pH paper, a Kryptofix test strip, TLC plate spotted with FDG standard compound, a labeled vial for GC sample, a labeled vial for half-life testing, and a plastic tube containing 3.9 mL sterile water for both TLC and endotoxin testing. The QC chemist takes up the dose (~0.4 mL) and deposits 0.1 mL into the plastic tube (creating a dilution of 1:40), 0.1 mL into the GC vial, 0.1 mL into the half-life vial, adds one drop to the Kryptofix test strip, and three drops across the pH test strip.

Then the GC and half-life tests are started, followed closely by the endotoxin test, as these take the longest amount of time. The diluted sample is spotted onto the TLC plate, and the TLC plate set up to run. Then sterile water and Kryptofix standard are spotted on to the Kryptofix test strip below the dose spot. At this point all tests should be running, and the chemist can record them each as they are completed (pH and Kryptofix being the first as they have immediate readouts). Each QC chemist has their own order of operations to ensure that each test is done and in a timely fashion.

Testing of FDG doses is conducted according to the guidelines outlined in 21CFR212. Daily QC testing consists of visual inspection (doses must be clear, colorless and free of particulates), pH (pH paper, must be 4.5 – 7.5), residual $K_{2.2.2}$ (spot test, must be ≤50 μg/mL), radiochemical purity (TLC, must be >90%), radiochemical identity (TLC, R_F of radiotracer and reference standard match), radionuclidic identity (half-life must be 105 – 115 min), residual solvent analysis (GC, <410 ppm MeCN; <5000 ppm EtOH), sterile filter integrity (bubble point, ≥50 psi), bacterial endotoxin analysis (Endosafe, ≤175 endotoxin units / dose), and sterility per USP Chapter 71 (fluid thioglycolate media and soybean casein digest agar media tubes, no evidence of microbial growth found). Additional periodic QC testing including radionuclidic purity (MCA, ≥99.5%) and osmolality (osmometer, 270-330 mOsmol/kg) was conducted quarterly. All doses of FDG discussed in this article met or exceeded all of these quality control release criteria and were stable for 24 h after end-of-synthesis (EOS).

Once all QC testing is completed and all tests on a given batch of FDG passed, the dose vial is placed into a lead pig, which is placed into a second pig as part of a Department of Transportation (DoT) certified radioactivity transportation box. Before the

dose can be delivered to the hospital (via a route approved by RSS) the dolly and box containing the dose must be monitored and swiped to ensure the absence of any radioactive contamination on the surface. These numbers are documented on a transport record that is signed by the nuclear pharmacist who receives the dose in the hospital so there are records of how much activity is delivered.

For the second dose of [^{18}F]FDG, typically the afternoon dose, the same procedure is followed except for the initial assembly of the FASTLab cassette, instead the production chemist is able to follow the prompts on the computer to prepare the synthesis module for the second synthesis. A new intermediate and vent vial can be attached to the second product transfer line, and the Manuela will be carefully stripped of the previous dispensing cassette and cleaned in preparation for the next synthesis.

iv. Updating the [^{18}F]-cyclotron target and FDG Synthesis Modules

For the last ten years, the U of M PET center has generated fluorine-18 on a GE PETTrace cyclotron equipped with Ag fluorine-18 targets, and manufactured FDG using the GE TRACERLab$_{MX\text{-}FDG}$ synthesis module. Daily production of [^{18}F]FDG began by generating [^{18}F]fluoride with the PETTrace cyclotron via the ^{18}O(p,n)^{18}F reaction. The previously used Ag target was filled with [^{18}O]H_2O (~1.6 mL) and bombarded with a 40 μA proton beam for 22 minutes. This nuclear reaction produced 1011 ± 116 mCi of [^{18}F]fluoride. FDG was then prepared by nucleophilic substitution fluorination of mannose triflate (**4.9**), followed by base hydrolysis (Scheme 4-2). Yields of [^{18}F]FDG using this method were 527 ± 95 mCi (n = 2137), corresponding to 52% non-corrected radiochemical yield. As mentioned earlier, there has been a drastic increase in patients

scanned per day at Michigan Medicine (Figure 4-3). Doses of ~500 mCi, twice a day, were adequate when scanning up to ~15 or 16 patients per day. However, the increase in daily scans, as well as inquiries about the possibility of our center supplying FDG to a number of outside entities dictates a need for higher yielding doses of [^{18}F]FDG. During this time of incredible growth, GE released an “end-of-life” announcement for the TRACERLab$_{MX-FDG}$ due to obsolete parts. As a result, it was necessary to update to our FDG production operation with the replacement of two TRACERLab$_{MX-FDG}$ modules with FASTLab 2 synthesis modules.

Transitioning [^{18}F]FDG synthesis from TRACERLab$_{MX-FDG}$ modules to FASTLab 2 occurred without incidence. Replacement of both modules was staggered, safeguarding clinical production, but was completed within 7 business days. In accordance with FDA regulations, the update was documented in the annual report for our ANDA. As mentioned above, FASTLab cassettes are available for multiple PET tracers. The FDG DUO Citrate cassettes allow manufacture of two batches of FDG within a 26-h period. With the installation of two FASTLab 2 modules and choice of DUO cassettes our production capacity increased to 200% of our previous levels. Before the installation of the FASTLab 2 modules, FDG production capacity of our lab doubled from 2 batches of FDG per day on 2 x TRACERLab$_{MX-FDG}$ modules. Now it is possible to produce 4 batches of FDG per day on 2 x FASTLabs. A combination of the size of the new modules (their size allows installation in existing mini-cells), with the availability of the DUO Citrate cassette allowed for increase of capacity without the need to install costly new hot-cells in the laboratory. Also due to the relatively small size of the modules, it would have been possible to install both into a single mini-cell; this would have left one of the mini-cells

unoccupied and available for other applications. However, splitting the FASTLabs between min-cells allows for uninterrupted [^{18}F]FDG production while maintenance is performed on one FASTLab, and also decreases the FDG chemists' radiation exposure as it is possible to give over 24 hours for decay of any residual radionuclides before it is necessary to open and clean the mini-cell. The workflow and inventory management has also been simplified by this transition, as all the reagents needed for two FDG production runs are contained in a single FASTLab DUO Cassette. Compared to ordering, receiving and utilizing separate hardware kits, reagent vials, and other components required for 2 separate runs a day using the TRACERLab$_{MX\text{-}FDG}$ modules, the FASTLab modules and cassettes are obviously an upgrade.

With the new FASTLab modules installed, and an anticipated increase to ~25 patients scanned with FDG per day at our facility, the beam time was increased to 30 min for FDG production. Thus, bombarding the Ag target containing ~1.6 mL of [^{18}O]H_2O with a 40 µA proton beam for 30 min produced 1179 ± 106 mCi of [^{18}F]fluoride. FDG was then produced using the FASTLab 2 in yields of 839 ± 77 mCi (n = 383), corresponding to 71% non-corrected RCY. This observed ~20% increase in yield was an excellent reward for the optimized manufacturing process developed for the FASTLab.

A short 6 months after the installation and validation of the FASTLabs (late 2017), the number of patients scanned with FDG per day was again increased; this time to 30 – 32 per day. One method for producing larger doses of FDG is to increase the cyclotron beam time, in turn delivering more radioactivity to the FASTLabs for production of higher activity doses of FDG. Due to the complex, and often incredibly full, schedule of the PET Center at U of M, running the cyclotron for hours a day for FDG alone is not an option. It

was necessary to determine the best way to increase the amount of FDG produced, while still maintaining the production of 4 radiotracers for routine clinical use, 35 other radiotracers produced for clinical research, as well as basic science research developing radiochemistry methodology and novel PET radiotracers. It is also not possible to deliver doses more than 750 mCi of FDG, due to the compatibility of the multi-dose Bayer Medrad® Intego PET Infusion System (Figure 4-10). Any dose above 700-750 mCi cannot be reliably shielded, and proper dose preparation could be compromised (Bayer Medrad Intego Brochure, 2017). In short, we needed an efficient way to increase our yields of [^{18}F]fluoride from the cyclotron (and the corresponding yields of FDG), without running a long beam (≤30 min), such that 2 FDG beams (morning and afternoon) could be efficiently slotted in around 10 – 12 other beams that are run on our cyclotron during a typical work day.

Fortunately, in January 2018, a second round of updates occurred at the U of M PET Center. The PETTrace cyclotron underwent the manufacturer-recommended ten-year life extension and refurbishment (TYLER) maintenance. This maintenance overhaul updated numerous aspects of the cyclotron, including updating the outdated Ag body fluorine-18 targets with new high yield niobium (Nb) body self-shielded fluorine targets. These new Nb targets use 2.7 mL of [^{18}O]H_2O and can be run on our updated system at increased beam currents (up to 85 μA) on a single target, allowing the production of more activity in the same amount of time. Self-shielding refers to the tungsten-copper alloy in which the target is housed; this alloy is specified to lead to a 10 to 20-fold reduction in exposure resulting from the target foil, and 100-fold reduction in exposure due to any residual ^{18}F in the target.

With the new Nb targets in place, the Center's goal was to generate ~950 mCi of FDG at end of synthesis (EOS). Removal of sterility (2.5 mL) and QC (0.5 mL) samples, would provide ~850 mCi in the patient vial to be transported to the PET imaging suite. A further 0.5 h can be allotted for radioactive decay for the time associated with completion of QC testing and transporting FDG to the PET suite. This would lead to the delivery of a ~700 mCi dose, which is compatible with the limits of the Intego PET Infusion system (discussed above). As with all new instruments several optimization studies with the updated cyclotron were required before a 55 μA proton beam for 22 min was decided upon. This generates 1330 ± 153 mCi of [^{18}F]fluoride (n = 235). These cyclotron beam parameters combined with the DUO cassettes on FASTLab 2 results in radiochemical yields (RCYs) of 957 ± 102 mCi at EOS, corresponding to 72% non-corrected radiochemical yield. Production of this sized dose of FDG twice daily, once at 8:00 am

Figure 4-10: Bayer Medrad® Intego PET Infusion System.

and once at 2:00 pm allows for the scanning of up to 32 patients a day with FDG over 12 hours on two clinical PET scanners.

C. Experimental Methods

i. Synthesis of [^{18}F]Fludeoxyglucose ([^{18}F]FDG, FDG)

Synthesis of FDG was performed on either a GE TRACERLab$_{MX\text{-}FDG}$ as previously described,[28] or GE FASTLab 2 synthesis module as follows: [^{18}F]fluoride (produced on a GE PETTrace via the ^{18}O(p,n)^{18}F) was delivered from the cyclotron and trapped on a quaternary methylammonium (QMA) cartridge. Potassium carbonate (K_2CO_3) and kryptofix-2.2.2 ($K_{2.2.2}$) were used to elute the [^{18}F]fluoride from the QMA into the reactor, followed by azeotropic drying. A solution of mannose triflate **4.9** in acetonitrile was added to the reaction vial and radiofluorination of the mannose triflate precursor was conducted at 125 °C for 2 min to give [^{18}F]fluoro-1,3,4,6-tetra-*O*-acetyl-D-glucose ([^{18}F]FTAG, **4.10**, Scheme 4-2). The reaction mixture containing **4.10** was diluted with water and passed through a C-18 Sep-Pak cartridge, trapping the intermediate **4.10**. Base hydrolysis occurred on the cartridge at room temperature using 2N NaOH for 3 min to give [^{18}F]FDG. The hydrolyzed product was then eluted from the cartridge with citrate buffer, passed through a second C-18 Sep-Pak (to remove any un-hydrolyzed [^{18}F]FTAG), followed by an alumina-N cartridge (to remove any residual [^{18}F]fluoride ion). The final product was then transferred into a sterile intermediate vial pre-charged with water for injection, USP, and sodium phosphate buffer for injection, USP. Dispensing of the resulting solution (~28 mL) took place by passing the solution through a 0.22 μm sterile filter, and into patient

(~25 mL), quality control (~0.5 mL) and sterility (2.5 mL) vials using an Eckert and Ziegler Modular Lab automated dispensing system (Figure 4).

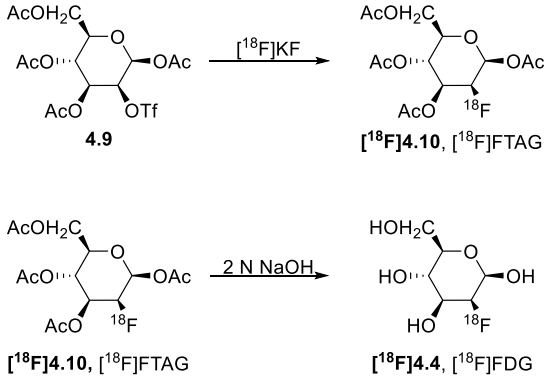

Scheme 4-2. Synthesis of FDG

ii. Quality Control of [^{18}F]Fludeoxyglucose

Quality control testing of each FDG doses was conducted according to the guidelines outlined in 21CFR212 as described below.

a. Visual Inspection

The [^{18}F]FDG dose must be clear, colorless, and free of particulate matter. This must be inspected behind proper shielding. A PET L-block barrier system was used.

b. Radiochemical Identity and Purity

Radiochemical identity and purity was determined by thin layer chromatography (TLC) using silica gel chromatography plates and a Bioscan AR-2000 TLC scanner (Figure 4-11). The plate was spotted with approximately 10 µg of FDG reference standard solution and then spotted with a sample of [^{18}F]FDG dose. The FDG TLC reference standard solution was prepared by dissolving 10 mg of 2-fluoro-2-deoxy-d-glucose in a 1:1 mixture of MeCN and water (50 µL:50 µL). The developing solution, or mobile phase, contained 95% acetonitrile and 5% water. The plate was developed in this solvent system in a glass

TLC jar reserved for FDG analysis, and the solution allowed to run just to the top of the plate. The developed plate was dried using a warm laboratory hot plate (temperature setting 5) and placed on the TLC scanner for analysis. The Bioscan TLC Scanner measured the radiochemical purity, which must be greater than or equal to 90%.

Radiochemical identity was determined by analysis and comparison of the retention factor of the standard and dose on TLC. Both purity and identity analysis are completed from a single TLC plate that was developed and dried, as described above. Heating the plate

Figure 4-11: BioScan RadioTLC scanner.

caused the standard to appear visibly brown, after which the plate was removed and placed on the TLC scanner for analysis. The Rf was calculated for the radiolabeled [^{18}F]FDG sample by the TLC scanner. The “cold” FDG reference standard retention factor was calculated manually and compared with the [^{18}F]FDG sample, the radioactivity distribution of which is determined by use of the Bioscan AR-2000 TLC scanner. This method provides excellent separation of free [^{18}F]fluoride, desired [^{18}F]FDG, and acetylated (non-hydrolized) [^{18}F]FDG ([^{18}F]FTAG) with Rf values of about 0.45, 0.0, and 0.85, respectively.

c. Radionuclidic Identity

A Capintec CRC-15R Radioisotope Dose Calibrator was used to measure activities. A sample of the [^{18}F]FDG product was placed in the Capintec Dose Calibrator located behind an L-block lead shield and measured, noting both the time and activity. After a period of at least 15 min, time and activity was noted again. The half-life was calculated using Equation 4-1, which must be within the range of 105–115 min for the dose to be released to the clinic.

$$t_{\frac{1}{2}} = -\ln 2 \left(\frac{\text{time difference}}{\ln \left[\frac{\text{ending activity}}{\text{starting activity}} \right]} \right)$$

Equation 4-1: Calculation of half-life.

d. Residual Solvent Analysis

Residual solvent analysis (RSA) of [^{18}F]FDG was performed on a Shimadzu GC-2010 Gas Chromatograph. The [^{18}F]FDG doses were tested for acetonitrile and ethanol concentration levels and compared with a standard solution in accordance with the US Pharmacopeia (USP). The standard solution contained known concentrations of acetonitrile and ethanol, 0.01% and 0.1%, respectively. GC conditions were as follows: a Restek Stabilwax with Integra-Guard 30 m × 0.25 mm GC column, with helium carrier gas. Concentration percentages were calculated, and no more than 0.5% ethanol and 0.04% acetonitrile can be found in the dose, according to the USP. ICH Hamonised Tirparitite Guildlines limit acetonitrile, a class 2 solvent, levels to <410 ppm per patient per day. Ethanol, a class 3 solvent, has a limit of <5000 ppm/day.

e. Dose pH

Dose pH of a small amount [^{18}F]FDG dose was analyzed with colorpHast© nonbleeding pH strips. The chosen colorpHast nonbleeding pH strips have specification range of 2.0–9.0, and the determination of pH was done by visual comparison of the pH strip with the reference card supplied with the strips. The pH must be within the range of 4.5–7.5 to meet the release criteria.

f. Residual Kryptofix-[2.2.2] Analysis

Kryptofix-[2.2.2] (K_{222}) is a phase transfer catalyst (PTC) used to facilitate the nucleophilic fluorination reaction for [^{18}F]FDG. Toxicity of K_{222} necessitates the verification of the absence of this PTC in the dose before its release. Residual Kryptofix-[2.2.2] levels in [^{18}F]FDG were analyzed using the established spot test. Both water (negative control) and a 50-µg/mL standard (positive control) were used in this test.

Kryptofix standards were prepared by serial dilution of a 1.0 mg/mL stock solution using deionized water. Indicator strips were prepared by immersing pre-cut strips of thin-layer silica gel in a stock iodoplatinate reagent for 5-10 seconds, when complete saturation occurred. Once the strips had been completely saturated by the reagent, they were allowed to dry overnight and then stored at room temperature in a vented glass jar. This stock reagent was prepared using 5 mL of water mixed with 0.26 g of chloroplatinic acid, and then mixing this solution with 45 mL of water and 5 g of potassium iodide and diluted with an additional 100 mL of water.

A single droplet of the [^{18}F]FDG dose was applied to the indicator strip, before the additional droplets of both the negative water control and the Kryptofix standard (50

µg/mL) were applied and allowed to dry for 5–10 min. All three spots were analyzed, and a visual determination of the relative concentration of Kryptofix-[2.2.2] was made for the [^{18}F]FDG dose.

Kryptofix-[2.2.2] presents as an appearance of a blue-black ring around a white circle of silica surrounded by a pink ring of unreacted reagent. At very low or no concentrations of Kryptofix, a faint pink core remains in the center of the white circle, with no visible blue-black ring, and the spot will look more similar to the sterile water negative control, than the 50 µg/mL positive standard. The dose must contain <50 µg/mL for the dose to be acceptable for release.

g. Sterile Filter Integrity Test

The integrity of the sterile filter used for sterile dispensing of the dose must also be validated before the release of the dose to the clinic. The dose sterility results will not be available until 14 days post-production of the [^{18}F]FDG dose, and so the filter integrity test is essential in testing [^{18}F]FDG product sterility. The Millex-GS sterile filter from the [^{18}F]FDG dispensing was attached to the nitrogen supply through a calibrated regulator. The filter is then connected to a needle so that the filter does not need to be submerged in water. The tip of the needle was then submerged in water. The nitrogen flow was gradually turned on to increase the nitrogen pressure on the filter. The pressure was increased to greater than 30 psi, which is the acceptance criterion for the Millipore-GS filter. If the pressure reaches 30 psi or more without resulting in a stream of bubbles in the water, the filter is considered intact. The pressure at which a steady stream of bubbles

appears is recorded. If a steady stream of bubbles is seen before the minimum bubble point pressure is reached, the test fails, and the dose is rejected.

h. Endotoxin Analysis

The Charles River Portable Testing System (PTS) with Limulus Amoebocyte Lysate (LAL) test cartridges, purchased from Charles River were used to determine the endotoxin content in the [^{18}F]FDG doses. A volume of 0.1 mL of the [^{18}F]FDG dose was added to a plastic tube containing 3.9 mL of Endosafe LAL Reagent water and mixed for 10 s using a vortex. A 25 µL sample of the diluted [^{18}F]FDG sample was added to each well on the Charles River PTS cartridge, and the test began. This was performed in accordance with the USP. The dose must contain ≤175 Endotoxin Units (EU) per dose.

i. Sterility Testing

To verify that the process by which each PET radiopharmaceutical is produced is consistently sterile and suitable for human use, sterility testing must also be performed on all doses of [^{18}F]FDG produced. Sterility testing was performed by inoculating samples of [^{18}F]FDG into both a fluid thioglycolate media (FTM) and a soybean casein digest media (SCDM). SCDM is used for the detection of aerobic bacteria and fungi, while the general purpose of FTM is to detect common aerobic, facultative, and anaerobic microorganisms.

The [^{18}F]FDG inoculated medium was incubated along with positive and negative controls for 14 days. Incubation temperatures were 32°C and 22°C for FTM and SCDM, respectively, according to current USP guidelines for sterility testing. The media was visually inspected on the third, eighth, and fourteenth days of the incubation test period

and compared to the positive and negative controls. The positive control must show growth (cloudiness or turbidity) in the medium, and the [^{18}F]FDG samples and negative control must show no growth after 14 days of incubation in order for the dose to pass the sterility test.

iii. Experimental Results and Conclusion

For comparison of the TRACERLab$_{MX\text{-}FDG}$ module produced [^{18}F]FDG doses with those produced by the new FASTLab 2 modules, yields, as well as all QC results were compiled for comparison. Table 4-1 represents the QC results for all of the FASTLab [^{18}F]FDG doses produced in the U of M PET Center in 2017. Each dose meets or exceeds the necessary specifications.

Table 4-1: Tabulated results for n = 386 production runs of [18F]FDG on the FASTLab 2 modules.

For [^{18}F]FDG Doses Produced by FastLab (n= 386)	**Specification**	**Results**
Yield @ EOS	N/A	747.8 ± 76.7 mCi
Visual Inspection	Clear, colorless, no precipitate	Passes
Identity (difference in TLC plate)	<0.05	0.02 ± 0.01
Purity	>90%	98.5 ± 1.7 %
pH	5.0 - 7.0	5.9 ± 0.2
RSA Acetonitrile	<0.5% (v/v)	0.215 ± 0.046%
RSA Ethanol	<0.04% (v/v)	0.003 ± 0.001%
Filter integrity (bubble point)	>30 psi	54 ± 4
Endotoxin	<9.00	2.00 ± 0.04
Sterility	Sterile	Passes

The plots in figure 4-11 demonstrate the vast increase in overall yield produced by the FASTLab synthesis module as compared to the TracerLab MX-FDG module (left,747.8±76.7 mCi and right, 449.3±60.4 mCi, averages ± StDev respectively). Although the overall average yields for the FASTLab were higher, the standard

deviation indicates that there are still some issues with consistency. This is due to a multitude of factors including how often the cyclotron has been run in a given day, as well as any maintenance that may have taken place either in the hot cell, on the module itself, or on the cyclotron or targets. It is expected that the next year of FASTLab production will be more consistent, the cyclotron just having had its 10-year preventative maintenance and target replacements.

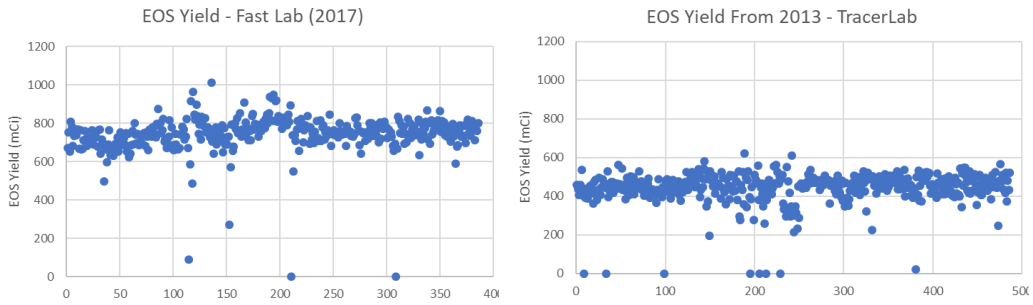

Figure 4-12: End of synthesis (EOS) yields for the FASTLab (left) and the TRACERLab$_{MX\text{-}FDG}$.

This chapter has discussed the history, regulation, utility and daily production of [^{18}F]FDG. Also discussed was the recent update of the [^{18}F]FDG production workflow in the U of M PET Center. The combination of the FASTLab 2 synthesis modules and self-shielded Nb fluorine-18 cyclotron targets has been shown to be reliable, demonstrating repeatable manufacture of high yielding doses of FDG. The FASTLab modules haven proven to be a robust and reliable platform with an uptime >99% over the past 18 months of continued twice daily FDG production. The simplification of our workflow, inventory management and regulatory compliance as a result of the synthesis module and cyclotron upgrade, leading to a decrease in patient wait times for FDG PET by half, from four days to two days at our nuclear medicine clinic, as a result of our increased FDG production capacity.

D. REFERENCES

(1) Ido, T.; Wan, C.-N.; Casella, V.; Fowler, J. S.; Wolf, A. P.; Reivich, M.; Kuhl, D. E. *J. Label. Compd. Radiopharm.* **1978**, *14* (2), 175–183.

(2) Reivich, M.; Kuhl, D.; Wolf, A.; Greenberg, J.; Phelps, M.; Ido, T.; Casella, V. *Circ. Res.* **1979**, *44* (1), 127–137.

(3) Pacák, J.; Točík, Z.; Černý, M. *J. Chem. Soc. D* **1969**, No. 2, 77.

(4) Basu, S.; Hess, S.; Nielsen Braad, P. E.; Olsen, B. B.; Inglev, S.; Høilund-Carlsen, P. F. *PET Clin.* **2014**, *9* (4), 355–370.

(5) Houn, F. Review of F-18 Fluoro-2-Deoxyglucose (F-18 FDG) Positron Emission Tomography in the Evaluation of Malignancy - August 4, 1999 https://www.fda.gov/Drugs/DevelopmentApprovalProcess/Manufacturing/ucm182668.htm#References (accessed Aug 9, 2018).

(6) Avril, S.; Muzic, R. F.; Plecha, D.; Traughber, B. J.; Vinayak, S.; Avril, N. *J. Nucl. Med.* **2016**, *57* (Supplement_1), 34S–39S.

(7) Spick, C.; Herrmann, K.; Czernin, J. *J. Nucl. Med.* **2016**, *57* (3), 420–430.

(8) Delbeke, D. *J. Nucl. Med.* **1999**, *40* (4), 591–603.

(9) Kim, Y. K.; Lee, D. S.; Kun, S. L.; Chun Chung Kee; Chung, J.-K.; Lee, M. C. *J Nucl Med* **2002**, *43* (9), 1167–1174.

(10) Smailagic, N.; Lafortune, L.; Kelly, S.; Hyde, C.; Brayne, C. *J. Alzheimer's Dis.* **2018**, *64* (4), 1175–1194.

(11) Ahmadian, A.; Pawar, S.; Govender, P.; Berman, J.; Ruberg, F. L.; Miller, E. J. *J. Nucl. Cardiol.* **2017**, *24* (2), 413–424.

(12) Manabe, O.; Ohira, H.; Yoshinaga, K.; Naya, M.; Oyama-Manabe, N.; Tamaki, N.

Ann. Nucl. Cardiol. **2017**, *3* (1), 117–120.

(13) Osborne, M. T.; Hulten, E. A.; Murthy, V. L.; Skali, H.; Taqueti, V. R.; Dorbala, S.; DiCarli, M. F.; Blankstein, R. *J. Nucl. Cardiol.* **2017**, *24* (1), 86–99.

(14) PET Imaging Market Summary Report 2018. https://imvinfo.com/product/pet-imaging-market-summary-report-2018/ (accessed Aug 11, 2018).

(15) Nelson, C. A.; Wang, J. Q.; Leav, I.; Crane, P. D. *Nucl. Med. Biol.* **1996**, *23* (4), 533–541.

(16) Spieth, M. E.; Kasner, D. L. *J. Nucl. Med.* **2001**, *42* (5), 1S–93S.

(17) Groheux, D.; Giacchetti, S.; Hatt, M.; Marty, M.; Vercellino, L.; De Roquancourt, A.; Cuvier, C.; Coussy, F.; Espié, M.; Hindié, E. *Br. J. Cancer* **2013**, *109* (5), 1157–1164.

(18) Evans, J. D.; Jethwa, K. R.; Ost, P.; Williams, S.; Kwon, E. D.; Lowe, V. J.; Davis, B. J. *Pract. Radiat. Oncol.* **2018**, *8* (1), 28–39.

(19) Bohnen, N. I.; Djang, D. S. W.; Herholz, K.; Anzai, Y.; Minoshima, S. *J. Nucl. Med.* **2012**, *53* (1), 59–71.

(20) Minoshima, S.; Foster, N. L.; Sima, A. A. F.; Frey, K. A.; Albin, R. L.; Kuhl, D. E. *Ann. Neurol.* **2001**, *50* (3), 358–365.

(21) Juhász, C.; Chugani, H. T. *Neuroimaging Clin. N. Am.* **2003**, *13* (4), 705–716.

(22) Lamusuo, S.; Jutila, L.; Ylinen, A.; Kalviainen, R.; Mervaala, E.; Haaparanta, M.; Jaaskelainen, S.; Partanen, K.; Vapalahti, M.; Rinne, J. *Arch Neurol* **2001**, *58* (6), 933–939.

(23) *Current good manufacturing practice for positron emission tomography drugs: preliminary draft proposed rule.*; 1995; Vol. 60, p 10594.

(24) World Health Organization. Radiopharmaceuticals: Final text for addition to The International Pharmacopoeia http://www.who.int/medicines/publications/pharmacopoeia/Radgenmono.pdf.

(25) Burr, R. H.R.1411 - Food and Drug Administration Regulatory Modernization Act of 1997 https://www.congress.gov/bill/105th-congress/house-bill/1411/text (accessed Aug 7, 2018).

(26) Food and Drug Administration of the United States of America. *Fed. Regist.* **2000**, *65* (48), 12999–13010.

(27) Schwarz, S. W.; Dick, D.; VanBrocklin, H. F.; Hoffman, J. M. *J. Nucl. Med.* **2014**, *55* (7), 1132–1137.

(28) Richards, M. L.; Scott, P. J. H. In *Radiochemical Syntheses: Radiopharmaceuticals for Positron Emission Tomography, Volume 1*; Scott, P. J., Hockley, B. G., Eds.; 2012; pp 3–13.

Chapter 5

Overall Conclusions and Future Outlook

A. Summary and Future Outlook

Reported in this thesis are the most recent efforts towards development of GAT-1 selective PET radiotracers. Through the synthesis, radiolabeling, and evaluation, both *in vivo* and *in vitro*, it has been found that the classical GABA uptake inhibitors modeled after tiagabine are not suitable for PET imaging of the potentially underutilized biological target GAT-1. These classical GAT-1 inhibitors utilized nipecotic acid as the biologically active moiety, with a lipophilic side chain to increase blood-brain barrier (BBB) penetration. Such compounds have proven effective for therapeutic dosing, where it is possible to titrate a dose over a timespan of weeks to accumulate enough drug in the brain to elicit a pharmacological effect. However, we have shown such strategies are not applicable to the PET field, where the amount of tracer used is on the microgram scale and the short-lived radionuclides employed dictate the necessity for rapid uptake in the brain at sufficient levels to obtain a PET scan, in only ~60-90 minutes post-injection.

The work reported in Chapters 2 and 3 of this thesis demonstrate that simple nipecotic acid derivatives do not penetrate the blood-brain barrier, and even incorporation of highly lipophilic side chains to increase log P of the radiotracer does not facilitate brain uptake. While reasons for the lack of brain uptake of compounds like (*R, E/Z*)-**[^{18}F]2.11** have not been confirmed, studies presented in this thesis suggest that the highly zwitterionic character of the carboxylic acid moiety on nipecotic acid could be a

contributing factor. It has been hypothesized that one way to overcome this challenge and adapt classical GABA uptake inhibitors for application in PET imaging is through the use of a bioisosteric replacement of the carboxylic acid functionality. Preliminary work towards addressing this issue has been discussed in Chapter 3 of this thesis. The preliminary studies included initial evaluation of bioisosteres in a brain homogenate GABA uptake inhibition assay, and attempted synthesis of various bioisosteres such as the piperidinyl-3-tetrazole and piperidinyl-3-thiazole. While synthesis of the piperidinyl-3-tetrazole has proved challenging to date, it remains a scaffold of interest for future development.

In lieu of the tetrazole, a more lipophilic 5-membered hetero-ring, the thiazole, was evaluated. Derivatives of nipecotic acid bearing the thiazolyl bioisostere have proven to be readily accessible, and it has been shown that a **[^{11}C]3.31** is readily prepared in high yields (131 ± 61 mCi) and high specific activity (2500 ± 1000 mCi). Initial *in vitro* evaluation of **[^{11}C]3.31** determined that it has high affinity for GAT-1 (K_d = 2.26 nM), while *in vivo* evaluation showed excellent brain uptake in rodents and nonhuman primates. There was high uptake in the cortex, which is to be expected for a GAT-1 radiotracer.

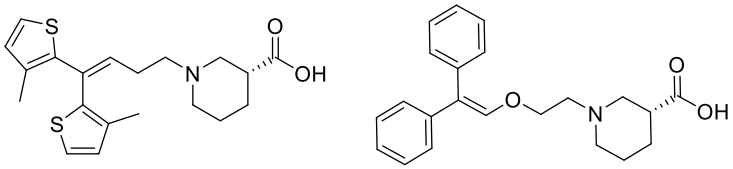

5.1, tiagabine **5.2**

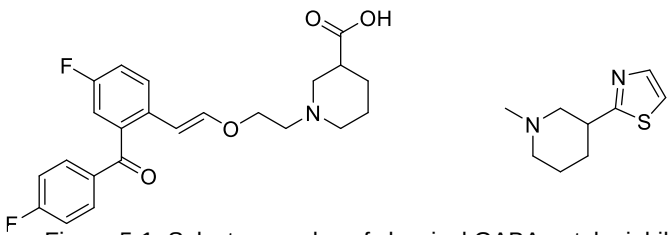

Figure 5-1: Select examples of classical GABA uptake inhibitors employing nipecotic acid and selective for GAT-1 (**5.1, 5.2, 2.11**). And the successful thiazole bioisostere (**3.31**).

Future work will be focused on further evaluation of **[^{11}C]3.31** to determine its imaging properties and selective target engagement. This can be achieved by using

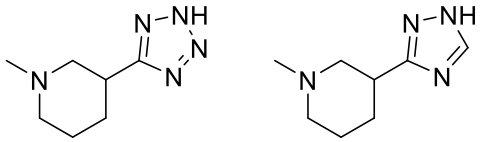

5.3, ClogP 0.114 **5.4**, ClogP 0.286

Figure 5-2: Tetrazole and triazole molecules for use as nipecotic acid bioisosteres.

nipecotic acid and tiagabine in competition assays. If selectivity between GABA transporter subtypes is not achievable with **3.31**, further investigation of a thiazole as a successful bioisostere could include the incorporation of the thiazole into the scaffold of the GAT-1 selective scaffolds described throughout this thesis (Figure 5-1).

A triazole based scaffold could also be of interest for bioisosteric replacement of the carboxylic acid. A triazole, such as **5.4**, still contains an acidic proton, while retaining slightly more lipophilicity than the tetrazole based scaffold.

Since the nipecotic acid core is the most-well known GAT pharmacophore, it is also worth determining if it can be modified in other ways to enhance brain uptake. One attractive approach often used in drug design is the incorporation of fluorine atoms into a given scaffold.[1] It is known that careful introduction of fluorine into drug molecules can drastically alter pK_a and pharmacokinetics (See Figure 5-3). Thus it is worth exploring the difluorinated nipecotic acids such as **5.6** (Figure 5-3); incorporation of such difluorinated

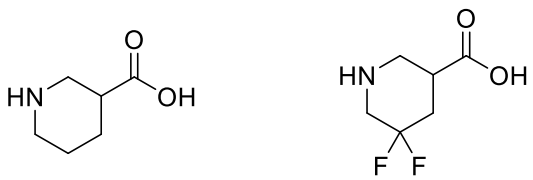

5.5, pKa: 9.984, 2.610 **5.6**, pKa: 7.828, 2.209

Figure 5-3: Comparison of pKas of non- and di-fluorinated nipecotic acid.

piperidines has been shown in the literature to improve BBB permeability.[2] The fluorination of the piperidine of nipecotic acid would make the amine much less basic, alleviating the hypothesized zwitterionic character of the parent nipecotic acid, and allowing for the use of the carboxylic acid pharmacophore in a GAT-1 PET radiotracer. Radiotracers incorporating such a fluorinated nipecotic acid moiety could potentially be radiolabeled with high specific activity fluorine-18 or carbon-11 using the radiochemistry methods described throughout this thesis. *In vitro* and *in vivo* evaluation using the same imaging, autoradiography and immunohistochemistry techniques described herein will be required to determine the effects of fluorine incorporation on BBB permeability and the pharmacological profile of the GAT pharmacophore.

Finally, other GABA transporters continue to be relatively under investigated, but recent studies have reported selective and potent inhibitors of other subtypes such as GAT-2 and GAT-3.[3,4] For example, a small library of amino-methyl tetrazoles were recently reported (**5.7**).[5] These non-classical GABA uptake inhibitors are based on a bioisostere of glycine. Another attractive scaffold that shows selectivity for inhibition of glial GABA uptake was reported by Clausen and coworkers in 2006 (**5.8**).[6] These molecules are lipophilic derivatives of *exo*-THPO, a muscimol analog. Both of these scaffolds could prove to be interesting for development of a PET tracer for imaging of the glial GABA transporter.

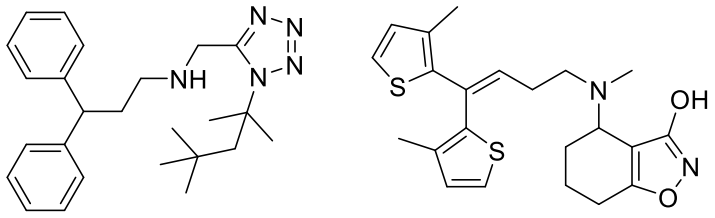

5.7 **5.8**

Figure 5-4: Molecules for the potential targeting of glial uptake PET imaging.

B. Overall Conclusions

In summary, we and others have spent considerable research effort to enable PET imaging of GABA transporters, with a focus on neuroimaging of GAT-1. However, challenges with brain uptake of classical GAT-1 inhibitors in the time frame of a PET scan means that PET imaging of GAT-1 currently remains elusive. Nevertheless, this thesis provides an important contribution to the GAT-1 literature as it suggests that we will never be able to develop PET radiotracers for GAT-1 by employing the nipecotic acid core because its highly polar zwitterionic nature is not conducive to BBB permeability. As the acid group is necessary for high affinity binding to GAT-1, it cannot be simply removed or esterified. Therefore, future efforts in GAT-1 radiotracer design will need to investigate carboxylic acid bioisosteres or analogs of nipecotic acid (such as fluorinated nipecotic acid derivatives) in an attempt to improve brain uptake while maintaining affinity for GAT-1. Our preliminary efforts in this direction have shown good promise and will be pursued further going forward.

C. References

(1) Gillis, E. P.; Eastman, K. J.; Hill, M. D.; Donnelly, D. J.; Meanwell, N. A. *J. Med. Chem.* **2015**, *58* (21), 8315–8359.

(2) Gomez, L.; Massari, M. E.; Vickers, T.; Freestone, G.; Vernier, W.; Ly, K.; Xu, R.; McCarrick, M.; Marrone, T.; Metz, M.; Yan, Y. G.; Yoder, Z. W.; Lemus, R.; Broadbent, N. J.; Barido, R.; Warren, N.; Schmelzer, K.; Neul, D.; Lee, D.; Andersen, C. B.; Sebring, K.; Aertgeerts, K.; Zhou, X.; Tabatabaei, A.; Peters, M.; Breitenbucher, J. G. *J. Med. Chem.* **2017**, *60* (5), 2037–2051.

(3) Falch, E.; Perregaard, J.; Frølund, B.; Søkilde, B.; Buur, A.; Hansen, L. M.; Frydenvang, K.; Brehm, L.; Bolvig, T.; Larsson, O. M.; Sanchez, C.; White, H. S.; Schousboe, A.; Krogsgaard-Larsen, P. *J. Med. Chem.* **1999**, *42* (26), 5402–5414.

(4) Clausen, R. P.; Moltzen, E. K.; Perregaard, J.; Lenz, S. M.; Sanchez, C.; Falch, E.; Frølund, B.; Bolvig, T.; Sarup, A.; Larsson, O. M.; Schousboe, A.; Krogsgaard-Larsen, P. *Bioorganic Med. Chem.* **2005**, *13* (3), 895–908.

(5) Schaffert, E. S.; Höfner, G.; Wanner, K. T. *Bioorg. Med. Chem.* **2011**, *19* (21), 6492–6504.

(6) Clausen, R. P.; Frølund, B.; Larsson, O. M.; Schousboe, A.; Krogsgaard-Larsen, P.; White, H. S. *Neurochem. Int.* **2006**, *48* (6–7), 637–642.